DYNAMICS OF CURRENTS AND SEDIMENT IN ESTUARIES WITH DIFFERENT DENSITY STRATIFICATIONS

Wei Chen

Institute for Marine and Atmospheric research Utrecht (IMAU)
Faculty of Science, Department of Physics
Utrecht University, The Netherlands

Cover Image: The MODIS image of a sediment plume over the East China Coast captured by NASA's Terra satellite on November 9, 2017 (source: https://earthobservatory.nasa.gov/IOTD/view.php?id=91325&src=iotdrss)

ISBN: 978-94-6299-884-1
Printing: Ridderprint BV
Copyright © 2018, Wei Chen. All Rights Reserved.

DYNAMICS OF CURRENTS AND SEDIMENT IN ESTUARIES WITH DIFFERENT DENSITY STRATIFICATIONS

Dynamica van stromingen en sediment in estuaria met verschillende dichtheidsstratificaties

(met een samenvatting in het Nederlands)

ter verkrijging van de graad van doctor aan de Universiteit Utrecht op gezag van de rector magnificus, prof.dr. G.J. van der Zwaan, ingevolge het besluit van het college voor promoties in het openbaar te verdedigen op woensdag 7 maart 2018 des middags te 4.15 uur

door

WEI CHEN

geboren op 24 februar 1986 te Songzi, China

PROMOTOREN: Prof.dr. H. E. de Swart

This thesis was accomplished with financial support from China Scholarship Council (CSC).

CONTENTS

SUMMARY

Estuaries are important geomorphic units of coastal zones, as they provide critical habitat and shelter for a large variety of living species and moreover, they have a high economic demand. Due to different intensities of tidal currents at the estuarine mouth and river discharge from land, estuaries show large variations in density stratification and are characterized by complex hydrodynamic and sediment processes. Inspired by field observations and recent studies, this thesis focuses on gaining further knowledge about three key issues, i.e., tidal currents, residual currents and suspended sediment trapping in estuaries with different density stratifications.

Several field studies in bays and estuaries have revealed pronounced subsurface maxima in the vertical profiles of either the current amplitude of the principal tidal harmonic, or of its vertical shear. To gain fundamental understanding about these phenomena, a semi-analytical model is designed and analysed in chapter 2. The new analytical solutions of the tidal current amplitude are used to explore their dependence on the degree of surface turbulence, the vertical shape of eddy viscosity in the upper part of the water column and on the density stratification. Sources of surface turbulence are wind and whitecapping. Results show three types of current amplitude profiles of tidal harmonics, characterised by monotonically decreasing shear towards the surface, "surface jumps" (vertical shear of tidal current amplitude has a subsurface maximum) and "subsurface jets" (maximum tidal current amplitude below the surface), respectively. The physics causing the presence of surface jumps and subsurface jets is different. The "surface jumps" occur for moderate stratifications and if the eddy viscosity in the upper part of the water column decreases faster than linearly to the surface. Under these conditions, the turbulence is strong enough so that near the surface the generation vertical shear of tidal currents by the curvature of eddy viscosity overcomes the decay of the vertical shear of tidal currents by turbulent exchange processes. "Subsurface jets" occur in highly stratified conditions, in which turbulent vertical exchange of horizontal momentum only takes place in the bottom boundary layer. Here, the primary balance between local inertia, the horizontal pressure gradient force and the friction causing an exponentially decaying oscillatory vertical structure of the tidal current amplitude with increasing height above the bottom.

In chapter 3, residual currents generated by Eddy viscosity-Shear Covariance (ESCO) in a narrow estuary is investigated with a numerical model. New aspects concern the dependence of the spatial structure of ESCO current on (1) longitudinal depth variation for fixed semi-diurnal tidal forcing, (2) vary-

ing amplitude of the semi-diurnal tidal forcing, and (3) mixed tidal forcing for fixed stratification at the mouth. Here, mixed tidal forcing concerns an externally forced tide that contains one semi-diurnal and two diurnal constituents. Regarding (1) and (2), it appears that ESCO current merely involves the components due to the semi-diurnal tide (u_{τ,M_2}) and quarter-diurnal tide (u_{τ,M_4}). For a periodically stratified estuary, u_{τ,M_2} is stronger than u_{τ,M_4} in the middle reach, and weaker in the upper (landward) and lower (seaward) reach, while both show a two-layer structure with seaward current near the surface. For weak stratification, u_{τ,M_2} has a three-layer structure with seaward current in the middle layer, while u_{τ,M_4} has a two-layer structure and contributes significantly to the total residual current in the upper and lower reach. For a highly stratified estuary, u_{τ,M_2} dominates the ESCO current (being weak compared to the total residual current), and it has a reversed two-layer structure (seaward current near the bottom). Regarding (3), if diurnal and semi-diurnal tides are of a similar order, the ESCO current due to diurnal tides dominates and it has a two-layer structure. If diurnal tides prevail, the ESCO current induced by the current that caused by the long-period variation in stratification is the main contributor to the total residual current in the upper and lower reach of the estuary. This long-periodic tide is generated by joint action of the two diurnal components.

Chapter 4 investigates the longitudinal variation in locations where lateral entrapment of suspended sediment occurs, as is observed in some tidal estuaries. In particular, field data from the North Passage of the Yangtze Estuary are analysed, which reveal that in one cross-section two maxima of suspended sediment concentration (SSC) occur close to the south and north side, while in a cross-section 2 km down-estuary only one SSC maximum on the south side is present. This pattern is found during both spring tide and neap tide, which are characterised by different intensities of turbulence. To understand longitudinal variation in lateral trapping of sediment, results of a new three-dimensional exploratory model are analysed. The hydrodynamic part contains residual currents due to fresh water input, density gradients, Coriolis force and due to channel curvature induced leakage. The leakage is a net water transport through the end of the cross-sections result from the depth integration of lateral residual current. It occurs because due to centrifugal forces, in the surface water layer flows from inner bend to outer bend and causes a set up of water at the outer bend, where net water mass will overflow the channel bank. Moreover, the model includes a spatially varying eddy viscosity that accounts for variation of intensity of turbulence over the spring-neap cycle. By imposing morphodynamic equilibrium (i.e., averaged over the tidal period, erosion balances deposition of sediment), the three-dimensional distribution of sediment in the domain is obtained analytically by a novel procedure. Results reveal that the occurrence of the SSC maximum near the north side of the first cross-section

is by sediment transport due to curvature induced leakage. The sediment trapping at the south side is due to lateral density gradients. Coriolis deflection of longitudinal current also contributes the trapping of sediment near the north side. This mechanism is important in the upper estuary, where the current due to lateral density gradients is weak.

The investigations that are reported in this thesis have provided new insight into several aspects of the dynamics of tidal currents, residual currents and sediment trapping. Still, further aspects deserve attention in future studies in estuaries. One example concerns the effect of depth variations in the lateral direction and multiple tidal constituents (such that the spring-neap cycles related to semi-diurnal harmonics is accounted for) on the generation of ESCO currents. Another example is the impact of tidal pumping (i.e., the net sediment transport due to covariance between tidal currents and the tidally varying SSC) on residual sediment trapping, which requires explicit resolving tidal motion for better understanding. Moreover, it is also important to investigate the covariance between temporally varying eddy diffusivity and the temporally varying vertical gradient of SSC on the residual trapping of sediment.

SAMENVATTING

Estuaria zijn de overgangsgebieden tussen rivier (zoet water) (zout water). Het zijn belangrijke geomorfologische eenheden van kustzone, o.a. omdat ze een leefomgeving en schuilmogelijkheden bieden voor planten en dieren. Tevens zijn estuaria vanuit economisch oogpunt belangrijk, b.v. voor transport van mensen en goederen. Als gevolg van verschillende sterktes in getijstromingen en in zoetwatertoevoer laten estuaria grote verschillen zien in dichtheidsstratificatie en worden ze gekenmerkt door complexe hydrodynamische en complexe sedimentdynamica. Gemotiveerd door veldwaarnemingen en recente studies ligt de nadruk van dit proefschrift op het verkrijgen van meer fundamentele kennis over drie onderwerpen: getijstromingen, reststromingen en accumulatie van fijn sediment in estuaria met verschillende dichtheidsstratificaties.

Diverse observationele studies in baaien en estuaria hebben het bestaan aangetoond van maxima in de amplitudo van de stroomsnelheid, of in die van de verticale schering van de stroomsnelheid, op locaties onder het wateroppervlak. Om het bestaan van deze fenomenen te doorgronden is in hoofdstuk 2 een semi-analytisch model ontworpen en geanalyseerd. De nieuwe analytische oplossingen van de getijstroomamplitudo zijn gebruikt om hun afhankelijkheid te bestuderen van de mate van turbulentie aan het wateroppervlak, de verticale structuur van de turbulente verticale viscositeitscoëfficiënt in het bovenste deel van de waterkolom en van de dichtheidsstratificatie. De bronnen van turbulentie aan het wateroppervlak zijn wind en het breken van golven. Resultaten tonen aan dat er een drietal types profielen bestaan van de amplitudo van de stroomsnelheid. Zij worden achtereenvolgens gekenmerkt door een monotoon afnemende schering richting het wateroppervlak, door 'surface jumps' (verticale schering van de stroomsnelheidsamplitudo heeft een maximum onder het oppervlak) en door 'surface jets' (de amplitudo van de stroomsnelheid heeft een maximum onder het oppervlak). De 'surface jumps' manifesteren zich voor matige dichtheidsstratificatie en voor een profiel van de turbulente verticale viscositeitscoëfficiënt dat sneller dan lineair afneemt richting het wateroppervlak. In die omstandigheden kan nabij het wateroppervlak de generatie van verticale schering van getijstromingen t.g.v. de kromming van de verticale turbulente viscositeitscoëfficiënt groter zijn dan de afname van de schering t.g.v. turbulente menging. 'Surface jets' in estuaria en baaien manifesteren zich bij hoge dichtheidsstratificatie, wanneer er alleen significante turbulente uitwisselingsprocessen plaatsvinden in een dunne grenslaag nabij de bodem. Hier zorgt de primaire balans tussen lokale traagheid, drukgradiëntkracht en turbulente uitwisseling van horizontale impuls voor een exponentieel afnemende oscillerende verticale

structuur van de getijstroomamplitudo met toenemende afstand boven de bodem.

In hoofdstuk 3 is de dynamica van reststromingen, gegenereerd door 'Eddy viscosity-Shear COvariance' (ESCO), in een nauw estuarium bestudeerd m.b.v. een numeriek model. Zulke reststromingen ontstaan als de variatie van de turbulente viscositeitscoëfficiënt gedurende de getijperiode is gecorreleerd met de schering van de getijstroming. Andere bronnen voor reststromingen zijn o.a. rivierafvoer en horizontale dichtheidsgradiënten. Nieuwe aspecten die zijn onderzocht zijn de gevoeligheid van de ruimtelijke structuur van de ESCO stroming voor 1) longitudinale variaties in de waterdiepte voor constante getijforcering, 2) variaties in de amplitudo van het dubbeldaagse M2 getij bij de monding van het estuarium en 3) 'gemengde' getijforcering, bestaande uit een combinatie van één dubbeldaagse en twee enkeldaagse componenten, voor dezelfde dichtheidsstratificatie nabij de monding. Met betrekking tot 1) en 2) blijkt dat de ESCO stroming voornamelijk bestaat uit componenten die worden bepaald door het dubbeldaagse getij (u,M2) en door het M4 getij (u,M4). Voor een periodiek gestratificeerd getij is u,M2 groter dan u,M4 in het middelste gedeelte van het estuarium, en zwakker in het landwaartse en zeewaartse deel, terwijl beiden een tweelagenstructuur hebben met zeewaartse stroming nabij het oppervlak. Voor zwakke stratificatie heeft u,M2 een drielagenstructuur, met zeewaartse stroming in de middelste laag, terwijl u,M4 een tweelagenstructuur heeft en tevens significant bijdraagt aan de totale reststroming in het landwaartse en zeewaartse deel van het estuarium. Voor een sterk gestratificeerd estuarium is u,M2 de dominante ESCO component (welke zwak is t.o.v. de totale reststroming) en deze heeft een 'omgekeerde' tweelagenstructuur, met zeewaartse stroming nabij de bodem. Met betrekking tot 3), als de enkeldaagse en dubbeldaagse getijcomponenten van vergelijkbare grootteorde zijn domineert de enkeldaagse component de ESCO stroming en deze heeft een tweelagen structuur. Als de enkeldaagse getijcomponenten dominant zijn t.o.v. de dubbeldaagse component blijkt de ESCO stroming vooral bepaald te worden door de stroming welke wordt bepaald door de langperiodieke variatie in dichtheidsstratificatie. Laatstgenoemde wordt opgewekt door het samenspel van de twee enkeldaagse getijcomponenten.

Het onderwerp van hoofdstuk 4 betreft de longitudinale variaties van locaties in estuaria waar laterale accumulatie van fijn sediment optreedt. Zo blijkt uit analyse van waarnemingen in de 'North Passage' van het Yangtze Estuarium dat in een bepaalde dwarsdoorsnede twee maxima in zwevend stof concentratie optreden (nabij de noord- en zuidzijde van deze sectie), terwijl in 2 km verderop (zeewaartse) dwarsdoorsnede er slechts één maximum (aan de zuidzijde) blijkt te zijn. Deze patronen worden waargenomen gedurende zowel springtij als doodtij, welke worden gekenmerkt door verschillende intensiteit van turbulentie en verschillende dichtheidsstratificatie. Teneinde deze fenome-

nen te verklaren zijn resultaten van een nieuw driedimensionaal model geanalyseerd. Het hydrodynamische deel beschrijft reststromingen ten gevolge van rivierafvoer, horizontale dichtheidsgradiënten, Corioliskracht en ten gevolge van lekkage van kanaaldeel naar de overloopdelen. Laatstgenoemde wordt veroorzaakt door kromming van het kanaal, welke zorgt voor een centrifugaalkracht waardoor water in de oppervlaktelaag van binnenbocht naar buitenbocht stroomt. Het model bevat verder een ruimtelijk variabele turbulente viscositeitscoëfficiënt, die ook veranderingen in intensiteit van turbulentie over de spring-doodtij cyclus beschrijft. Door het toepassen van de conditie van morfodynamisch evenwicht (netto balans tussen erosie en depositie over een getijperiode) is de driedimensionale verdeling van sediment analytisch berekend d.m.v. een iteratieprocedure. Resultaten laten zien dat het optreden van een maximum in zwevend stof concentratie aan de noordzijde het gevolg is van sedimenttransport dat wordt veroorzaakt door de kromming geïnduceerde lekkage. De dwarssnelheid welke wordt veroorzaakt door Coriolisafbuiging van de longitudinale snelheid draagt ook bij aan accumulatie van sediment aan de noordzijde. Dit mechanisme is belangrijk in het rivierdeel van het estuarium, waar laterale dichtheidsgradiënten (welke voor accumulatie van sediment nabij de zuidzijde zorgen) zwak zijn.

De bevindingen welke zijn beschreven in dit proefschrift hebben tot nieuwe inzichten geleid met betrekking tot de dynamica van getijstromingen, reststromingen en accumulatie van sediment in estuaria. Er zijn echter nog aspecten, die verder toekomstig onderzoek behoeven. Een voorbeeld betreft de invloed van laterale dieptevariaties en van getijforcering met meerdere dubbeldaagse en enkeldaagse componenten op de generatie van ESCO reststromingen. Een ander voorbeeld betreft het bestuderen van de rol van sedimenttransport t.g.v. tijd variërende stroming en zwevend stof concentratie (bekend als 'tidal pumping') op de structuur van de tijdsgemiddelde zwevend stof concentratie te onderzoeken. Tot slot is het belangrijk om te onderzoeken in welke mate laterale en longitudinale accumulatie van sediment wordt beïnvloed door netto sediment transport welke wordt veroorzaakt door correlatie tussen de verticale turbulente diffusiecoëfficiënt en verticale gradiënten in zwevend stof concentratie.

1 INTRODUCTION

This thesis discusses the hydrodynamics and sediment dynamics of estuaries with different density stratification conditions. In this introduction, first (section 1.1) a physical definition of an estuary is given and some of its characteristics are described. After that (section 1.2), the relevance of studying hydrodynamics and sediment dynamics in estuaries is discussed, which is followed by a brief review of the present knowledge and gaps (in section 1.3). Finally, in section 1.4 the research questions are formulated and the outline of the remaining part of the thesis is presented.

1.1 ESTUARIES AND SOME OF THEIR CHARACTERISTICS

From a physical perspective, an estuary is defined as "a semi-enclosed body of water which has a free connection with the open sea and within which sea water is measurably diluted with fresh water derived from land drainage" (Pritchard, 1967). Here, the focus is on temperate estuaries, in which the sources of fresh water are rivers and the dilution is due to turbulent mixing that results primarily from tidal currents that move over a rough bottom. Examples of such estuaries are the Yangtze Estuary (east coast of China), the Ems Estuary (at the German-Dutch border) and the James River Estuary (east coast of the U.S.).

As is shown in Figure 1-1, for a given estuarine geometry, the longitudinal and vertical structure of the tidally averaged salinity is determined by the river discharge at the head and the intensity of tidal currents at the mouth. For high river discharge and weak tides, the estuary is known as a salt wedge estuary, in which vertical profiles of the tidally averaged salinity profiles exhibit a sharp pycnocline (Figure 1-1a). With smaller river discharge and stronger tides, the salt water is mixed upward, fresh water is mixed downward and the conditions in the estuaries change from strongly stratified (Figure 1-1b) to weakly stratified (Figure 1-1c) and ultimately to well-mixed (Figure 1-1d).

The hydrodynamics and sediment dynamics of estuaries are quite complex (Figure 1-2). The tides at the adjacent sea force currents in the estuary that con-

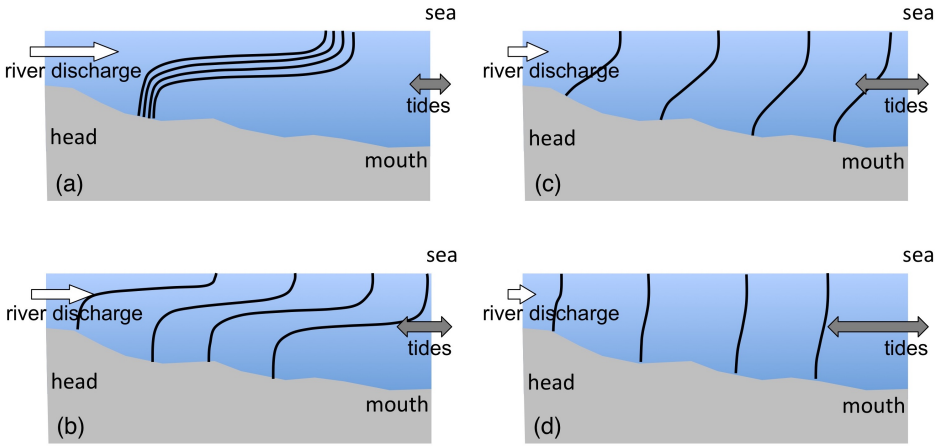

Figure 1-1: Examples of longitudinal-vertical distributions of tide-averaged salinity (black solid lines) in an estuary with different tidal forcing (intensity of tidal currents at the mouth) and river discharge at the head. Adapted version of Figure 1.3, Chapter 1 of Valle-Levinson (2010).

sist of different harmonics (Figure 1-2, the arrow denoted by ①, see section 1.3 for details). The river discharge at the head forces a seaward directed current (Figure 1-2, arrow ②) and also sets up a horizontal density gradient. The latter forces a so-called density driven current, which is directed landward near the bottom and seaward near the surface (Pritchard, 1956; Hansen and Rattray, 1965). As the time scale of these currents is much larger than the period of the dominant tide, it is called a subtidal current or residual current.

Tides also create residual currents (Figure 1-2, ③), owing to the nonlinear hydrodynamics. For example, covariance between the rise and fall of tidal level and the tidal currents generates a net landward water transport, which is compensated in the estuary by a seaward current, i.e., the Stokes return current (Ianniello, 1977). Moreover, net advection of tidal momentum by tidal currents (Fischer, 1972; Lerczak and Geyer, 2004; Huijts et al., 2009), channel curvature (Lacy and Monismith, 2001; Chant, 2002) and the covariance of tidally varying eddy viscosity and the vertical gradient of tidal velocity (Geyer and MacCready, 2014) are drivers of residual currents. Subtidal currents are further generated by, e.g., wind (Scully et al., 2009) and are modified by Coriolis deflection due to earth rotation (Winant, 2008). All subtidal currents together constitute the so-called estuarine circulation. Subtidal currents also affect tidal currents (Figure 1-2, ④), e.g., by enhancing the bottom friction that the latter experience (Godin, 1999; Hoitink and Jay, 2016).

Both tidal and residual currents not only directly transport salt (Figure 1-2 ⑤) and sediment (Figure 1-2 ⑥), but also affect salinity and SSC though turbu-

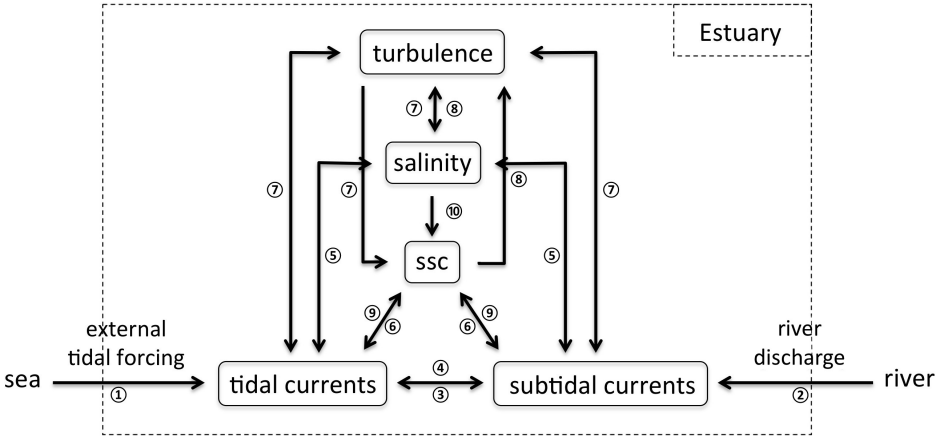

Figure 1-2: Sketch of physical processes in estuaries. Black dashed box denotes the area of the estuary. Here, "ssc" denotes suspended sediment concentration.

lence (Figure 1-2 ⑦). Moreover, turbulence erodes sediment from the bottom. Meanwhile, salinity and suspended sediment concentrations (SSC) affect the structure of turbulence (Figure 1-2 ⑧) and of currents (Figure 1-2 ⑨). For example, horizontal density gradients due to sediment concentration (Talke et al., 2009a) induce a residual current, while vertical density gradients due to salt and due to SSC suppress turbulence (Ozmidov, 1965). Furthermore, as the settling velocity of sediment particles depends on salinity-induced flocculation (Thill et al., 2001), SSC is also directly affected by salt (Figure 1-2 ⑩).

The concepts discussed so far have been implemented in many different models. Figure 1-3 illustrates, based on model results of Geyer and MacCready (2014), how the competition between river discharge and tidal forcing results in different stratification conditions at the estuary mouth. This classification scheme uses two dimensionless parameters. The first parameter (Fr_f) is the freshwater Froude number, which is the ratio between the river discharge and the scale of the maximum possible frontal propagation speed. The second parameter (M) is the ratio between the tidal timescale and the timescale of vertical turbulent mixing. Figure 1-3 reveals that estuaries around the world show great diversities in stratification, because of their different values of Fr_f and M. Moreover, within one estuary, e.g., the seasonal variation of river discharge results in variations of Fr_f while the variation of tidal forcing (e.g. over a spring-neap cycle) results in variations of M.

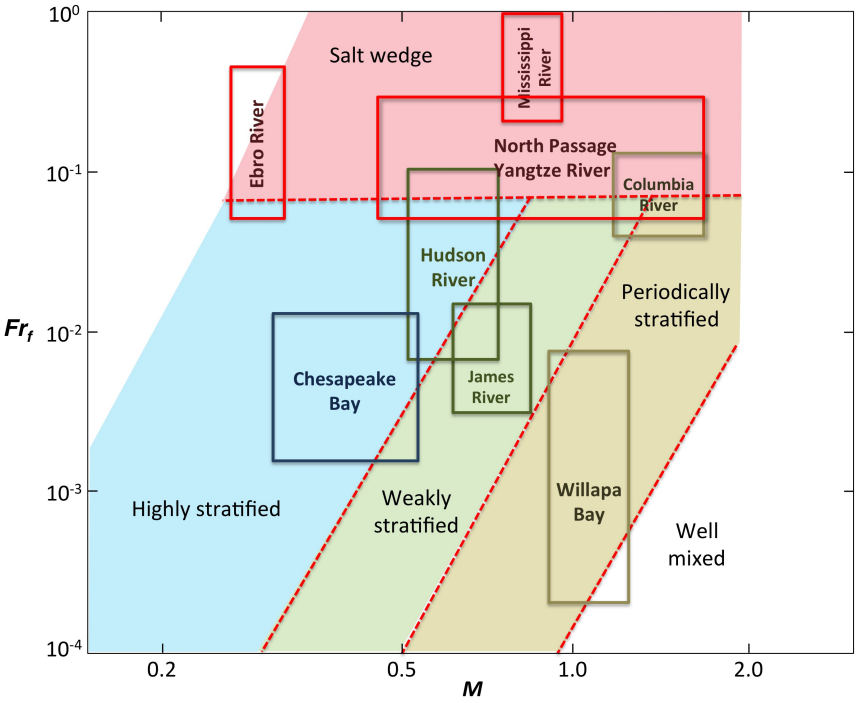

Figure 1-3: Classification of estuaries according to hydrodynamics, in terms of the parameters Fr_f and M (adapted from Figure 6, Geyer and MacCready, 2014). Four stratification regimes, i.e., salt wedge (red), highly stratified (blue), weakly stratified (green) and periodically stratified (yellow), are indicated in the diagram, which are separated by red dashed lines. Here, the terms 'highly stratified' and 'weakly stratified' are used instead of 'Fjord' and 'Bay' in the original paper. Estuaries at different locations of the world are mapped in this figure via computing the values of Fr_f and M.

1.2 RELEVANCE

Understanding the hydrodynamics and sediment dynamics of estuaries is relevant for society. From an economic perspective, out of the 32 largest cities in the world, 22 are located at the borders of estuaries (Ross, 1995). In many of these estuaries, big harbours and waterways are being built and extended in order to meet increasing economic demand. Physical insight into mechanisms of water circulation and sediment transport allows for a more efficient infrastructure management, as e.g. navigation channels often suffer from significant siltation and require extensive maintenance. For example, in the North Passage of the Yangtze Estuary, after the construction of Deepwater Navigation Channel, a severe siltation of sediment occurred in its center part. The present-day yearly dredging volume of sediment is an order of magnitude larger than the amount before the construction (Fan, 2010).

Knowledge of estuarine circulation and sediment is also relevant for ecological reasons. Estuaries are among the most productive systems on earth. They provide critical habitat and shelter for many fish nurseries, migratory bird species, amphibians, and other wildlife. Changes in the patterns and intensities of currents and SSC may have a negative effect on the functioning of estuaries. Specifically, deepening of estuarine channels caused severe tidal amplification (Winterwerp et al., 2013), which increases flood risk. Moreover, enhanced saltwater intrusion in deepened channels threatens freshwater resources (Wu et al., 2010). Deepening also resulted in intensive increasing of SSC in the Loire Estuary, Humber Estuary and Ems estuary, located respectively in France, UK and Germany (see Winterwerp et al., 2013; Jonge et al., 2014, and references herein). The high SSC frequently causes oxygen deficits because suspended sediment contains organic material that consumes oxygen (Cox, 2003). Moreover, high SSC limits the light that is needed for phytoplankton to grow (see e.g. the review by Cloern et al., 2013) and thereby reduces the amount of living organisms.

1.3 OVERVIEW OF PRESENT KNOWLEDGE AND GAPS

The focus of this thesis is on the role of density stratification on the dynamics of tides, residual currents and SSC in estuaries. In the following subsections, a brief state of the art of these three topics is presented.

1.3.1 *Tidal currents*

Tidal currents in estuaries are forced by tides in the adjacent sea. The latter contain many constituents that originate from orbital motion of the moon, sun

and earth, such as the semi-diurnal lunar M_2 tide, the semi-diurnal solar S_2 tide, the diurnal lunar O_1 tide, the diurnal solar K_1 tide and long-periodic tides. Additionally, there are overtides (M_4, M_6, etc.) constituents that are generated by the nonlinear nature of the hydrodynamics.

The structure of tidal currents in estuaries has been extensively studied and successfully simulated with complex numerical models that apply sophisticated closure schemes for turbulence (e.g. Warner et al., 2005; Burchard and Hetland, 2010). Besides, additional studies are important that focus on identifying and analysing processes that explain specific aspects of tidal currents. For this, consider Figure 1-4 that shows examples of observed vertical profiles of the M_2 tidal current amplitude. The study of Heaps and Jones (1981) revealed a pronounced surface maximum in the profile of the observed M_2 tidal current amplitude in the Liverpool Bay. This is referred to as a surface jump. In contrast, field data from the Columbia River Estuary (Jay and Musiak, 1994, 1996) and from the Yangtze Estuary (Jiang et al., 2013) show a vertical distribution of the M_2 tidal current amplitude with a subsurface maximum (i.e., subsurface jet). To understand these phenomena, idealised models (e.g. Johns, 1966; Ianniello, 1977; Winant, 2007) are useful tools. However, these models treated turbulence with simple time independent formulations of eddy viscosity, thereby neglecting the influence of density stratification on the structure of eddy viscosity profile (Geyer et al., 2000). So far, the dynamic link between stratification conditions and vertical structures of tidal currents has not yet been systematically investigated.

1.3.2 *Residual currents*

This thesis also aims at gaining more knowledge about the residual current that is generated by covariance between tidally varying intensity of turbulence (measured by the eddy viscosity) and vertical shear of tidal currents. It was shown by Ruijter (1983) and van Aken (1986) that horizontal advection (straining) of density by vertically sheared currents affects density stratification. Simpson et al. (1990) applied this concept to estuarine conditions and considered density straining by tidal currents, i.e. tidal straining. They explained that during flood, salt oceanic water is strained over fresher water, thereby causing an unstable stratification that enhances intensity of turbulence. During ebb the opposite occurs.

In a periodically stratified estuary, the residual current due to this mechanism has a structure that is similar to the 'classical' two-layer structure of the residual current induced by a horizontal density gradient, i.e., seaward current near the water surface and landward current near the bottom (Jay and Musiak, 1994; Stacey et al., 2001). Burchard and Hetland (2010) showed that this current

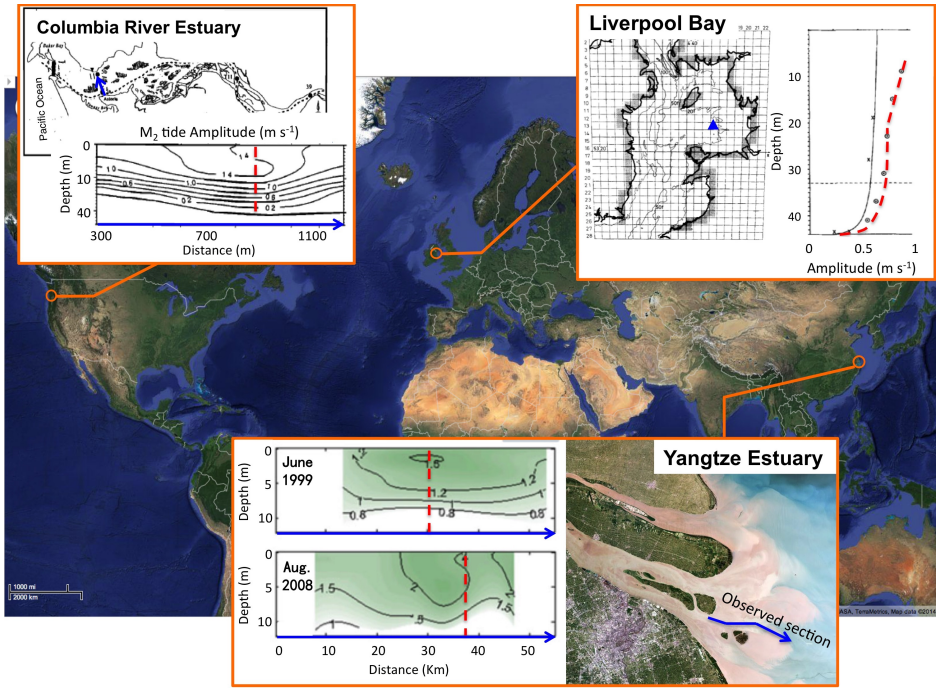

Figure 1-4: Examples of observed M_2 tidal current amplitude versus depth. For Liverpool Bay, adjusted versions of Figures 2 and 6 of Heaps and Jones (1981) are shown. The blue triangle shows the location of the observation site. The red dashed line follows the observed data, which shows a surface jump, and the black solid line shows model results. Regarding Columbia Estuary, adjusted versions of Figures 2 and 5a of Jay and Musiak (1994) are presented. The red dashed line indicates the location in the cross-section (blue arrow line) where the largest subsurface maximum is observed. For Yangtze Estuary, an adjusted version of Figure 7 of Jiang et al. (2013) is shown. Red dashed lines show the locations in the sampled section (blue arrow lines) where the largest subsurface maxima occur.

is about twice as large as the density driven current. Cheng et al. (2011, 2013) performed a numerical study on residual currents due to tidally varying eddy viscosity in both periodically stratified, weakly stratified and highly stratified estuaries. They found that with increasing stratification, these residual currents first have a classical two-layer structure, next a three-layer structure and ultimately a 'reversed' two-layer structure (i.e., seaward current near the surface and landward current near the bottom). Recently, Dijkstra et al. (2017), who referred to the covariance between eddy viscosity and tidal shear as ESCO, demonstrated that even if the external tidal forcing consists of only M_2, the residual current due to the nonlinearly generated M_4 tide also contributes to

the total residual current. However, that study considered only constant depth and the ESCO current was analysed at fixed locations and for a fixed river discharge and tidal forcing at the mouth. Additionally, all works mentioned above only focus on the residual current that is induced by ESCO in the case that tidal forcing is a single semi-diurnal tide. In many estuaries, tidal forcing consists of multiple constituents (semi-diurnal, diurnal, etc.), which potentially induces extra ESCO currents. This has not been investigated yet.

1.3.3 *Trapping of sediment*

Many studies have seeked for explanations of observed entrapment of suspended sediment in estuaries. This trapping is due to the convergence of tidally mean sediment transport, which mainly result from two processes. These are the sediment transport due to residual currents and that caused by covariance of tidally varying SSC and tidal currents, i.e. tidal pumping (Dyer, 1988).

Regarding longitudinal trapping, a classical explanation is that it results from the seaward transport caused by river flow and the landward transport by the density driven current (Postma, 1961; Festa and Hansen, 1978). Later studies also stressed the importance of convergence of sediment transport related to residual currents and tidal pumping (Jay and Musiak, 1994; Chernetsky et al., 2010), and the dependence of sediment transport on horizontal variations in density stratification (Geyer, 1993), flocculation and hindered settling (Winterwerp, 2002; Donker and Swart, 2013).

Regarding lateral trapping of sediment, Huijts et al. (2006) demonstrated the importance of convergence of sediment transport related to the density driven current and that caused by Coriolis deflection of the longitudinal residual current. Other studies demonstrated trapping of sediment related to lateral trapping of sediment at a fixed cross-section due to lateral currents caused by channel curvature (Kim and Voulgaris, 2008), boundary mixing at the slope of the shoals (Chen and Sanford, 2009) and M_4 tidal pumping (Yang et al., 2014).

There are few works that investigate the trapping of sediment in cross-sections at different longitudinal locations, whereas longitudinal variations in lateral trapping of sediment are frequently observed. Geyer et al. (2001) observed in the upper reach of the Hudson River Estuary elevated SSC at both left and right sides of a specific cross-section, and near the mouth only one on the left side of that cross-section (when looking into the estuary). Understanding such phenomena requires knowledge about the joint presence of longitudinal and lateral trapping processes. Kumar et al. (2017) developed an idealised model that deals with three-dimensional structures of the turbidity field in well-mixed estuaries. However, the model uses a constant value for eddy viscosity, which limits its application to well mixed estuaries.

1.4 RESEARCH QUESTIONS, METHODOLOGY AND OUTLINE OF THIS THESIS

This thesis aims at answering the following questions:

1. What is the quantitive role of tidally averaged density stratification, causing specific structures of the tidally averaged eddy viscosity in the water column, in the occurrence of pronounced surface maxima and subsurface maxima in the vertical distribution of the tidal current amplitude?

2. (a) How do spatial patterns and intensities of the residual current induced by the covariance between tidally varying eddy viscosity and tidal shear (ESCO) change if estuaries with varying longitudinal bottom slope are considered?
   (b) What is the quantitative role of tidally averaged density stratification on the spatial structure of the residual current induced by ESCO?
   (c) How does tidal forcing that contains both diurnal and semi-diurnal tidal constituents affect the spatial patterns and intensities of the residual current induced by ESCO?

3. (a) What physical mechanisms are responsible for observed longitudinal variations in lateral distribution of suspended sediment in estuaries?
   (b) What is the effect of differences in density stratification on the pattern of suspended sediment distribution?

The first research question is addressed in **chapter 2**, where a new 1D vertical column model for tidal currents is presented. The new aspect concerns the eddy viscosity profile, which is formulated such that it accounts for the bottom turbulence, surface mixing and density stratification. This model has analytical solutions for any choices of these three parameters. The model will be used to study the vertical structure of the tidal current amplitude for different stratification conditions and its results will also be compared with field data of the Liverpool Bay and the Yangtze Estuary (see Figure 1-3).

Chapter 3 focuses on the estuarine residual current induced by ESCO (research questions 2a, b and c). For this, the numerical model Delft3D-FLOW (Lesser et al., 2004) will be applied to explicitly resolve the temporal and spatial structure of vertical eddy viscosity and tidal current at different locations in a narrow estuary. The model will be used to systematically explore the dependence of residual current due to ESCO on longitudinal bottom slope, stratification (by varying external tidal forcing) and on tidal forcing that contains both diurnal and semi-diurnal constituents. The residual current due to ESCO will be decomposed into terms that are related to ESCO due to individual tidal harmonics that have different frequencies. The structure and relative importance

of ESCO currents due to individual tidal harmonics with respect to the total ESCO currents and total residual currents will be analysed.

Chapter 4 focuses on understanding observed longitudinal differences in lateral distribution of sediment (research questions 3a and b). For this, a new analytical model will be presented that describes hydrodynamics and sediment dynamics in an idealised three-dimensional domain. The turbulence closure scheme is based on the formulations developed in chapter 2. Model results will be presented for different forcing conditions and compared to observations.

Finally, **chapter 5** summarises the main results of the thesis and presents an outlook for future research.

2

DYNAMIC LINKS BETWEEN SHAPE OF THE EDDY VISCOSITY PROFILE AND THE VERTICAL STRUCTURE OF TIDAL CURRENT AMPLITUDE IN BAYS AND ESTUARIES

2.1 INTRODUCTION

Tides are often a significant, if not dominant, constituent of the water motion in bays and estuaries. Knowledge of the spatial and temporal characteristics of tides is important, as they play a key role in e.g. the mixing and transport of salt, sediment and nutrients. Nowadays, surface tides and tidal currents are successfully simulated with detailed numerical models (e.g. Warner et al. 2005; Burchard and Hetland 2010). These studies showed explicit results of tides obtained with models that apply second order closure schemes for turbulence, which is parameterised with the coefficient of eddy viscosity. It appears that, in order to achieve good representations of the vertical structure of tidal currents, sophisticated formulations are required for vertical eddy viscosity, the latter representing the degree of vertical mixing. When the main interest is rather in gaining fundamental insight into tidal dynamics, i.e. to identify and analyse processes that cause a specific observed feature, such models are less suitable tools, owing to their complexity. For such purposes, idealised models have been developed and analysed, which rely on simple formulations of eddy viscosity (Johns, 1966; Ianniello, 1977; Friedrichs and Hamrick, 1996; Huijts et al., 2006; Winant, 2007; Zitman and Schuttelaars, 2012).

This study focuses on two specific phenomena that appear in vertical profiles of the current amplitude of a single tidal harmonic component and which are, as yet, not well understood. The first is called a surface jump (SJ-I) and it is related to the presence of a subsurface maximum in the shear of the tidal current amplitude (i.e., in the vorticity). It was observed by Heaps and Jones (1981) in Liverpool Bay, but they were unable to capture it with their model that uses a simple formulation for eddy viscosity. The second feature, called a subsurface jet (SJ-II), refers to the presence of a subsurface maximum in the M_2 tidal current amplitude itself. It was observed by Jay and Musiak (1996) in the

Columbia estuary and by Jiang et al. (2013) in the Yangtze estuary.

Note that surface jumps and subsurface jets as defined above are not identical to surface and subsurface maxima in the instantaneous current during the ebb or flood phase. This is because the instantaneous current comprises all tidal harmonics, including overtides and residual currents. For example, subsurface maxima during flood are frequently detected, but as already explained by Jay and Musiak (1994), they may result from the joint effect of a primary tidal component (which shows no subsurface maximum in its current amplitude) and a residual current and overtides. Likewise, Lacy et al. (2003) showed that of subsurface velocity maxima result from lateral tidal advection of slower moving surface water from the margins of the estuarine channel.

The objective of the present study is to provide an explanation for the SJ-I and SJ-II phenomenon in the vertical profile of the current amplitude of a primary tidal constituent, as is described above. Using a theoretical model, Lamb (1932) and Prandle (1982) showed that in unstratified seas, tidal current amplitude maxima occur below the water surface if the thickness of the frictional boundary layer is much smaller than the water depth. Such conditions would require depths of at least several hundreds of meters. The way to obtain a smaller boundary layer thickness in shallow bays and estuaries is by means of density stratification. In particular, Geyer et al. (2000) showed that in partially mixed estuaries the maximum viscosity occurs only a few meters above the bottom, which is called the well mixed part of the boundary layer. Moreover, a recent numerical study by Cheng et al. (2013) showed that, with increasing density stratification in an estuary, the maximum eddy viscosity becomes smaller and its location shifts towards the bottom.

These considerations motivate the hypothesis of the present study, viz. the emergence of surface jumps and subsurface jets is related to a specific distribution of eddy viscosity with depth, which results from bottom turbulence, surface mixing and density stratification.

To test the formulated hypothesis, an idealised model has been designed, which allows for new analytical solutions for tidal flow. Using these new solutions, a sensitivity study of the characteristics of tidal current amplitude profiles to parameters that characterise a family of eddy viscosity profiles is conducted.

The subsequent sections are organised as follows: The model and methods are introduced in section 2.2. In section 2.3, vertical structures of tidal current amplitudes resulting from different eddy viscosity profiles are presented. Section 2.4 contains the discussion, including a physical interpretation of the results, and conclusions are presented in section 2.5.

2.2 MODEL AND METHODS

2.2.1 *Model*

The along-estuary current is governed by the shallow water momentum balance in terms of a scaled vertical coordinate $\sigma = (z-\eta)/D$. Here, z is a vertical coordinate, $z = 0$ is the undisturbed water level, $z = \eta$ is the free surface, $z = -h$ the bottom and $D = h + \eta$ is the total depth. Thus, $\sigma = -1$ and $\sigma = 0$ represent the bottom and and the free surface, respectively. This choice is convenient because often field observations (Bowden and Sharaf El Din, 1966; Lane et al., 1997; Jiang et al., 2013) are measured and analysed at levels $\sigma =$ constant. It is assumed that the amplitude Z of sea surface variation η is small compared to the undisturbed water depth h. This identifies a small parameter $\varepsilon = Z/h$. After applying the perturbation analysis similar to Ianniello (1977), the model equation at leading order reads

$$\frac{\partial u}{\partial t} = -g\frac{\partial \eta}{\partial x} + \frac{1}{h^2}\frac{\partial}{\partial \sigma}(A_v\frac{\partial u}{\partial \sigma}). \tag{2-1}$$

Here, u denotes the local along-estuary velocity, t is time, g =9.8 ms^{-2} is gravitational acceleration and $\partial\eta/\partial x$ is the along-estuary gradient of the free surface. Note that for small ε, $\sigma \simeq z/h$, hence at this order of approximation output of Eq 2-1 at σ-levels can be straightforwardly transformed to output at z-levels and compared with field data collected at z-coordinates. (e.g., Jay and Musiak 1996; Geyer et al. 2000). This equation has been shown to capture the gross characteristics of observed tidal flow quite well, in case that an appropriate formulation for the vertical eddy viscosity coefficient A_v is chosen (Friedrichs and Hamrick, 1996; Huijts et al., 2009). Note that in shallow bays, where depth is relatively large and flow is unconstrained by side walls, the longitudinal tidal dynamics may be also affected by Coriolis veering (Prandle, 1982; Soulsby, 1983; Souza, 2013). This will be further discussed in section 2.4.

The eddy viscosity coefficient A_v is formulated as

$$A_v = \kappa |u_*| h \, A_\sigma. \tag{2-2}$$

where $\kappa = 0.41$ is the von Karman's constant, u_* is the friction velocity and A_σ describes the profile of the eddy viscosity coefficient. Note that at the present order of approximation ($\varepsilon \ll 1$) $\sigma = z/h$, hence the function A_σ does not depend on time.

At the bottom, the no-slip condition is applied:

$$u = 0 \qquad \text{at} \qquad \sigma = -1 + \sigma_0. \tag{2-3}$$

In this expression, formally $\sigma_0 = z_0/(h+\eta)$ and z_0 denotes the local roughness length. In the present model $\eta \ll h$, consequently

$$\sigma_0 = \frac{z_0}{h}. \tag{2-4}$$

At the free surface, it is assumed that tidal motion is stress free and satisfies the kinematic boundary condition

$$A_v \frac{\partial u}{\partial \sigma} = 0 \qquad \text{at} \qquad \sigma = 0. \tag{2-5}$$

The along-estuary gradient of the free surface reads

$$\frac{\partial \eta}{\partial x} = \frac{dN}{dx} \cos(\omega t), \tag{2-6}$$

with dN/dx prescribed and ω is the imposed radian frequency of the tide.

2.2.2 *Formulation of eddy viscosity*

In this study, the water column consists of two layers. A continuous family of profiles of A_σ is considered, which include both classical profiles as well as profiles that mimic key aspects of observed profiles of time-mean eddy viscosity. The formulation for A_σ in Eq. 2-2 reads

$$A_\sigma = (\sigma+1)(\sigma_p - \sigma), \qquad -1 \leqslant \sigma \leqslant \sigma_h; \quad \text{(lower layer)}, \tag{2-7a}$$

$$A_\sigma = (A_I - A_S)\left|\frac{\sigma}{\sigma_h}\right|^n + A_S, \qquad \sigma_h \leqslant \sigma \leqslant 0; \quad \text{(upper layer)}, \tag{2-7b}$$

in which $A_I = (\sigma_h+1)(\sigma_p - \sigma_h) \equiv A_\sigma|_{\sigma=\sigma_h}$.

Thus, Eqs. 2-7a and 2-7b contain four parameters, viz. σ_p, σ_h, A_S and n (Figure 2-1). The introduction of two layers is based on the argument that the length scale for mixing is related to the thickness of bottom boundary layer (Stacey and Ralston, 2005; Ralston et al., 2008). Hence, the boundary layer height scales with $(1+\sigma_p)$; more details will be discussed in Section 2.4.

Physical arguments (e.g. the law of the wall) imply that there are three constraints on the eddy viscosity. First, $dA_\sigma/d\sigma$ is positive near the bottom. Second, $dA_\sigma/d\sigma \leqslant 0$ in the upper layer, i.e. it is assumed that the turbulent mixing generated at the surface (by wind stress, breaking waves, etc.) is never larger than the maximum turbulent mixing induced by the tide. Third, $dA_\sigma/d\sigma$ is continuous in the entire water column. This constraint is accordance with Ianniello

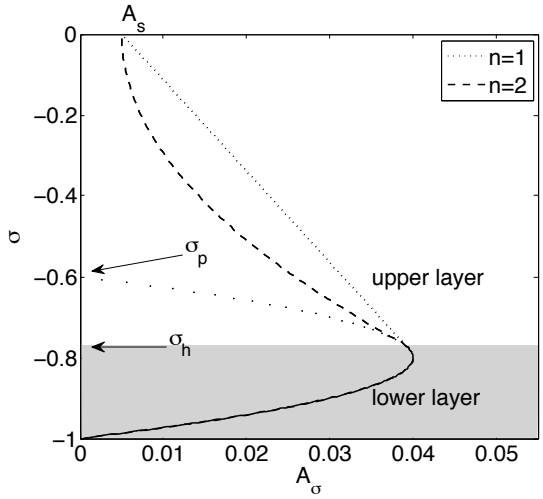

Figure 2-1: Typical vertical distributions of the vertical structure of eddy viscosity A_σ. The dotted line in the upper layer indicates the extension of function Eq. 2-7a into the upper layer, to show the location of the level $\sigma = \sigma_p$.

(1977) and Cheng et al. (2013).

The first two constraints imply $(1 + \sigma_p) > 0$ and $A_S \leqslant A_I$. Moreover, these constraints suggest that A_σ attains its maximum in the lower layer. It follows straightforwardly that this maximum value is $A_{\sigma,max} = (1 + \sigma_p)^2/4$ and it occurs at $\sigma = (\sigma_p - 1)/2$, which must be below $\sigma = \sigma_h$. Thus $\sigma_h \geqslant (\sigma_p - 1)/2$ and the value of is determined by the third constraint. Finally, since $\sigma_h \leqslant 0$ (see Eq. 2-7b), it follows $\sigma_p \leqslant 1$, thereby overall values of parameter σ_p vary between -1 and 1. A parameter $r_a = A_S/A_{\sigma,max}$ is introduced hereafter to indicate the relative degree of surface mixing with respect to maximum mixing. The exponent n determines the shape of A_σ in the upper layer ($n = 1$ linear, $n = 2$ parabolic, etc). Note that, $r_a = 1$ together with the third constraint, implies a constant eddy viscosity $A_\sigma = A_{\sigma,max}$ in the upper water layer and therefore covers the case that $n = 0$. Hence, the formulation of eddy viscosity contains three independent free parameters, i.e. σ_p, r_a and n.

The dependencies of parameters σ_h and A_I on σ_p, r_a and n are shown in Figure 2-2. By choosing values of σ_p, n and r_a, the formulation Eq. 2-7 is able to mimic different shapes of eddy viscosity profiles presented in earlier studies (Figure 2-3), such as the combined parabolic and vertical invariant profile employed by Ianniello (1977) (Figure 2-3a), and the parabolic profile (Figure 2-3b) studied by Burchard and Hetland (2010) and Zitman and Schuttelaars (2012). Two typical profiles that manifest themselves if the water column is highly stratified are shown by Burchard and Hetland (2010), as well as by Cheng et al.

(2013). The formulation in Eq. 2-7 is also able to mimic these two profiles (Figure 2-3c and Figure 2-3d). Note that solutions can be obtained for any finite r_a, no matter how small its value. Thus the choice $r_a \ll 1$ and $\sigma_h = 0$ yields the parabolic eddy viscosity profile.

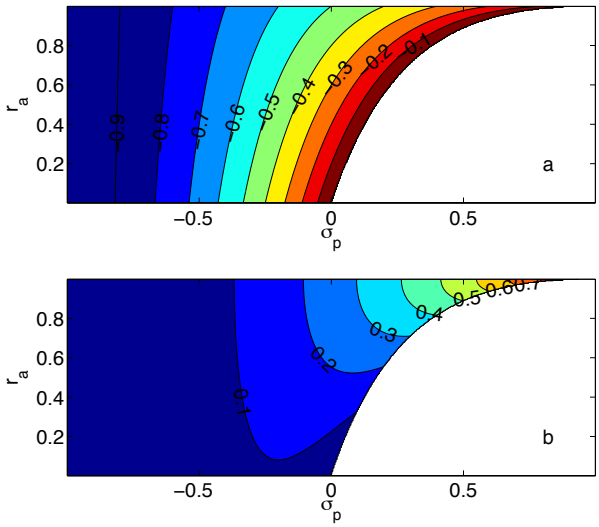

Figure 2-2: Contour plots of parameters σ_h (a) and A_I (b), defined in Eq. 2-7, as functions of the free parameters r_a and σ_p when $n = 2$.

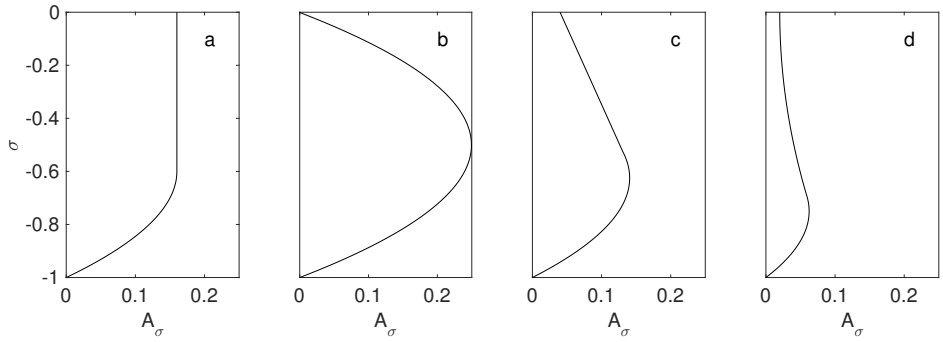

Figure 2-3: Different vertical profiles of eddy viscosity as governed by Eq. 2-7: a. $\sigma_p = -0.3, r_a = 0.99$; b. $\sigma_p = -0.001, r_a = 0.01$ c. $\sigma_p = -0.3, r_a = 0.25$; d. $\sigma_p = -0.6, r_a = 0.25$.

2.2.3 *Linearisation of the friction*

By definition, the friction velocity is related to the kinematic bottom shear stress, as

$$u_* |u_*| = \frac{A_v}{h} \left. \frac{\partial u}{\partial \sigma} \right|_{\sigma=-1+\sigma_0} . \tag{2-8}$$

Thus, the momentum equation (Eq. 2-1) with A_v closed Eq. 2-2 is nonlinear. To linearise the equation, here a representative constant $\tilde{u}_*$ is introduced to replace $|u_*|$ in Eq. 2-2 and 2-8. It is assumed that, in a tidally dominant estuary or bay, with this representative $\tilde{u}_*$, the modified bottom shear stress gives the same energy dissipation rate as the nonlinear bottom stress $\rho u_* |u_*|$ (Lorentz, 1922; Kajiura, 1964; Zimmerman, 1982). The consequence of linearisation of Eq. 2-1, together with the forcing as given in Eq. 2-6 is that u is harmonic in time and moreover, u_* is harmonic in time, with amplitude $\hat{u}_*$. Development of the energy criterion yields

$$\tilde{u}_* = \frac{8}{3\pi} \hat{u}_*, \tag{2-9}$$

which hereafter is referred to as the representative friction velocity. Hence, for a selected A_σ, analytical solutions for tidal flow u are constructed that depend on $\tilde{u}_*$. With prescribed roughness height in the estuarine channel, an iteration procedure is used to determine the linearised bottom shear stress and the eddy viscosity coefficient.

2.2.4 *Analytical solutions*

Analytical solutions for the tidal currents governed by Eqs. 2-1 to 2-9 are

$$u = \Re\{\hat{U} e^{-i\omega t}\}, \tag{2-10}$$

where $\Re$ denotes taking the real part of a complex variable. Furthermore, $\hat{U}$ is the complex, σ-dependent amplitude of the tidal current. Note that $\hat{U} = U e^{i\phi}$, with U the real-valued amplitude and ϕ the phase. Substitution of Eq. 2-10 into Eq. 2-1 and using Eq. 2-2, with $|u_*|$ replaced by $\tilde{u}_*$, and using Eqs. 2-3 to 2-7, it follows that

$$\hat{U} = -i \frac{g}{\omega} \frac{dN}{dx} p. \tag{2-11}$$

In this result, p is a function of h and σ. Explicit analytical expressions for p are given in Appendix A for the cases $n = 0$, $n = 1$ and $n = 2$. For other values of n, solutions in the lower layer are still analytical, but for the upper layer p is determined numerically. Note that these expressions are readily programmed (a sample Mathematica file is added as supplementary material), which allow fast computations of tidal current profiles.

2.2.5 *Methods*

To test the hypothesis that the two SJ phenomena relate to specific vertical structures of eddy viscosity, different series of sensitivity experiments, in particular for $n = 1$ and $n = 2$, were conducted. Solutions were obtained for different values of r_a and σ_p within their physically acceptable range of values (see Section 2.2.2).

For each combination of parameter values the possible occurrence of a "surface jump" (SJ-I) was assessed by checking the presence of local extrema in the vertical shear of the tidal current amplitude. If a subsurface maximum in U, called U_{max}, was detected, it should be sufficiently large with respect to the surface value U_s, in order to classify the profile as one having an SJ-II. For this, the parameter ξ was computed, defined as

$$\xi = \frac{U_{max} - U_s}{U_s}, \tag{2-12}$$

If $\xi \geqslant 0.01$ the vertical profile of the tidal current amplitude was considered to show an SJ-II.

2.3 RESULTS

Figure 2-4 shows eddy viscosity, tidal current amplitude and its vertical shear (proportional to vorticity) for $n = 2$, $r_a = 0.2$ and varying σ_p for the default parameter values given in Table 2-1. The panels in this figure reveal that for $n = 2$ there are combinations of σ_p and r_a that yield different vertical structures of the current amplitude. As is illustrated in Figure 2-4b, the profiles of the tidal current amplitude for $\sigma_p = -0.27$ and -0.54 show a surface jump (SJ-I), as follows from the presence of a subsurface maximum in the tidal shear for these parameter values (Figure 2-4c). In contrast, for $\sigma_p = -0.83$ the profile of the tidal current amplitude shows a subsurface jet (SJ-II); the value of parameter ξ, as defined in Eq. 2-12, is $\xi = 0.13$.

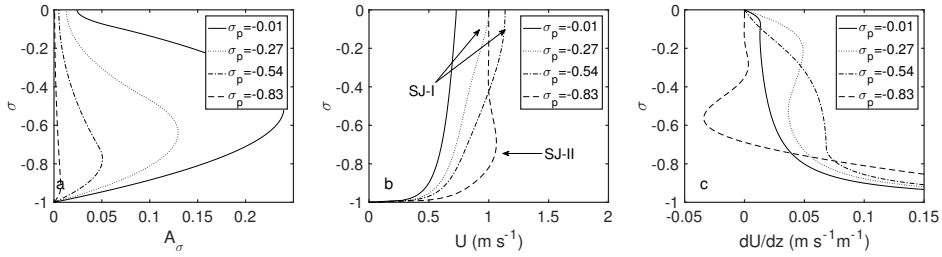

Figure 2-4: a. The vertical distribution of A_σ for different values of σ_p, $n = 2$ and $r_a = 0.2$, b. As a. but for the tidal current amplitude and c the corresponding vertical distribution of the vertical shear. Other parameter values as in Table 1. Values for representative friction velocity $\tilde{u}_*$, as defined by Eq. 2-9 are 0.033 m s^{-1}, 0.03 m s^{-1}, 0.02 m s^{-1} and 0.01 m s^{-1}

Table 2-1: Model input parameters for the default case

Parameter	Symbol	Value
Mean water depth	h	10 m
Tidal frequency	ω	1.4×10^{-4} s^{-1}
Roughness height	z_0	0.008 m
Sea surface gradient	dN/dx	1.4×10^{-5} m m^{-1}

Figure 2-5 shows the regions in the σ_p-r_a parameter space (for $n = 1$ and $n = 2$, respectively) where the SJ-I/II phenomena occur. The SJ-I phenomena are found in the lower middle part of the diagram for $n = 2$ (Figure 2-5b). In the case when $n = 1$, the SJ-I phenomenon is not found. Instead, for values of σ_p and r_a where SJ-I is found if $n = 2$, the current amplitude in the case $n = 1$ increases almost linearly to the surface, as is shown in Figure 2-6a. Correspondingly, the velocity shear, i.e. the vorticity becomes a constant in the upper part of the water column, before reaching the surface (Figure 2-6b). These results suggests that the SJ-I occurs if the eddy viscosity in the upper layer of water column decreases faster than linearly towards the surface $(n > 1)$.

Another interesting result is that the SJ-II phenomenon is found in the left part of the diagrams shown in Figure 2-5, both for $n = 1$ and $n = 2$. Note that in the latter case, the areas where SJ-I and SJ-II phenomena occur partly overlap, viz. between $\sigma_p = -0.5$ and -0.6. Indeed, as is shown in Figure 2-7, for parameter values in the latter area the tidal current amplitude reveals both SJ-I/II phenomena. The vorticity has a negative extremum near the surface of water column and two positive extrema in the interior. Moreover, the maximum current amplitude is found in the interior of the water column.

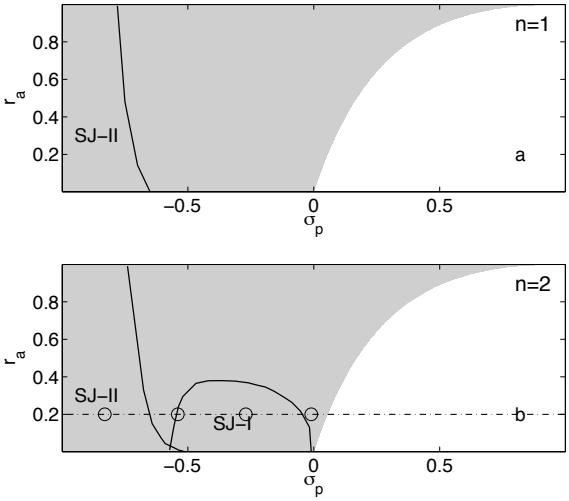

Figure 2-5: Regions in the $\sigma_p - r_a$ parameter space where the SJ-I (surface jump) and/or SJ-II (subsurface jet) phenomena occur. Panels a and b show results for $n = 1$ and $n = 2$, respectively. The grey-shaded area indicates values of σ_p and r_a that are physically possible. The circles on the dashed line in panel b indicate the parameter values that were used in Figure 2-4.

As has been stated in the previous section, the solutions for tidal flow were obtained by an iteration procedure to determine the friction velocity u_*. To quantify the sensitivity of the model results to the choice of the bottom roughness hight σ_0, the friction velocity was computed for different values of the bottom roughness length z_0. The friction velocity, which relates to the shear stress at the bottom, is not affected by the turbulence from the water surface and is therefore not sensitive to the choice of r_a and n. A transect for $r_a = 0.01$, with different σ_p, was selected to show the representative friction velocity ($\tilde{u}_*$) computed for three different values of the dimensionless bottom roughness length $\sigma_0 = z_0/h$, which represent respectively a smooth bottom ($\sigma_0 = 0.2 \times 10^{-3}$), a moderately rough bottom ($\sigma_0 = 1 \times 10^{-3}$) and a rough bottom ($\sigma_0 = 2 \times 10^{-3}$). Results are shown in Figure 2-8. The representative friction velocities during the tidal cycle are in general lower than 0.035 m s^{-1} and show the same dependency on σ_p. No linear relation is found between the representative friction velocity and σ_p. Moreover, the difference in representative friction velocity between the smooth and rough bottom is small (less than 0.005 m s^{-1}). With the representative friction velocity, the eddy viscosity is computed and the results show that the values of the eddy viscosity coefficient range from 0 to 0.045 $m^2\,s^{-1}$, which are close to the values observed in the field (Bowden and

Sharaf El Din, 1966; Jay and Musiak, 1996; Geyer et al., 2000) or calculated by numerical models (Stacey et al., 2008; Cheng et al., 2013).

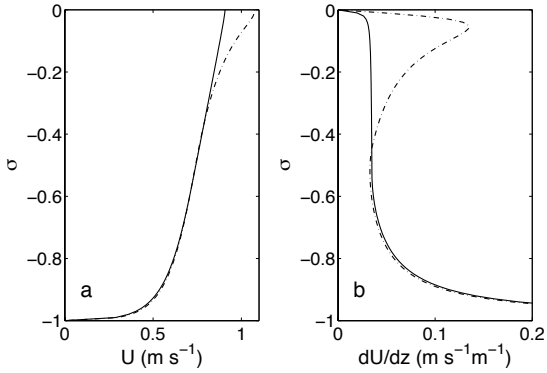

Figure 2-6: a. The tidal current amplitude computed with the model for $\sigma_p = -0.25$, $r_a = 0.01$, $n = 1$ (solid line) and $n = 2$ (dashed line). b. The corresponding vertical gradient of the tidal current amplitude. Other parameter values as in Table 1.

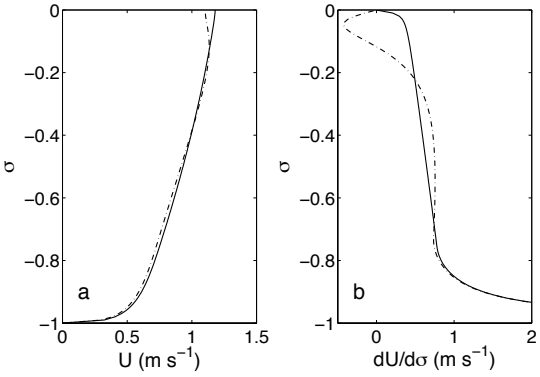

Figure 2-7: a. The tidal current amplitude computed with the model for $\sigma_p = -0.57$, $r_a = 0.01$, $n = 1$ (solid line) and $n = 2$ (dashed line). b. The corresponding vertical gradient of the tidal current amplitude. Other parameter values as in Table 1.

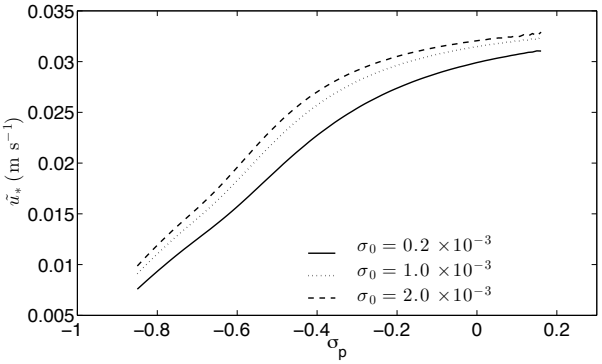

Figure 2-8: The representative friction velocity $\tilde{u}_*$ computed with the model for $n = 2$ and $r_a = 0.01$ for different values of the dimensionless roughness length σ_0.

2.4 DISCUSSION

2.4.1 *Interpretation of* σ_p

The physical meaning of σ_p is linked to the degree of stratification in the water column. This can be understood as follows. Note that a decrease of σ_p in the model implies a smaller thickness of the lower layer and a smaller value of the maximum value of the eddy viscosity, A_I (see Figures 2-1 and 2-2). This means that the length scale of turbulent eddies generated by bottom friction decreases with decreasing σ_p. As this is what typically happens if stratification increases, a relationship was sought between σ_p and a measurable parameter that quantifies stratification, viz. the estuarine bulk Richardson number (Dyer, 1997)

$$R_i = g\frac{\Delta\rho H}{\rho_0 {U_m}^2}. \tag{2-13}$$

In this expression, $\Delta\rho$ is the residual density difference between bottom and surface, ρ_0 the reference density and U_m is the depth averaged tidal current amplitude. Thus, for different field sites values of R_i and σ_p were determined from the observations. Results reported by Bowden and Sharaf El Din (1966) for the Mersey Estuary, Jay and Musiak (1996) for the Columbia River Estuary, Geyer et al. (2000) for the Hudson River Estuary, Li and Zhong (2009) for the Chesapeake Bay and Basdurak et al. (2013) for the channel of James River Estuary, were used. Values of R_i were obtained from measured tidal current speed and bottom-to-top density differences (see Appendix B for the data). Values of σ_p were taken such that at each site the eddy viscosity profile in Eq. 2-7

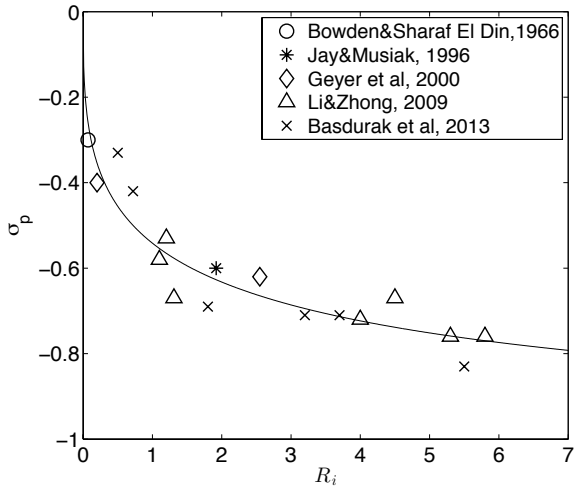

Figure 2-9: Relationship between bulk Richardson number R_i and σ_p as traced from field studies and outcome of numerical models. The black line is the fit $\sigma_p = [\exp(-0.78{R_i}^{0.36})]^{-1} - 1$.

mimicked the tidally mean eddy viscosity profile, as was reconstructed from observed shear stresses and velocity shear, or calculated from the numerical model. The results are shown in Figure 2-9. Indeed, it reveals a relationship between σ_p and R_i, viz. $\sigma_p = [\exp(a{R_i}^b)]^{-1} - 1$ with $a = 0.78$, $b = 0.36$ and with a goodness of fit coefficient (r^2) of 0.86.

Further important insight into the meaning of parameter σ_p is obtained as follows. By application of a Taylor expansion, the modelled eddy viscosity near the bottom reads

$$A_v\Big|_{\sigma=-1+\tilde{\sigma}} = A_v\Big|_{\sigma=-1} + \frac{\tilde{\sigma}}{h}\frac{\partial A_v}{\partial \sigma}\Big|_{\sigma=-1} + ... = \tilde{\sigma}\tilde{u_*}\kappa(1+\sigma_p) + ..., \quad (2\text{-}14)$$

in which $\tilde{\sigma} = (h+z)/D$ is a small relative height above bottom. This means that the flow close to the bottom is logarithmic with a "modified" von Karman's constant $\kappa(1+\sigma_p)$. Based on Figure 2-9, it follows that σ_p decreases with increasing stratification. This finding is consistent with that found by Wang (2002), in which the modified von Karman's constant reads $\kappa(1+AR_f)^{-1}$. Here, A is an empirical constant that does not depend on R_f, the latter being the flux Richard-

son number, which is given by Mellor and Yamada (1974) as a function of the so-called gradient Richardson number R_g as

$$R_f = 0.725\left[R_g + 0.186 - \left(R_g^2 - 0.316R_g + 0.0346\right)^{1/2}\right]. \tag{2-15}$$

In the present study, it was assumed that $R_i \simeq R_g$, following Dyer (1997). Equating the two expressions for the modified von Karman constant yields a relation between σ_p and R_f, viz.

$$\sigma_p = (1 + AR_f)^{-1} - 1. \tag{2-16}$$

Constant A was subsequently calculated by application of a least square fit computed via Eq. 2-15 and Eq. 2-16, with R_i from the corresponding field data. The computed $A = 6.7$ is close to values reported in earlier studies (Anwar, 1983; Wang, 2002).

2.4.2 *Interpretation of* r_a

The behaviour of eddy viscosity is determined by sources of turbulent mixing. For bottom-generated turbulence in an unstratified water column, the turbulent velocity scale is the friction velocity. As was argued by Stacey et al. (1999), in shallow estuaries the turbulent velocity decreases linearly towards the surface, as in the absence of a wind stress there is no stress at the latter location. Assuming the length scale of the eddies to be the distance above the bottom, the parabolic eddy viscosity profile is found, which is used in many studies (Burchard and Hetland, 2010; Zitman and Schuttelaars, 2012). However, there might be additional sources of turbulent mixing at the water surface, viz. breaking waves (whitecapping), wind stress, etc. To account for these sources, the eddy viscosity profile is modified such that $A_v(\sigma = 0) \neq 0$. Thus, parameter r_a, defined as the ratio of the eddy viscosity at the surface and the maximum eddy viscosity in the water column, measures the relative importance of surface mixing.

2.4.3 *Physical conditions resulting in surface jumps and subsurface jets*

The information from the previous subsections will now be used to explain why for specific combinations of parameters σ_p, r_a and n the surface jump (SJ-I) and/or the subsurface jet (SJ-II) phenomenon occurs. The presence of

SJ-I requires a subsurface extremum in the vertical shear of the tidal current amplitude. Now consider the equation for vertical current shear, which follows from deriving Eq. 2-1 with regard to σ:

$$\frac{\partial}{\partial t}\frac{\partial u}{\partial \sigma} = \frac{1}{h^2}\left(\frac{\partial^2 A_v}{\partial \sigma^2}\frac{\partial u}{\partial \sigma} + 2\frac{\partial A_v}{\partial \sigma}\frac{\partial^2 u}{\partial \sigma^2} + A_v\frac{\partial^2}{\partial \sigma^2}\frac{\partial u}{\partial \sigma}\right). \tag{2-17}$$

If this equation is considered in the area where the current shear attains a maximum, the second term on the right hand side is small (vanishing curvature of the current). The third term acts diffusive, therefore it reduces tidal shear. Thus, in order to have local increase of the tidal shear, it should be generated by the first term at the right hand side. Clearly, this occurs if $A_{v,c} = \partial^2 A_v/\partial\sigma^2$ is positive. Note that for a parabolic eddy viscosity profile, $A_{v,c}$ is negative, therefore no SJ-I occurs in this case. The same holds for the eddy viscosity profiles considered in this study if parameter $n \leqslant 1$. Thus, a necessary condition for the SJ-I to occur is that eddy viscosity decreases faster than linearly $(n > 1)$ towards the surface. Physically, this means that for SJ-I to occur, a surface pycnocline must be present in which mixing is reduced and in which tidal shear increases. The reason why SJ-I only occurs for moderate stratification ($\sigma_p \sim -0.5 - 0$) is that in the strongly stratified case the maximum mixing is weak, hence $A_{v,c}$ itself is small and in Eq 2-17 the first term on the right hand side is too small to overcome the diffusive third term. Solutions of Eq 2-1 for other values of n support the previous analysis. Further details are shown in the supplementary material.

The presence of a subsurface jet is related to the ratio of the thickness of the turbulent boundary layer h_b and the water depth h. As was already stated in the introduction, Lamb (1932) and Prandle (1982) showed that in unstratified waters subsurface maxima in the profile of the current amplitude of a harmonic constituent occur if $h_b \ll h$, where $h_b \sim (A_{v,max}/\omega)^{1/2}$. Typically for tides, $h_b \sim h$ and thus the SJ-II phenomenon does not occur. However, if the water column becomes more stratified, mixing is suppressed and thus h_b becomes smaller. This explains why the SJ-II phenomenon in the present model occurs for small values of $(1 + \sigma_p)$. The value of r_a does not control the occurrence of SJ-II, as long as it is within the imposed range $0 \leqslant r_a \leqslant 1$. This is because for strong stratification the maximum mixing $A_{v,max}$ is small, hence also surface mixing will be small. Furthermore, note that the presence of SJ-II is also independent of the value of n; the physical control parameter is h_b/h, which in this model is controlled by σ_p (stratification) and the magnitude of the pressure gradient force (which affects friction velocity $\tilde{u}_*$).

2.4.4 *Comparison of modelled and observed vertical structures of tidal current amplitudes*

So far model results have been shown for fixed values of parameters, like depth and pressure gradient force (see Table 2-1). As is shown in Figure 2-5, regimes were identified in the $\sigma_p - r_a$ parameter space for which the model simulates the SJ-I and/or SJ-II phenomenon. An important question to address is whether the model is also able to mimic the SJ phenomena for parameter values that are representative for the sites where these phenomena were actually observed.

First, the case of Liverpool Bay was investigated, where the observed tidal current profile shows an SJ-I phenomenon (Heaps and Jones, 1981). The depth $h = 44$ m was obtained from their paper. Time series of observed salinity data were obtained from Simpson et al. (2002), whose field site LB2 is close to that of Heaps and Jones (1981). Thus, the tidally mean bulk Richardson number as defined in Eq. 2-13 was estimated by assuming that stratification was similar at the two locations. Here $\Delta\rho = \beta\Delta S$, where ΔS is the tidally mean top to bottom salinity difference and β being the saline contraction coefficient ~ 0.78 kgm^{-3}psu^{-1}. For these parameter values, the regions in the $\sigma_p - r_a$ parameter space where the SJ-I/II phenomena occur are similar as those computed by the model with the default parameter setting (Figure 2-5b). The value of σ_p that corresponds to R_i was obtained from Figure 2-9. The result is $\sigma_p = -0.21$, which falls in the regime where SJ-I is found (see Figure 2-5). The pressure gradient was prescribed such that the depth averaged east-directed tidal current amplitude was similar to that observed by Heaps and Jones (1981). The surface turbulent parameter r_a was calculated by application of a least square fit between the observed and the modelled velocity in the upper water column. With $r_a = 0.01$, the model captures the SJ-I phenomenon (see Figure 2-10a) shown by Heaps and Jones (1981). Note that r_a may vary due to time variations in wind stress and whitecapping. The results of Figure 2-5 indicate that if $n = 2$ and $r_a > 0.4$ (surface mixing that is larger than approximately 40% of the maximum mixing induced by tides) or $n \leqslant 1$, then the subsurface jet will vanish. The model result suggests that in this specific case, $r_a = 0.01$, so surface mixing is weak. This is consistent with the weak wind of 2.5 m s^{-1} (weatherspark.com) during the 12-hours data taken in April 8 to 9, 1977 (Wolf, 1980). Average wind conditions at this site are a factor 3 larger, thus resulting in larger r_a. This might explain why the SJ-I is not present in the current profile shown by Heaps and Jones (1981) for a full month of data.

Second, the case of the Yangtze Estuary was investigated, where the SJ-II phenomenon was detected by Jiang et al. (2013). The default values for mean water depth, roughness height (see Table 2-1) and $n = 2$ were used in this case. Moreover, salinity and along-channel velocity data were obtained during the field campaign in August, 2012 at a location close to where the M_2 tidal

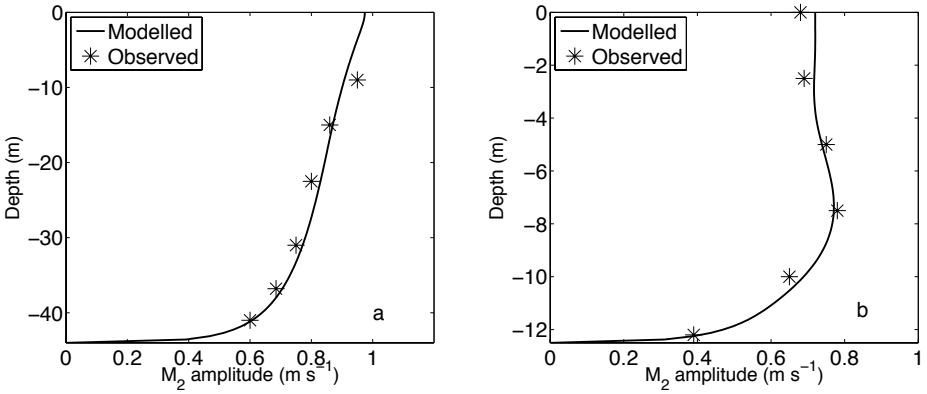

Figure 2-10: Vertical profile of the tidal current amplitude. Observed values are represented by stars $*$ and model results are represented by black lines. a. The comparison between the model profile and that reconstructed from field data by Heaps and Jones (1981) at a site in Liverpool Bay. b. As a., but for at location close to station CS3 in the Yangtze Estuary (Jiang et al., 2013).

current amplitude shows a subsurface jet. A similar procedure as for the Liverpool Bay case was conducted, resulting in $\sigma_p = -0.78$ and $r_a = 0.2$ for the Yangtze estuary. Figure 2-10b shows that the model is able to capture the observed profile of the tidal current amplitude. The subsurface maximum is also found for the tidal current amplitude during neap tide in the dry season at the same location. It implies that this is a persistent phenomenon in the Yangtze estuary. As the data were obtained in the estuarine turbidity maximum region, sediment-induced stratification is important in causing the decrease of the bottom boundary layer height (Song and Wang, 2013).

2.4.5 *Effect of earth rotation on tidal current profiles*

The earth rotation causes veering of tidal current with depth. To account for this, an extension of the model to two horizontal directions was made, following Bowden et al. (1959), Prandle (1982) and Soulsby (1983), to study the effect of earth rotation on the results. The present work applied the derivation similar to that presented by Soulsby (1983). The complex tidal current amplitudes $\hat{U}$ and $\hat{V}$ are written as

$$\hat{U} = R_+ + R_-; \tag{2-18a}$$

$$\hat{V} = iR_+ - iR_-; \tag{2-18b}$$

in which, the anticlockwise R_+ and clockwise R_- velocity vector read

$$R_\pm = -i\frac{g}{\omega \pm f} S_\pm \, p_\pm. \tag{2-19}$$

Here, the quantities S_+ and S_- represent anticlockwise and clockwise rotary components of surface gradient, respectively, and $f(\sim 10^{-4}\ s^{-1})$ is the Coriolis parameter. Moreover, the complex function p as introduced in Eq. 2-11 is also subdivided into anticlockwise (p_+) and clockwise (p_-) components. The expressions for $p_\pm$ follow p by replacing δ in expressions Eq. 2.A.1a and 2.A.1b of Appendix A by $\delta_\pm$, in which $\delta_\pm = \kappa\tilde{u}_*/[h(\omega \pm f)]$.

Soulsby (1983) showed that at the observation site of Heaps and Jones (1981) the depth mean tidal current is almost rectilinear. The surface gradient components ($S_\pm$) are therefore solved by imposing the constraint that the depth mean tidal current amplitudes are a given U_{mean} and $V_{mean} = 0$. The solutions become

$$\hat{U} = \frac{1}{2} U_{mean} \left(\frac{p_+}{P_+} + \frac{p_-}{P_-} \right), \tag{2-20}$$

and

$$\hat{V} = \frac{i}{2} U_{mean} \left(\frac{p_+}{P_+} - \frac{p_-}{P_-} \right). \tag{2-21}$$

The quantities $P_\pm$ are depth mean values of $p_\pm$. The computed eccentricity is below 10%, which is consistent with that was found in Souza (2013). It suggests that veering of the tidal current due to earth rotation is small at the site of the Heaps and Jones (1981) and that the surface jump on tidal current amplitude is still found (Figure 2-11). It turns out that earth rotation slightly enhances the surface jump.

2.4.6 *Model limitations and potential other drivers of surface jumps and subsurface jets*

The model that is presented in this study is highly idealised. It only describes tidal flow at a specific point, so the sea surface gradient has to be imposed, rather than that it is computed by the model. Furthermore, the formulation for eddy viscosity has three independent parameters, where two of them (σ_p and r_a) have a clear physical meaning. Values of n can only be estimated from known eddy viscosity profiles, e.g. calculated with a numerical model that

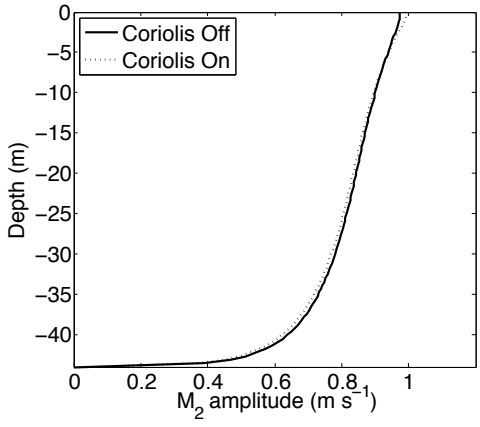

Figure 2-11: Vertical profile of the M_2 tidal current amplitude. Parameter values are as in Figure 2-10a. Solid line and dashed line represent the result for the case without and with the Coriolis effect, respectively.

employs a sophisticated closure for mixing, or reconstructed from data. Limitation of the present model is that it only allows for analytical solutions if $n = 0, 1$ and 2. This however in itself is not a serious limitation, as numerical solutions of the present model for any n can be obtained by straightforward means (see supplementary material S.1.1). It has been mentioned in section 2.2 that the applied linearisation approach is suitable in weakly to partially stratified water columns, where the tide is the main constituent of the water motion. In highly stratified estuaries, where residual current is of the same order of magnitude, or even larger than tidal flow, the eddy viscosity computed by Eq. 2-2 is too small because the value of $\tilde{u}_*$ obtained by means of the imposed linearisation procedue is underestimated. Finally, it should be realised that several field studies have revealed complex vertical profiles of eddy viscosity (Bowden and Sharaf El Din, 1966; Geyer et al., 2000; Basdurak et al., 2013), which can not be captured in detail by the eddy viscosity formulation that was used in this study.

It is also relevant to identify and discuss other potential drivers of surface velocity jumps and subsurface velocity jets that were not considered in this study. Before doing so, it is once more stressed (see also the introduction) that here the focus is on vertical profiles of current amplitudes of a single tidal constituent, rather than on profiles of instantaneous currents during flood and ebb, as were investigated by Jay and Musiak (1994) and Lacy et al. (2003). The crucial difference is that instantaneous currents include all tidal harmonics and consequently, a subsurface jet in an instantaneous current profile does not necessarily imply a subsurface jet in e.g. the M_2 tidal current amplitude. This is

apparent from Figure 4 of Jay and Musiak (1994), from which it can be concluded that a superposition of an M_2 tidal current (showing no SJ-I or SJ-II) and a residual current that is seaward in the upper layer and landward in the bottom layer may result in a subsurface jet during flood, and in a surface jump during ebb.

A different driver of surface jumps in the current amplitude of a tidal constituent is wind. If the wind stress varies periodically in time and has a positive correlation with the direction of the tidal current induced by a specific harmonic, it will create a surface jump (SJ-I) in the current amplitude of that tidal harmonic. An area where this might occur is San Francisco Bay, where the wind has a pronounced diurnal variation and where strong diurnal tidal constituents occur (Conomos et al., 1985).

Other potential drivers of SJ-I and SJ-II phenomena are advection terms, which were neglected in the present study because it was assumed that the amplitude of the sea surface variations is much smaller than the depth. If advection terms are not small and the instantaneous current also contains a residual component and overtides, they affect the profile of the tidal current. The arguments below apply to the M_2 tidal harmonic. As a first example, consider the advection of M_2 tidal momentum by along-channel residual currents. Furthermore, assume that the tidal current amplitude decreases towards the land and that the residual current is seaward in the upper layer and landward in the bottom layer, as is the case in many estuaries. Advection of M_2 tidal momentum by this residual current results in a reduction of the M_2 current speed near the surface and an intensification of the M_2 current speed near the bottom. This process thus leads to the occurrence of an SJ-II phenomenon.

As a second example, assume the advection of residual along-channel momentum by the tidal current. Consider the same conditions as in the first example, with the additional information that the residual overturning intensifies when moving into the estuary; this is typically the case at the seaward side of the salinity front. In that area, advection of residual current by the M_2 tidal current causes the M_2 tidal current speed to increase in the upper layer and to decrease in the lower layer. It thus leads to an SJ-I phenomenon. Further details, as well as other examples including lateral advection of along-channel momentum, are given in the supplementary material S.1.2.

Additional potential drivers of SJ-I and SJ-II are vertical gradients of turbulent stresses that vary at the M_2 tidal period and that arise from time-dependent mixing. Examples are stresses generated by the product of the M_2 component of vertical eddy viscosity A_v and a residual current shear, by the M_4 component of A_v and M_2 tidal shear, etc. In tidally dominated estuaries, which are considered in this study, these turbulent stresses are small compared to the turbulent stress that is retained, i.e. the one that originates from the product of the mean eddy viscosity and tidal shear. The M_2 component of A_v

describes tidal asymmetry in mixing that for example results from tidal straining of the density field, by both along-channel tidal flow (Simpson et al., 1990) and lateral tidal flow (Lacy et al., 2003; Lerczak and Geyer, 2004). Moreover, an M_2 component in A_v is generated by the friction velocity u_* that results from the joint action of all tidal harmonics. The M_4 component of A_v is mainly generated by tidal variation of the friction velocity. Whether the turbulent stresses related to time-varying mixing result in SJ-I and SJ-II depends on the vertical structure of both the harmonic components of A_v and the instantaneous current. These depend on stratification and have to be determined from the analysis of either field data or from output of numerical models.

2.5 CONCLUSIONS

The core objective of this study was to explain why at some field sites vertical profiles of observed tidal current amplitudes show either a subsurface maximum in the shear (surface jump) or a subsurface maximum in the current amplitude itself (subsurface jet). The key hypothesis was that these phenomena are related to site specific conditions, in particular density stratification and sources of turbulence at the surface. The hypothesis was tested within the context of a new, semi-analytical model that governs the vertical distribution of tidal flow. The model contains a formulation for eddy viscosity that can mimic turbulent mixing over a wide range of stratified conditions, measured by parameter σ_p, which is shown to be linked to the bulk Richardson number R_i, and the amount of surface turbulence. The model results show that surface jumps occur for relatively low surface turbulence, weakly to moderately stratified conditions and if eddy viscosity in the upper layer decreases faster than linearly towards the surface (parameter $n > 1$). Interestingly, if $n = 2$, stratification parameter σ_p is between -0.5 and -0.6 (R_i between 0.75 and 1.5) and surface turbulence is weak ($r_a \leqslant 0.05$), the model yields tidal current profiles that show both a surface jump and subsurface jet. Modelled tidal current amplitudes agree well with observations if parameter values are selected that are representative for conditions at a specific field site (depth, pressure gradient force, bulk Richardson number, bottom roughness and surface turbulence). This suggests that surface jumps and/or subsurface jets may be transient phenomena. On the other hand, field data in the North Passage of the Yangtze estuary show that subsurface jets are quite persistent.

2.A APPENDIX

2.A.1 *The solution for* p

The expression for function p in Eq. 2-11 reads as follows.

In the lower layer ($\sigma \in [-1, \sigma_h]$):

$$p = 1 + FP_\nu(\sigma') - GQ_\nu(\sigma'). \tag{2.A.1a}$$

In the upper layer ($\sigma \in [\sigma_h, 0]$):

$$p = \begin{pmatrix} 1 + c_1 \left[P_{\nu'}\left(\sigma''\right) - \frac{P_{\nu'+1}\left(\sigma_s'\right)}{Q_{\nu'+1}\left(\sigma_s'\right)} Q_{\nu'}\left(\sigma''\right) \right], & n = 2 \\ 1 + c_1 \left[I_0\left(\sigma'''\right) + \frac{I_1\left(\sigma_s'''\right)}{K_1\left(\sigma_s'''\right)} K_0\left(\sigma'''\right) \right], & n = 1 \end{pmatrix}. \tag{2.A.1b}$$

Here, $P_\nu(\sigma')$ and $Q_\nu(\sigma')$ are Legendre functions of the first and second kind and $I_n(m)$, while $K_n(m)$ denote modified Bessel functions of first and second kind, respectively. Furthermore,

$$F = \frac{F_3}{F_1 + F_2}, \quad G = \frac{1 + FP_\nu\left(\sigma_0'\right)}{Q_\nu\left(\sigma_0'\right)},$$

$$F_1 = P_\nu\left(\sigma_h'\right) - \frac{P_\nu\left(\sigma_0'\right)}{Q_\nu\left(\sigma_0'\right)} Q_\nu\left(\sigma_h'\right),$$

$$F_2 = -\beta \left(\left. \frac{\partial P_\nu\left(\sigma'\right)}{\partial \sigma} \right|_{\sigma_h} - \frac{P_\nu\left(\sigma_0'\right)}{Q_\nu\left(\sigma_0'\right)} \left. \frac{\partial Q_\nu\left(\sigma'\right)}{\partial \sigma} \right|_{\sigma_h} \right),$$

$$F_3 = \frac{Q_\nu\left(\sigma_h'\right)}{Q_\nu\left(\sigma_0'\right)} - \beta \frac{1}{Q_\nu\left(\sigma_0'\right)} \left. \frac{\partial Q_\nu\left(\sigma'\right)}{\partial \sigma} \right|_{\sigma_h},$$

$$\beta = \beta_1 / \beta_2 ,$$

$$\beta_1 = \begin{pmatrix} P_{\nu'}\left(\sigma_h''\right) - \frac{P_{\nu'+1}\left(\sigma_s'\right)}{Q_{\nu'+1}\left(\sigma_s'\right)} Q_{\nu'}\left(\sigma_h''\right), & n = 2 \\ I_0\left(\sigma_h'''\right) + \frac{I_1\left(\sigma_s'''\right)}{K_1\left(\sigma_s'''\right)} K_0\left(\sigma_h'''\right), & n = 1 \end{pmatrix},$$

$$\beta_2 = \begin{pmatrix} \left. \frac{\partial P_{\nu'}\left(\sigma'\right)}{\partial \sigma} \right|_{\sigma_h} - \frac{P_{\nu'+1}\left(\sigma_s'\right)}{Q_{\nu'+1}\left(\sigma_s'\right)} \left. \frac{\partial Q_{\nu'}\left(\sigma'\right)}{\partial \sigma} \right|_{\sigma_h}, & n = 2 \\ -\frac{2i}{\chi_2 \sigma_h'''} \left[I_1\left(\sigma_h'''\right) - \frac{I_1\left(\sigma_s'''\right)}{K_1\left(\sigma_s'''\right)} K_1\left(\sigma_h'''\right) \right], & n = 1 \end{pmatrix},$$

$$c_1 = F \frac{F_1}{\beta_1} - \frac{Q_\nu\left(\sigma_h'\right)}{Q_\nu\left(\sigma_0'\right)} \frac{1}{\beta_1},$$

$\nu = \frac{-\sqrt{\delta}+\sqrt{4i+\delta}}{2\sqrt{\delta}}$, $\nu' = \frac{-\sqrt{\chi_1}+\sqrt{-4i+\chi_1}}{2\sqrt{\chi_1}}$,
$\delta = \kappa\tilde{u}_*/(\omega h)$,
$\sigma' = \frac{2\sigma+1-\sigma_p}{1+\sigma_p}$, $\sigma'' = \frac{i\sigma}{\sqrt{A_S\rho_1}}$, $\sigma''' = 2\sqrt{\frac{-i(\rho_2+\sigma)}{\chi_2}}$,
$\sigma_h{}' = \frac{2\sigma_h+1-\sigma_p}{1+\sigma_p}$, $\sigma_h{}'' = \frac{i\sigma_h}{\sqrt{A_S\rho_1}}$, $\sigma_h{}''' = 2\sqrt{\frac{-i(\rho_2+\sigma_h)}{\chi_2}}$,
$\sigma_s{}' = \frac{1-\sigma_p}{1+\sigma_p}$, $\sigma_s{}''' = 2\sqrt{\frac{-i\rho_2}{\chi_2}}$, $\sigma_0{}' = \frac{2\sigma_0-1-\sigma_p}{1+\sigma_p}$,
$\chi_1 = \delta\rho_1{}^{-1}$, $\rho_1{}^{-1} = \frac{[(1+\sigma_h)(\sigma_p-\sigma_h)-A_S]}{\sigma_h{}^2}$,
$\chi_2 = \delta\rho_2{}^{-1}$, $\rho_2^{-1} = \frac{[(1+\sigma_h)(\sigma_p-\sigma_h)-A_S]}{\sigma_h}$.

If $n = 0$, the expression for p has the same solution structure as equation (A-1a) in the lower layer but in the upper layer

$$p = 1 + 2c_1 \cos\left[\frac{(1+i)\,\sigma}{\sqrt{\chi_3}}\right] \quad \text{for} \quad \sigma \in [\sigma_h, 0]\,. \tag{2.A.2}$$

In this expression, $\sigma_h = (\sigma_p - 1)/2$. The coefficient $c_1 = \frac{(FP_\nu(0)-GQ_\nu(0))}{2\beta_1}$, in which the polynomial F is a function of F_1, F_2 and F_3 as presented in the solutions of the case of $n = 1$ and $n = 2$ (see above), but with $\beta = \beta_1/\beta_2$ such that $\beta_1 = \cos\left[\frac{(1+i)(\sigma_p-1)}{2\sqrt{\chi_3}}\right]$ and $\beta_2 = -\frac{(1+i)}{\sqrt{\chi_3}}\sin\left[\frac{(1+i)(\sigma_p-1)}{2\sqrt{\chi_3}}\right]$, with $\chi_3 = \delta\,(1+\sigma_p)^2/2$.

In the supplementary material S.1.3, a Mathematica code is provided that allows users to calculate vertical profiles of tidal current amplitudes.

2.A.2 *Data used to produce Figure 2-9*

Regarding the paper of Bowden and Sharaf El Din (1966), data from station 1 to 4 were used. Because the observed sites are close to each other and results are similar, average values of the four stations were taken and shown. The value of parameter $\sigma_p = -0.3$ was estimated from their Table 4. Regarding the paper of Jay and Musiak (1996), the value $\sigma_p = -0.6$ was estimated by applying their equation (1) and (2).

In Geyer et al. (2000), the authors showed the eddy viscosity profiles at flood and ebb peak for both spring and neap tide. Estimates of the tidally mean eddy viscosity from these data were obtained by taking the mean values of spring and neap tide, respectively. Data and corresponding eddy viscosity values from the paper Li and Zhong (2009) were estimated from the figures by averaging over a tidal period. A similar approach was applied to obtain data from Basdurak et al. (2013). Only data from the channel was used.

Note that some of the references present top-to-bottom salinity differences.

These were converted to top-to-bottom density differences by using the relation $\Delta\rho = \beta\Delta s$. The summary of all data are presented in Table 2.A.1.

Table 2.A.1: Data, including their sources, that were used to produce Figure 2-9. In the table, Stat. is Station, h is depth, U_m is depth averaged tidal amplitude, $\Delta\rho$ is tidally mean bottom-to-surface density difference and bulk R_i is computed from Eq. 2-13.

Reference	Description	h (m)	U_m (m s^{-1})	$\Delta\rho$ (kg m^{-3})	bulk R_i
Bowden and Sharaf El Din (1966)		17	1.38	0.80	0.07
Jay and Musiak (1996)		20	1.00	10.00	1.92
Geyer et al. (2000)	neap	15	0.70	8.70	2.56
	spring	15	1.00	1.50	0.22
Li and Zhong (2009)	Stat.B	14	0.60	3.51	1.31
	Stat.A, neap	10	0.30	5.46	5.83
	Stat.A, spring	10	0.50	3.12	1.20
	Stat.C, neap	20	0.29	2.34	5.35
	Stat.C, spring	20	0.32	2.73	4.54
	Stat.D, neap	7	0.28	4.68	4.01
	Stat.D, spring	7	0.40	2.73	1.15
Basdurak et al. (2013)	Feb.23,04	15	1.00	3.50	0.5
	Sep.30,04	16	0.80	3.00	0.72
	Nov.04,04	15	0.50	6.50	3.75
	Feb.23,05	15	0.60	8.00	3.20
	May.18,05	15	0.50	9.50	5.47
	May.23,05	15	0.56	4.00	1.80

3

SPATIAL STRUCTURE OF MODELLED ESTUARINE RESIDUAL CURRENT INDUCED BY EDDY VISCOSITY-SHEAR COVARIANCE: DEPENDENCE ON LONGITUDINAL BOTTOM SLOPE, INTENSITY OF TIDAL FORCING AND MIXED TIDAL FORCING

3.1 INTRODUCTION

It has been noted in many studies that residual current, driven by a shear stress that is due to the covariance between tidally varying eddy viscosity and the vertical gradient of tidal velocity, is a significant component of the estuarine circulation (Jay and Musiak, 1994; Stacey et al., 2001, 2008; Burchard and Hetland, 2010; Cheng et al., 2010; Stacey et al., 2010; Burchard and Schuttelaars, 2012; Geyer and MacCready, 2014). Following Dijkstra et al. (2017), this covariance is referred to as 'Eddy viscosity Shear COvariance' (ESCO). One process that causes variations in eddy viscosity is the advection of the density field by horizontal currents that have vertical shear (Ruijter, 1983; van Aken, 1986; Simpson et al., 1990). In the case of tidal currents, during flood, salt oceanic water is strained over fresher water, causing stratification to decrease, thereby resulting in increased turbulence. In contrast, during ebb, relatively light water is advected over salt water, the stratification is enhanced and this suppresses turbulence. In tidally energetic estuaries, this so-called tidal straining mechanism results in variation of eddy viscosity at the period of the primary tide, which is often the semi-diurnal M_2 tide (Burchard and Baumert, 1998; Geyer et al., 2000; Stacey et al., 2001; Simpson et al., 2002, 2005).

The background stratification of the water column has a strong impact on the temporal variation of turbulent eddy viscosity that results from the straining process, and thereby on the structure of the residual current that is driven by ESCO. Using a 1D numerical model, Stacey et al. (2008) found that in a periodically stratified water column, the ESCO current always shows a two-layer structure in the vertical direction, with the current direction in the layers depending on the tidal phase at which a perturbation in the density field is

externally imposed. The onset of stratification during the ebb phase results in landward current near the bottom and seaward current near the surface. This is referred to as a 'classical' two-layer structure, because it is identical to that of the estuarine circulation driven by horizontal density gradients. However, if stratification is imposed during the flood phase, the ESCO current has a 'reversed' two-layer structure (landward directed in the upper layer and seaward below it). Similar findings were reported by Cheng et al. (2010), who investigated the ESCO current in weakly stratified to highly stratified estuaries by using a 3D numerical model (Cheng et al., 2011, 2013), in which the variation in stratification was computed internally, rather than being imposed. The degree of stratification in the estuary is controlled by a varying amplitude of a single externally forced tide, i.e., the semi-diurnal tide. Their results show that under periodically stratified conditions the residual current due to ESCO has a classical two-layer structure. If stratification increases, first a transition to a three-layer structure occurs, and for highly stratified conditions a reversed two-layer structure is obtained. Note that the tidal mean stratification not only affects the temporal evolution of turbulent eddy viscosity, but also the vertical shear of the semi-diurnal tidal current (see in chapter 2, also in Chen and Swart, 2016), which is also a part of ESCO.

Apart from tidal straining, the covariance between eddy viscosity and tidal velocity shear could also result from, e.g., tidal variation of eddy viscosity induced by wind (Verspecht et al., 2009). Recently, Dijkstra et al. (2017) showed with 1D and 2D numerical models that at a specific location in the (partially stratified and M_2 dominated) Scheldt River Estuary, the covariance between M_4 eddy viscosity and M_4 tidal velocity shear contributes about 8% to the total residual current (other drivers of residual current are horizontal density gradients, Stokes transport, etc.). Sources of M_4 tidal velocity are, e.g., nonlinear advection of the M_2 tidal momentum by M_2 tidal currents and depth dependent friction (e.g. Ianniello, 1977). The M_4 eddy viscosity component is generated by the friction velocity of the M_2 tide, and by intratidal variations of the density stratification (Simpson et al., 2005).

So far, the studies on ESCO mainly considered estuaries of constant depth with the M_2 being the dominant tide and the ESCO current was analysed at fixed locations. These observations motivate three research aims of the present study. First (RA.1), to investigate the effect of longitudinal depth variation on the structure of ESCO current for fixed tidal forcing that consists of a single semi-diurnal constituent. Second (RA.2), to quantify the effect of tidal mean stratification on the ESCO current at all locations in the estuary. Third (RA.3), to investigate the ESCO-induced residual current in the case that the externally forced tide contains multiple constituents with frequencies that do not have an integer ratio and stratification at the mouth is kept fixed. The latter is relevant because tidal forces generate not only M_2, but also e.g. diurnal constituents P_1,

K_1 and O_1 and a semi-diurnal constituent S_2. As highlighted by Geyer and MacCready (2014), systematic investigation of dynamics of estuaries in which the tidal motion is forced by multiple constituents is "surprisingly" late. One important consequence of the joint action of tidal constituents with different frequencies is that nonlinear interactions between any two single tidal constituents will influence other tidal constituents and generate new constituents, in particular a long-periodic tide, which also contribute to the ESCO residual current.

To address these objectives, the numerical model Delft3D-current (Lesser et al., 2004) is applied to explicitly resolve the temporal and spatial structure of vertical eddy viscosity and tidal current at different locations. The focus of this work is on the longitudinal dynamics driven by tides. Hence, the estuary is assumed to be straight and narrow, without lateral variations in depth. Moreover, effects of wind and the Coriolis force are not considered. The latter conditions imply a weak lateral current, which also causes straining of the density field (e.g. Lacy et al., 2003; Burchard and Schuttelaars, 2012; Basdurak et al., 2013).

In section 3.2, the numerical model and the design of the experiments are presented. Furthermore, the methods to calculate residual current induced by ESCO, and to decompose the ESCO forcing into contributions due to different tidal constituents are described. Model results are presented in section 3.3, followed by a discussion in section 3.4. Finally, section 3.5 contains the conclusions.

3.2 MATERIAL AND METHODS

3.2.1 *Model*

The numerical hydrodynamic model Delft3D-current (for a description, see Delft Hydraulics, 2006) is used to simulate currents, salinity and turbulence in an idealised estuary-shelf system (Figure 3-1). Temperature is kept constant so that density variations are due to salinity variations only. An x, y, σ—coordinate system is adopted, in which $\sigma = (z - \eta)/D$, with $z = \eta$ being the vertical level of the free-surface, D being the distance from free-surface to the bottom and x, y, z are Cartesian coordinates. The straight channel is located between river head $x = 0$ and estuary mouth $x = L_c$. It has an undisturbed depth $H(x)$ and a constant width B_c. The adjacent sea has straight open boundaries that are positioned at a distance B_s from the estuary mouth and it has a depth that increases linearly from the coast to the eastern boundary. Freshwater is prescribed at the estuary head $x = 0$ with a constant discharge Q. At the three open boundaries of the sea, tidal sea surface elevations with given amplitudes and frequencies are imposed. Moreover, fixed values of salinity are imposed at these boundaries. A two-equation $k - \varepsilon$ turbulence scheme is used to compute

vertical eddy viscosity and eddy diffusivity. Horizontal eddy viscosity and diffusivity are assumed to be constant.

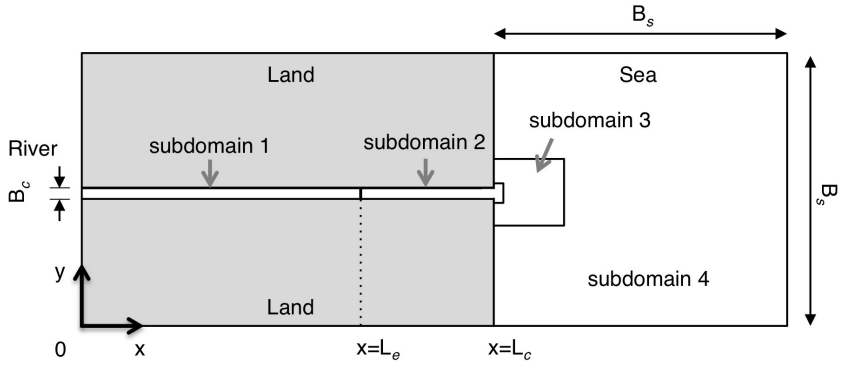

Figure 3-1: Geometry of the idealised estuary-shelf sea system. The subdomains are introduced for reasons of numerical efficiency (see text for details).

3.2.2 *Setup of Experiments*

First, a setting of experiments is designed to address the first research aim (RA.1). For this, a fixed river discharge is prescribed at the landward side, while at the seaward boundaries a tide is imposed with a single frequency that in each boundary point has the same amplitude and phase. Furthermore, the bottom is flat from river head to the location $x = L_e$, which is inside the estuary (see Figure 3-1), whilst seaward of this location water depth linearly increases to the estuary mouth ($x = L_c$) with different values of the bottom slope. Three different series of experiments are considered. In the first series, the depth $H_e = H\,(x = L_e)$ is kept fixed and $H_c = H\,(x = L_c)$ increases with increasing bottom slope. In series 2, H_e decreases and H_c increases such that the volume of the estuary is kept fixed. Finally, in series 3, H_e decreases and H_c is kept fixed.

The fourth series of experiments is designed to address the second research aim (RA.2). To focus on the effect of varying tidal mean stratification on the spatial structure of the ESCO current, a constant depth is used between river head and estuary mouth. The forcing is identical to that of the previous series, but now the amplitude of the tide at the open boundaries is varied, such that a different degree of stratification is obtained in the estuary.

Finally, the fifth series of experiments addresses the third research aim (RA.3), i.e., to assess the spatial structure of the ESCO current in an estuary

in which tidal motion is driven by tides imposed at the seaward boundaries that contain multiple constituents with different amplitudes. The constituents that are considered are a semi-diurnal tide with radian frequency ω and two diurnal tidal constituents with frequencies $\frac{1}{2}\omega - \Delta\omega$ and $\frac{1}{2}\omega + \Delta\omega$, respectively, where $\Delta\omega$ is a constant. The reason for this choice is that including two diurnal tidal constituents will create spring-neap cycles in tidal currents with period $\pi/\Delta\omega$. Selecting only one semi-diurnal tide will avoid additional spring-neap cycles, which would complicate the analysis. In this series, different values of amplitudes of semi-diurnal tide and diurnal tides at the open boundaries are chosen, such that the amplitude ratio between diurnal tides and semi-diurnal tides changes from 0 to 1, while the amplitude of the friction velocity at the mouth of the estuary, U_*, is fixed (see section 3.2.6 for details). The latter is done because U_* is used to indicate the intensity of external tidal forcing of the estuary.

Table 3-1: The framework of the model experiments design.

Aim	Experiments	Controlled conditions		
		Bottom slope	Tidal amplitude	Tidal constituents
RA.1	Series 1, 2, 3	Varied	Fixed	Single
RA.2	Series 4	Fixed (no slope)	Varied	Single
RA.3	Series 5	Fixed (no slope)	Varied*	Multiple

* Varied amplitude of each tide constituent but with a fixed amplitude of friction velocity U_* at the mouth.

The relations between the research aims and the series of experiments are summarised in Table 3-1. The model input parameters that are constant for all experiments are listed in Table 3-2. These values are representative for a typical single channel tidal estuary. In the experiments of series 1, 2 and 3, the tidal amplitude is 1 m at the three open boundaries and depth values at $x = L_e$ and $x = L_c$ are given in Table 3-3. Recall that the depth for $x < L_e$ equals that at $x = L_e$. In the experiments of series 4 and 5, a constant depth $H = 10$ m is applied for the entire channel ($0 < x < L_c$).

For reasons of numerical efficiency, the semi-diurnal tide (hereafter called M_2') is assumed to have a radian frequency $\omega = 1.45 \times 10^{-4}$ s^{-1} (i.e., with a period of 12 hours). Likewise, the two diurnal tidal constituents are called O_1' and K_1', respectively. Furthermore, for series 5, a strict tidal mean (to compute tidal residual current) can only be calculated if $\omega/\Delta\omega$ is an integer ratio. The larger this ratio, the longer the period over which the tidal mean has to be computed. To avoid long computational times of the tidal mean, $\Delta\omega$ is adjusted in such a way that both diurnal and semi-diurnal constituents repeat themselves

after a single spring-neap cycle (with period $\pi/\Delta\omega$). As is shown in Table 3-2, $\Delta\omega = \omega/18$ yields a spring-neap tidal cycle of 4.5 days. The values of tidal amplitudes ($A_{M_2'}$, etc.) of all tidal constituents (M_2', ...) are given in Table 3-3.

Table 3-2: Values of the model input parameters.

Parameter	Symbol	Unit	Value
Channel length	L_c	km	260
Channel width	B_c	km	3
River section length	L_e	km	210
Depth at eastern seaward boundary	H_{sea}	m	50
Shelf sea size	B_s	km	100
Freshwater discharge	Q	$m^3 s^{-1}$	1500
Salinity at open boundaries	S	psu	31
Background temperature	T	°C	15
Horizontal eddy viscosity	A_h	$m^2\ s^{-1}$	50
Horizontal eddy diffusivity	K_h	$m^2\ s^{-1}$	50
Semi-diurnal tidal frequency	ω	s^{-1}	1.45×10^{-4}
Half of spring-neap tidal frequency	$\Delta\omega$	s^{-1}	8.06×10^{-6}

Table 3-3: Values of the control parameters in all 5 series of experiments. Here, $A_{M_2'}$, $A_{O_1'}$ and $A_{K_1'}$ are the tidal sea surface amplitudes at the open boundaries of the sea adjacent to the estuary.

Series	Control parameter	Values (m)							
1	$H\ (x = L_e)$	10	10	10	10	10			
	$H\ (x = L_c)$	10	11.25	12.5	13.75	15			
2	$H\ (x = L_e)$	10	9.375	8.75	8.125	7.5			
	$H\ (x = L_c)$	10	10.625	11.25	11.875	12.5			
3	$H\ (x = L_e)$	10	8.75	7.5	6.25	5			
	$H\ (x = L_c)$	10	10	10	10	10			
4	$A_{M_2'}$	Range from 0.5 m to 1.5 m at intervals of 0.05 m							
5	$A_{M_2'}$	0.75	0.73	0.70	0.65	0.60	0.55	0.35	0
	$A_{O_1'}, A_{K_1'}$	0	0.1	0.20	0.35	0.50	0.65	0.80	0.90

The model is spun up from rest, with $S = 31$ psu everywhere in the domain and runs span a time that is sufficiently long to ensure that the transient effects of initial conditions are no longer present. This was verified in series 1-4 by comparing the results from the last tidal cycle with those of the previous one.

In series 5, this was done by comparing the results of the last spring-neap cycle with those of the preceding cycle.

3.2.3 *Numerical aspects*

To increase the efficiency of the model computation, the model domain is divided into four subdomains (Figure 3-1). All subdomains have 20 sigma layers that are uniformly divided in the vertical direction. The grid cells in all subdomains have the same size in $x-$ and $y-$direction. The ratio between the horizontal grid sizes of two adjacent subdomains (the value of the larger grid size over the smaller grid size) is 3. The first subdomain is from $x = 0$ to $x = L_e$. Here, the number of grid points in each $\sigma-$layer is 282 (along-channel) by 6 (across-channel) and the longitudinal grid size is 750 m. Subdomain 2 is from $x = L_e$ to $x = L_c + l$, where $l = 3$ km. It has in each $\sigma-$layer of 200 by 12 grid points in the channel and 14 by 26 grid points on the shelf. The longitudinal grid size is 250 m. For each $\sigma-$layer, in the two horizontal directions, subdomain 3 consists of 38 grid points and subdomain 4 contains 46 grid points. The longitudinal grid sizes in subdomains 3 and 4 are 750 m and 2.25 km, respectively. Here, the relatively smaller grid size around the corner of the estuary mouth allows detailed simulation of the hydrodynamics around the estuarine mouth.

3.2.4 *Decomposition of residual current*

The residual current contains components that are generated by different drivers, e.g., river discharge, horizontal density gradients and nonlinear advection of tidal momentum by tidal current (Geyer and MacCready, 2014). To identify the residual current induced by ESCO, the tidally mean longitudinal momentum equation and continuity equation are considered that only include the ESCO forcing (Burchard and Hetland, 2010; Cheng et al., 2013). The solutions of these equations read

$$u_\tau = \int_{-1}^{\sigma} H \frac{1}{\bar{A}_v} \left(gH \frac{\partial \eta_\tau}{\partial x} \tilde{\sigma} - \tau \right) d\tilde{\sigma}, \tag{3-1a}$$

$$\frac{\partial \eta_\tau}{\partial x} = \int_{-1}^{0} \int_{-1}^{\sigma} H \frac{\tau}{\bar{A}_v} d\tilde{\sigma} d\sigma \Big/ \int_{-1}^{0} \int_{-1}^{\sigma} gH^2 \frac{\tilde{\sigma}}{\bar{A}_v} d\tilde{\sigma} d\sigma, \tag{3-1b}$$

in which

$$\tau = \frac{1}{H}\overline{A'_v \frac{\partial u'}{\partial \sigma}} + \tau_a, \tag{3-2a}$$

$$\tau_a = \int_\sigma^0 \left[\overline{\frac{2\eta}{H^2}\frac{\partial}{\partial \tilde{\sigma}}\left(\bar{A_v}\frac{\partial u'}{\partial \tilde{\sigma}}\right)} + \overline{\frac{2\eta}{H^2}\frac{\partial}{\partial \tilde{\sigma}}\left(A'_v\frac{\partial \bar{u}}{\partial \tilde{\sigma}}\right)} + \overline{\frac{2\eta}{H^2}\frac{\partial}{\partial \tilde{\sigma}}\left(A'_v\frac{\partial u'}{\partial \tilde{\sigma}}\right)} \right] d\tilde{\sigma}. \tag{3-2b}$$

Here, $\tilde{\sigma}$ is a dummy variable, and the overbar $(\bar{})$ and prime $(')$ represent the tidally averaged and tidally varying part of a variable, respectively. The sea surface gradient $\frac{\partial \eta_\tau}{\partial x}$ is such that there is no mass transport by u_τ through the cross-section, as follows from mass conservation. The vertical eddy viscosity is denoted by A_v and g $(= 9.8\ m\ s^{-2})$ is the gravitational acceleration. The first component inside brackets in the r.h.s. of Eq. 3-1a contains the barotropic pressure gradient. Variable τ is a (kinematic) mean stress that is defined in Eq. 3-2a. The first part on the r.h.s of Eq. 3-2a represents the covariance between time-varying eddy viscosity and vertical tidal velocity shear at fixed σ—levels ($ESCO^\sigma$) and τ_a on the r.h.s of Eq. 3-2a ($ESCO^a$) is related to the covariance between the time-varying water surface elevation η and tidal shear, water surface elevation and eddy viscosity and triple covariance between water surface elevation, eddy viscosity, and vertical shear, respectively (Eq. 3-2b). The contribution τ_a to τ results from using σ—coordinates rather than z—coordinates.

3.2.5 *Quantification of stratification in the estuary*

The degree of stratification in the estuary is determined by the competition between buoyancy forcing and tidal forcing. In this study, the former is due to freshwater input and the latter is quantified by the friction velocity at the mouth of the estuary. Following Geyer and MacCready (2014), in the cases that the tidal forcing has a dominant constituent, two parameters Fr_f and M are used that control the degree of stratification at the mouth, i.e.,

$$Fr_f = \frac{U_R}{N_0 H_c}, \quad \text{and} \quad M = \frac{U_*}{(\omega N_0)^{1/2} H_c}. \tag{3-3}$$

Here, Fr_f is the freshwater Froude number, which expresses a ratio between the river current U_R $(= \frac{Q}{H_c B_c})$ and the scale of the maximum possible frontal propagation speed. In Eq. 3-3, $N_0 = (\beta g S/H_c)^{1/2}$, with H_c the depth at the mouth, is an estimate of the buoyancy frequency in the case of maximum top-to-bottom salinity variation in an estuary, in which S is the salinity at the open boundaries and $\beta = 7.8 \times 10^{-4}\ psu^{-1}$ is the salinity contraction coefficient. The

second parameter M expresses the ratio of the tidal timescale to the vertical turbulent mixing timescale at the mouth.

In this study, the parameters Fr_f and M are used to classify the estuary, based on the regime diagram shown in Geyer and MacCready (2014). However, Fr_f and M do not yield information about the degree of stratification at the locations inside the estuary. For this reason, an alternative parameter, $\Delta S/S$ is used, in which ΔS is the tidal mean top-to-bottom salinity difference that depends on x, and $S = 31$ psu is the salinity at the open boundaries.

3.2.6 *Mixed tidal forcing*

In case that the tidal forcing contains M_2', O_1' and K_1', nonlinear interactions between these constituents will result in additional constituents with sum and difference frequencies. For example, quadratic nonlinear terms (like advection) generate additional constituents like ter-diurnal tides (MO_3' and MK_3'), a quarter-diurnal tide (M_4') and a long-periodic tide (Mf'). Note that nonlinear interaction involving these new constituents will further result in additional constituents, e.g. the interaction of M_2' and M_4' will generate an M_6' tide.

The characteristics of the forced mixed tide are measured by parameter

$$F' = \frac{F}{1+F} \quad \text{and} \quad F = \frac{\sqrt{U_{m,O_1'}{}^2 + U_{m,K_1'}{}^2}}{\sqrt{U_{m,M_2'}{}^2 + U_{m,O_2'}{}^2 + U_{m,K_2'}{}^2}}. \tag{3-4}$$

Here, F was introduced by Defant (1958) and it measures the ratio of the maximum diurnal tidal amplitude and that of the semi-diurnal tide. In Eq. 3-4, $U_m = U_*/C_d^{1/2}$ (where $C_d \simeq 1 - 2.5 \times 10^{-3}$ denotes a drag coefficient) is the cross-sectional mean tidal current amplitude at the estuary mouth. When $0.2 < F' < 0.75$, the tidal motion is considered as a mixed tide. The tide is considered semi-diurnal dominant when $0 < F' < 0.2$, and diurnal dominant when $0.75 < F' < 1$.

3.2.7 *Harmonic analysis*

Harmonic analysis is used in order to quantify the relative contribution of different tidal constituents to the total signal. Below, the kinematic shear stress component $ESCO^\sigma$ is considered (the first term of Eq. 3-2a). Consequently,

the harmonic decomposition is applied to the time series of the velocity shear ($\frac{1}{H}\frac{\partial u'}{\partial \sigma}$) and the vertical eddy viscosity (A'_v), respectively. This yields

$$\frac{1}{H}\frac{\partial u'}{\partial \sigma} = \sum_n \frac{1}{H}\left[\frac{\partial u_n}{\partial \sigma}\right]\cos(\omega_n t - \varphi_n), \tag{3-5a}$$

$$A'_v = \sum_n A_{v,n}\cos(\omega_n t - \psi_n), \tag{3-5b}$$

where $\frac{1}{H}\left[\frac{\partial u_n}{\partial \sigma}\right]$ denotes the amplitude of the vertical shear of tidal velocity of a specific tidal constituent (O'_1, K'_1, M'_2, M'_4, ...). Furthermore, ω_n is the radian frequency and φ_n is the phase. Similarly, $A_{v,n}$ and ψ_n are the amplitude and phase of eddy viscosity of the tidal harmonic n, respectively.

Substitution of Eq. 3-5a and 3-5b into Eq. 3-2a (and ignoring ESCO[a] at this stage) yields

$$\tau = \underbrace{\tau_{O'_1} + \tau_{K'_1}}_{\text{diurnal}} + \underbrace{\tau_{O'_2} + \tau_{K'_2} + \tau_{M'_2}}_{\text{semi-diurnal}} + \underbrace{\tau_{MO'_3} + \tau_{MK'_3}}_{\text{ter-diurnal}} + \underbrace{\tau_{M'_4}}_{\text{quarter-diurnal}} + \ldots, \tag{3-6}$$

with

$$\tau_n = \frac{1}{H}A_{v,n}\left[\frac{\partial u_n}{\partial \sigma}\right]\frac{1}{2}\cos(\varphi_n - \psi_n). \tag{3-7}$$

Similarly, the term τ_a in Eq. 3-2a is decomposed into contributions due to different tidal constituents. The ESCO current components and corresponding sea surface gradients are

$$u_{\tau,n} = \int_{-1}^{\sigma} H\frac{1}{\bar{A}_v}\left(gH\frac{\partial \eta_{\tau,n}}{\partial x}\tilde{\sigma} - \tau_n\right)d\tilde{\sigma}, \tag{3-8a}$$

$$\frac{\partial \eta_{\tau,n}}{\partial x} = \int_{-1}^{0}\int_{-1}^{\sigma} H\frac{\tau_n}{\bar{A}_v}d\tilde{\sigma}d\sigma \Big/ \int_{-1}^{0}\int_{-1}^{\sigma} gH^2\frac{\tilde{\sigma}}{\bar{A}_v}d\tilde{\sigma}d\sigma. \tag{3-8b}$$

In Eq. 3-8a, $u_{\tau,n}$ denote the residual flows generated by ESCO due to individual tidal frequencies, with n representing O'_1, K'_1, M'_2, M'_4, ... The sea surface gradients $\frac{\partial \eta_{\tau,n}}{\partial x}$ in Eq. 3-8b is related to $u_{\tau,n}$.

3.2.8 *Quantifying the importance of the ESCO current due to individual tides and their structures*

The relative importance of the residual current induced by ESCO of individual harmonic frequencies with respect to the total ESCO current is computed as

$$r_n = \frac{\frac{1}{2}\int_{-1}^{0} u_{\tau,n}^2 d\sigma}{\sum \frac{1}{2}\int_{-1}^{0} u_{\tau,m}^2 d\sigma}. \tag{3-9}$$

Parameter r_n measures the ratio between the depth-integrated kinetic energies of one ESCO current component and the sum of the depth-integrated kinetic energy of all ESCO current components. The ESCO current due to an individual tide is considered as a dominant component when $r_n > 0.5$. Furthermore, the ESCO current due to an individual tide is small when $r_n < 0.05$.

Likewise, the relative importance of the ESCO current with respect to the residual current due to other drivers (e.g., river current, density driven current etc.) is computed as

$$r_E = \frac{\frac{1}{2}\int_{-1}^{0} u_\tau^2 d\sigma}{\frac{1}{2}\int_{-1}^{0} \overline{u}^2 d\sigma}, \tag{3-10}$$

where $\overline{u}$ is the total residual current. The ESCO current is considered relevant when $r_E > 0.05$.

To indicate the structure of ESCO flows, first, layers are identified in which the vorticity $\frac{1}{H}\frac{\partial u_\tau}{\partial \sigma}$ has a fixed sign. This is done because vorticity is a measure of the degree of overturning in such a layer. For the classical estuarine circulation there is one layer in which the vorticity is positive if seaward current is defined as positive. The boundaries of these layers $\sigma_i (i = 1, 2, \ldots I-1,$ ordered from surface to bottom$)$ are defined as the levels at which u_τ attains an extremum $u_{\tau,i}$. Here, $I \geqslant 2$ denotes the total number of extreme values in the vertical profiles of u_τ. Next, a measure of the vorticity $\mathcal{V}_i$ is calculated as

$$\mathcal{V}_i = \frac{u_{\tau,i} - u_{\tau,i+1}}{H(\sigma_i - \sigma_{i+1})}. \tag{3-11}$$

Note that at the bottom ($\sigma = -1$), $u_\tau = 0$ is not accounted for in the calculation of the vorticity. Positive (negative) $\mathcal{V}_i$ denotes clockwise (anti-clockwise) overturning (Figure 3-2).

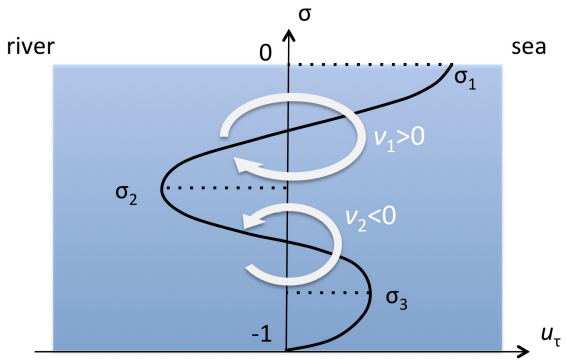

Figure 3-2: Example of an ESCO current that is characterised by three current layers and two vorticity layers. Positive (negative) values of the ESCO current (black line) is seaward (landward). Overturning of the current is indicated by white arrows.

3.3 RESULTS

3.3.1 *Structure of u_τ for varying longitudinal depth (RA.1)*

Figure 3-3 shows results for model runs with a flat bottom (first experiment of series 1 in Table 3-3) and a bottom with a slope of 1×10^{-4} (last experiment of series 1 in Table 3-3). The computed Fr_f and M are 3.2×10^{-2} and 1.2 for the former case, respectively, 1.8×10^{-2} and 0.64 for the latter case. Upon tracing these values in the regime diagram of Geyer and MacCready (2014), it follows that the estuary is periodically stratified in the flat bottom case and it is at the transition between weakly stratified to highly stratified in the sloping bottom case. In panels (a) and (b), the degree of stratification $\Delta S/S$ and the strength of the ESCO current with respect to total residual current r_E are plotted as a function of longitudinal distance. In both cases, $\Delta S/S$ increases from zero at the riverside up to the maximum value at 254 km, and subsequently decreases to the estuary mouth. At each location, the value of $\Delta S/S$ in the latter case is larger than that in the former case. Two distinct structures are identified in u_τ for the two model configurations. Note that results are shown in the part of the estuary where the value of $\Delta S/S$ varies in the longitudinal direction. In the flat bottom case (Figure 3-3c), a two-layer structure is observed with landward current near the bottom and seaward current near the surface. In the case of the sloping bottom (Figure 3-3d), a three-layer structure is found, with landward current both near the surface and near the bottom, and seaward current in the middle. Panels (e) and (f) show the longitudinal distribution of the total residual current for the two cases. Comparing (c) with (e) and (d) with

(f) reveals that the contribution of the ESCO current to the total residual current is relevant ($r_E > 0.05$) between 252 km and 260 km in the flat bottom case and between 239 km to 259 km in the sloping bottom case (Figure 3-3a and b).

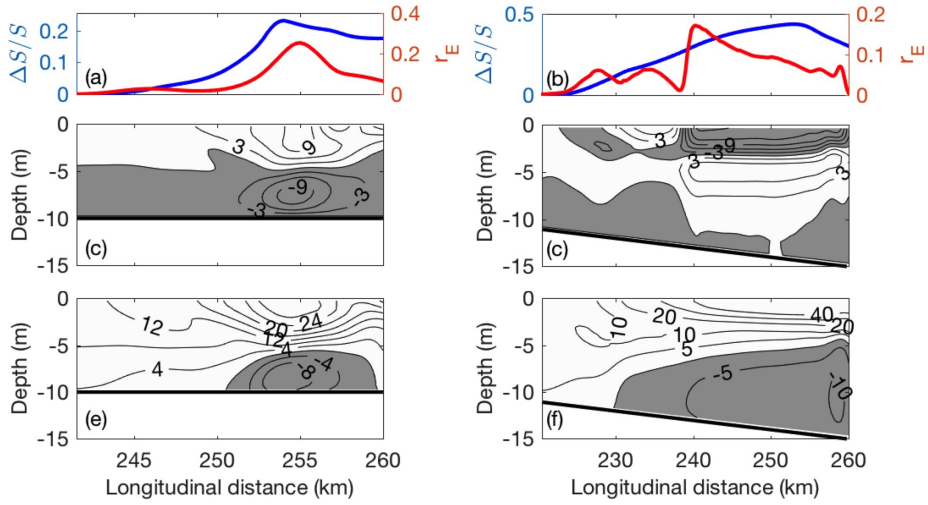

Figure 3-3: (a) Longitudinal distribution of $\Delta S/S$ (blue line) and r_E (red line) for a flat bottom case, with ΔS the tidal mean top-to-bottom salinity difference and $S = 31$ psu. The parameter r_E is the fraction that the ESCO current contributes to the depth-integrated kinetic energy of the total residual current. (b) As (a), but for a bottom with slope 1×10^{-4} between $x = L_e = 210$ km and the mouth $x = L_c = 260$ km; for $x < L_e$ depth is 10 m. (c) and (d): Contour plots of the ESCO current (u_τ, in cm s^{-1}) as functions of longitudinal distance and depth for the flat bottom case and the sloping bottom case, respectively. Positive values (white areas) denote seaward and negative values (grey areas) denote landward current. (e) and (f): as (c) and (d), but for the total residual current. Data for the longitudinal distance that $\Delta S/S \simeq 0$ inside the estuary is not shown.

Harmonic analysis of ESCO$^\sigma$ identifies two main contributions to u_τ, i.e., the ESCO current due to the M_2' tide ($u_{\tau,M_2'}$) and that due to the M_4' tide ($u_{\tau,M_4'}$). The relative contribution $r_{M_4'}$ of $u_{\tau,M_4'}$ to the kinetic energy of total ESCO current (see Eq. 3-9) for the two model configurations is shown in Figure 3-4a and b, respectively. Furthermore, the spatial structure of the ESCO current due to $u_{\tau,M_2'}$ and that due to $u_{\tau,M_4'}$ are shown in the second and third row of Figure 3-4. In the flat bottom case, the ESCO current due to the M_4' tide is small ($r_{M_4'} < 0.05$) between 254 km and 256 km and dominant ($r_{M_4'} > 0.5$) both near the mouth ($257 < x < 260$ km) and in the upper reach ($x < 253$ km). In the sloping bottom case, it is relevant in the entire estuary. With no bottom

slope, $u_{\tau,M_2'}$ is dominant between 253 km and 257 km, and it is seaward near the surface and landward near the bottom (Figure 3-4c). This is similar to that of u_τ. However, further upstream and downstream, $u_{\tau,M_2'}$ has a reversed two-layer structure. Note that at the riverside ($x < 245$ km), $u_{\tau,M_2'}$ also shows a two-layer structure, but current velocities are rather small here. In the case of the sloping bottom (Figure 3-4d), $u_{\tau,M_2'}$ has a reversed two-layer structure. Regarding $u_{\tau,M_4'}$, it typically shows a two-layer structure both in the flat bottom and in the sloping bottom case (Figure 3-4e-f). Interestingly, near the bottom the magnitude of the landward current of $u_{\tau,M_4'}$ is larger than that of the seaward current of $u_{\tau,M_2'}$. The residual current due to ESCO^a is also computed and the energy ratio between current due to ESCO^a and that due to ESCO$^\sigma$ is less than 0.05 (not shown). This was also found for all other parameter settings in this study. Thus the residual current due to ESCO^a is not considered in the following subsections.

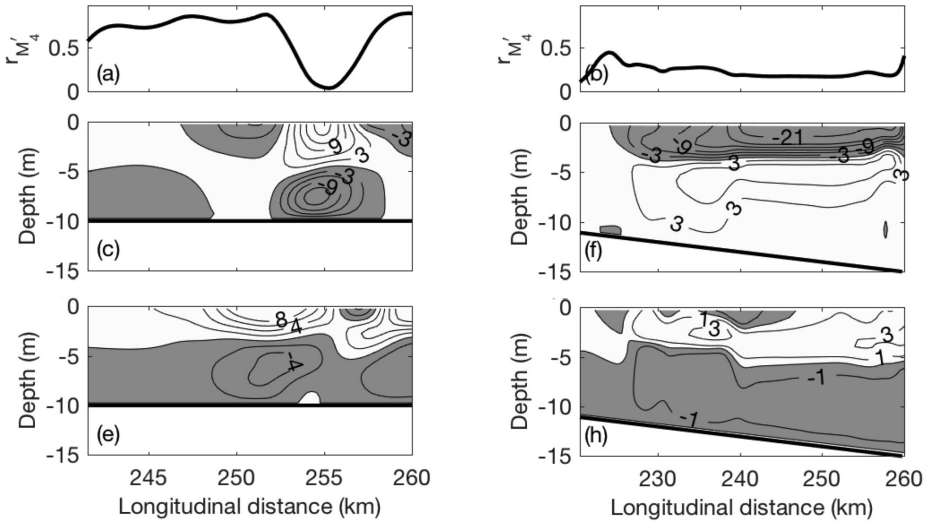

Figure 3-4: (a) and (b): Longitudinal distribution of the ratio $r_{M_4'}$ between the depth-integrated kinetic energy of the M_4' ESCO current $u_{\tau,M_4'}$ and that of the total ESCO current. (c) and (d): Contour plots of the ESCO current due to the M_2' tide ($u_{\tau,M_2'}$, in cm s^{-1}) as functions of longitudinal distance and depth for a flat bottom and a bottom with slope 1×10^{-4} between $x = L_e = 210$ km and the mouth $x = L_c = 260$ km, respectively. (e) and (f): As (c) and (d), but for the ESCO current due to the M_4' tide ($u_{\tau,M_4'}$). In panels (c) to (f), positive values (white areas) denote seaward and negative values (grey areas) denote landward current.

Next, results are presented for the experiments of series 1, 2 and 3 (see Table 3-1), in which the bottom slope between $x = L_e$ and $x = L_c$ was varied. Figure 3-5 shows the values of the fresh water Froude number Fr_f and of parameter M (for definitions see Eq. 3-3). It is found that for the bottom slope varying from 0 to 1×10^{-4}, variations of Fr_f and M in series 2 and 3 are smaller than those in series 1 (Figure 3-5). When considering these data points in the regime diagram of Geyer and MacCready (2014), it follows that the largest variations in stratification due to changes in the bottom slope are obtained in the case that the longitudinal mean depth increases (series 1). In this subsection, detailed results are presented for experiments of series 1. Additional results for experiments of series 2 and 3 are given in the supplementary material S.2.1.

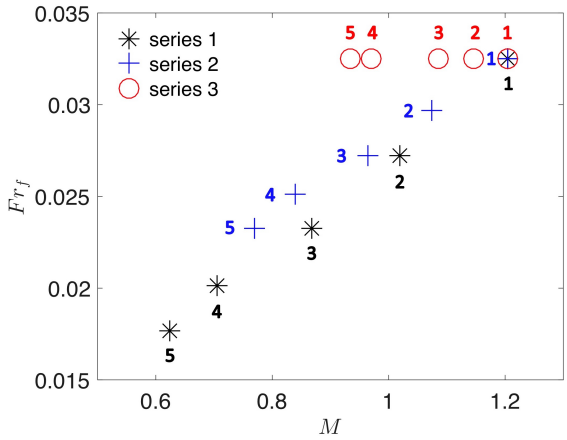

Figure 3-5: Values of the fresh water Froude number Fr_f and of parameter M, which measures the ratio of the ratio of the tidal timescale to the vertical turbulent mixing timescale, of the experiments of series 1, 2 and 3. These parameters are defined in Eq. 3-3, and they control the stratification at the mouth. The numbers 1-5 denote the experiments in which the bottom slope between $x = L_e = 210$ km and the mouth $x = L_c = 260$ km is $0, 0.25 \times 10^{-4}, 0.5 \times 10^{-4}, 0.75 \times 10^{-4}, 1 \times 10^{-4}$, respectively.

In the case of experiment series 1, the decrease of values of Fr_f and M (Figure 3-5) implies a transition of the estuary from periodically stratified to highly stratifiied. To identify the structure of the ESCO current, Figure 3-6 shows vorticities in the upper layer ($\mathcal{V}_1$) and the layer below that ($\mathcal{V}_2$) as functions of longitudinal distance and bottom slope. The left, middle and right panels are results related to u_τ, $u_{\tau,M_2'}$ and $u_{\tau,M_4'}$, respectively. When the ESCO current shows a classical two-layer structure or a reversed two-layer structure, only $\mathcal{V}_1$ exists. When the ESCO current has a three-layer structure, both $\mathcal{V}_1$ and $\mathcal{V}_2$ exist and they have opposite signs. Vorticities with absolute values below 1×10^{-3} s^{-1}

are blanked. These small values occur in the freshwater zone (where mean salinity is less than 1 psu) and around locations where $\mathcal{V}_1$ changes sign. Black solid lines in Figure 3-6 denote the locations in the estuary where the depth and time mean salinity is 1 psu. Moreover, the degree of stratification ($\Delta S/S$) as a function of longitudinal distance and bottom slope is indicated by black dashed contours. Figure 3-6 shows that $\mathcal{V}_1$ related to u_τ is positive (clockwise overturning) when the bottom slope is smaller than 0.1×10^{-4}. Moreover, positive $\mathcal{V}_1$ is also found near the mouth ($257 < x < 260$ km) for bottom slopes between 0 and 0.6×10^{-4}. At other locations and for other bottom slopes $\mathcal{V}_1$ is negative, and meanwhile positive $\mathcal{V}_2$ is observed. The vorticity $\mathcal{V}_1$ related to $u_{\tau,M_2'}$ is mainly negative for all experiments, while that related to $u_{\tau,M_4'}$ shows positive signs. It is also shown that larger negative values of $\mathcal{V}_1$ are obtained for larger $\Delta S/S$.

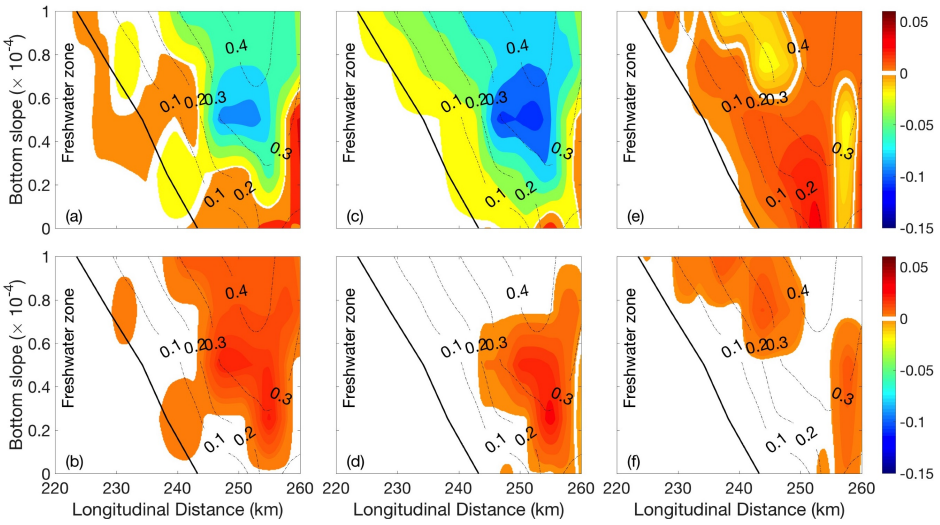

Figure 3-6: Colour plots of vorticities $\mathcal{V}_1$ (upper layer, first row) and $\mathcal{V}_2$ (second layer below surface, second row) as functions of longitudinal distance and bottom slope. Unit of $\mathcal{V}_n$ is s^{-1}. Panels in the left, middle and right columns are results related to the total ESCO current u_τ, and ESCO flows $u_{\tau,M_2'}$ and $u_{\tau,M_4'}$ due to the M_2' tide and the M_4' tide, respectively. Black solid lines denote the location where depth and time mean salinity is 1 psu. Areas in which vorticities $|\mathcal{V}_n| < 0.001$ s^{-1} are blanked. Dashed lines are contours of $\Delta S/S$.

The positive vorticities in the lower layer that are related to $u_{\tau,M_2'}$ and $u_{\tau,M_4'}$ have distinct spatial structures for different bottom slopes. The vorticity $\mathcal{V}_2$ related to $u_{\tau,M_2'}$ is dominant near the mouth and in the middle of the estuary ($250 < x < 260$ km) when bottom slopes are smaller than 0.7×10^{-4}. However,

$\mathcal{V}_2$ related to $u_{\tau,M_4'}$ is found near the salt intrusion limit and in the middle of the estuary when bottom slopes are larger than 0.7×10^{-4}.

Note that from vorticities $\mathcal{V}_i$ and thicknesses $H(\sigma_i - \sigma_{i+1})$ of the vorticity layers, one can compute the overturning volume transport rate per unit width, i.e., $\mathcal{T}_i = \frac{1}{2}\mathcal{V}_i H^2(\sigma_i - \sigma_{i+1})^2$. A positive (negative) value of $\mathcal{T}_i$ denotes the amount of net water per unit width that overturns clockwise (anti-clockwise) within a vorticity depth $H(\sigma_i - \sigma_{i+1})$ in layer i. Results of the thicknesses of the vorticity layers as functions of longitudinal distance and bottom slope are presented in the Electronic Supplement. It turns out that typical overturning rates of ESCO current are $\mathcal{T}_1 = 0.5\ m^3\ m^{-1}\ s^{-1}$ for the flat bottom case and $\mathcal{T}_1 = -0.6\ m^3\ m^{-1}\ s^{-1}$, $\mathcal{T}_2 = 0.2\ m^3\ m^{-1}\ s^{-1}$ for the case that the bottom slope is 1×10^{-4}.

To quantify the importance of the ESCO current $u_{\tau,M_4'}$, its relative contribution $r_{M_4'}$ to the depth-integrated kinetic energy of the total ESCO current (see Eq. 3-9) is computed for all experiments of series 1 and plotted as a function of scaled distance $\tilde{x}$ and bottom slope (Figure 3-7a). Here, $\tilde{x} = (x - L_s)/(L_c - L_s)$, with L_s denoting the location of 1 psu isohaline. The salt intrusion limit is at $\tilde{x} = 0$ and the mouth is at $\tilde{x} = 1$. Hence, the freshwater zone, where the ESCO current is small, is excluded. Results show two separate parts in the estuary where $u_{\tau,M_4'}$ is important. One is near the mouth ($0.8 < \tilde{x} < 1$) for bottom slopes smaller than 0.6×10^{-4}. The other is located inside the estuary between $0 < \tilde{x} < \tilde{x}_m$, where $\tilde{x}_m$ depends on the bottom slope and has a maximum value of 0.65. The contribution of $u_{\tau,M_4'}$ becomes negligible when the bottom slope is larger than 0.7×10^{-4}. Figure 3-7b shows the relative contribution r_E of ESCO current to the depth-integrated kinetic energy of the total residual current as a function of scaled distance $\tilde{x}$ and bottom slope. It appears that the contribution of ESCO is relevant ($r_E > 0.05$) when $0.4 < \tilde{x} < 1$ for all bottom slopes (Figure 3-7b).

3.3.2 *Structure of u_τ for different tidal forcing and related changes in stratification (RA.2)*

Results of experiments of series 4 are presented. In this setting, the freshwater Froude number is a constant, viz. $Fr_f = 3.2 \times 10^{-2}$. The imposed changes in the amplitude of the M_2' tide at the seaward boundary result in values of the parameter M in the range from 0.64 to 1.55. According to the regime diagram of Geyer and MacCready (2014), these experiments simulate the estuary in conditions from highly stratified to periodically stratified.

Figure 3-8 is similar to Figure 3-6, but for vorticities $\mathcal{V}_1$ and $\mathcal{V}_2$ as functions of longitudinal distance and M. In panel (a), both positive and negative values of $\mathcal{V}_1$ (anticlockwise overturning) are obtained with the sign changing at $M \simeq$

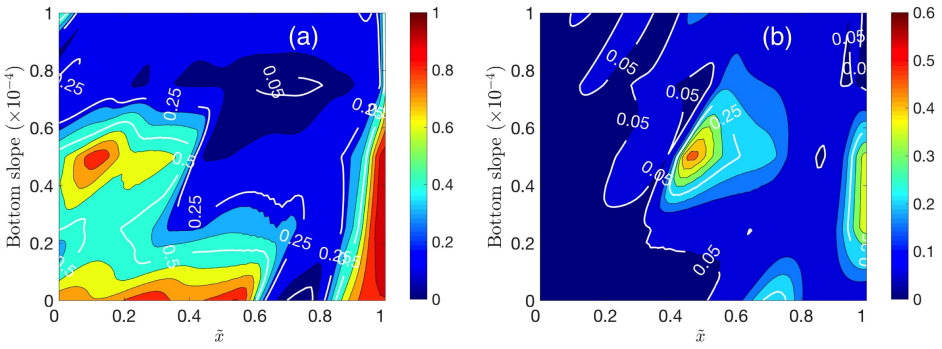

Figure 3-7: a. Colour-contour plot of the relative contribution $r_{M_4'}$ of the ESCO current due to the M_4' tide to the depth-integrated kinetic energy of the total ESCO current as a function of scaled longitudinal distance $\tilde{x}$ and bottom slope, experiment series 1. Here, $\tilde{x} = 0$ is the location where depth and time mean salinity equals 1 psu and $\tilde{x} = 1$ is the estuary mouth. The white contour lines indicate borders in the figure where the M_4' tide contribution to the ESCO current is small ($r_{M_4'} < 0.05$), important ($r_{M_4'} > 0.25$) and dominant ($r_{M_4'} > 0.5$). (b): As panel (a), but for r_E, i.e., the ratio between the depth-integrated kinetic energy of the ESCO current and that of the total residual current. Note colour bars of panel (a) and (b) have different ranges.

1.1. In panel (b), $\mathcal{V}_2$ only shows positive values (clockwise overturning), mainly for $0.8 < M < 1.1$ and the value of $\mathcal{V}_2$ depends on the location in the estuary. The largest (both positive and negative) values of $\mathcal{V}_1$ and $\mathcal{V}_2$ are obtained at 5 km upstream from the mouth, where $\Delta S/S$ attains its maximum value. The overall distribution of $\mathcal{V}_1$ related to $u_{\tau,M_2'}$ (see Figure 3-8c) is similar to that of $\mathcal{V}_1$ related to u_τ. However, for $1.1 < M < 1.5$, in the segments between 245 and 253 km and 257 km to the mouth, negative $\mathcal{V}_1$ is observed. Vorticity $\mathcal{V}_2$ exists between $0.8 < M < 1.1$, but only between 253 km and the mouth (Figure 3-8d). Contour plots of thicknesses $H(\sigma_1 - \sigma_2)$ and $H(\sigma_2 - \sigma_3)$ of the two vorticity layers as functions of $\tilde{x}$ and M are shown in the supplementary material S.2.2.

Figure 3-9 is similar to Figure 3-7, and presents the energy ratio $r_{M_4'}$ (of the M_4' ESCO current and the total ESCO current) and r_E (of the total ESCO current and the total residual current) for the experiments of series 4 as functions of the scaled coordinate $\tilde{x}$ and parameter M (see Eq. 3-3). In the middle of the estuary, the ESCO current is due to the M_2' tide, where also the maximum $\Delta S/S$ is observed. For $M < 0.8$, the ESCO current due to the M_4' tide is always small ($r_{M_4'} < 0.05$). Overall, with increasing M, values of $r_{M_4'}$ increase, and $r_{M_4'} > 0.05$ is found for a wider range of $\tilde{x}$ values. When $0.9 < M < 1.4$, the ESCO current due to the M_4' tide $u_{\tau,M_4'}$ is dominant for $\tilde{x} < 0.6$ and $0.8 < \tilde{x} < 1$. The parameter $r_{M_4'}$ reaches its maximum value of 0.9 near the mouth and at $\tilde{x} = 0.4$. When

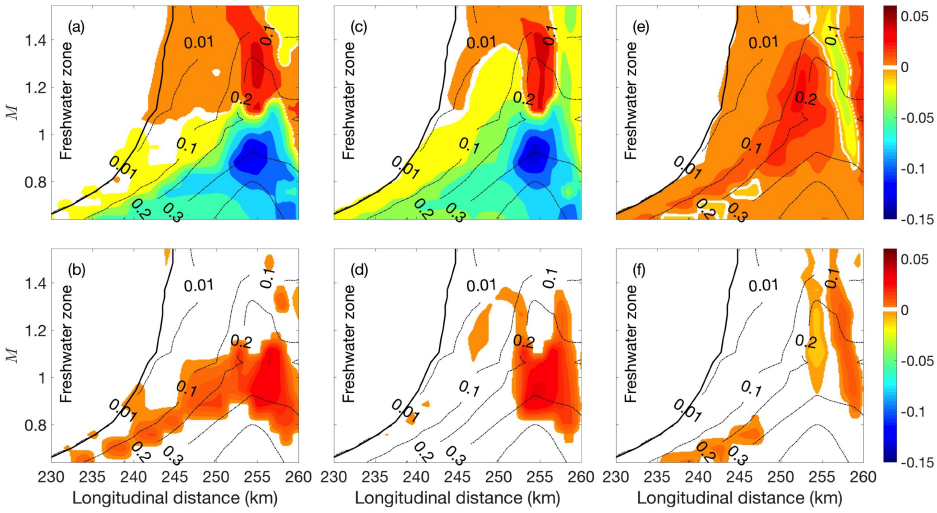

Figure 3-8: As Figure 3-6, but for experiment series 4: vorticities $\mathcal{V}_1$ (first row) and $\mathcal{V}_2$ (second row) are plotted as functions of longitudinal distance and parameter M that measures the tidal timescale to the vertical turbulent mixing timescale at the mouth (see Eq. 3-3) for the total ESCO current (left column), the ESCO current due to the M_2' tide (middle column) and due to the M_4' tide (right column).

$M > 1.4$, $u_{\tau,M_4'}$ becomes less intense, but it is still important for the total ESCO current in the areas $0 < \tilde{x} < 0.25$ and $0.65 < \tilde{x} < 0.8$. Figure 3-9b further reveals that values of $r_E > 0.05$ (i.e., ESCO current significantly contributes to the total residual current) are found mainly between $0.4 < \tilde{x} < 0.9$. The maximum value of r_E is obtained for $M = 0.9$ and $\tilde{x} = 0.7$.

For $1.1 < M < 1.4$, the modelled ESCO current u_τ shows a classical two-layer structure in the estuary, where in the sections between 252 to 257 km, u_τ is mainly due to $u_{\tau,M_2'}$, and in the other sections, u_τ is due to $u_{\tau,M_4'}$. When $0.8 < M < 1.1$, u_τ has a three-layer structure. In the section between 252 km and 257 km, this structure is mainly due to the $u_{\tau,M_2'}$. Near the mouth (257 to 260 km) and in the upper reach (from the location of 1 psu to 252 km), $u_{\tau,M_4'}$ is moderate to dominant. If $M < 0.7$, u_τ in the entire estuary is mainly due to $u_{\tau,M_2'}$ and it has a reversed two-layer structure. The same holds for $0.7 < M < 0.8$, but only in the middle reach.

Figure 3-9 further reveals that for $M > 0.9$ and $0 < \tilde{x} < 0.4$, although the intensity of $u_{\tau,M_4'}$ is much larger than that of $u_{\tau,M_2'}$, total ESCO current itself is negligible with respect to total residual current ($r_E < 0.05$). For $0.9 < M < 1.1$ (weakly stratified estuaries), $u_{\tau,M_4'}$ is significant in the middle and lower reach ($\tilde{x} > 0.4$), where ESCO current is an important component in the total

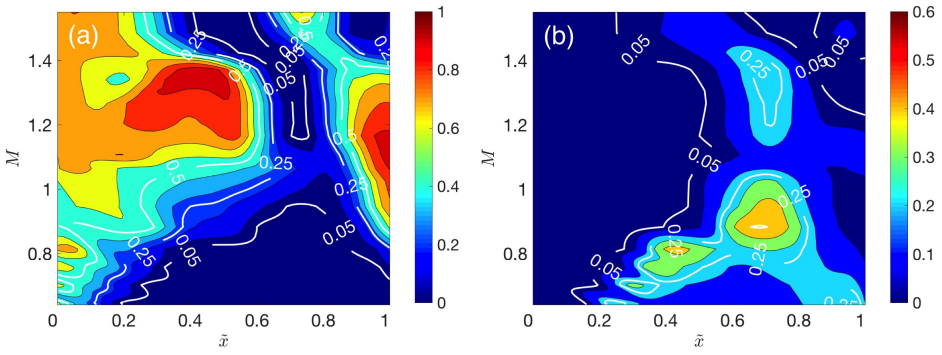

Figure 3-9: As Figure 3-7, but for experiments of series 4. (a): Colour-contour plot of $r_{M_4'}$ (relative contribution of the M_4' ESCO current to the depth-integrated kinetic energy of the total ESCO current) as a function of scaled longitudinal distance $\tilde{x}$ and parameter M that measures the tidal timescale to the vertical turbulent mixing timescale at the mouth (see Eq. 3-3). (b): As panel (a), but for r_E, i.e., the ratio between depth-integrated kinetic energy of the ESCO current and that of the total residual current. Note that colour bars of panel (a) and (b) have different ranges of values.

residual current. Moreover, although in the middle reach ($0.5 < \tilde{x} < 0.8$) $u_{\tau,M_4'}$ is weaker than $u_{\tau,M_2'}$ ($r_{M_4'} < 0.25$), the former is essential for obtaining a three-layer structure in the vertical distribution of the total ESCO current.

3.3.3 *Structure of u_τ for mixed tidal forcing (RA.3)*

The effect of mixed tidal forcing on the structure of the ESCO current is examined by analysing model results of the experiments of series 5. In each of these experiments, stratification conditions at the estuary mouth are kept fixed.

Figure 3-10 is similar to Figure 3-6 and it shows colour-contour plots of vorticities $\mathcal{V}_1$ (first row) and $\mathcal{V}_2$ (second row) as functions of longitudinal distance and parameter F' (defined in Eq. 3-4). Moreover, contours of $\Delta S/S$ are shown (black dashed lines). Regarding vorticity $\mathcal{V}_1$ that is related to u_τ, negative values (anticlockwise overturning) are observed for $F' < 0.2$ and positive (clockwise overturing) for $F' > 0.2$ (Figure 3-10a). Meanwhile, negative $\mathcal{V}_2$ is only found when $F' < 0.2$ (Figure 3-10b). For the ESCO current due to diurnal tides (Figure 3-10c and d), positive $\mathcal{V}_1$ is observed in most of the estuary for $0 < F' < 0.6$, and between 245 and 257 km for $F' > 0.6$. The maximum positive $\mathcal{V}_1$ is obtained when $F' \simeq 0.5$. The vorticity $\mathcal{V}_2$ does not exist for this component. For the ESCO current due to semi-diurnal tides (Figure 3-10e and f), the overall distributions of $\mathcal{V}_1$ and $\mathcal{V}_2$ are similar to those of the vorticities related to u_τ, but with a much weaker clockwise overturning for $F' > 0.4$.

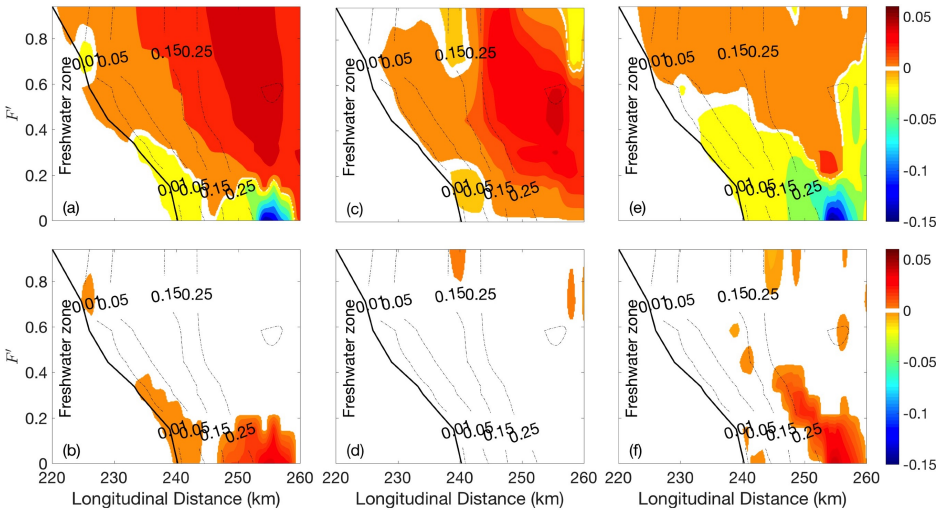

Figure 3-10: As Figure 3-6, but for vorticities $\mathcal{V}_1$ (first row) and $\mathcal{V}_2$ (second row) related to (left column) total ESCO current u_τ, (middle column) the ESCO current due to diurnal tides and (right) the ESCO current due to semi-diurnal tides plotted as functions of longitudinal distance and parameter F' that measures the degree of mixture of externally imposed tides. Small F' (< 0.2) implies semi-diurnal tide is the dominant constituent and large F' (> 0.75) implies diurnal tides are dominant constituents.

The vorticities due to the ESCO current caused by ter-diurnal tides, the quarter-diurnal tide and the long-periodic tide (with frequency $2\Delta\omega$) are shown in Figure 3-11. In general, $\mathcal{V}_1$ related to these ESCO components has positive values. However, each of them attain a maximum value for a different F'. For the ESCO current due to ter-diurnal tides, the maximum $\mathcal{V}_1$ is obtained around $F' = 0.4$, while for the ESCO current due to the quarter-diurnal tide and the long-periodic tide, the maximum $\mathcal{V}_1$ is obtained when $F' = 0$ and $F' \simeq 0.95$, respectively. In areas where the vorticity $\mathcal{V}_2$ due to the ESCO current driven by these tide exists, its values are negative, but rather small. Contour plots of thicknesses $H(\sigma_1 - \sigma_2)$ and $H(\sigma_2 - \sigma_3)$ of the two vorticity layers as functions of $\tilde{x}$ and F' are shown in the Electronic Supplement.

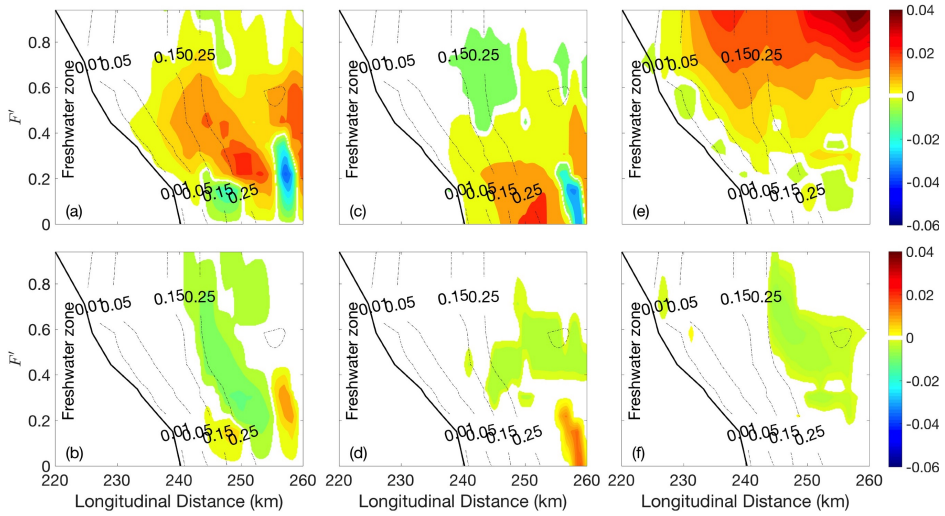

Figure 3-11: As Figure 3-10, but for vorticities of the ESCO current due to ter-diurnal tides (left column), due to the quarter-diurnal tide (middle column) and due to the long-periodic tide (right column).

The importance of the ESCO current due to different tidal harmonics as a function of dimensionless longitudinal distance $\tilde{x}$ and F' is shown in Figure 3-12. Panels (a) to (e) show the relative contribution to the depth-integrated kinetic energy of total ESCO current of ESCO current driven by diurnal tides, semi-diurnal tides, ter-diurnal tides, the quarter-diurnal tide and the long-periodic tide, respectively. In panel (f), the relative contribution of the total ESCO current to the depth-integrated kinetic energy of the total residual current is presented. It appears that for semi-diurnal tide dominant conditions ($F' < 0.2$), the total ESCO current is relevant in the lower reach of the estuary ($0.6 < \tilde{x} < 1$), where the main contributions to u_τ are the ESCO current due to

semi-diurnal tides (between $0.6 < \tilde{x} < 0.8$) and that due to the quarter-diurnal tide (between $0.8 < \tilde{x} < 1$). For mixed tide conditions ($0.2 < F' < 0.75$), the ESCO current is a significant part of the total residual current for $0.2 < \tilde{x} < 1$, where the main contribution to u_τ is the ESCO current due to diurnal tides. Note that in the middle reach ($0.2 < \tilde{x} < 0.5$) and near the mouth ($0.8 < \tilde{x} < 1$), the ESCO current due to ter-diurnal tides also contributes to the residual current. For diurnal tide dominant conditions ($F' > 0.75$), the ESCO current due to diurnal tides is significant in the area $0.5 < \tilde{x} < 0.7$; elsewhere, the main contributor to u_τ is the ESCO current due to the long-periodic tide.

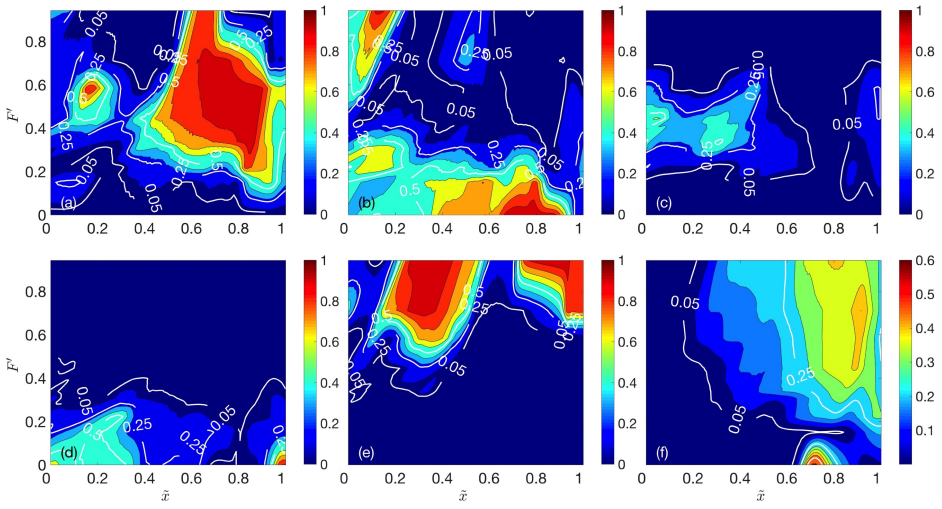

Figure 3-12: (a)-(e). Colour-contour plots of ratios between depth-integrated kinetic energies of the ESCO current driven by different tidal harmonics and the depth-integrated kinetic energy of total ESCO current as functions of $\tilde{x}$ and F'. (f). As (a)-(e), but for the ratio between energy of the total ESCO current and that of the total residual current. Panels are due to (a) diurnal tides ($r_{O_1'} + r_{K_1'}$), (b) semi-diurnal tides ($r_{M_2'} + r_{O_2'} + r_{K_2'}$), (c) ter-diurnal tides ($r_{MO_3'} + r_{MK_3'}$), (d) the quarter-diurnal tide ($r_{M_4'}$) and (e) the long-periodic tide ($r_{Mf'}$), respectively. Note panels (a)-(e) and panel (f) have different ranges of values.

3.4 DISCUSSION

3.4.1 *Analysis of vertical structures of* u_τ

Sections 3.3.1 and 3.3.2 show that in a semi-diurnal tide dominant estuary the ESCO current u_τ is mainly forced by two components that are related to M_2'

and M_4' tides. The spatial structures of these flows strongly depend on density stratification. Motivated by the analysis of Cheng et al. (2013), who considered total ESCO current, here the vertical distribution of the ESCO current $u_{\tau,M_2'}$ and $u_{\tau,M_4'}$ induced by the M_2' and M_4' tide are explained from the structure of the ESCO shear stress τ_n and of $gH\frac{\partial \eta_{\tau,n}}{\partial x}\sigma$, where $n = M_2'$ or M_4' (see Eq. 3-8). Here, τ_n is given by Eq. 3-7 and the term $gH\frac{\partial \eta_{\tau,n}}{\partial x}\sigma$ is the contribution that results from integrating the barotropic pressure gradient force between level σ and the surface (the first term in the bracket of Eq. 3-8a). The latter is referred to as a depth-integrated barotropic term.

First, the structure of the variables that constitute the ESCO shear stress is determined. As a specific example, this is done below for a setting of experiment series 4 (tidal forcing amplitude $A_{M_2'} = 1.1$ m, i.e., stratification parameter $M = 1.3$) at location $\tilde{x} = 0.6$, where $r_E \simeq 0.1$. Here, the ESCO current is a significant component of the estuarine circulation. Figure 3-13a and b show the amplitude of (blue line) the M_2' and (red line) M_4' component of vertical tidal shear $\left[\frac{\partial u}{\partial z}\right] = \frac{1}{H}\left[\frac{\partial u}{\partial \sigma}\right]$ and of eddy viscosity, respectively. Note that $\left[\frac{\partial u}{\partial z}\right]$ shows a local extremum at -6 m, which implies a "surface jump" shape of the M_2' tidal current amplitude. The occurrence of such a phenomenon is physically explained by Chen and Swart (2016). The product of the vertical tidal shear and eddy viscosity amplitude is shown in Figure 3-13c, whilst panel (d) shows $\cos(\varphi_{M_2'} - \psi_{M_2'})$ and $\cos(\varphi_{M_4'} - \psi_{M_4'})$, where $\varphi_n - \psi_n$ is the phase difference between tidal shear and eddy viscosity of constituent with label n. The kinematic shear stresses τ_n, which result from the multiplication of the variables shown in panels (c) and (d), are plotted in Figure 3-13e (solid lines). The dotted lines in this panel are the depth-integrated barotropic terms. Finally, panel (f) shows the residual current that is driven by the ESCO stress, $u_{sh,n} = -\int_{-1}^{\sigma} H\frac{1}{A_v}\tau_n d\tilde{\sigma}$ and by the depth-integrated barotropic term, $u_{ba,n} = \int_{-1}^{\sigma} H\frac{1}{A_v}gH\frac{\partial \eta_{\tau,n}}{\partial x}\tilde{\sigma}d\tilde{\sigma}$. The blue and red lines are components related to the M_2' tide and M_4' tide, respectively. Furthermore, in (f) the ESCO current $u_{\tau,M_2'} = u_{sh,M_2'} + u_{ba,M_2'}$ and $u_{\tau,M_4'} = u_{sh,M_4'} + u_{ba,M_4'}$ are shown by the black solid line and the black dashed line, respectively.

Figure 3-13 reveals that the amplitude of the M_2' vertical tidal shear is larger than that of the M_4' vertical tidal shear, whereas the amplitude of the M_2' eddy viscosity is small compared to that of the M_4' eddy viscosity. Interestingly, the product of amplitudes of vertical tidal shear and eddy viscosity of M_2' and of M_4' have comparable magnitudes. For the M_2', the value of $\cos(\varphi_{M_2'} - \psi_{M_2'})$ is around -1 in the entire water column. This means that M_2' eddy viscosity peaks for maximum flood current (large negative vertical shear), which is caused by tidal straining. For the M_4' tidal shear and eddy viscosity, $\cos(\varphi_{M_4'} - \psi_{M_4'})$ is

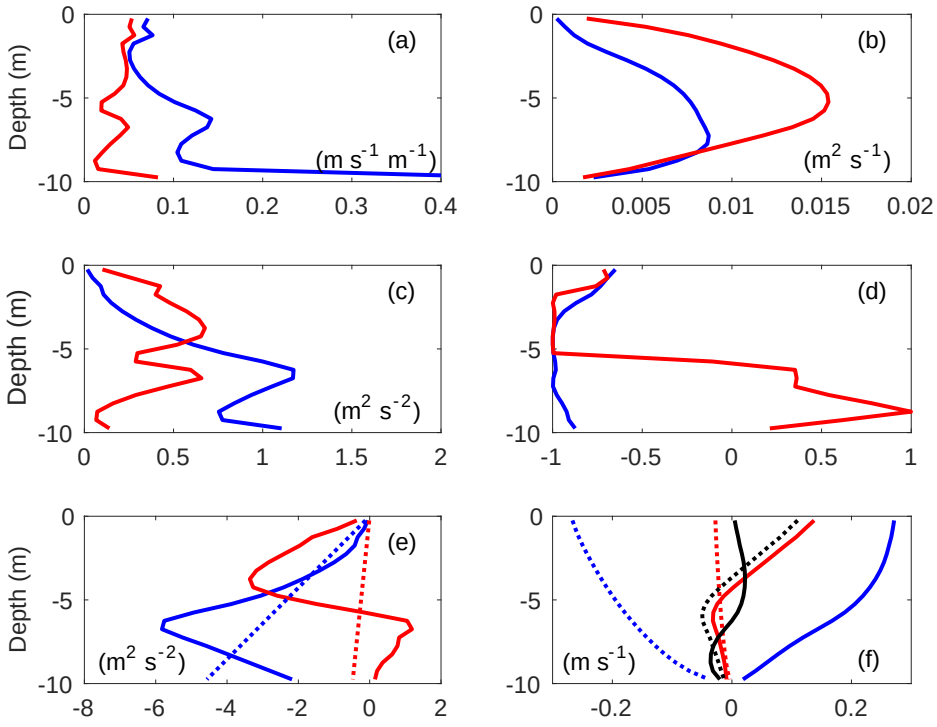

Figure 3-13: Vertical distribution of variables that constitute the ESCO current due to the M_2' tide and M_4' tide. Data for experiment series 4, with the tidal amplitude at sea boundaries of $A_{M_2'} = 1.1$ m at $\tilde{x} = 0.6$ (equivalent to $x = 250$ km) are plotted. (a) Amplitude of tidal shear $\left[\frac{\partial u}{\partial z}\right]$ of M_2' (blue line) and M_4' (red line) component. (b) As (a), but for the amplitude of eddy viscosity $[A_v]$. (c) The product $[A_v] \times \left[\frac{\partial u}{\partial z}\right]$ of M_2' (blue line) and M_4' (red line). (d) The value of $\cos(\psi - \varphi)$ of M_2' (blue line) and M_4' (red line), in which φ is the phase of tidal shear and ψ is the phase of eddy viscosity. In (e), solid lines are $\tau_{M_2'}$ (blue) and $\tau_{M_4'}$ (red), while dotted lines are the depth-integrated barotropic terms $gH\frac{\partial \eta_{\tau,M_2'}}{\partial x}\sigma$ (blue) and $gH\frac{\partial \eta_{\tau,M_4'}}{\partial x}\sigma$ (red). (f) The residual current $u_{sh,M_2'}$ due to τ_n (solid blue), $u_{sh,M_4'}$ (solid red) and the residual flows $u_{ba,M_2'}$ (dotted blue), $u_{ba,M_4'}$ (dotted red) due to the depth-integrated barotropic term, $u_{M_2'}$ (solid black) and $u_{M_4'}$ (dotted black).

-1 in the upper part of the water column and around 0.5 in the lower water column.

The sudden jump in $\cos(\varphi_{M_4'} - \psi_{M_4'})$ can be understood as follows. First, consider the phase $\psi_{M_4'}$ of M_4' eddy viscosity $A_{v,M_4'}$. The primary source of $A_{v,M_4'}$ is tidal variation of the absolute value of the friction velocity, which peaks

at M_2' flood and ebb. Therefore $\psi_{M_4'} \simeq 2\varphi_{M_2'}$, which is almost constant over depth. Hence, the observed jump is due to the phase $\varphi_{M_4'}$ of M_4' tidal shear. The latter turns out to have two important drivers, viz. $\frac{A_{v,M_4'}}{H}\frac{\partial \bar{u}}{\partial \sigma}$ and the M_4' component of $\frac{A_{v,M_2'}}{H}\frac{\partial u_{M_2'}}{\partial \sigma}$. Regarding the first driver, $A_{v,M_4'} \sim \cos(\omega_{M_4'} t - 2\varphi_{M_2'})$, as discussed above, and the shear of the residual current, $\frac{1}{H}\frac{\partial \bar{u}}{\partial \sigma}$, is positive. The second driver behaves like $\cos(\omega_{M_4'} t - \varphi_{M_2'})$. Since M_2' eddy viscosity peaks at maximum flood, it follows $\psi_{M_2'} \simeq \varphi_{M_2'} + \pi$. This result implies that the second driver of M_4' tidal current shear is out of phase with the first driver. Since the drivers have different magnitudes, it means that rapid changes of $\varphi_{M_4'}$ over the depth may occur.

Panel (e) of Figure 3-13 shows that $\tau_{M_2'} < 0$ in the entire water column. When ignoring the depth integrated barotropic term, the response to this shear stress is a stress $\bar{\tau} = \frac{\bar{A_v}}{H}\frac{\partial \bar{u}}{\partial \sigma}$ that equals $-\tau_{M_2'}$. Since the velocity is zero at the bottom, it follows that $\tau_{M_2'}$ drives a seaward residual current $u_{sh,M_2'}$ (see Eq. 3-8a) at all vertical levels, as is visible in panel (f). Since the ESCO current must have a vanishing mean in the vertical direction, a landward directed barotropic pressure gradient force (i.e., $\frac{\partial \eta_{\tau,M_2'}}{\partial x} > 0$) is required, which drives a landward current $u_{ba,M_2'}$. As $(gH\frac{\partial \eta_{\tau,M_2'}}{\partial x}\sigma - \tau_{M_2'}) < 0$ near the bottom (see panel (e)) and $u_{M_2'} = 0$ at the bottom, a landward directed $u_{M_2'}$ occurs near the bottom (see panel (f)). Somewhat higher in the water column, $(gH\frac{\partial \eta_{\tau,M_2'}}{\partial x}\sigma - \tau_{M_2'})$ is positive and $u_{M_2'}$, which results from the depth-integration of $(gH\frac{\partial \eta_{\tau,M_2'}}{\partial x}\sigma - \tau_{M_2'})$, becomes seaward towards the surface. By performing a similar analysis for $u_{\tau,M_4'}$, it follows that it is seaward near the surface and landward near the bottom.

The vertical profiles of the kinematic shear stresses $\tau_{M_2'}$ and $\tau_{M_4'}$ strongly depend on stratification and on the structure of the tidal forcing. Below, this is discussed for different stratification conditions that result from changing the intensity of M_2' tidal forcing (experiment series 4). As is shown in Figure 3-14a, when M is large (the estuary is periodically stratified), $\tau_{M_2'}$ and $\tau_{M_4'}$ both have a parabolic distribution over the vertical. The value of $(gH\frac{\partial \eta_{\tau,M_2'}}{\partial x}\sigma - \tau_{M_2'})$ and that of $(gH\frac{\partial \eta_{\tau,M_4'}}{\partial x}\sigma - \tau_{M_4'})$ are positive in the upper water layer and negative in the lower water column. In this case, both $u_{\tau,M_2'}$ and $u_{\tau,M_4'}$ have landward current near the bottom and seaward current near the surface.

When M is moderate (the estuary is weakly stratified), $(gH\frac{\partial \eta_{\tau,M_2'}}{\partial x}\sigma - \tau_{M_2'})$ is positive near the bottom and negative near the surface. A reversed two-layer structure is obtained in $u_{\tau,M_2'}$. Note that in that case $\tau_{M_2'}$ is positive in the upper water column, implying that M_2' eddy viscosity peaks at ebb. The reason for

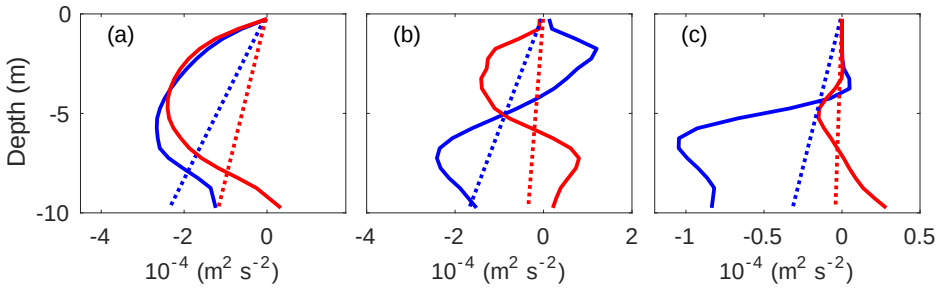

Figure 3-14: Vertical distribution of shear stress components $\tau_{M_2'}$ (solid blue), $\tau_{M_4'}$ (solid red) and depth-integrated barotropic terms (M_2': dashed blue, M_4': dashed red) at (a) $\tilde{x} = 0.5$ when $M = 1.4$ (periodically stratified), at (b) $\tilde{x} = 0.6$ when $M = 1.1$ (weakly stratified) and at (c) $\tilde{x} = 0.8$ when $M = 0.7$ (highly stratified). Here $\tilde{x} = (x - L_s)/(L_c - L_s)$, is defined in section 3.3.1, expresses the relative distance from the salt intrusion limit, whilst M is the stratification parameter (see Eq. 3-3). These plots are selected such that they represent estuaries with different types of stratification but for identical values of r_E (i.e. ratio between depth-integrated kinetic energy of the ESCO current and that of the total residual current).

this is that with increasing stratification residual current becomes stronger and tidal current weakens. Thus, in the upper water column, where the residual current is seaward, the friction velocity is larger during ebb than during flood. This contributes to A_v peaking at ebb. This mechanism thus counteracts that due to tidal straining. In contrast, the M_4' ESCO forcing $(gH\frac{\partial \eta_{\tau,M_4'}}{\partial x}\sigma - \tau_{M_4'})$ is negative in the lower water column and positive in the upper water column (Figure 3-14b). The residual current $u_{\tau,M_4'}$ has a structure opposite to that of $u_{\tau,M_2'}$. Because $u_{\tau,M_2'}$ and $u_{\tau,M_4'}$ are different in the intensities at different water depth, the combination of these two components results in an ESCO current that has a rather complicated structure.

When M is small (the estuary is highly stratified), in the lower layer, $\tau_{M_2'}$ is significant whereas $\tau_{M_4'}$ is negligible (Figure 3-14c). They are both small in the upper layer since turbulence is weak there. A reversed two-layer ESCO current is obtained. Finally, note that the reversed two-layer structure is not found in the total estuarine circulation, which would otherwise imply a continuous increase in buoyancy. In fact, in highly stratified conditions, with decreasing M, the ESCO shear stress decreases and the ESCO current becomes less significant compared to the density driven current. However, ESCO weakens the overturning of the total estuarine circulation.

3.4.2 *Sensitivity of model results to the input parameters*

For all model runs, horizontal eddy viscosity and diffusivity values were 50 $m^2\ s^{-1}$. Using A_h and K_h with values being an order of magnitude smaller slightly affects model results. For example, when A_h and K_h were set to 5 $m^2\ s^{-1}$ in model runs, top-to-bottom salinity difference increased about $1-2$ psu and the vertical eddy viscosity slightly changed (see Electronic Supplement).

To test the sensitivity of model results to the choice of frequency difference $\Delta\omega$ between O_1' and K_1' tide, Experiment Series 2 was re-run but for $\Delta\omega = \omega/26$. With the new value of $\Delta\omega$, one spring-neap cycle takes 6.5 days. Results of the new model runs were compared with those of the default setting (i.e., $\Delta\omega = \omega/18$, see Figure 3-8). It turned out that changing $\Delta\omega$ only slightly modifies the relative importance of the ESCO current due to individual tidal harmonics. Furthermore, the total residual salinity and current distribution in the estuary hardly changed when compared with those of the default model runs (not shown). Hence, changing the value of $\Delta\omega$ does not affect the overall findings presented in the previous sections.

Model experiments were also conducted for the domain with smaller grid size (grid size in subdomain 2 is 150 m) and/or more vertical sigma layers (number of vertical layers is 40). Results are not sensitive to the changing of the size of cells in model domains.

3.4.3 *Limitations*

The model domain in this study is a straight channel with no lateral bottom differences. Thus the impact of lateral processes on the vertical turbulent mixing, and thereby on longitudinal ESCO current are neglected. There are many sources that drive lateral current and consequently change turbulent eddy viscosity and tidal velocity shear covariance. Examples of drivers are differential advection of salinity due to lateral bottom gradients (Nunes and Simpson, 1985; Lerczak and Geyer, 2004; Cheng et al., 2009), lateral advection of longitudinal tidal momentum (Lerczak and Geyer, 2004; Huijts et al., 2009; Huijts et al., 2011), lateral gradients in turbulent mixing (Scully and Friedrichs, 2007; Basdurak et al., 2013; Cheng, 2014), channel curvature (Seim and Gregg, 1997; Chant, 2002), Coriolis (Huijts et al., 2009) and lateral current induced by channel width convergence Burchard et al. (2014).

A second limitation of this study is that values of the radian frequencies of diurnal and semi-diurnal tidal constituents are slightly different from those in nature. Moreover, tidal constituents like the semi-diurnal solar tide S_2' are not considered. These choices were made to keep the analysis as simple as possible. Hence, a direct comparison of modelled and observed residual current for

mixed tides conditions is not yet possible, but it is considered as an interesting topic for future work.

It appeared that the Delft3D-current model is not able to capture strong vertical circulation in unstable stratified water column (weakly stratified conditions) at the subtidal time scale (Delft Hydraulics, 2006, chapter B.12). In our study, this occurs when $0.9 < M < 1.1$. However, it turned out that this did not affect model results at the tidal time scale (typically 12 hours). This was concluded after by comparing the present model results with those of Cheng et al. (2011, 2013), who used a different numerical model (ROMS), which revealed minor differences.

Finally, note that in the present study, a weakly nonlinear system is considered (i.e., the sea surface elevation η is small compared to the water depth H). Consequently, the terms $ESCO^a$ (in Eq. 3-2b, which involve triple correlation between tidally varying sea surface, eddy viscosity and tidal current, were neglected. Moreover, the nonlinear interactions between different tidal constituents are small. Studying residual current and ESCO current in an estuary characterised by strong tides and highly nonlinear dynamics (Giddings et al., 2014) would be interesting to investigate in future.

3.5 CONCLUSIONS

This study investigated the structure of residual current induced by covariance between tidally varying eddy viscosity and tidal velocity shear (ESCO) computed with a numerical model that was applied to an idealised estuary (straight, narrow). The total ESCO current was decomposed into terms that are induced by individual tidal constituents. The main findings of this study are:

· The ESCO current is significant with respect to the total residual current in parts of the estuary if stratification is weak to moderate.

· For estuaries forced by a single semi-diurnal tidal constituent, the ESCO current is mainly made up by the components related to the semi-diurnal tide and to the quarter-diurnal tide are identified. The former is dominant in the middle reach, whilst the latter is important in the upper reach and near the mouth.

· The ESCO current due to the semi-diurnal tide has either a two-layer, three-layer or reversed two-layer structure. The occurrence of each structure depends on the degree of stratification at the mouth and the longitudinal position in the estuary. The ESCO current due to the quarter-diurnal tide mainly shows a two-layer structure.

· For estuaries with multiple tidal forcing (mixing of a semi-diurnal tide and two diurnal tides), the ESCO current due to diurnal tides dominates the total

ESCO current. The current due to ter-diurnal tides also contribute to the total ESCO current. They both show a two-layer structure in the vertical direction.

· For estuaries that are primarily forced by two diurnal tidal constituents, the ESCO current due to the long periodic tide, which also shows a two-layer structure, is an important component of the total ESCO current, in particular in the upper and lower reach.

4

LONGITUDINAL VARIATION IN LATERAL TRAPPING OF FINE SEDIMENT IN TIDAL ESTUARIES: OBSERVATIONS AND A 3D EXPLORATORY MODEL

4.1 INTRODUCTION

In many estuaries, one or more locations are present where the tidally mean suspended sediment concentration (SSC) attains a maximum. Understanding the mechanisms resulting in these so-called estuarine turbidity maxima (ETMs) is important, as mouth bar is frequently formed in ETMs and hampers marine traffic (Liu et al., 2011) and it has a significant impact on the ecological functioning of estuaries (Cloern et al., 2013), e.g. it causes deficits in oxygen (Talke et al., 2009a; Zhu et al., 2011). The latter is due to the fact that SSC contains organic material that consumes oxygen. Moreover, high sediment concentrations strongly limit the light that is needed for phytoplankton to grow (May et al., 2003; Jiang et al., 2015).

The locations of turbidity maxima depend on estuarine settings and forcing conditions. Many studies have focused on the mechanisms underlying the distribution of turbidity related to either longitudinal or lateral sediment transport. An important process that results in longitudinal sediment trapping is the joint action of seaward transport caused by river current and the landward transport by the density driven current (Postma, 1967; Festa and Hansen, 1978; Schubel and Carter, 1984; Geyer, 1993; Talke et al., 2009b). In that case, the maximum SSC occurs at the landward limit of the salt intrusion. Furthermore, the suppression of turbulence by stratification of the water column significantly enhances trapping of sediment at the landward end of the salinity intrusion (Geyer, 1993). Jay and Musiak (1994) and Sanford et al. (2001) demonstrated that net sediment transport due to ebb-flood asymmetry in intensity of turbulence during a tidal cycle significantly affects the location of the turbidity maximum. A similar conclusion was made by Chernetsky et al. (2010) with respect to net sediment transport that results from the interaction between the M_2 tide and external M_4 tide. Recent studies (Donker and Swart, 2013; Winterwerp

et al., 2013) stressed the role of flocculation and hindered settling in sediment trapping. Other studies focused on lateral trapping of suspended sediment at a fixed cross-section (Huijts et al., 2006; Kim and Voulgaris, 2008; Chen and Sanford, 2009; Yang et al., 2014). Interestingly, little attention has been devoted to quantifying and understanding how the joint presence of longitudinal and lateral processes in an estuary results in a three-dimensional structure of the turbidity field.

Field data reveal that lateral distribution of suspended sediment concentration shows longitudinal differences. In the Hudson River Estuary, Geyer et al. (2001) observed that, in a cross-section in the upper reach, turbidity maxima occurred on both left and right sides, whereas in a cross-section near the mouth only one turbidity maximum was only found on the left side (when looking into the estuary). Recent data collected in the North Passage of the Yangtze Estuary, China also show different turbidity maxima at two separate cross sections. Moreover, the magnitudes of observed SSC during spring and neap tide are markedly different, whereas the lateral distribution is similar (data are presented in section 2). These observations motivate the overall objective of the present study, i.e., to identify possible mechanisms that cause the lateral trapping of suspended sediment at different longitudinal locations and at different stages of the spring-neap cycle.

To gain thorough understanding of sediment entrapment mechanisms in tidal estuaries, both numerical and analytical models are important tools. The former allow for detailed simulation of current and SSC distribution under controlled conditions (Burchard et al., 2004; Song and Wang, 2013; van Maren et al., 2016) while the latter have been frequently used to obtain fundamental knowledge of physical processes (Huijts et al., 2006; Talke et al., 2009b; Schuttelaars et al., 2013; Yang et al., 2014). The aim of this work is to gain fundamental understanding about longitudinal variations in lateral sediment trapping in an estuary, rather than to reproduce all details of sediment transport in a specific estuary. Huijts et al. (2006) showed that at a fixed longitudinal location, the locations of sediment accumulation in a cross-section depend on the relative importance of lateral current components induced by Coriolis deflection of longitudinal current and by lateral density gradients. Inspired by their work, the first hypothesis of the present study is that the intensities of lateral current components vary in the longitudinal direction, thereby resulting in different trapping locations of SSC. The second hypothesis is that the relative importance of each lateral current component to the trapping of sediment is not sensitive to the varying intensity of turbulence from spring tide to neap tide.

To test these two hypotheses, a new three-dimensional exploratory model is employed. It extends the model of Huijts et al. (2006) in that conditions in the longitudinal direction are not uniform. The present model also extends an earlier model of Festa and Hansen (1978) in the sense that it includes both

longitudinal and lateral dynamics. Besides, more sophisticated formulations for turbulent eddy viscosity and eddy diffusivity are used that depend on the degree of stratification and which allow for studying conditions during both spring and neap tide.

The details of the new field data (of the Yangtze Estuary), model and methods are presented in section 4.2. In section 4.3, the model results are presented and used to verify the two hypotheses. This is followed by a discussion in section 4.4, and by the conclusions in section 4.5.

4.2 MATERIAL AND METHODS

4.2.1 *Data*

Two cross-sections in the North Passage of the Yangtze Estuary were sampled during spring and neap tide in February, 2013 (Figure 4-1) by the Estuarine and Coastal Science Research Center, Shanghai (ECSRC). The first cross-section is labelled A and, it is 38 km downstream from the reference point (see Figure 4-1b). The second cross-section (labelled B) is 2 km downstream from A. Velocities, water depth, salinity and SSC data were collected synchronously by instruments on board of two vessels that continuously moved back and forth at two cross-estuary transects during two full tidal cycles (25 hours). The south and north sides of the two sampled transects are located on the regulation lines (see Figure 4-1), which connect the most offshore ends of the groins that are present on either side of the channel banks, i.e., the training walls. Vessels completed 3 km transects in $30-45$ min. Velocities and depths were measured with 600 kHz broadband Acoustic Doppler Current Profilers. Optical Backscatter Sensors were used to measure SSC from water surface to the bottom at seven fixed locations that were evenly distributed over the two transects. The data were processed by ECSRC and were interpolated at hourly intervals and at six σ-levels, following the method of Shi (2004), i.e. at relative depths of 0 (surface), $-0.2, -0.4, -0.6, -0.8, -1$ (actually 0.5 m above the bottom). The data were subsequently decomposed into tidally averaged components and components related to tides with specific frequencies (M_2, M_4, O_1, K_1, ...) by applying harmonic analysis. The freshwater discharge of the Yangtze River during the observation period (from neap to spring tide) was $16000-17000$ m^3 s^{-1}, of which roughly $20-25\%$ entered the North Passage. During neap tide, the measured tidal range was about 2.1 m and maximum instant tidal current speed was 1.7 m s^{-1}, while during spring tide, they were 3.5 m and 3.0 m s^{-1}, respectively.

Time averaged SSC collected at the two cross-sections A and B are shown in Figure 4-2 (orientations are into the estuary). Note here that the vertical

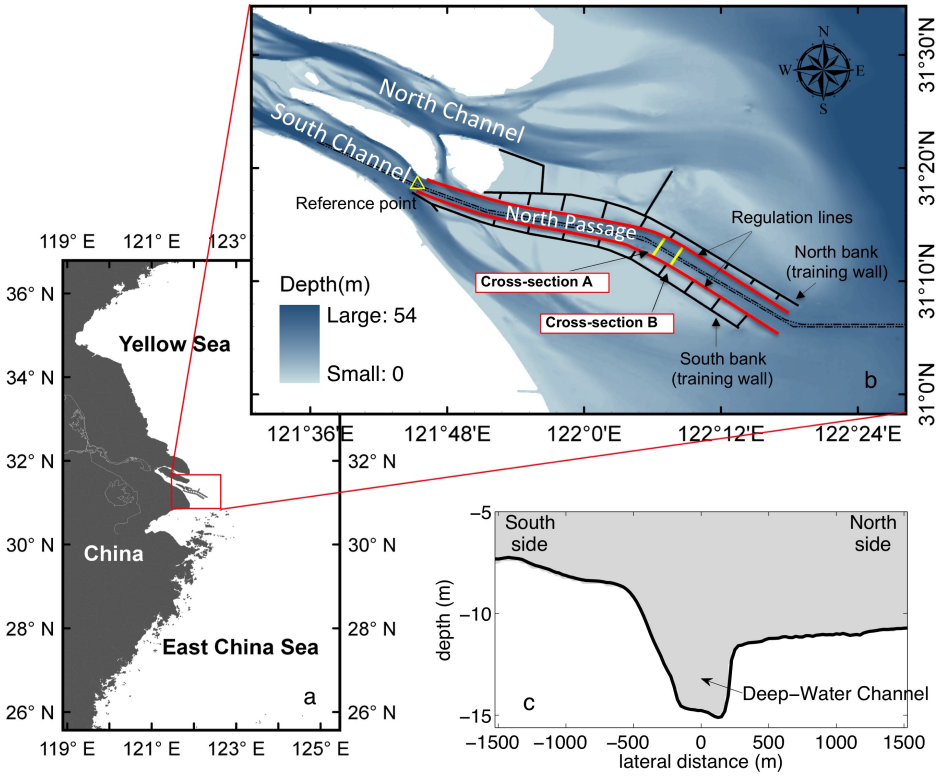

Figure 4-1: a. Map of the study area in the central and lower part of the Yangtze Estuary. b. Zoom-out map of the study area including the location of the cross-sections at which measurements are available. The two cross-sections are located 38 km and 40 km downstream from the reference point (yellow triangle). The regulation lines, which connect the offshore ends of the groins along the banks, are denoted by red solid lines. c. A typical cross-estuary depth profile (cross-section A).

distance $z^{\dagger} = \sigma h(y)$ is the time-mean vertical position of a certain σ−surface, with $h(y)$ representing the undisturbed depth. During spring tide, SSC at cross-section A attains maxima near both the south and north side (Figure 4-2a). At cross-section B (Figure 4-2b) however, a turbidity maximum is found only near the south side. During neap tide (Figure 4-2c and d), values of SSC in both two cross-sections are an order of magnitude lower than those during spring tide. Nevertheless, the basic lateral sediment distribution pattern remains unchanged, i.e., turbidity maxima occur on both the south and north sides at cross-section A and only one maximum is found (on the south shoal) at cross-section B.

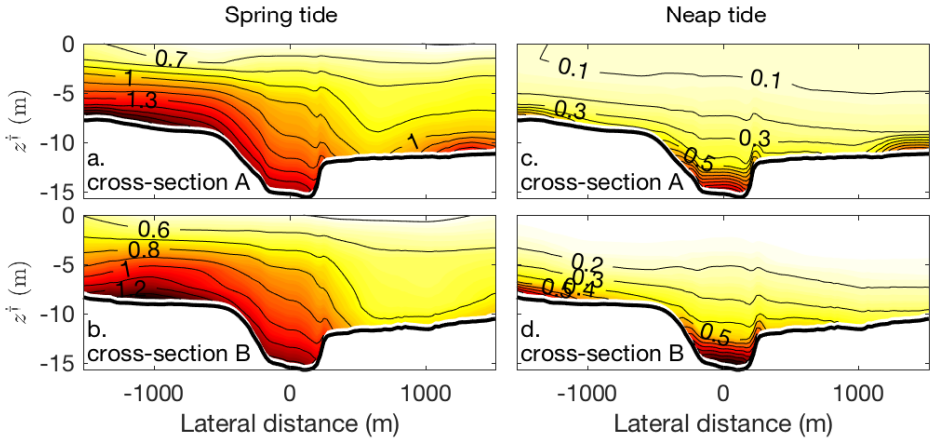

Figure 4-2: Distribution of residual SSC (in kg m^{-3}) in a. cross-section A during spring tide; b. cross-section B during spring tide; c. cross-section A during neap tide and d. cross-section B during neap tide. Locations are indicated in Figure 4-1; $z^\dagger$ is distance to the mean water surface. Orientation of all plots is into the estuary.

As the stability of the water column and residual currents affect the distribution of SSC, data for salinity and residual currents are presented. Tidally averaged salinity at the two cross-sections exhibits variation in the vertical direction, with values in the deep channel ranging from 9 psu (Figure 4-3a and b) and 4 psu (Figure 4-3c and d) near the water surface, to 20 psu (Figure 4-3a and b) and 22 psu (Figure 4-3c and d) near the bottom during spring tide and neap tide, respectively. The water column is moderately stratified during spring tide, with bottom-to-surface salinity difference (Δs) of 6.3 psu and 6.6 psu at A and B, respectively (Figure 4-3a and b). During spring tide, saltier water occurs near the north side and fresher water near the south side. During neap tide, the observed Δs are 14.5 psu at A and 16.5 psu at B (Figure 4-3c and d).

The bulk Richardson number (Dyer, 1997)

$$Ri = g\frac{\Delta\rho_m H}{\rho_r {U_m}^2} \tag{4-1}$$

yields a quantitative measure of the ratio of stratification and destratification mechanisms at the two cross-sections. Here, $g = 9.8\ m\ s^{-2}$ is gravitational acceleration, $\rho_r = 1000\ kg\ m^{-3}$ is a constant reference density, and $\Delta\rho_m = \beta\Delta s$ is the laterally averaged residual density difference between bottom and surface. It is assumed that water density only depends on salinity and $\beta = 0.78\ kg\ m^{-3}\ psu^{-1}$ is the salinity contraction coefficient. Furthermore, H is the

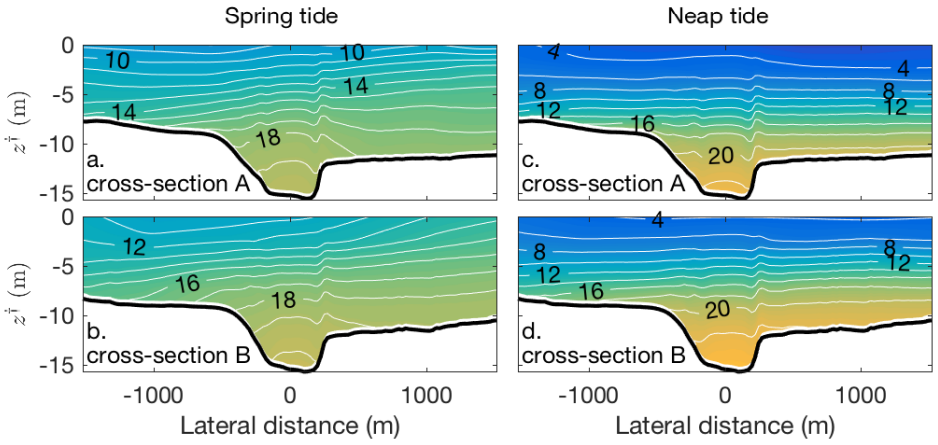

Figure 4-3: Distribution of residual salinity (in psu) at a. cross-section A during spring tide; b. cross-section B during spring tide; c. cross-section A during neap tide and d. cross-section B during neap tide; $z^\dagger$ is distance to the mean water surface. Orientation of all the plots is into the estuary.

laterally averaged water depth and U_m is the laterally averaged tidal current amplitude. Harmonic analysis shows that the M_2 tide is the dominant constituent, with $U_m = 1.6$ m s^{-1} during spring tide and $U_m = 0.8$ m s^{-1} during neap tide. Substitution of the measured values into Eq. 1 yields for both cross-sections that $Ri \simeq 0.3$ during spring tide and $Ri \simeq 2.0$ during neap tide. These numbers indicate that the water column is weakly stratified during spring tide and strongly stratified during neap tide.

The spatial patterns of the measured longitudinal residual current in the two cross-sections are presented in Figure 4-4. During spring tide, outflow occurs in most of the two cross-sections, with a maximum of 0.8 m s^{-1} near the surface (Figure 4-4a and b). In contrast, a clear two layer current structure is observed during neap tide, with an outflow of 0.4 m s^{-1} near the surface and inward current of 0.2 m s^{-1} near the bottom of the channel (Figure 4-4c and d).

Figure 4-5 shows the lateral residual current observed in the two cross-sections. During spring tide a clockwise transverse residual circulation is observed. Moreover, the maximum northward current is observed at the surface near the north side, with values of 0.2 m s^{-1} (Figure 4-5a) in cross-section A and 0.1 m s^{-1} in cross-section B (Figure 4-5b), respectively. Integrating lateral residual current over the depth at the end of transects yields a net water transport through the north side. This phenomenon is referred to as water leakage. During neap tide, a more complicated residual circulation pattern is observed.

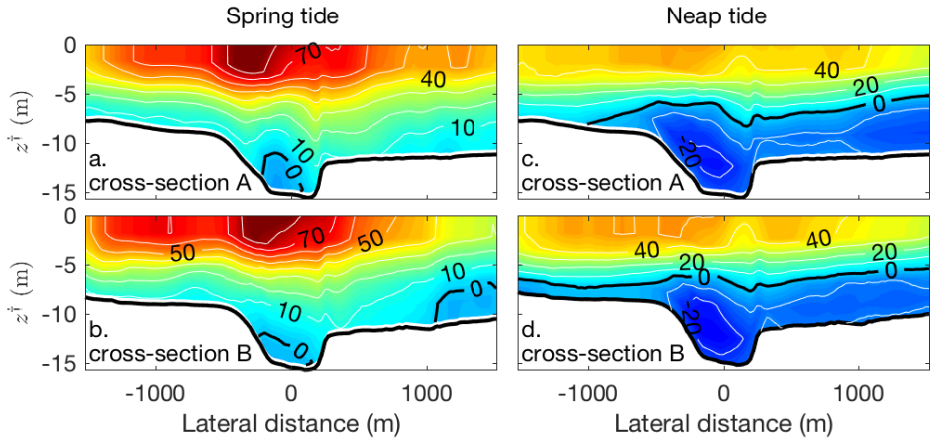

Figure 4-4: Distribution of longitudinal residual current (in cm s^{-1}) in a. cross-section A during spring tide; b. cross-section B during spring tide; c. cross-section A during neap tide and d. cross-section B during neap tide; $z^\dagger$ is distance to the mean water surface. Orientation of all the plots is into the estuary.

In both cross-sections, a clockwise structure is found over the north shoal. However, in cross-section A, an anti-clockwise circulation is observed over the south shoal (Figure 4-5c). In cross-section B, a three layer structure is observed close to the south side, with southward current near both the water surface and the bottom and northward current in the middle water layer. The magnitude of the transverse residual current has a similar value, of about 0.1 m s^{-1} during both spring and neap tide, and it occurs at the surface near the north side (Figure 4-5d).

4.2.2 *Model*

The observations presented in section 4.2.1 reveal differences in structure of lateral residual current and of residual SSC in the two cross-sections during both spring and neap tide. These data add to both observational and model studies that focus on longitudinal distribution of SSC in the Yangtze Estuary (Wu et al., 2012; Jiang et al., 2013; Song and Wang, 2013; Wan and Zhao, 2017). Differences in each cross-section between spring and neap tide mainly concern the intensity of lateral current. Thus, these data support the two hypotheses of the present study, which will be tested with an exploratory 3D model.

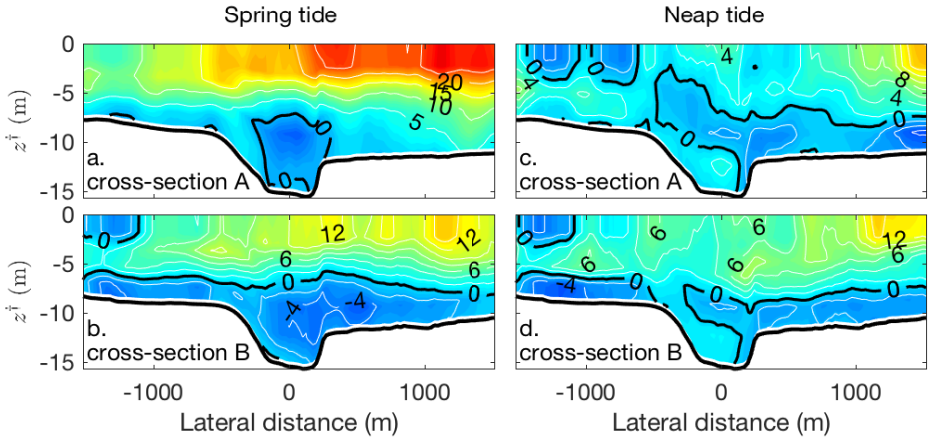

Figure 4-5: Distribution of lateral residual current (in cm s^{-1}) in a. cross-section A during spring tide; b. cross-section B during spring tide; c. cross-section A during neap tide and d. cross-section B during neap tide; $z^\dagger$ is distance to the mean water surface. Orientation of all the plots is into the estuary. In panels b and d, positive (negative) values denote northward (southward) current.

4

4.2.2.1 *Model domain*

The model domain represents an estuarine channel with two straight parts, connected by a curved segment (Figure 4-6). This configuration mimics the gross characteristics of an estuary, like the one considered in section 4.2.1. The channel has a constant width, an along-channel uniform bathymetry and open boundaries at both the landward and the seaward end. In the lateral direction, a smooth bottom profile is imposed. The length and half width of channel are denoted by L and B, respectively. A curvilinear x, y and σ—coordinate system is adopted (Figure 4-6a), with the origin at the free surface and middle of the landward side section ($x = 0$). Here, x follows the along-channel direction, $y = -B$, B are the locations of the southern/northern regulation lines and $\sigma = (z - \eta_s)/D$, in which z is vertical distance to the undisturbed water surface and $z = \eta_s$ is the level of the instantaneous free surface. The bottom is located at $z = -h(y)$ (Figure 4-6b). The curvature varies as a function of x and is described by $R = R_{min}\check{R}(x)$, in which R_{min} is the minimum radius of the curvature and $\check{R} = \left\{\frac{1}{2} + \frac{1}{2}\cos\left[\frac{2\pi(x-x_{cur})}{x_2-x_1}\right]\right\}^{-1}$ is a dimensionless function. Here, the limits of the curved segment are denoted by x_1 and x_2. At $x_{cur} = (x_1 + x_2)/2$ the radius of curvature reaches its minimum (Figure 4-6c). Note that $D = h + \eta_s$ is the total instantaneous depth, hence, $z = z^\dagger + \eta_s(\sigma + 1)$. In the present study, it is assumed that the typical amplitude $[\eta_s]$ of the instantaneous sea surface

elevation is small compared to the undisturbed depth h, i.e., $\varepsilon \equiv [\eta_s]/h \sim 0.1$, which implies that $z \simeq z^{\dagger}$.

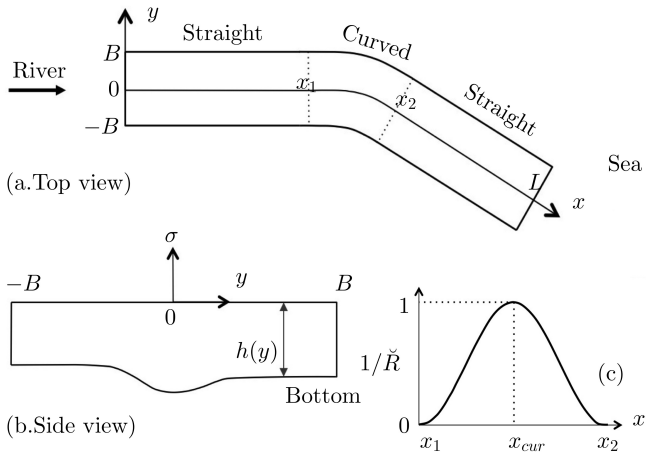

Figure 4-6: Sketch of the model domain; (a) top view and (b) side view. A σ-coordinate system (x, y, σ) is used with the origin at the free surface and middle of the landward side, where freshwater input from the river is imposed. The landside entrance (0 km) is located at the reference point (see Figure 4-1b). The positive x-axis points seaward, the y-axis points from left to right when looking landward, and σ denotes the relative depth from surface $(\sigma = 0)$ to the bottom $(\sigma = -1)$. The bottom profile $z = -h(y)$ is uniform in the x direction and is arbitrary in the y direction. c. Dependence of dimensionless function $\breve{R}^{-1} = R_{min}/R$ on longitudinal coordinate x, where R is the radius of the curvature and R_{min} is the minimum value of R.

4

4.2.2.2 *Hydrodynamics*

Following earlier studies (e.g. Hansen and Rattray, 1965), a linear model for steady currents is applied. The Coriolis term in the longitudinal direction is ignored because it is small compared to other terms. The equations for residual

current in 3D σ−coordinates (see the supplementary material S.3.1.1 for their derivation) read

$$0 = -g\frac{\partial \eta}{\partial x} - \frac{g}{\rho_r} h \int_\sigma^0 \left(\frac{\partial \rho}{\partial x}\right)^* d\tilde{\sigma} + \frac{1}{h^2}\frac{\partial}{\partial \sigma}\left(A_v \frac{\partial u}{\partial \sigma}\right), \tag{4-2a}$$

$$0 = -fu - g\frac{\partial \eta}{\partial y} - \frac{g}{\rho_r} h \int_\sigma^0 \left(\frac{\partial \rho}{\partial y}\right)^* d\tilde{\sigma} + \frac{1}{h^2}\frac{\partial}{\partial \sigma}\left(A_v \frac{\partial v}{\partial \sigma}\right), \tag{4-2b}$$

$$\frac{\partial}{\partial x}\int_{-1}^0 h u d\sigma + \frac{\partial}{\partial y}\int_{-1}^0 h v d\sigma = 0. \tag{4-2c}$$

Here, Eq. 4-2a is the longitudinal tidally averaged momentum balance, which contains the barotropic pressure gradient force, the baroclinic pressure gradient force and the internal friction force. Eq. 4-2b is the lateral momentum balance with on its right hand side the Coriolis force, forces due to barotropic pressure gradient, baroclinic pressure gradient and friction. The superscript $*$ denotes that the horizontal density gradients in both the longitudinal and lateral direction are taken at a fixed $z^\dagger$ level. Eq. 4-2c expresses tidally mean conservation of mass. A dimensionless parameter $\sigma_0 \simeq z_0/h$ is defined, in which z_0 denotes the local roughness length. In these equations, u, v are the tidal mean current components in the longitudinal and lateral direction, respectively. It is assumed that u and v are zero inside the roughness element layer. The Coriolis parameter $f \sim 10^{-4}$ s^{-1} and A_v is a spatially varying eddy viscosity and expression will be given in Section 4.2.2.4. Note that channel curvature can induce lateral residual circulation (Kim and Voulgaris, 2008) as well as transport through boundaries (as shown in section 4.2.1). The curvature induced circulation is ignored in the present work, as it is much smaller than that induced by the lateral density gradient (for details see the supplementary material S.3.3).

In the model, density gradients are prescribed and values are motivated by field data. First, following Warner et al. (2005), it is assumed that

$$< s >= \frac{1}{2} s_* \left[1 + \tanh\left(\frac{x + x_c - L}{x_L}\right)\right]. \tag{4-3}$$

Here, s_* (~ 35 psu) is the salinity at sea, $< s >$ denotes the time-independent cross-sectional mean density, $x = L - x_c$ the position at which the salinity is half of its value at sea, the salinity intrusion limit (where the salinity $< s >= 0.12 s_*$) is at $x = L - (x_L + x_c)$. Parameters x_c and x_L are determined by fitting data to Eq 4-3. Furthermore, it is used that $\left(\frac{\partial \rho}{\partial x}\right)^* = \beta \frac{\partial < s >}{\partial x}$.

It is further assumed that $\left(\frac{\partial \rho}{\partial y}\right)^*$ is constant in the vertical direction and it is imposed as a function of the lateral distance: $\left(\frac{\partial \rho}{\partial y}\right)^* = a_r(y/B) + b_r$, in

which a_r and b_r are constants that are determined from the field data. Finally, the aspect ratio of the lateral and longitudinal density gradient is assumed to be constant in the x-direction, i.e. $\frac{(\partial\rho/\partial y)^*}{(\partial\rho/\partial x)^*} = \frac{(\partial\rho/\partial y)^*}{(\partial\rho/\partial x)^*}\Big|_{x=x_m}$ with x_m being the location where $(\partial\rho/\partial x)^*$ attains its maximum value.

The boundary conditions at the free surface and at the bottom are given by

$$\frac{1}{h}A_v\frac{\partial u}{\partial\sigma} = 0, \quad \frac{1}{h}A_v\frac{\partial v}{\partial\sigma} = 0 \qquad \text{at} \qquad \sigma = 0, \tag{4-4a}$$

$$u = 0, \quad v = 0 \qquad \text{at} \qquad \sigma = -1. \tag{4-4b}$$

At $y = -B$, it is assumed that there is no net water transport. At $y = B$, net water transport is allowed, in order to be able to mimic situations as were discussed in section 4.2.1. This results in the following boundary conditions:

$$\int_{-1}^{0} hv\,d\sigma = 0 \qquad \text{at} \qquad y = -B, \tag{4-5a}$$

$$\int_{-1}^{0} hv\,d\sigma = q_o f(x) \qquad \text{at} \qquad y = B. \tag{4-5b}$$

Here, q_o is a constant water transport (imposed in the model) and $f(x)$ is a dimensionless function that describes the distribution of net water transport in the longitudinal direction. The water leakage through the side, as expressed by the right-hand side of Eq. 4-5b, occurs when the water elevation is higher than the channel side during part of a tidal cycle. The amount of water leakage at the north side is assumed to be proportional to $\check{R}^{-1}$, i.e., the reciprocal of the dimensionless channel curvature. This is because due to centrifugal forces, surface water layer flows from inner bend to outer bend and causes a set up of water at the outer bend. It is assumed that in the remaining reaches the amount of water lost at the curved segment returns through the north side of the channel with a constant rate $q_o f_c$, where $f_c = L^{-1}\int_{x_1}^{x_2}\check{R}^{-1}dx$. Hence, $f(x)$ along the channel reads

$$f(x) = \begin{cases} 1/\check{R} - f_c, & x_1 \leqslant x \leqslant x_2, \\ -f_c, \qquad 0 \leqslant x \leqslant x_1 \ \text{ and } \ x_2 \leqslant x \leqslant L. \end{cases} \tag{4-6}$$

At the landward entrance, a net transport of freshwater is imposed with a constant discharge Q_r,

$$\int_{-B}^{B}\int_{-1}^{0} hu\,d\sigma\,dy = Q_r \qquad \text{at} \qquad x = 0. \tag{4-7}$$

4.2.2.3 *Sediment dynamics*

Mass conservation of sediment yields an equation for SSC (see S.3.1.2), which to a first approximation reads

$$\frac{\partial}{\partial\sigma}\left(w_s c + \frac{K_v}{h}\frac{\partial c}{\partial\sigma}\right) = 0. \tag{4-8}$$

Here, c is the SSC and w_s is the constant settling velocity and K_v is the vertical eddy diffusion coefficient, which will be discussed in the next section. At the surface, there is no flux of sediment,

$$w_s c + \frac{K_v}{h}\frac{\partial c}{\partial\sigma} = 0 \quad \text{at} \quad \sigma = 0. \tag{4-9}$$

At the bottom, a vertical turbulent diffusive flux is imposed that describes the amount of sediment being eroded from the bed:

$$E_s \equiv -\frac{K_v}{h}\frac{\partial c}{\partial\sigma} = w_s \hat{c} \quad \text{at} \quad \sigma = -1 + \sigma_a. \tag{4-10}$$

Here, $\hat{c}$ is a reference concentration, which depends on bottom stress (in principle known) and an as yet unknown sediment availability. Moreover, $z_a = h\sigma_a$ is the reference height. For simplicity, $\sigma_a = \sigma_0$ is chosen. The solution of the SSC equation (Eq. 4-8) reads

$$c = \hat{c}\ \phi(\sigma, h(y)), \tag{4-11}$$

with $\phi(\sigma, h(y))$ describing the vertical distribution of SSC, which can be determined for a given K_v (e.g., if K_v/w_s is a constant, $\phi(\sigma, h(y))$ is an exponential function). Note that $\hat{c}$ is the approximation of the tidally mean bottom SSC. In order to determine $\hat{c}$, the condition of morphodynamic equilibrium (i.e., averaged over the tidal period, erosion balances deposition of sediment) is applied to the full SSC equation. This implies that the divergence of the sediment transport must vanish, hence

$$\frac{\partial T_x}{\partial x} + \frac{\partial T_y}{\partial y} = 0, \tag{4-12}$$

in which T_x, T_y are the residual sediment transport in the x, y direction, given by

$$T_x = \int_{-1}^{0} h \left(u\, c - K_{hx} \frac{\partial c}{\partial x} \right) d\sigma, \tag{4-13a}$$

$$T_y = \int_{-1}^{0} h \left(v\, c - K_{hy} \frac{\partial c}{\partial y} \right) d\sigma. \tag{4-13b}$$

Furthermore, K_{hx} and K_{hy} are constant horizontal eddy diffusion coefficients in the longitudinal and lateral direction and will be further discussed in the next section. In this model, u and v in Eq. 4-13a and b are residual currents, thus sediment transport due to tidal pumping is not considered. Substitution of Eq. 4-11 into Eq. 4-12 and 4-13a, b yields an equation for $\hat{c}$, i.e.,

$$\frac{\partial}{\partial x} \left(I_1 \hat{c} + I_2 \frac{\partial \hat{c}}{\partial x} \right) + \frac{\partial}{\partial y} \left(I_3 \hat{c} + I_4 \frac{\partial \hat{c}}{\partial y} \right) = 0, \tag{4-14}$$

with

$$\begin{aligned} I_1 &= \int_{-1}^{0} hu\phi \, d\sigma, \qquad I_2 = -\int_{-1}^{0} hK_{hx}\phi \, d\sigma, \\ I_3 &= \int_{-1}^{0} h \left(v\phi - K_{hy} \frac{\partial \phi}{\partial y} \right) d\sigma, \qquad I_4 = -\int_{-1}^{0} hK_{hy}\phi \, d\sigma. \end{aligned} \tag{4-15}$$

Here, I_1 and I_3 are transports of sediment in the longitudinal and lateral direction in the case of unlimited sediment supply and I_2 $\partial\hat{c}/\partial x$, I_4 $\partial\hat{c}/\partial y$ are transports induced by gradients in the reference concentration.

The conditions for sediment at the two lateral boundaries are

$$T_y = 0 \quad \text{at} \quad y = -B, \tag{4-16a}$$

$$T_y = q_{sed} f(x) \quad \text{at} \quad y = B. \tag{4-16b}$$

Here, q_{sed} is a given constant sediment transport and function $f(x)$ is described in Eq. 4-6. Physically, the right-hand side of Eq. 4-16b represents the amount of sediment leakage at the north side of the channel, which is related to water leakage. Furthermore, sediment transport at the landward entrance is given by

$$\int_{-B}^{B} T_x \, dy = Q_{sed} \quad \text{at} \quad x = 0. \tag{4-17}$$

where Q_{sed} is a constant sediment discharge. Finally, it is imposed that

$$\frac{1}{2BL}\int_{-B}^{B}\int_{0}^{L}\hat{c}\ dxdy = c_b, \tag{4-18}$$

where c_b is a given domain averaged near-bed sediment concentration.

4.2.2.4 *Turbulence closure*

Previous studies, such as Geyer et al. (2000), have shown that in an unstratified water column the maximum eddy viscosity is usually observed in the middle of the water column, but with increasing stratification it becomes smaller and its location shifts to the bottom. Hence, to capture the basic characteristics of turbulent exchange processes in both weakly stratified (spring tide) and highly stratified (neap tide) situation, a formulation of vertical eddy viscosity is used that depends on σ. The vertical eddy viscosity coefficient follows that of Chen and Swart (2016),

$$A_v = \kappa \check{u}_* h\, A_\sigma. \tag{4-19}$$

In this expression, $\kappa = 0.41$ is the von Karman's constant, $\check{u}_*$ is a constant friction velocity, h is depth and A_σ describes the dependence of eddy viscosity on coordinate σ. Parameter $\check{u}_*$ is calculated from the expression (for derivation see the supplementary material S.3.1.3):

$$\check{u}_* = \frac{16}{15\pi} C_d^{1/2} U_T \left[1 + 2\left(\left(\frac{U_{res}}{U_T}\right)^2 + \frac{3}{2}\left(\frac{U_t}{U_T}\right)^2\right)\right]. \tag{4-20}$$

Here, $C_d \sim 1\cdot 10^{-3}$ is a drag coefficient, U_{res}, U_t and $U_T = U_{res} + U_t$ are characteristic scales of the overall residual current, tidal current and total current. In this study, observations in cross-section A are used to estimate the values for U_{res}, U_t and U_T during spring tide and neap tide, respectively (see section 4.2.1).

The function A_σ in Eq. 4-19 reads

$$A_\sigma = \begin{cases} (\sigma+1)(\sigma_p - \sigma), & -1 \leqslant \sigma \leqslant \sigma_h, \\ (A_I - A_s)\left|\frac{\sigma}{\sigma_h}\right|^2 + A_s, & \sigma_h \leqslant \sigma \leqslant 0. \end{cases} \tag{4-21}$$

with $A_I = (\sigma_h + 1)(\sigma_p - \sigma_h)$ the value of A_σ at $\sigma = \sigma_h$ and A_s is the value of A_σ at the free surface. A sketch of A_σ as a function of σ is presented in Figure 4-7. The formulation of A_σ contains two input parameters, viz. A_s and σ_p, with

the values determined from field data. The first parameter measures intensity of turbulence at the surface. Based on surface eddy viscosity results from Figure 2 of Cheng (2014), A_s is formulated as $Log_{10}(A_s) = a_s(h - h_{min})h_{mean}^{-1} + b_s$, which describes lower surface eddy viscosity values with increasing water depth. Here a_s and b_s are input parameters. The second parameter is related to the height of the turbulent bottom boundary layer (h_b), i.e., $h_b = (1 + \sigma_p)h$ (see Figure 4-7). As discussed by e.g. Ralston et al. (2008), h_b decreases when the water column becomes more stratified. By fitting Eq. 4-21 to observed vertical eddy viscosities, it was found in chapter 2 (also see in Chen and Swart, 2016) that

$$h_b \equiv h(1 + \sigma_p) = h[\exp(0.78Ri^{0.36})]^{-1}, \tag{4-22}$$

where Ri is the bulk Richardson number defined in Eq. 4-1. In this model, Ri is an input parameter and its value will be determined from field data. The values for parameters σ_h and A_I in Eq. 4-21 follow by requiring that at σ_h both A_σ and its derivative $\partial A_\sigma/\partial\sigma$ are continuous.

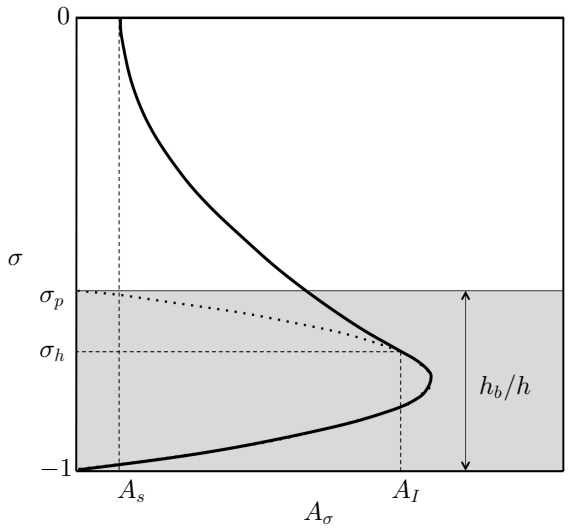

Figure 4-7: Vertical profile of A_σ (solid line) according to Eq. 4-21 (adjusted from Figure 1 of Chen and Swart (2016). Note that h_b/h is the scaled turbulent bottom boundary layer, as is denoted by the grey area.

The vertical diffusion coefficient K_v is calculated as $K_v = S_c A_v$, in which S_c is the Schmidt number given as

$$S_c = \frac{(1 + 3.33Ri)^{-1.5}}{(1 + 10Ri)^{-0.5}}. \tag{4-23}$$

This choice is based on the results of Munk and Anderson (1948), who presented Eq. 4-23 in terms of the gradient R_i. Here, the bulk Richardson number is used as an estimation of the gradient Richardson number.

The horizontal turbulent eddy diffusion coefficients in the longitudinal (K_{hx}) and lateral direction (K_{hy}) are assumed to have different values. The longitudinal coefficient is due to both vertical and horizontal shear dispersion and the lateral diffusion coefficient is mainly the result of vertical shear dispersion. In tidal estuarine environments, K_{hx} is typically $100 \sim 200$ $m^2 s^{-1}$ and values of K_{hy} are an order of magnitude smaller (Zimmerman, 1986).

4.2.3 *Solutions*

As is detailed in section S.3.2.1 S2-1 andS.3.2.2 of the supplementary material, the residual current reads

$$u = u_d + u_Q, \tag{4-24a}$$
$$v = v_f + v_d + v_R. \tag{4-24b}$$

The longitudinal residual current contains two contributions. The first (u_d) is driven by the longitudinal density gradient ($\partial\rho/\partial x$). The second contribution (u_Q) is induced by the longitudinal net water discharge, which results from two sources: the leakage of water at the north side (Eq. 4-5b) and the fresh water input at the landward entrance (Eq. 4-7). In the lateral direction, the residual current contains three contributions that are due to Coriolis deflection of longitudinal residual current (fu), the lateral density gradient $\partial\rho/\partial y$ and leakage (R), respectively.

The equation and boundary conditions for $\phi = c/\hat{c}$ are obtained by substitution of Eq. 4-11 into Eqs. 4-8 to 4-10 and subsequently dividing all terms by $\hat{c}$. After that, integration of the equation and application of the boundary conditions yield an explicit expression for ϕ, which is given in supplementary material S.3.2.3.

To find the solution for the reference sediment concentration $\hat{c}$, the morphodynamic equilibrium condition Eq. 4-14 must be solved. Note that in contrast to

previous studies (e.g., Huijts et al. (2006) and Chernetsky et al. (2010)), the equation is two-dimensional. Solutions are obtained by a novel iteration procedure, where in the initial step only the term involving the lateral sediment transport is considered. The error made in the initial step (by ignoring the longitudinal sediment transport) is then compensated at further iteration steps ($n = 1, 2, ...$). It means that Eq. 4-14 is solved, where in the first term $\hat{c}$ at iteration step $(n-1)$ and in the second term $\hat{c}$ at step n is used. The details of the iterative procedure and expressions for $\hat{c}$ are presented in the Appendix.

4.2.4 *Set-up of experiments*

First, two experiments were carried out to verify whether the model results is able to mimic the main characteristics of current and SSC distribution that are also observed in the field. The first experiment is referred to as RS, which describes the reference state at spring tide, and the latter is referred to as RN, which represents the reference case at neap tide. The parameter values used as model input are given in Table 4-1. These values are representative for the North Passage of the Yangtze Estuary in China, during spring and neap tide, respectively. Parameters that adopted from this study and other references are cited in the footnote of this table.

Next, additional experiments were conducted to verify the first hypothesis, i.e., the longitudinal variation in intensities of the lateral current components v_f, v_d and v_R are responsible for the longitudinal variation of sediment entrapment in the lateral direction. Settings of the first experiments are the same as that in RS, except that lateral residual current is only driven by Coriolis deflection of longitudinal residual current. In the second experiment, the lateral current is only induced by the density gradient. The third experiment is as RS, but in the lateral direction only the effect of leakage is accounted for. The fourth experiment is as RS, but it excludes the leakage.

To test the second hypothesis, i.e., that differences in SSC between spring and neap tide mainly concern their intensities, four more experiments were carried out. These experiments were designed like those in the first series, except that parameter values mimic the conditions at neap tide (reference case RN) instead of at spring tide. The details of all experiments are summarised in Table 4-2.

Table 4-1: Values of the model input parameters

Parameter description	Symbol	Unit	Value	
			spring tide	neap tide
Channel length (a)	L	km	57	
Half of channel width (a)	B	m	1525	
Mean water depth (a)	H	m	11.3	
River discharge (a)	Q_r	$m^3 s^{-1}$	3.5×10^3	
Coriolis parameter (a)	f	s^{-1}	0.7×10^{-4}	
Minimum radius of the curvature (b)	R_{min}	km	50	
Roughness height (c)	z_0	m	5×10^{-3}	
Bulk Richardson number (a)	Ri		0.3	2.0
Distance from seaside of which $s = s_*/2$ (a)	x_c	km	10	12
Intrusion length parameter (a)	$x_c + x_L$	km	32	35
Lateral salinity gradient parameter I (a)	a_r	psu m^{-1}	-1×10^{-3}	0
Lateral salinity gradient parameter II (a)	b_r	psu m^{-1}	11×10^{-3}	6×10^{-3}
Water input rate at the curved side(a)	q_o	$m^2 s^{-1}$	1.0	
Overall tidal current (a)	U_t	m s^{-1}	1.5	0.7
Overall residual current (a)	U_{res}	m s^{-1}	0.3	0.2
Settling velocity (d)	w_s	mm s^{-1}	1.5	0.2
Sediment leakage per unit width	q_{sed}	kg s^{-1} m^{-1}	0.1	0
Sediment discharge at landside entrance	Q_{sed}	kg s^{-1}	800	8
Surface eddy viscosity parameter I	a_s		-3	
Surface eddy viscosity parameter II	b_s		-2	
Domain averaged near-bed SSC (a)	c_b	kg	1.5	0.5
Longitudinal horizontal diffusion coefficient	K_{hx}	m^2 s^{-1}	150	
Lateral horizontal diffusion coefficient	K_{hy}	m^2 s^{-1}	60	

Sources are (a) from this study, (b) Chen and Le (2005), (c) Wu et al. (2009) and (d) Shi et al. (2003) and Wang et al. (2006)

Table 4-2: Description of model experiments

Aim	Case	Description
	RS	parameters for spring tide condition are used as the model input
	RN	parameters for neap tide condition are used as the model input
1	RS-1	as RS, but for $\partial\rho/\partial y = 0$ and $q_o = 0$
	RS-2	as RS, but for Coriolis parameter $f = 0$ and $q_o = 0$
	RS-3	as RS, but for Coriolis parameter $f = 0$ and $\partial\rho/\partial y = 0$
	RS-4	as RS, but for $q_o = 0$
2	RN-1	as RN, but for $\partial\rho/\partial y = 0$ and $q_o = 0$
	RN-2	as RN, but for Coriolis parameter $f = 0$ and $q_o = 0$
	RN-3	as RN, but for Coriolis parameter $f = 0$ and $\partial\rho/\partial y = 0$
	RN-4	as RN, but for $q_o = 0$

4.3 RESULTS

In this section, output of the model in two cross-sections and in one horizontal surface is presented. The first two are sections T1 and T2, and they are located at similar positions as cross-sections A and B in the North Passage of the Yangtze Estuary (see Figure 4-1), respectively. The horizontal surface is the $\sigma = -0.95$, located near the bed. The results of the cases RS and RN are shown in section 4.3.1, followed by those of the sensitivity experiments in section 4.3.2. In section 4.3.3, the near-bed SSC distribution results of the experiments is presented.

4.3.1 *Cases RS and RN*

Figure 4-8 shows the modelled transverse distribution of longitudinal and lateral residual current and of SSC in cross-sections T1 and T2 for case RS. The model results resemble main features of the observed situation at spring tide that were presented in section 4.2.1. The longitudinal residual current (Figure 4-8a and b) is mostly seaward at both two cross-sections. Weak landward current is only found near the bottom of the deep channel. In Figure 4-8c and d, the modelled transverse residual current in T1 and T2 is shown. The panels reveal three main aspects of the observed lateral current (Figure 4-5a and b). First, the circulation is clockwise in both cross-sections, but northward current is more dominant in T1 than in T2. Second, the maximum residual current is found both at the surface above the deep channel and near the north side of T1 and T2. Third, the circulation in T2 is weaker than that in T1. Furthermore, the lateral distribution of SSC shows two maxima in T1 and only one near the

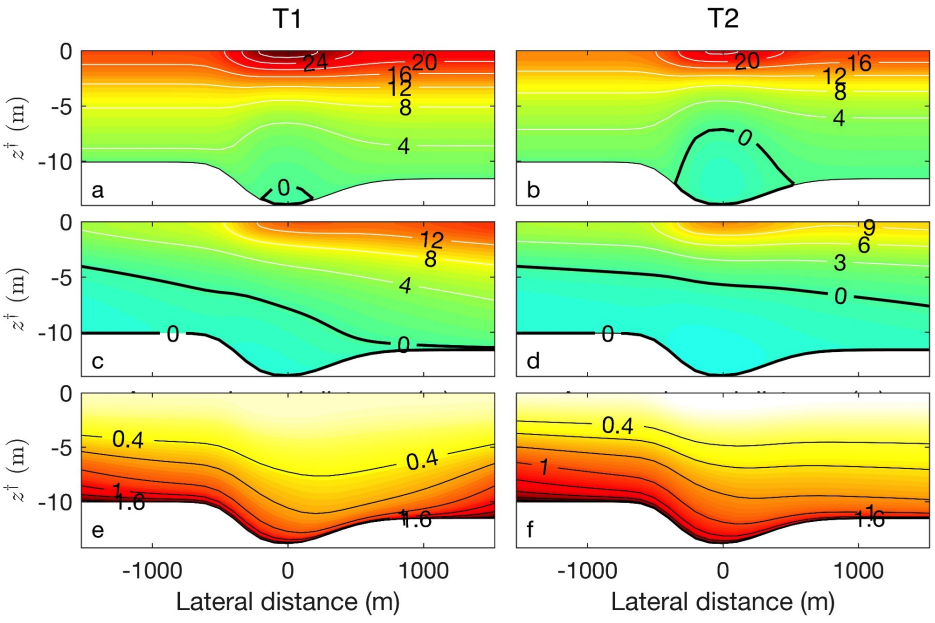

Figure 4-8: Transverse distribution of (a and b) longitudinal residual current, (c and d) lateral residual current, and (e and f) SSC in the RS case (spring tide). The left/right column denotes the model results in cross-sections T1/T2. Here, $z^\dagger$ denotes distance to the mean water surface. Units of values are cm s^{-1} in a-d, and kg m^{-3} in e and f. Orientation of all plots is into the estuary.

south shoal in T2 (Figure 4-8e and f), which is consistent with the observations (Figure 4-2 and b).

The results of reference case RN are presented in Figure 4-9 and show that the main characteristics of the residual current and SSC in neap tide are captured by the model as well. Regarding the longitudinal current, the observed two layer structure (Figure 4-4c and d) is reproduced by the model (Figure 4-9a and b). In the lateral direction, both the observations (Figure 4-5c and d) and model (Figure 4-9c and d) show a clockwise circulation, and a maximum northward current at the surface near the north side. The basic pattern of the modelled SSC (Figure 4-9e and f) is similar as that during spring tide (Figure 4-8e and f), and consistent with the data (Figure 4-2c and d).

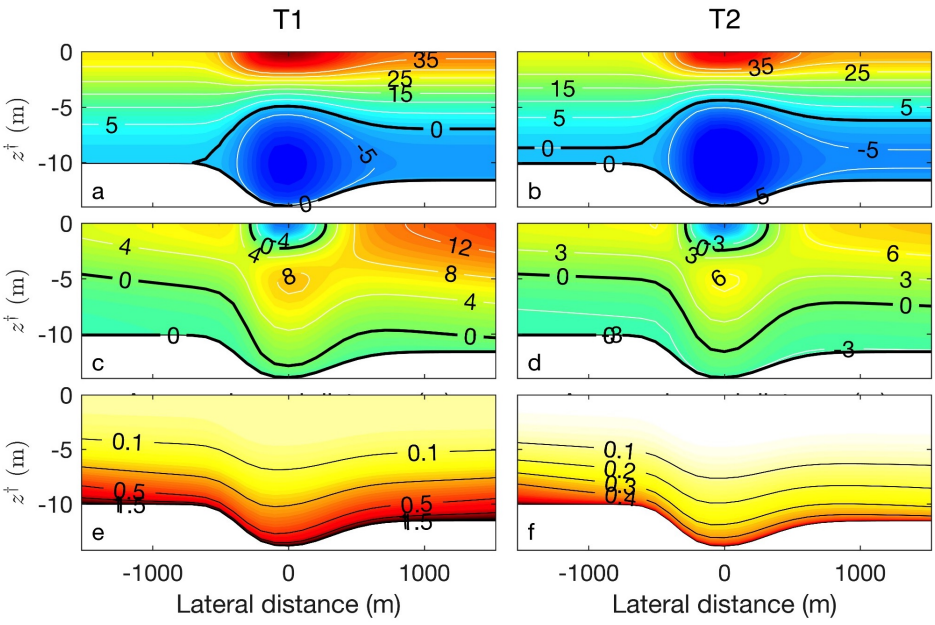

Figure 4-9: Transverse distribution of (a and b) longitudinal residual current, (c and d) lateral residual current, and (e and f) SSC in the RN case (neap tide). The left/right column denotes the model results in cross-sections T1/T2. Here, $z^\dagger$ denotes distance to the mean water surface. Units are cm s^{-1} in a-d, and kg m^{-3} in e and f. Orientation of all plots is into the estuary.

4.3.2 *Sediment distribution due to individual mechanisms*

Figure 4-10 displays the modelled transverse distribution of SSC of four different cases (for spring tide condition). In case RS-1, when the lateral current is only driven by Coriolis deflection of longitudinal current, SSC slightly increases from the south side to the north side in both T1 and T2 (Figure 4-10a and b). On the contrary, if the residual current is driven by density gradient (RS-2), SSC increases from the north side to the south side (Figure 4-10c and d). When the lateral process is due to leakage only (RS-3), the SSC in T1 has a minimum near the south side and it increases towards the north side. The SSC near the north side is much larger than that near the south (Figure 4-10e). In T2, the SSC also increases from the south to the north, however the difference between the two sides is much smaller than that in T1 (Figure 4-10f). In case that all current components are included except the one due to leakage (RS-4), the SSC distributions in the two cross-sections are similar to that of case RS-2,

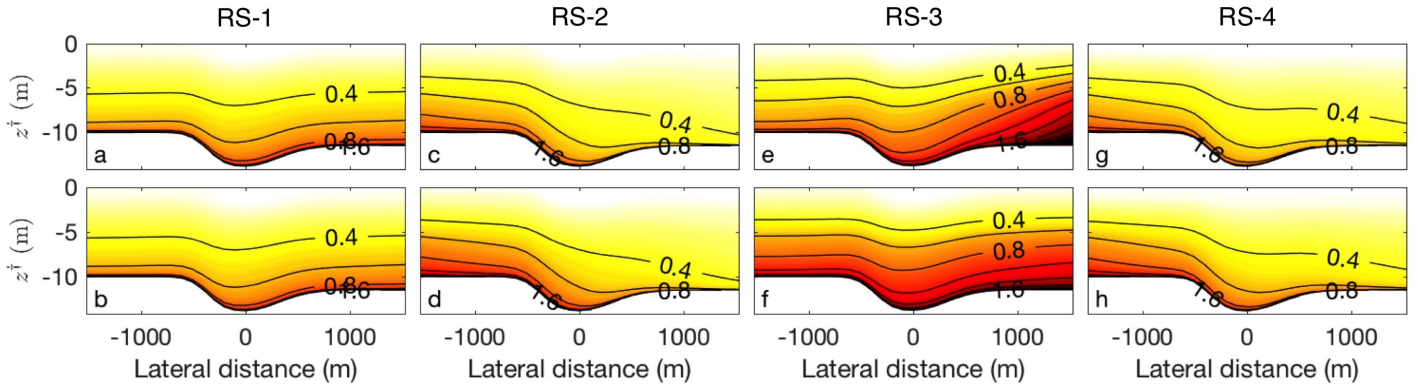

Figure 4-10: Transverse distribution of SSC (in kg m^{-3}) of (a) and (b) case RS-1, (c) and (d) RS-2, (e) and (f) RS-3 and (g) and (h) RS-4. The upper panel and lower panel show the results in T1 and T2, respectively. Here, $z^\dagger$ denotes distance to the mean water surface. Orientation of all plots is into the estuary.

i.e., only one maximum value is observed on the south side (Figure 4-10g and h). Comparing the results of these cases with those shown for RS (Figure 4-8e and f) reveals that the SSC maxima near the south sides of T1 and T2 are mainly due to the suspended sediment trapping by the lateral density gradient, while the second SSC maximum near the north side of T1 is caused by leakage.

Figure 4-11 shows the modelled transverse distribution of SSC of four different cases for neap tide condition. Comparing the results with those shown in case RN (Figure 4-9e and f) shows that all of the three mechanisms that are investigated in this model are important at T1, in which the Coriolis effect (RN-1) and the leakage (RN-3) cause sediment trapping near the north side while the density gradient (RN-2) pushes sediment to the south side. At T2, high SSC near the south side is mainly caused by the lateral density gradient (Figure 4-11d). Note that Coriolis effect causes an increase of SSC from the south side to the north side during neap tide (Figure 4-11a and b), which does not occur during spring tide (Figure 4-10a and b). When the lateral current is only driven by the density gradient (Figure 4-11c and d) or leakage (Figure 4-11e and f), the transverse distribution of SSC shows similar spatial patterns to those during spring tide (Figure 4-10c-f), but with smaller SSC values. Results of case RN-4 also show only one SSC maximum on the south side of the two cross-sections, but with values that are much smaller than those of RS-4 (Figure 4-10g and h).

Since the lateral distribution of SSC is induced by residual current, it is relevant to present the structure of each single current component. As is shown in (Figure 4-12a and b), during spring tide the residual current induced by Coriolis deflection of longitudinal current in the two cross-sections shows an anti-clockwise structure, whereas its magnitude is rather small. On the other hand, the density driven current shows a clockwise structure and is important in both T1 and T2 (Figure 4-12c and d). The residual current due to leakage is northward in the entire cross-section, however, it is only important in T1 (Figure 4-12e and f). During neap tide, the residual current components that are driven by these mechanisms show the same patterns as those during spring tide (not shown).

4.3.3 *Near bed SSC distribution in the estuary*

The magnitudes of Coriolis induced lateral current and density driven lateral current largely vary in the estuary, and thus changes in the trapping characteristics of SSC on the scale of the entire estuary are to be expected. Hence, it is interesting to present an overall picture of SSC distribution in the estuary. Figure 4-13a displays the near bed (at level $\sigma = -0.95$) SSC distribution for the RS case (spring tide). In this case, the two modelled cross-sections T1 and T2 are located in the core of the turbidity maximum. The zones where SSC is large are

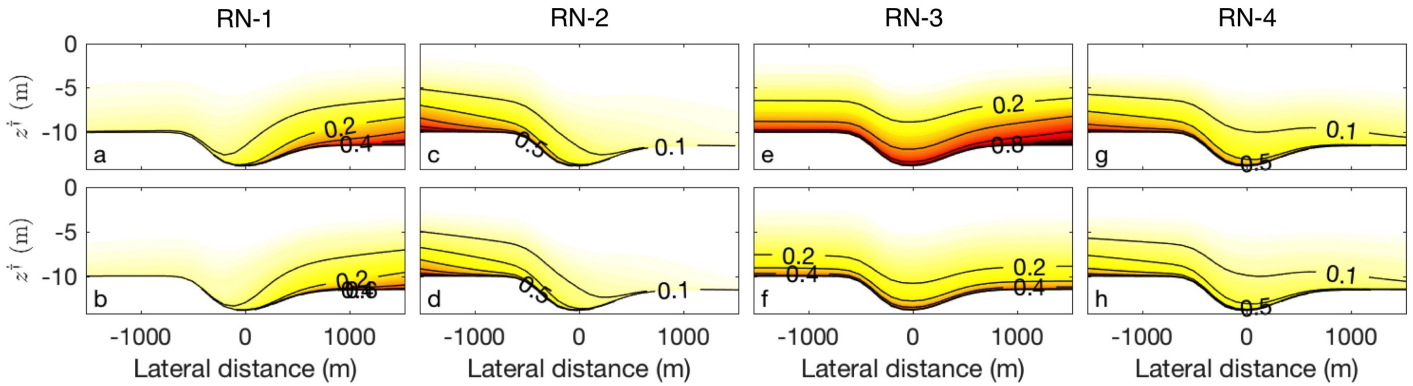

Figure 4-11: Transverse distribution of the residual SSC (in kg m^{-3}) of (a) and (b) case RN-1, (c) and (d) RN-2, (e) and (f) RN-3 and (g) and (h) RN-4. The upper panel and lower panel show the results in T1 and T2, respectively. Here, $z^\dagger$ denotes distance to the mean water surface. Orientation of all plots is into the estuary.

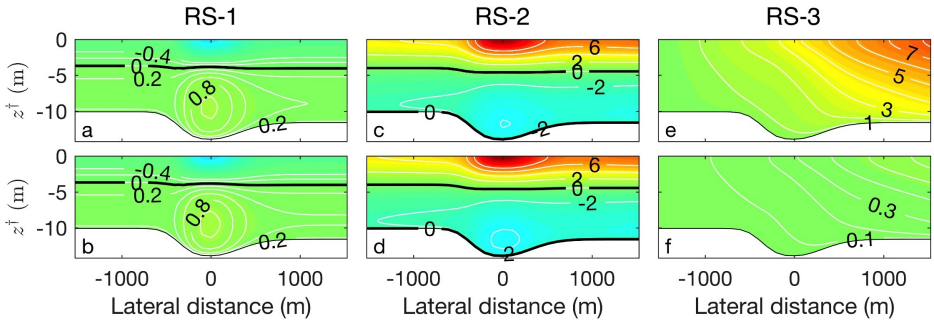

Figure 4-12: Transverse distribution of the residual current (in cm s^{-1}) in (a) and (b) RS-1, (c) and (d) RS-2 and (e) and (f) RS-3. The upper panel and lower panel show the results in T1 and T2, respectively. Here, $z^\dagger$ denotes distance to the mean water surface. Orientation of all plots is into the estuary.

found in the middle ($30-40$ km) and at the seaward boundary, respectively. This results from the joint action of down-estuary sediment transport by the river current and up-estuary sediment transport by the longitudinal density driven current, which has its largest value around 50 km. Moreover, note that in the middle of the estuary, two high SSC values do not appear at the same longitudinal location. The one near the north side is at 35 km and the one on the south side is at 40 km. This difference is attributed to the sediment distribution due to individual lateral current mechanisms. When the lateral current is only driven by Coriolis deflection of longitudinal current, the largest SSC is found at 35 km near the north side (Figure 4-13b), whereas if the residual current is only driven by density gradient, higher SSC values are found on the south side of the estuary with the maximum located at 40 km (Figure 4-13c). The sediment trapping caused by leakage also occurs at 35 km at the north side (Figure 4-13d). The results of case RS-4 (Figure 4-13e, Coriolis and density gradient are included, but no leakage) reveal that there is only one SSC maximum in all cross-sections. At the riverside, SSC has a higher value on the north side than on the south side. Towards the seaside, more sediment is trapped on the south side of the domain. In the lower reach, the value of SSC is larger near the south side than near the north side.

In the RN case (neap tide), Figure 4-13 shows that the cross-sections T1 and T2 are located downstream of the turbidity maximum. SSC values are high in the middle of the estuary, with local maxima near both lateral sides (Figure 4-13f). Moreover, Coriolis deflection induced lateral current causes sediment trapping at 30 km (Figure 4-13g), which is further up-estuary when compared with that in spring tide (Figure 4-13b). When the lateral residual current is driven

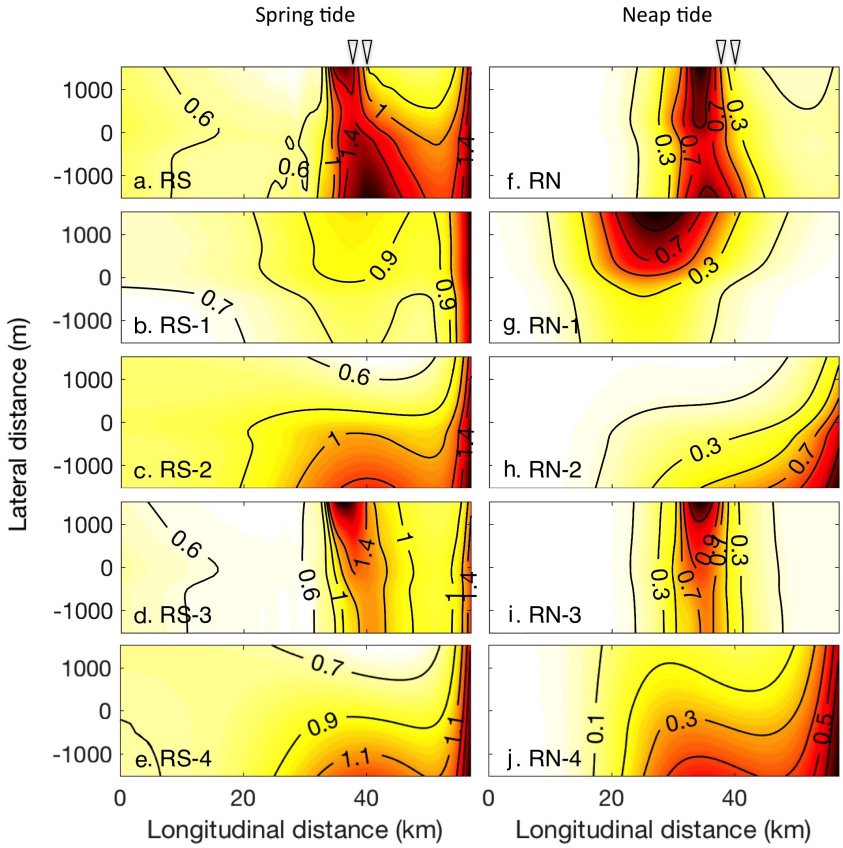

Figure 4-13: Near bed (level $\sigma = -0.95$) distribution of the residual SSC (in kg m^{-3}) in the estuary during spring tide (left column) and during neap tide (right column). Subplots a-e are the results of experiments RS, RS-1 (only Coriolis deflection), RS-2 (only lateral density gradients), RS-3 (only leakage) and RS-4 (Coriolis deflection and lateral density are included, but no leakage). The subplots f-j represent the SSC computed from RN, RN-1, 2, 3 and 4, respectively. The landside entrance (0 km) is located at the reference point (see Figure 4-1b). The triangles denote the locations of two modelled cross-sections T1 and T2.

by across-channel density gradients, the SSC maximum is located at the end of the estuary (Figure 4-13h). Figure 4-13i shows the distribution of SSC caused by the lateral current due to leakage, which is the same as that during spring tide. Finally, Figure 4-13j shows the modelled near bed surface SSC distribution for the case RN-4, which is similar to that during spring tide (RS-4).

4.4 DISCUSSION

4.4.1 *Model assumptions and their connection to field data*

The present study focuses on gaining fundamental understanding about longitudinal variations in the lateral trapping of sediment. Therefore, a highly idealised model has been designed that includes a minimum number of processes in order to explain gross aspects of observed residual velocity and turbidity characteristics in the North Passage, a branch of the Yangtze Estuary. The key processes in this model are sediment transport by river current, density driven current, leakage and by lateral current that results from Coriolis deflection of residual longitudinal current.

By construction, the model yields a simplified view on what happens in real estuaries. In particular with regard to the Yangtze Estuary, analysis of both field data (Li and Zhang, 1998; Jiang et al., 2013) and of numerical model output (Song and Wang, 2013) indicates that longitudinal trapping of sediment is not only due to gravitational circulation, as is the case in the present model. Other important processes are tidal pumping (i.e., net transport due to the correlation between tidal currents and tidally varying SSC), sediment transport by Stokes return current and transport by residual current that results from tidal straining. Other studies also point at the importance of wind (North et al., 2004), stirring of sediment by wind waves at the intertidal areas (Green, 2011) and flocculation processes (Winterwerp et al., 2013). Note that in the present model, flocculation is only considered in a simple way, by using different values of settling velocity during spring tide and neap tide.

The presence of Stokes return current is evident from Figure 4-4, which shows the observed structure of longitudinal residual current at the two transects. During spring tide the Stokes return current is larger than during neap tide, because it scales quadratically with the tidal amplitude (Ianniello, 1977). This explains why the observed discharge through the cross-sections was larger during spring than during neap tide, albeit the river discharge was almost the same at those times.

The reasons to ignore processes in the model other than those included are twofold. First, earlier subtidal models have proven to be remarkably successful in explaining observed amplitudes of the estuarine circulation (Scully et al., 2009) and of lateral and longitudinal distribution of SSC (Huijts et al., 2006; Talke et al., 2009b). The present study further supports the success of subtidal models. Second, adding new processes has to be done with extreme care, as some of them lead to seaward sediment transport (such as Stokes return current), whereas others result in landward sediment transport (e.g., residual current due to tidal straining, see Burchard et al. (2013)) and they partially cancel.

There are three other aspects that deserve discussion. First, the observed SSC maxima in the deep channel of the two transects (Figure 4-2), especially those during the neap tide, are not captured by the model. This is attributed to the fact that in reality, the channel in the North Passage of the Yangtze Estuary is deep and narrow (compared to the cross-sectional mean depth and width, see Figure 4-1). The vigorous tidal currents in the channel stir sediment from the bottom, but the steep slopes prevent the sediment to be laterally distributed. Mimicking that situation in the model is not possible, given the assumptions that nonlinear terms are small (in fact, they scale with the bottom slope), the lateral density gradient is uniform and that sediment transport does not contain a component that is directly forced by bottom slopes.

Second, the assumption that the bottom profile is uniform in the longitudinal direction limits a straightforward application of the present model to estuaries that have strong longitudinal variations in depth, e.g., the Hudson River Estuary (see Figure 1 of Geyer et al. (2001)). Depth variations in both lateral and longitudinal direction will result in much more complicated residual current phenomena (Monismith et al., 2002; Valle-Levinson et al., 2003). For future research, it would be interesting to investigate lateral trapping of sediment at different longitudinal locations in more tidal estuaries.

Third, the depth-integrated net water transport obtained from field data evidently shows a northward directed component at two sampled transects (see the supplementary material S.3.4 for details). Note that lateral eddies created by groins that are orthogonal to the channel banks may also contribute to observed leakage. As shown by Ge et al. (2012), these eddies mainly occur in the area between the training walls and the regulation lines. More data at different along channel positions are needed to quantify the possible contribution of these eddies to leakage.

Moreover, Eq. 4-6 describes that the water and sediment leaking through the north side in the curved part of the channel is uniformly returned to the channel in the rest of the domain. Compensation for leakage may take place in a different way, and that might affect model results in the straight segment of the estuary. The sensitivity of model results to the way how leakage compensation at lateral boundaries was tested, for the settings of RS and RN, respectively. In these two experiments, water loss due to leakage was compensated by inflow through the south bank. Results (S.3.5) show that SSC distributions are slightly changed when comparing with those in default cases (Figure 4-13a and f). Furthermore, the impact of the formulation for leakage on model results was investigated. The relation between the longitudinal distribution of leakage and channel curvature was generalised as

$$f(x) = \begin{cases} \frac{1}{R^n} - \frac{1}{L}\int_{x_1}^{x_2} \frac{1}{R^n} dx, & x_1 \leqslant x \leqslant x_2, \\ -\frac{1}{L}\int_{x_1}^{x_2} \frac{1}{R^n} dx, & 0 \leqslant x \leqslant x_1 \ , \ x_2 \leqslant x \leqslant L, \end{cases} \tag{4-25}$$

in which parameter $n > 0$. When $n = 1$, Eq. 4-25 boils down to Eq. 4-6. The near bed sediment distribution was modelled by using the settings of RS, but for $n = 0.5$ and 2 in Eq. 4-25, respectively. Results of these new experiments reveal that the parameterisation of leakage has some local effect on the SSC distribution near the curved segment of the channel, but it does not affect the overall findings presented in the previous sections (see in S.3.5).

4.4.2 *Interpretation of model results*

The model results confirm the hypothesis that the different trapping locations of SSC in the estuary result from the variable intensities of lateral current components at different longitudinal locations. The occurrence of the SSC maxima near the south side of both T1 and T2 is due to the lateral density gradient, while the second SSC maximum near the north side of T1 is due to leakage. Coriolis deflection of longitudinal residual current also causes trapping of sediment near the north side, but in T1 and T2 it is small compared to the former current components, both during spring and neap tide. Thus, the difference in lateral pattern of sediment distribution between T1 and T2 is mainly due to the difference in leakage. From Figure 4-13 it appears that at other locations in the estuary, different processes are responsible for lateral trapping of sediment. This is because the magnitude of Coriolis induced lateral current and density driven lateral current vary on the scale of the entire estuary. As is shown in Figure 4-13a and f, in the upper reach of the estuary, the lateral current related to Coriolis effects (that causes sediment trapping at the north side, see Figure 4-13b and g) becomes more important than that driven by the density gradients (that causes sediment trapping on the south side, see Figure 4-13c and h). As a result, SSC tends to be distributed more uniformly in the lateral direction or becomes slightly larger near the north side. In the lower reach of the estuary, where the density gradients are strong, higher SSC values are obtained near the south side (Figure 4-13e and j).

The difference in longitudinal locations of SSC maxima at spring and neap tide induced by different current components (see Figure 4-13) is due to the fact that turbulence during spring is more intense than during neap. When the lateral current is driven by only Coriolis deflection, sediment is trapped near the north side, where during spring tide the longitudinal residual current is mostly seaward (Figure 4-8a and b). During neap tide, this lateral current is intensified because it experiences less turbulent friction. Moreover, the lower

intensity of turbulence causes the larger SSC to be closer to the bed, hence more sediment is trapped near the north side. Meanwhile, at that time longitudinal current (Figure 4-9a and b) is landward near the bottom, causing sediment to be moved up-estuary and thus a landward shift of the SSC maximum occurs. When the lateral current is driven by the lateral density gradient, intensified residual current at neap tide (compared to spring tide) causes entrapment of sediment near the south side, which subsequently results in a seaward shift of the location of the SSC maximum.

4.4.3 *Sensitivity of results to values of model parameters*

To test the sensitivity of the SSC distribution to the choice of the scaled surface eddy viscosity A_s (see section 4.2.2.4), extra experiments were performed for the setting of RS and RN, respectively. A constant $A_s = 0.005$ was imposed, which was obtained by taking cross-sectional mean of A_s that was used in RS and RN. The transverse distribution of the longitudinal residual current for a constant A_s (Figure 4-8) shows that the maximum seaward current is found at the surface above the two shoals instead of at the surface above the deep channel. However, the overall distribution of SSC hardly changes with respect to that of RS and RN, respectively (see Electronic Supplement S5 for details).

The sensitivity of model results to the choice of q_{sed}, Q_{sed} and the formulation of leakage was also tested (figures are presented in Electronic Supplement S5). Two experiments were conducted with the setting of RS, except for $q_{sed} = 0.05$ kg s^{-1} m^{-1} and $q_{sed} = 0.2$ kg s^{-1} m^{-1}, respectively. It turns out that the SSC maxima near the north side increase with smaller q_{sed} and decrease with larger q_{sed}. These results suggest that the appearance of the maximum SSC values at this side is due to the competition between the accumulation of sediment by water leakage and the loss of sediment by its transport through the boundary.

The effect of varying Q_{sed} on the distribution of SSC was investigated by running the model with the setting of RS, but for two more different values of Q_{sed}, viz. 700 kg s^{-1} and 900 kg s^{-1}, respectively. It appears that the different choices of Q_{sed} only quantitatively change the longitudinal distribution of sediment. As Q_{sed} increases, the location of SSC maximum slightly moves up-estuary, whereas for a smaller Q_{sed}, the location of SSC maximum moves down-estuary and more sediment piles up at the seaward boundary.

4.5 CONCLUSIONS

A new three-dimensional exploratory model has been derived and analysed with the objective to gain fundamental understanding of the physics of sedi-

ment transport and the presence of turbidity maxima in tidal estuaries. It has been demonstrated that the model is able to capture the main features of the observed SSC distribution in two different cross-sections in the North Passage of the Yangtze Estuary during spring and neap tide. In one cross-section (T1), two high values of SSC occur near both south and north sides, while in the cross-section 2 km downstream (T2) only one near the south side was found. Analysis of model results has revealed that the occurrence of the SSC maxima near the south side of both T1 and T2 is due to sediment entrapment by lateral density gradients, while the second SSC maximum near the north side of T1 is due to sediment transport by leakage. Coriolis deflection of longitudinal current also causes trapping of sediment near the north side, but with less intensity than that of the lateral density driven current during both spring and neap tide.

Further study of the SSC on the scale of the entire estuary has demonstrated the lateral trapping of sediment depending on intensities of lateral current due to Coriolis, density gradients and curvature induced leakage. In the upper reach, where Coriolis deflection of longitudinal current is important with respect to the lateral density driven current, sediment is more uniformly distributed in the lateral direction or trapped near the north side. In the lower reach lateral density driven current is the largest and more sediment is found near the south side. The location of SSC maxima due to the residual current that induced by leakage remains at the same location, i.e., the position where the radius of the channel curvature attains the minimum, in both spring and neap tide. In the case without leakage, there is only one SSC maximum in the lateral direction at all longitudinal locations. It occurs on the north side in the upper reach. Further seaward, more sediment is found on the south side of the cross-section.

4.A APPENDIX

4.A.1 *Iterative method to construct approximate solutions for* $\hat{c}$

Eq. 4-14 is rewritten in terms of a scaled reference concentration $\alpha = \hat{c}/c_b$ and a formal ordering parameter $\epsilon\ (=1)$ is introduced, this yields

$$\epsilon\frac{\partial}{\partial x}(\underbrace{I_1\alpha + I_2\frac{\partial\alpha}{\partial x}}_{T_x}) + \frac{\partial}{\partial y}(\underbrace{I_3\alpha + I_4\frac{\partial\alpha}{\partial y}}_{T_y}) = 0, \tag{4.A.1}$$

with boundary conditions

$$\begin{aligned} &T_y = 0 \quad \text{at} \quad y = -B, \quad \text{and} \quad T_y = \epsilon q_{sed} f(x) \quad \text{at} \quad y = B, \\ &\int_{-B}^{B} T_x\,dy = Q_{sed} \quad \text{at} \quad x = 0, \quad \frac{1}{2BL}\int_{-B}^{B}\int_{0}^{L} \alpha\,dxdy = 1. \end{aligned} \tag{4.A.2}$$

The solution for α and the transport of sediment in the x and y direction are written as formal series in parameter $\epsilon(=1)$, i.e.

$$\begin{aligned} \alpha &= \epsilon^0\alpha_0 + \epsilon^1\alpha_1 + \epsilon^2\alpha_2 + ..., \\ T_x &= \epsilon^0 T_{x,0} + \epsilon^1 T_{x,1} + \epsilon^2 T_{x,2} + ..., \\ T_y &= \epsilon^0 T_{y,0} + \epsilon^1 T_{y,1} + \epsilon^2 T_{y,2} + ... \end{aligned} \tag{4.A.3}$$

in which the superscript/subscript $n = 0, 1, 2, ...$ denotes the iteration step. Substituting Eq. 4.A.3 into 4.A.1 and 4.A.2, then collecting terms with equal order of ϵ^n yields the equations at different iteration steps.

At the initial step ($n = 0$),

$$\frac{\partial}{\partial y}T_{y,0} = 0 \quad \text{with} \quad T_{y,0} = 0 \quad \text{at } y = \pm B \quad \text{for all } x, \tag{4.A.4a}$$

$$\frac{1}{2BL}\int_{0}^{L}\int_{-B}^{B} \alpha_0\,dxdy = 1. \tag{4.A.4b}$$

The solution reads

$$\alpha_0 = \hat{\alpha}_0(x)F_y, \quad F_y = \exp\left[-\int_{-B}^{y} I_3(\tilde{y})/I_4(\tilde{y})d\tilde{y}\right]. \tag{4.A.5}$$

Note that F_y depends on x and y. The integration coefficient $\hat{\alpha}_0(x)$ is determined by analysing Eq. 4.A.1 at the next iteration step ($n = 1$):

$$\frac{\partial}{\partial x}T_{x,0} + \frac{\partial}{\partial y}T_{y,1} = 0, \tag{4.A.6}$$

with boundary conditions

$$\begin{aligned} &T_{y,1} = 0 \quad \text{at} \quad y = -B, \quad \text{and} \quad T_{y,1} = q_{sed} f(x) \quad \text{at} \quad y = B, \\ &\int_{-B}^{B} T_{x,0}\,dy = Q_{sed} \quad \text{at} \quad x = 0, \quad \frac{1}{2BL}\int_{-B}^{B}\int_{0}^{L} \alpha_1 \; dxdy = 0. \end{aligned} \tag{4.A.7}$$

Integrating Eq. 4.A.6 over the lateral direction and using the boundary conditions at the lateral sides and then from the riverside boundary down-estuary yields

$$\int_{-B}^{B}\left(I_1\alpha_0 + I_2\frac{\partial\alpha_0}{\partial x}\right)dy = G(x) \tag{4.A.8}$$

with $G(x) = Q_{sed} - q_{sed}\int_0^x f(\tilde{x})d\tilde{x}$. Substitution of Eq. 4.A.5 into Eq. 4.A.8 yields

$$\frac{\partial\hat{\alpha}_0}{\partial x}\Gamma_a + \hat{\alpha}_0\Gamma_b = G(x), \tag{4.A.9}$$

in which, $\Gamma_a = \int_{-B}^{B} I_2 F_y dy$ and $\Gamma_b = \int_{-B}^{B}\left(I_1 F_y + I_2\frac{\partial F_y}{\partial x}\right)dy$ are functions of x. The solution for Eq. 4.A.9 reads

$$\begin{aligned} &\hat{\alpha}_0 = (\gamma_0 + \gamma_c)F_x, \quad F_x = \exp\left[-\int_0^x \Gamma_b/\Gamma_a d\tilde{x}\right], \\ &\gamma_c = \int_0^x \frac{G(x')}{\Gamma_a(x')}\exp\left[\int_0^{x'}\Gamma_b/\Gamma_a d\tilde{x}\right]dx'. \end{aligned} \tag{4.A.10}$$

Thus, α is subject to an unknown integration constant γ_0, which is determined by using the constraint Eq. 4.A.4b. The result is

$$\gamma_0 = \frac{2BL - \int_0^L\int_{-B}^{B}\gamma_c F_x F_y}{\int_0^L\int_{-B}^{B} F_x F_y\,dydx}. \tag{4.A.11}$$

If the iteration is truncated at the initial step, one error made at this stage is $\partial T_{x,0}/\partial x$. The equations for $n \geqslant 2$ read:

$$\frac{\partial}{\partial x}T_{x,n-1}+\frac{\partial}{\partial y}T_{y,n}=0, \tag{4.A.12}$$

with boundary conditions

$$\begin{aligned} &T_{y,n}=0 \quad \text{at} \quad y=-B, \quad \text{and} \quad T_{y,n}=0 \quad \text{at} \quad y=B,\\ &\int_{-B}^{B}T_{x,n-1}\,dy=0 \quad \text{at} \quad x=0, \quad \frac{1}{2BL}\int_{-B}^{B}\int_{0}^{L}\alpha_n\,dxdy=0. \end{aligned} \tag{4.A.13}$$

By integrating Eq. 4.A.12 from $y=-B$ to y and using the boundary condition that there is no sediment across the south side ($y=-B$), the solution reads

$$\alpha_n=\hat{\alpha}_n(x)F_y+\underbrace{F_y\int_{-B}^{y}\frac{-\frac{\partial}{\partial x}\int_{-B}^{y'}T_{x,n-1}\,d\tilde{y}}{I_4(y')}\exp\left[\int_{-B}^{y'}I_3/I_4\,d\tilde{y}\right]dy'}_{F_n}. \tag{4.A.14}$$

In Eq. 4.A.14, the unknown function $\hat{\alpha}_n(x)$ is found as follows: First, substituting Eq. 4.A.14 into Eq. 4.A.12 but for $n+1$. Second, integrating the obtained equation from $-B$ to B and then from $x=0$ to x and using the corresponding constraints in Eq. 4.A.13. The solution reads

$$\hat{\alpha}_n=(\gamma_n+\underbrace{\int_0^x\frac{-\Gamma_n(x')}{\Gamma_a(x')}\exp\left[\int_0^{x'}\Gamma_b/\Gamma_a\,d\tilde{x}\right]dx'}_{\gamma_d})F_x, \tag{4.A.15}$$

in which $\Gamma_n=\int_{-B}^{B}\left(I_1F_n+I_2\frac{\partial F_n}{\partial x}\right)dy$. Finally, the unknown constant γ_n is determined by using the last constraint of Eq. 4.A.13. The result is

$$\gamma_n=\frac{-\int_0^L\int_{-B}^{B}(\gamma_dF_xF_y+F_n)\,dydx}{\int_0^L\int_{-B}^{B}F_xF_y\,dydx}. \tag{4.A.16}$$

The change between two iteration steps is defined as $\xi=\frac{\left[\sum_{i=0}^{n-1}\alpha_i\right]_{max}}{\left[\sum_{i=0}^{n}\alpha_i\right]_{max}}$. The iterative process is terminated when $\xi\leqslant 0.1$.

5

SUMMARY AND OUTLOOK

This study provided new insight into several aspects of the dynamics of tidal currents, residual currents and sediment trapping in estuaries with different stratification conditions. The main findings and answers to the research questions (see chapter 1) are summarised in section 5.1. Each subsection covers one of the three research questions. In section 5.2, suggestions for further research are given.

5.1 MAIN FINDINGS

5.1.1 *Effect of tidal mean density stratification on the vertical structure of the tidal current amplitude*

The second chapter examined the link between tidal mean density stratification, which sets the spatial structure of the tidal mean vertical eddy viscosity, and the vertical distribution of the current amplitude of principal tidal harmonics in estuaries and coastal seas (research question 1 in chapter 1). A specific objective was to explain pronounced surface maxima (surface jumps) and subsurface maxima (subsurface jets) in the vertical profiles of observed tidal current amplitudes. For this, a semi-analytical model was designed and analysed.

As is illustrated in Figure 5-1, results show three types of tidal current amplitude profiles. For well-mixed conditions, eddy viscosity has a parabolic distribution with its maximum in the middle of the water column. In this case, the current amplitude has a logarithmic distribution over the vertical. For weakly stratified conditions and the same tidal forcing, the maximum eddy viscosity is smaller than that in well-mixed conditions and it occurs closer to the bottom. In this case, the vertical structure of the current amplitude is logarithmic in a thin layer close to the bottom. Outside this layer, the current amplitude shows a "surface jump", i.e. the value of current amplitude increases faster than in the logarithmic layer. For highly stratified conditions, the maximum eddy viscosity becomes even less and its location is even closer to the bottom. Above this thin

bottom boundary layer, the current amplitude shows a "subsurface jet", with a maximum value obtained below the surface.

Analysis of the model revealed the physics that causes the presence of surface jumps and subsurface jets. The jumps occur for moderate stratification conditions, in which the maximum eddy viscosity inside the water column is strong enough so that near the surface the generation of the vertical shear of tidal currents by the curvature of eddy viscosity overcomes the decay of the vertical shear of tidal currents by turbulent exchange processes. Meanwhile, a near-surface pycnocline (in which vertical density gradients are large) is present, in which the tidal shear is enhanced and then shear decreases toward the surface more quickly than what would otherwise follow from the law of the wall. Subsurface jets occur because in highly stratified conditions turbulent vertical exchange of horizontal momentum only takes place in the bottom boundary layer, thereby causing an exponentially decaying oscillatory vertical structure of the tidal current amplitude with increasing height above the bottom.

5.1.2 *Effect of longitudinal bottom slopes, intensity of tidal forcing and mixed tidal forcing on the spatial structure of ESCO current*

Chapter 3 investigated the dynamics of the residual currents in narrow straight estuaries that are induced by the covariance between tidally varying eddy viscosity and vertical shear of tidal currents (Eddy viscosity-Shear COvariance, i.e., ESCO) (research questions 2a, b and c in chapter 1). For this, experiments with a numerical model study were conducted and the total ESCO current was decomposed into terms that are induced by individual tidal constituents.

The ESCO current is important for the estuarine circulation in periodically to weakly stratified estuaries and it is small in highly stratified estuaries. As is sketched in Figure 5-2a-c, in the case of forcing by a semi-diurnal tide at the open sea, two main contributors to the ESCO current are the components due to the semi-diurnal tide and quarter-diurnal tide. For periodically and weakly stratified estuaries, the former is dominant in the middle reach, while the latter dominates in the upper reach. In highly stratified estuaries, the ESCO current is mainly due to the component related to the semi-diurnal tide.

Depending on the degree of stratification and the longitudinal position in the estuary, the ESCO current due to the semi-diurnal tide has either a two-layer, three-layer or reversed two-layer structure. The two-layer structure is generated by tidal straining, while the reversed two-layer structure is caused by tidal asymmetry in the friction velocity (that determines eddy viscosity) due to the joint action of tidal currents and residual currents. The ESCO current due to the quarter-diurnal tide mainly shows a two-layer structure. The quarter-

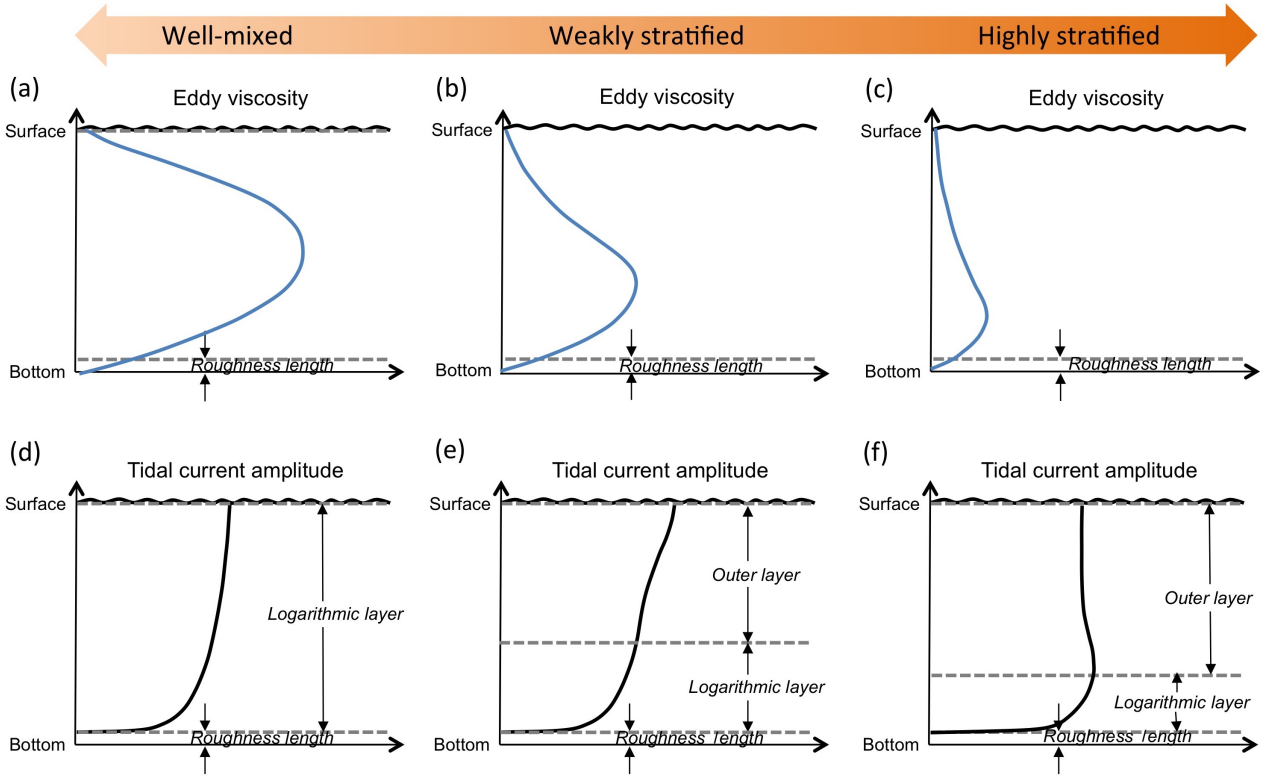

Figure 5-1: Examples of eddy viscosity profiles in (a) well-mixed, (b) weakly stratified and (c) highly stratified conditions. Panels (d), (e) and (f) show modelled profiles of the M_2 tidal current amplitude. For well-mixed conditions, the profile is logarithmic. If stratification is weak, the profile contains a "surface jump" and for highly stratified conditions, the profile shows a "subsurface jet".

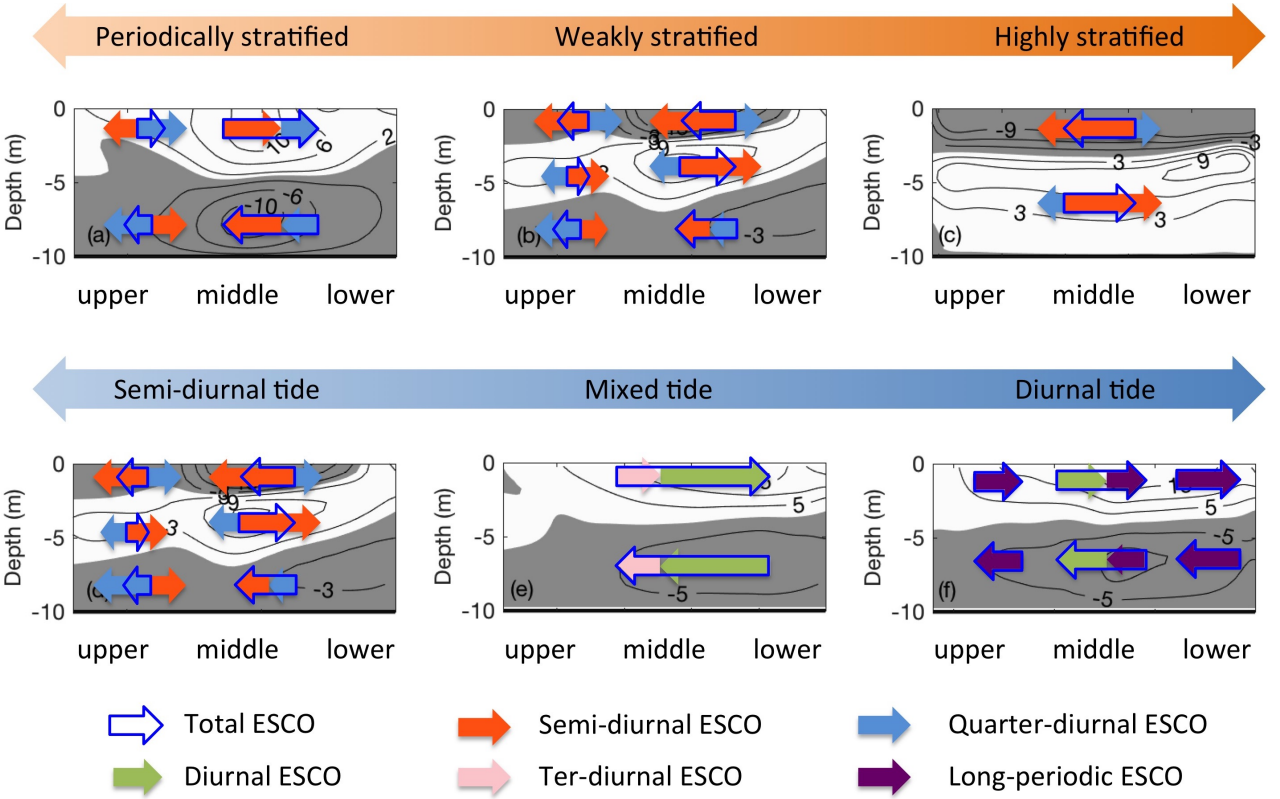

Figure 5-2: Spatial structure of the total ESCO current in a (a) periodically stratified, (b) weakly stratified and (c) highly stratified estuary in which the tidal current is forced by a semi-diurnal tide. Panels (d)-(f) are as (a)-(c), but for a weakly stratified estuary that is forced by (d) a semi-diurnal tide (e) a semi-diurnal tide and two diurnal tides and (f) two diurnal tides. Positive values (white areas) denote seaward and negative values (grey areas) denote landward currents. Directions and relative importance of the ESCO current due to individual tidal harmonics with respect to the total ESCO current are sketched with arrows in different colours.

diurnal eddy viscosity is mainly due to the time-dependent friction velocity, whilst the quarter-diurnal tidal shear is determined by nonlinear processes.

In case that the external tidal forcing is mixed, i.e., it contains a semi-diurnal tide and two diurnal tides (see Figure 5-2e), it turns out that main components that constitute the ESCO current are those due to diurnal tides and ter-diurnal tides. Both of the two components have a two-layer structure, but the former component is dominant. If tidal forcing is predominantly diurnal (Figure 5-2f), the ESCO current induced by the long-periodic tide yields the largest contribution to the total ESCO current in the upper and lower reach of the estuary.

5.1.3 *Longitudinal variation in lateral trapping of fine sediment and its dependence on density stratification*

In chapter 4, mechanisms were investigated that cause lateral trapping of suspended sediment at different longitudinal locations for different stratification conditions (research questions 3a and b in chapter 1). For this, field data collected at two cross-sections in the North Passage of the Yangtze Estuary (see Figure 5-3) were analysed. Note that part of the North Passage is curved. The analysis revealed that at one cross-section two high values of suspended sediment concentration (SSC) occur close to the south and north side, while at a cross-section 2 km down-estuary only one SSC maximum on the south side is present. This pattern is found during both spring tide and neap tide, which are characterised by different stratification conditions and different intensities of turbulence. To understand the observed phenomena, a new three-dimensional exploratory model was derived and analysed.

As is sketched in Figure 5-3 for spring tide conditions, in the cross-section closest to the channel curve the clockwise residual current (when looking into the estuary) due to lateral density gradient transports sediment to the south side, which results in a local SSC maximum. On the other side of the cross-section, a second SSC maximum occurs because of sediment transport by the northward residual current due to water leakage.

In the cross-section 2 km seaward from the first cross-section, the residual current due to the lateral density gradient still causes high SSC on the south side, whilst that due to leakage is weak and no high value of SSC occurs on the north side. Coriolis deflection of longitudinal current also causes trapping of sediment near the north side, but at the location of the two cross sections its contribution is weak. However, it is important in the upper estuary, where the lateral density current is weak.

During neap tide, as eddy viscosity becomes smaller compared to that during spring tide, due to stratification induced suppression of turbulence, residual currents are intensified. However, still lateral currents due to lateral density

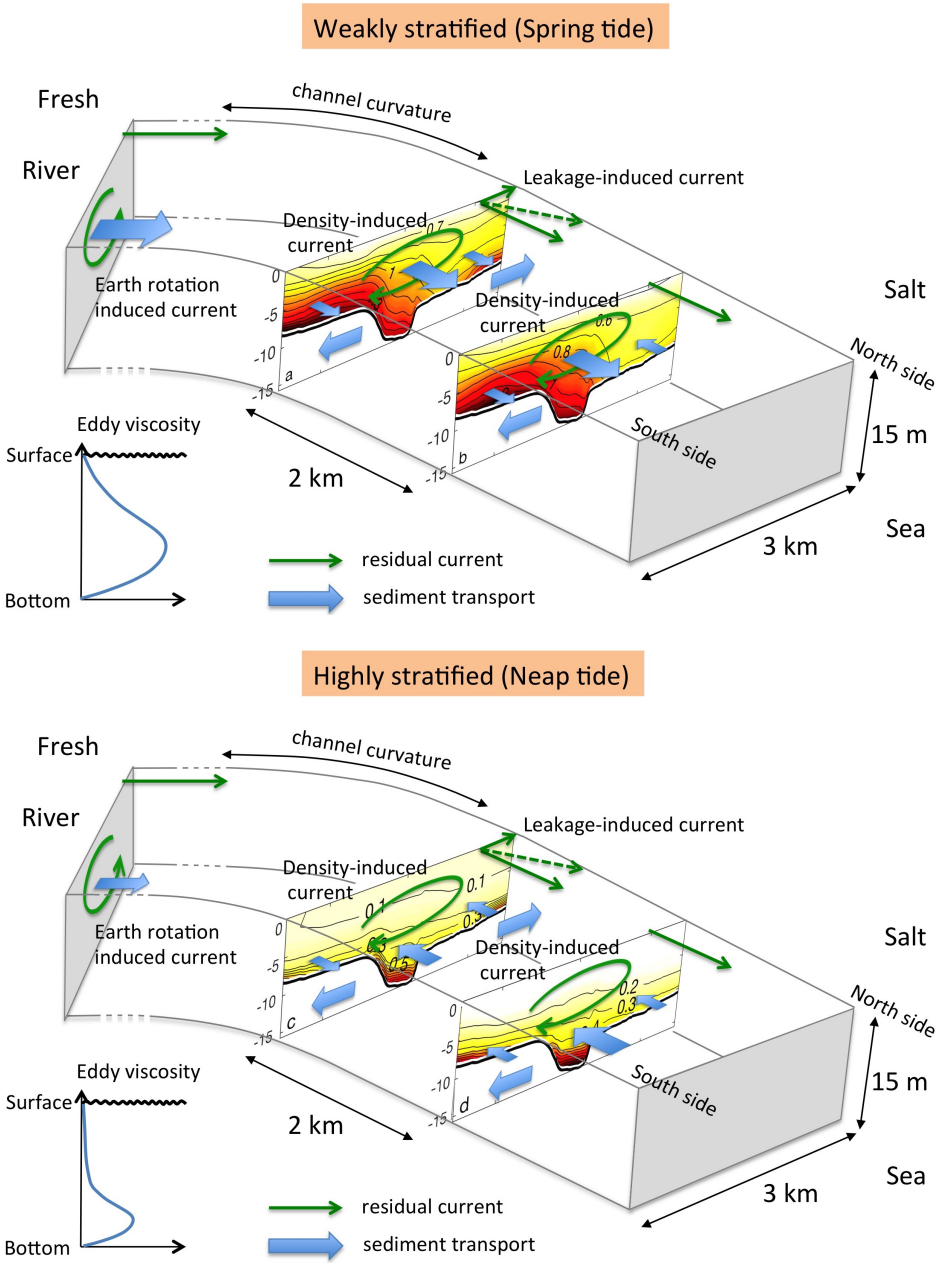

Figure 5-3: Sketch of the curved segment of the Yangtze Estuary and observed SSC at two cross-sections for weakly stratified (spring tide) and highly stratified (neap tide) conditions. The modelled tidally averaged eddy viscosity at spring and neap are presented as functions of depth. At each cross-section, the modelled residual current components are denoted by green arrows, and residual sediment transports (both in longitudinal and lateral direction) are represented by blue arrows.

gradient and leakage are dominant. A high SSC zone is observed on the south side of the two cross-sections. In the cross-section closer to the curve, the leakage induced current still causes the second SSC maximum on the north side.

5.2 OUTLOOK

5.2.1 *Tidal current amplitude*

In chapter 2, a new formulation of vertical eddy viscosity was applied, in which the friction velocity was obtained by linearising the bottom friction (Lorentz, 1922) at a fixed location and prescribed tidal forcing. The vertical structure of tidal current amplitudes also varies in the longitudinal and lateral direction (see Figurere 1-4, chapter 1). For a future study, it would be interesting to extend the current 1D column model to a cross-sectional 2D model. In that case, depth variations in the lateral direction could be included and the iteration process (as was explained in chapter 2) would be such that the modified bottom shear stress gives the same energy dissipation rate as the domain-averaged nonlinear bottom stress over a tidal period. It would also be interesting to investigate vertical profiles of other tidal components and of residual currents for different stratification conditions.

5.2.2 *ESCO mechanisms*

Chapter 3 focused on the longitudinal dynamics of the ESCO current. Lateral currents in the model were small, because the estuary was narrow and had no lateral variations in depth. In natural estuaries, lateral currents are not negligible and they affect the turbulence characteristics (e.g. by lateral tidal straining) and thereby the longitudinal ESCO. Moreover, the ESCO of the lateral tidal current may contribute to the secondary circulation. Cheng (2014) has examined the structure of the ESCO current in the middle reach of a straight estuary that has a triangle lateral bottom profile. For a further study, it would be interesting to investigate the full spatial structure of the ESCO current in a 3D domain. As a first step, simple lateral bottom profiles and the Coriolis effect due to earth rotation could be included.

Regarding ESCO currents driven by mixed tidal forcing, in chapter 3 it was assumed that the latter contains one semi-diurnal tide and two diurnal tides. It would be more realistic to include in a future study other constituents (in particular the semi-diurnal solar tide S_2 and the diurnal lunar tide P_1). For instance, adding S_2 will not only result in the ESCO current due to that tidal harmonic, but also together with M_2 will create a spring-neap cycle, besides the one due to two diurnal tides as was discussed in that chapter. Taking these

harmonics into account contribute to a better understanding of ESCO current and will facilitate comparison of modelled and observed residual currents for estuaries with mixed tides conditions.

The system considered in chapter 3 was analysed for tidal amplitudes that are small compared to water depth. However, in many estuaries, e.g. the Qiantang River Estuary (in Hangzhou Bay) and the Gironde estuary, tidal amplitudes that are comparable to the mean water depth. This implies highly nonlinear dynamics and thus the structure of the ESCO forcing becomes much more complicated. The role of nonlinear processes on the ESCO current could be studied systematically by increasing the intensity of tidal forcing, and/or reducing the depth, using a cross-sectional model, following the set-up used in Burchard et al. (e.g. 2011) and Schulz et al. (2015).

5.2.3 *Sediment trapping mechanisms*

The new semi-analytical model derived in chapter 4 has provided insight into how various physical processes affect the lateral distribution of sediment. There are however several more processes which also influence the trapping of sediment and they deserve attention in further research. For example, the model does not explicitly account for tides, apart from setting eddy viscosity, eddy diffusivity, and erosion parameters. Consequently, it ignores the sediment transport by the tide-induced residual currents, which result e.g. from nonlinear advection of tidal momentum and ESCO forcing (as studied in chapter 3). Also tidal pumping, i.e. the net sediment transport due to covariance between tidal currents and the tidally varying sediment concentration, is not considered. Several studies have demonstrated the importance of these processes on sediment trapping (Chernetsky et al., 2010; Song and Wang, 2013; Kumar et al., 2017). In a further study, it would be interesting to investigate how these processes affect sediment dynamics in estuaries with different stratification conditions.

Furthermore, chapter 3 has demonstrated that covariance between tidally varying eddy viscosity and tidal current shear (ESCO) result in residual currents. Likewise, covariance between temporally varying eddy diffusivity and the temporally varying vertical gradient of SSC would affect the residual sediment dynamics. This would also be an important topic for further consideration.

S

SUPPLEMENTARY INFORMATION

S.1 SUPPLEMENTARY MATERIAL FOR CHAPTER 2

S.1.1 *Numerical solutions of Eq. 2-1 to 2-9 of chapter 2 for different values of parameter "n"*

Eq. 2-1 to 2-9 of chapter 2 can be solved numerically for any positive value of parameter n. In this document, four cases $n = 0.5, 1, 1.5$ and 3 in Eq. 2-7 of chapter 2 are considered to show the dependence of vertical profiles of tidal current amplitude on the values of parameter n. Other parameter values are as in Table 2-1 of chapter 2. In Figure S1-1a, vertical profiles of eddy viscosity A_σ, as defined by Eq. 2-7 of chapter 2, are shown for $n = 0.5$ and different values of σ_p. The corresponding vertical profiles of the tidal current amplitude are shown in Figure S1-1b. Clearly, no SJ-I is observed in these results. The same conclusion applies to the case that $n = 1$ (results of Figure S1-1c,d). Note that if $n = 1$, the tidal current amplitude increases linearly to the water surface in the upper layer. However, in case that $n = 1.5$ (Figure S1-1e) the tidal current amplitude for $\sigma_p = -0.27$ shows a surface jump (Figure S1-1f). If $n = 3$, for the same value of $\sigma_p = -0.27$, the surface jump phenomenon in the tidal current amplitude is significantly enhanced.

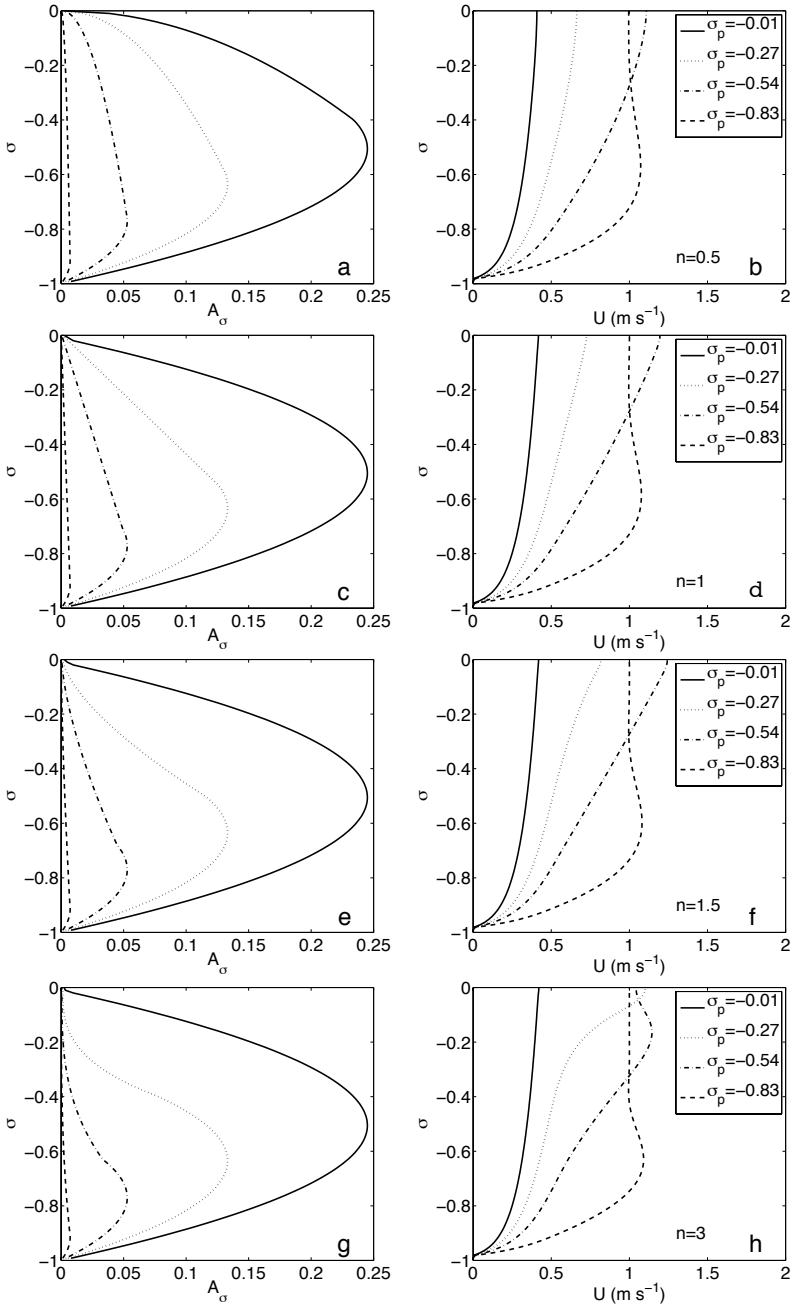

Figure S1-1: a. Vertical distribution of eddy viscosity A_σ for $n = 0.5$ and different values of σ_p. Other parameter values as in Table 2-1 of chapter 2. b. Vertical profiles of tidal current amplitude for $n = 0.5$ and different values of σ_p. Panels c and d: as panels a and b, bur for $n = 1$. Panels e and f: as panels a and b, but for $n = 1.5$. Panels g and h: as panels a and b, but for $n = 3$.

S.1.2 *Advection terms as drivers of SJ-I/II in the vertical profile of the amplitude of a single tidal constituent*

In this electronic supplement it is shown how advection terms can potentially result in SJ-I/II phenomena. Harmonic decomposition of tidal current yields

$$\Psi = \overline{\Psi} + \Psi_{M_2} + \Psi_{M_4} + ..., \tag{S1-1}$$

with Ψ representing any of the tidal current components u, v and w. Here, $\overline{\Psi}$ is the residual current, Ψ_{M_2} the semi-diurnal tide (M_2), Ψ_{M_4} the quarter-diurnal tide (M_4), etc. The advection terms that (in principle) appear at the left hand side of Eq. 2-1 of chapter 2 are

$$R = u\frac{\partial u}{\partial x} + v\frac{\partial u}{\partial y} + \frac{w}{h}\frac{\partial u}{\partial \sigma}. \tag{S1-2}$$

Substitution of Eq. S1-1 into Eq. S1-2 and subsequent collection of only M_2 tidal constituents yields

$$R_{M_2} = \underbrace{\overline{u}\frac{\partial u_{M_2}}{\partial x}}_{T_1} + \underbrace{u_{M_2}\frac{\partial \overline{u}}{\partial x}}_{T_2} + \underbrace{\overline{v}\frac{\partial u_{M_2}}{\partial y}}_{T_3} + \underbrace{v_{M_2}\frac{\partial \overline{u}}{\partial y}}_{T_4} + \underbrace{\frac{\overline{w}}{h}\frac{\partial u_{M_2}}{\partial \sigma}}_{T_5} + \underbrace{\frac{w_{M_2}}{h}\frac{\partial \overline{u}}{\partial \sigma}}_{T_6}. \tag{S1-3}$$

In the above equation, term T_1 is the advection of M_2 along channel momentum by along channel residual current and term T_2 is the advection of along channel residual momentum by along channel M_2 tide. Furthermore, term T_3 is the advection of M_2 along channel momentum by cross channel residual current, term T_4 is the advection of residual along channel momentum by cross channel M_2 tide, term T_5 is the advection of M_2 along channel momentum by vertical residual current and term T_6 is the advection of along channel residual momentum by vertical M_2 tidal current.

Now consider positive currents to be directed landward and assume (as an example) that the M_2 tidal current amplitude decreases towards the land. In this case, the along channel tidal current obeys $\partial u_{M_2}/\partial x < 0$ during flood whilst $\partial u_{M_2}/\partial x > 0$ during ebb. Further, note that in a typical estuary, residual current shows a two layer structure with seaward current near the surface and landward current near the bottom. Hence, during flood, term T_1 in Eq. S1-3 is positive in the upper layer and negative in the lower layer. It causes M_2 tidal momentum near the water surface to decrease and it increases M_2 tidal momentum near the bottom. Thus, in this specific case, the along channel M_2 tidal current would show a subsurface jet (SJ-II) (Figure S1-2a). During ebb,

the M_2 current reverses direction, but the residual current remains the same. The term T_1 acts in the same manner and thus the SJ-II occurs in the M_2 tidal current profile during the full tidal cycle.

Next, term T_2 is considered. In a weakly stratified estuary, residual current speed typically reaches maximum values near the density front, which is somewhere inside the estuary. Hence $\partial |\overline{u}| / \partial x$ is negative on the landward side of the front whilst it is positive on the seaside. Thus, landward of the front during flood $T_2 > 0$ in the upper layer (hence locally M_2 momentum decreases) and $T_2 < 0$ in the lower layer (M_2 momentum increases). This is also the case during ebb, because tidal momentum changes sign, however residual current does not. The M_2 tidal current profile thus would show SJ-II (see Figure S1-2b, right part). A similar reasoning for term T_2 in the area seaward of the density front leads to the identification of a surface jump (SJ-I) instead (see Figure S1-2b, left part).

Thirdly, term T_3 is analysed. Typically, an estuary has a deep channel in the middle, thus the along channel tidal current amplitude decreases from the middle to the sides. Hence, during flood phase $\partial u_{M_2} / \partial y$ is positive on the right side and negative on the left when looking into the estuary (Figure S1-2c). Now, assume a case where denser water occurs on the right side and lighter water on the left side. This generates a lateral overturning circulation, with $\overline{v} > 0$ (from right to left) in the lower layer and $\overline{v} < 0$ in the upper layer (Huijts et al., 2009). In that case, term T_3 is positive near the surface and negative near the bottom on the left shoal and it reverses on the right shoal. Consequently, T_3 potentially results in SJ-I at the right side of the channel and in SJ-II at the left side (Figure S1-2d).

To assess advection term T_4 in Eq. S1-3 the lateral variation $\partial \overline{u} / \partial y$ has to be quantified. As a result of lateral depth variation, along channel residual current is directed landward in the deep channel and seaward over shallow shoals (Friedrichs and Hamrick, 1996). It causes $\partial \overline{u} / \partial y < 0$ and $\partial \overline{u} / \partial y > 0$ on the left and right side shoal, respectively. Furthermore, assume that during the flood, lateral tidal current shows a clockwise structure due to Coriolis deflection of along-channel tidal current on the North Hemisphere (Huijts et al., 2009) (Figure S1-2e). Consequently, $T_4 > 0$ ($T_4 < 0$) on the left (right) side near the surface and it reverses near the bottom. This term may thus induce SJ-I at the right side of the channel and SJ-II at the left side.

Term T_5 results in no SJ-I/II phenomenon. This is because neither the vertical shear of the tidal current ($\partial u_{M_2} / \partial \sigma$) nor the vertical residual current shows a two layer structure over the water column. Finally, term T_6 is considered. Vertical shear of along channel residual current is positive only near the bottom of deep channel in the middle. It is negative near the surface of deep channel and also on both shoals (Figure S1-2f). Hence one may obtain SJ-I only in the middle channel and no SJ-I and/or SJ-II due to T_6 (Figure S1-2g).

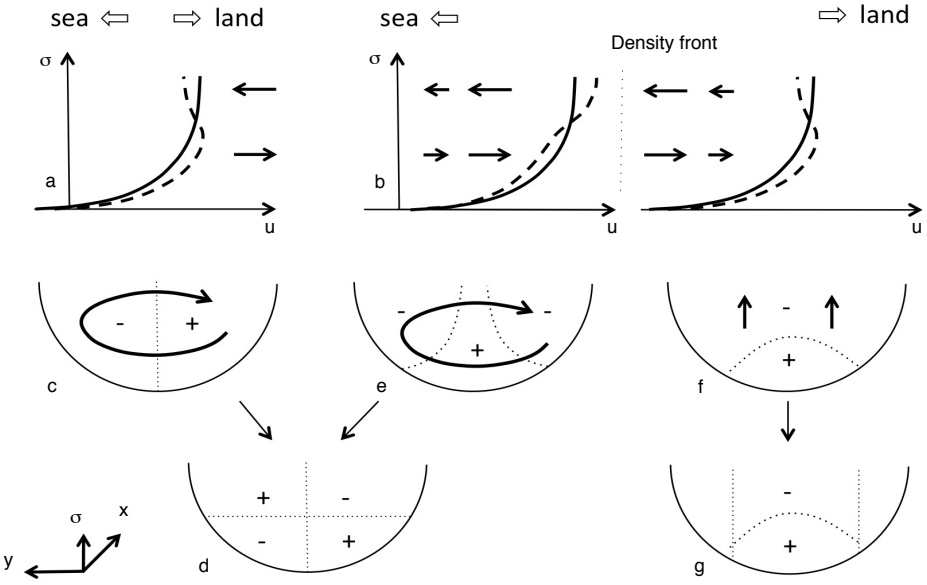

Figure S1-2: a. Typical logarithmic profile of flood tidal current (solid line) is deformed into a new profile (dashed lines) which potentially shows SJ-II due to advection term T_1 in Eq. S1-3b. The right part of this panel shows a potential SJ-II on landward of the density front (denoted by vertical dotted line) and the left part plot shows a potential SJ-I phenomenon on seaward of the density front. In a and b, the thick black arrows indicate the residual current ($\overline{u}$). c. Typical cross-section in an estuary; direction into the paper is towards the land. The curved arrow shows the overturning lateral residual current and positive sign "+" (negative sign "−") represents $\partial u_{M_2}/\partial y > 0$ (< 0) during flood (ebb). Dotted line indicates the location of the deep channel. In d, "+" and "−" indicate the signs of T_3. e. As panel c, but "+" and"−" indicate the signs of along channel residual current ($\overline{u}$) in areas that are separated by the dotted lines. Lateral tidal current during flood is represented by the curved arrow. Term T_4 shows the same structure as T_3 and is presented again in panel d. f. "+" and "−" indicate the signs of vertical shear of residual current and arrows are vertical tidal current during flood. g. As panel c, where "+" and "−" indicate the sign of term T_6. Within the area of two vertical dotted lines, SJ-I may occur.

S.1.3 *Code for calculating tidal current amplitude*

The code is programmed in Mathematica as follows:

```
ClearAll["Global`*"]
H = 10; (* water depth *)
dη0[sl] = 1.5 * 10^(-5); (* prescribed sea surface gradient at certain location *)
Avtype = 2; (* prescribed =1,linear above Av_max; =2, parabolic above Av_max;  *)
z0 = 2.5 * 10^(-4); (* roughness length *)
σp = -0.3;  (* prescribed *)
ratio = 0.01; (* ratio between A_s and Av_max *)
g = 10;
ka = 0.41; (* von Kamman constant *)
ω = 1.4 * 10^(-4); (* 1/s, frequency of imposed tidal flow *)
```

- **eddy viscosity coefficient**

```
Which[
  Avtype == 1, ntype = 1,
  Avtype == 2, ntype = 2
 ];

Amx = (1 + σp)^2 / 4;
As = ratio * Amx;
ratio = As / Amx;
Which[
  Avtype == 1, σh = -0.5 √(Abs[ratio - 4 σp + 2 ratio σp + ratio σp^2]),
  Avtype == 2, σh = (ratio - 4 σp + 2 ratio σp + ratio σp^2) / (2 (-1 + σp))
 ];
Ai = (1 + σh) * (σp - σh);
cp = (Ai - As) / σh^ntype;
Aσ[σ_] := (1 + σ) * (σp - σ) /; -1 ≤ σ ≤ σh
Aσ[σ_] := cp * σ^ntype + As /; σ ≥ σh
DAσ[σ_] := -1 - 2 σ + σp /; -1 ≤ σ ≤ σh
DAσ[σ_] := ntype * cp * σ^(ntype - 1) /; σ ≥ σh
```

- **tidal flow**

```
δ = ka * ustar / H / ω;
σ0 = z0 / H;
A = δ;
Pb = A * cp;
ν = (-1 + Sqrt[δ + 4 * I] / Sqrt[δ]) / 2;
νprime = (-1 + Sqrt[Pb - 4 * I] / Sqrt[Pb]) / 2;
σprime[σ_] = (2 σ + 1 - σp) / (1 + σp);

(* the following are for ntype = 1 *)
ff = As / cp;
σ3prime[σ_] = 2 √(-I * (σ + ff) / Pb);

Lp[σ_] = LegendreP[ν, σprime[σ]]; DLp[σ_] = D[LegendreP[ν, σprime[σt]], σt] /. σt → σ;
Qp[σ_] = LegendreQ[ν, σprime[σ]]; DQp[σ_] = D[LegendreQ[ν, σprime[σt]], σt] /. σt → σ;

BI[σ_] = BesselI[0, σ3prime[σ]]; BK[σ_] = BesselK[0, σ3prime[σ]];
BI1[σ_] = BesselI[1, σ3prime[σ]]; BK1[σ_] = BesselK[1, σ3prime[σ]];

β11 = BK[σh] * BI1[0] / BK1[0] + BI[σh];
β12 = 2 * I / Pb / σ3prime[σh] * (BK1[σh] * BI1[0] / BK1[0] - BI1[σh]);
βlin = β11 / β12;

F1 = (LegendreP[ν, σprime[σh]] - LegendreQ[ν, σprime[σh]] *
      LegendreP[ν, σprime[-1 + σ0]] / LegendreQ[ν, σprime[-1 + σ0]]);

F2 = -βlin *
    (DLp[σh] - DQp[σh] * LegendreP[ν, σprime[-1 + σ0]] / LegendreQ[ν, σprime[-1 + σ0]]);
```

```
F3 = (LegendreQ[ν , σprime[σh]] - βlin * DQp [σh]) / LegendreQ[ν , σprime[-1 + σ0 ]];

F = F3 / (F1 + F2);
G = (F * LegendreP[ν , σprime[-1 + σ0 ]] + 1) / LegendreQ[ν , σprime[-1 + σ0 ]];
G2 = (-LegendreQ[ν , σprime[σh]] / LegendreQ[ν , σprime[-1 + σ0 ]] + F * F1) / β11;

pp1 [σ_] = 1 + Lp [σ] * F - Qp [σ] * G;
pc1 [σ_] = 1 + G2 * (BK [σ] * BI1 [0] / BK1 [0] + BI [σ]);
p1 [σ_] := pp1 [σ] /;  σ ≤ σh
p1[σ_] := pc1 [σ] /;  σ ≥ σh

dpp1 [σ_] := D[pp1 [σt], σt] /. σt → σ;
dpc1 [σ_] := D[pc1 [σt], σt] /. σt → σ;

dp1 [σ_] := dpp1 [σ] /;  σ ≤ σh
dp1 [σ_] := dpc1 [σ] /;  σ ≥ σh

(* the following are for ntype = 2 *)
σ2prime[σ_] = Sqrt[Ai - As] * I * σ / Sqrt[As] / σh;

dPdσ[σ_] = D[LegendreP[ν, σprime[σ]], σ];
dQdσ[σ_] = D[LegendreQ[ν, σprime[σ]], σ];
dPprimedσ[σ_] = D[LegendreP[νprime, σ2prime[σ]], σ];
dQprimedσ[σ_] = D[LegendreQ[νprime, σ2prime[σ]], σ];

β1 = LegendreP[νprime, σ2prime[σh]] - LegendreQ[νprime, σ2prime[σh]] *
     LegendreP[νprime + 1, σ2prime[0]] / LegendreQ[νprime + 1, σ2prime[0]];
β2 = dPprimedσ[σh] - dQprimedσ[σh] * LegendreP[νprime + 1, σ2prime[0]] /
      LegendreQ[νprime + 1, σ2prime[0]];
β = β1 / β2;

FF1 = (LegendreP[ν, σprime[σh]] - LegendreQ[ν, σprime[σh]] *
      LegendreP[ν, σprime[-1 + σ0]] / LegendreQ[ν, σprime[-1 + σ0]]);
FF2 = -β * (dPdσ[σh] - dQdσ[σh] * LegendreP[ν, σprime[-1 + σ0]] /
        LegendreQ[ν, σprime[-1 + σ0]]);
FF3 = (LegendreQ[ν, σprime[σh]] - β * dQdσ[σh]) / LegendreQ[ν, σprime[-1 + σ0]];
FF = FF3 / (FF1 + FF2);

GG = (FF * LegendreP[ν, σprime[-1 + σ0]] + 1) / LegendreQ[ν, σprime[-1 + σ0]];
GG2 = (FF * FF1 - LegendreQ[ν, σprime[σh]] / LegendreQ[ν, σprime[-1 + σ0]]) / β1;

ptemp1[σ_] = 1 + LegendreP[ν, σprime[σ]] * FF - LegendreQ[ν, σprime[σ]] * GG;
ptemp2[σ_] = 1 + GG2 * (LegendreP[νprime, σ2prime[σ]] - LegendreQ[νprime, σ2prime[σ]] *
       LegendreP[νprime + 1, σ2prime[0]] / LegendreQ[νprime + 1, σ2prime[0]]);

(*  Here is the expression for "p" in U = -i*p*dη/dx.  *)
p2[σ_] := ptemp1[σ] /;  σ ≤ σh
p2[σ_] := ptemp2[σ] /;  σ ≥ σh

dp21[σ_] = FF * dPdσ[σ] - GG * dQdσ[σ];
dp22[σ_] = GG2 * (dPprimedσ[σ] - dQprimedσ[σ] *
      LegendreP[νprime + 1, σ2prime[0]] / LegendreQ[νprime + 1, σ2prime[0]]);

dp2[σ_] := dp21[σ] /;  σ ≤ σh
dp2[σ_] := dp22[σ] /;  σ ≥ σh

ddp1 [σ_] := D[dp21 [σt], σt] /. σt → σ;
ddp2 [σ_] := D[dp22 [σt], σt] /. σt → σ;

(*  Here is the expression for "dηdx" in U = -i*p*dη/dx.  *)
(*find solution for "p"*)
Which[Avtype == 1, p[σ_] := p1[σ], Avtype == 2, p[σ_] := p2[σ]]
Which[Avtype == 1, dp[σ_] := dp1[σ], Avtype == 2, dp[σ_] := dp2[σ]]

u0[σ_] = -I * g * dη0[sl] * p[σ] / ω;
du0h[σ_] = -I * g * dη0[sl] * dp[σ] / ω;

(*find the ture local shear velocity:*)
ustar = 0.027; cc = 0.05; (* give a random value to start the iteration *)
```

```
While[Abs[ustar - cc] > 0.001,
 ustar = cc;
 P = NIntegrate[p[σ], {σ, -1 + σ0, 0}];
 du0 = du0h[-1 + σ0];
 dtime = 2 * Pi / 100; ustarvari = Array[0 &, 101];
 Array[time, 101]; Table[time[cxc] = 0 + (cxc - 1) * dtime, {cxc, 1, 101}];
 For[cxc = 1, cxc ≤ 101, cxc++,
  {ustarvari[[cxc]] = ka * σ0 * (1 + σp - σ0) * Abs[du0] * Cos[time[cxc] - Arg[du0]]}];
 cc = Max[ustarvari] * 8 / 3 / Pi
]
ustar

(* Make Plots *)
imsize = 250;
Avplot = ParametricPlot[{{ka * ustar * H * Aσ[σ], σ}}, {σ, -1, 0}, ImageSize → imsize,
   AspectRatio → 1, Frame → True, FrameLabel → {"A_v (m^2/s)", "σ"}];
Umplot = ParametricPlot[{Abs[u0[σ]], σ}, {σ, -1 + σ0, 0}, PlotRange → All,
   ImageSize → imsize, AspectRatio → 1, Frame → True, FrameLabel → {"U_M2 (m/s)", "σ"}];
Ufplot = ParametricPlot[{Arg[u0[σ]], σ}, {σ, -1 + σ0, 0}, ImageSize → imsize,
   AspectRatio → 1, Frame → True, FrameLabel → {"Phase U_M2 (radi)", "σ"}];
Row[{Avplot, Umplot, Ufplot}, Spacer[5]]
```

S.2 SUPPLEMENTARY MATERIAL FOR CHAPTER 3

S.2.1 *Results for model experiments series 2 and 3*

In this electronic supplement, results for model experiments series 2 and 3 (see Table 3-3 in chapter 3) are presented. Figure S2-1 is similar to Figure 3-6 ofchapter 3, and shows vorticities related to the total ESCO current (u_τ), the ESCO current due to M_2' tide ($u_{\tau,M_2'}$) and the ESCO current due to M_4' tide ($u_{\tau,M_4'}$) for series 2. The way in which vorticities $\mathcal{V}_1$ and $\mathcal{V}_2$ are computed is explained in section 3.2.8 of chapter 3.

For the experiments of this series, the longitudinal mean depth between L_e and L_c (see Figure 3-1 of chapter 3) is fixed at 10 m. With increasing bottom slope, positive $\mathcal{V}_1$ in the upper vorticity layer is observed near the mouth and in the section between 245 to 250 km (Figure S2-1a). The vorticity $\mathcal{V}_2$ in the lower layer occurs in two areas of the figure. The first one is between 250 km and the mouth and the second one is near the salt intrusion limit (the location where mean salinity is 1 psu) (Figure S2-1b). As is shown in Figure S2-1c, the negative $\mathcal{V}_1$ that is related to $u_{\tau,M_2'}$ is observed in most of the estuary and for bottom slopes between 0 and 1×10^{-4}. The maximum negative value of $\mathcal{V}_1$ is obtained for the moderate slope (0.5×10^{-4}). The vorticity $\mathcal{V}_2$ in layer $i = 2$ below the surface is observed only in the area between 0 km to 8 km, with a maximum value for a bottom slope of 0.5×10^{-4} (Figure S2-1d). Regarding $u_{\tau,M_4'}$, Figure S2-1e shows that its vorticity $\mathcal{V}_1$ is positive in most of the estuary. Negative $\mathcal{V}_1$ occurs at the location around 3 km from the mouth, where also $\mathcal{V}_2$ exists (Figure S2-1f), but its value is rather weak.

Figure S2-2 is similar to Figure 3-7 of chapter 3, but for all experiments in series 2. It shows the importance of the ESCO current $u_{\tau,M_4'}$, its relative contribution $r_{M_4'}$ to the depth-integrated kinetic energy of total ESCO current. Additionally, the relative contribution r_E of ESCO current to the depth-integrated kinetic energy of the total residual current as a function of scaled distance $\tilde{x}$ and the bottom slope is presented. Results show two separate areas in the estuary where the ESCO current due to M_4' is important ($r_{M_4'} > 0.25$). One is near the mouth and the other is in the upper reach $0 < \tilde{x} < \tilde{x}_m$, where $\tilde{x}_m$ decreases with increasing bottom slope. Further comparison of the total ESCO current with the total residual current reveals that the former is relevant only in the section $0.5 < \tilde{x} < 1$.

Figure S2-3 is similar to Figure S2-1, but for model runs of series 3, in which the longitudinal mean depth between L_e and L_c (see Table 3-3 of chapter 3) decreases from 10 m to 7.5 m with bottom slope increasing from 0 to 1×10^{-4}. It appears that in these cases the longitudinal distribution of the vorticity patterns hardly changes by varying the bottom slope. Figure S2-4 is similar to Figure S2-2 but for model runs of series 3. It shows that the ESCO current due to M_2'

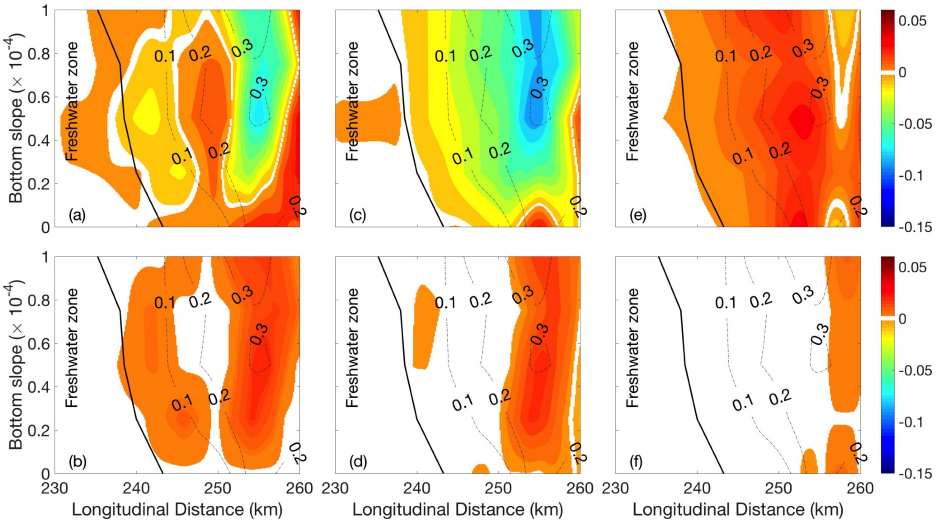

Figure S2-1: Color-contour plots of vorticities $\mathcal{V}_1$ (upper layer, first row) and $\mathcal{V}_2$ (second layer below surface, second row) as functions of longitudinal distance and bottom slope, experiment series 2 (see Table 3-3 of chapter 3). Unit of $\mathcal{V}_n$ is s^{-1}. In this series, depth between $x = 0$ km and $x = L_e$ ($L_e = 210$ km) is 10 m and it linearly increase towards the mouth seaward of L_e. Panels in the first, second and third columns are results related to total ESCO current u_τ, and ESCO flows $u_{\tau,M_2'}$ and $u_{\tau,M_4'}$ due to M_2' and M_4', respectively. Black solid lines denote the location where depth and time mean salinity is 1 psu. Areas in which vorticities $|\mathcal{V}_n| < 0.001$ s^{-1} are blanked. Dashed lines are contours of $\Delta S/S$, where ΔS is the tidal mean top-to-bottom salinity difference that depends on x, and $S = 31$ psu is the salinity at the open boundaries.

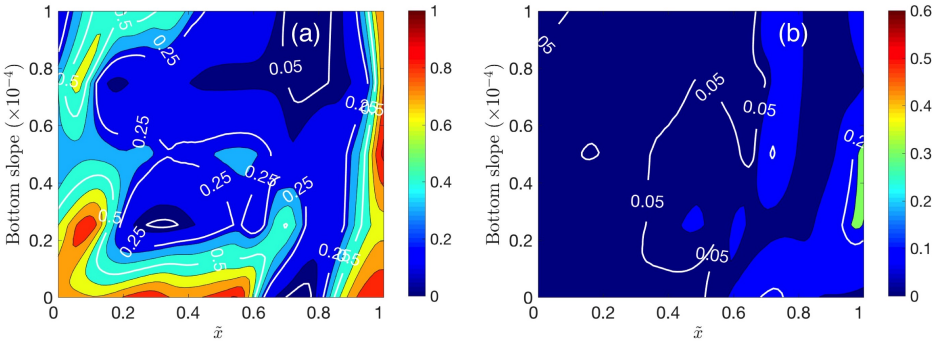

Figure S2-2: (a) Colour-contour plot of the relative contribution $r_{M_4'}$ of ESCO current due to M_4' tide to the depth-integrated kinetic energy of total ESCO current as a function of scaled longitudinal distance $\tilde{x}$ and bottom slope, experiment series 2. Here, $\tilde{x} = 0$ is the location where depth and time mean salinity equals 1 psu and $\tilde{x} = 1$ is the estuary mouth. The white contour lines indiate borders in the figure where the M_4' tide contribution to the ESCO current becomes small ($r_{M_4'} < 0.05$), important ($r_{M_4'} > 0.25$) and dominant ($r_{M_4'} > 0.5$). (b). As panel (a), but for r_E, i.e., the ratio between depth integrated kinetic energy of the ESCO current and that of the total residual current. Note colour bars of panel (a) and (b) have different ranges.

is dominant in the area $0.65 < \tilde{x} < 0.8$ for all model runs. Within the section where the total ESCO current significantly contributes to the residual current ($0.4 < \tilde{x} < 1$), the ESCO current due to M_4' is important in $0.4 < \tilde{x} < 0.65$ and $0.8 < \tilde{x} < 1$.

S.2.2 *Thickness of vorticity layers*

The thickness of the vorticity layers that are related to ESCO flows computed from experiments of series 1 are presented in Figure S2-5. Panel (a) shows the thickness of the upper vorticity layer related to the total ESCO current u_τ as a function of longitudinal distance and bottom slope. Thin layers, with thicknesses $H(\sigma_i - \sigma_{i+1}) < 0.1$ m, are blanked. Small values of the thickness of the upper vorticity layer are observed near the mouth, and they increase towards the upper reach. The value of $H(\sigma_1 - \sigma_2)$ reaches a maximum (about 8 m) near the salt intrusion limit. With increasing bottom slope, the thickness of the upper vorticity layer decreases. In panel (b), the thickness of the lower vorticity layer related to the total ESCO current u_τ is given, which appears for bottom slope larger than 0.2×10^{-4}. This layer occurs in two areas: One is close to the mouth (already for relatively small slopes) and one is close to the salt intrusion limit (requires larger bottom slope). Panel (c) shows the upper vorticity layer thickness related to the ESCO current $u_{\tau,M_2'}$. The value of $H(\sigma_1 -$

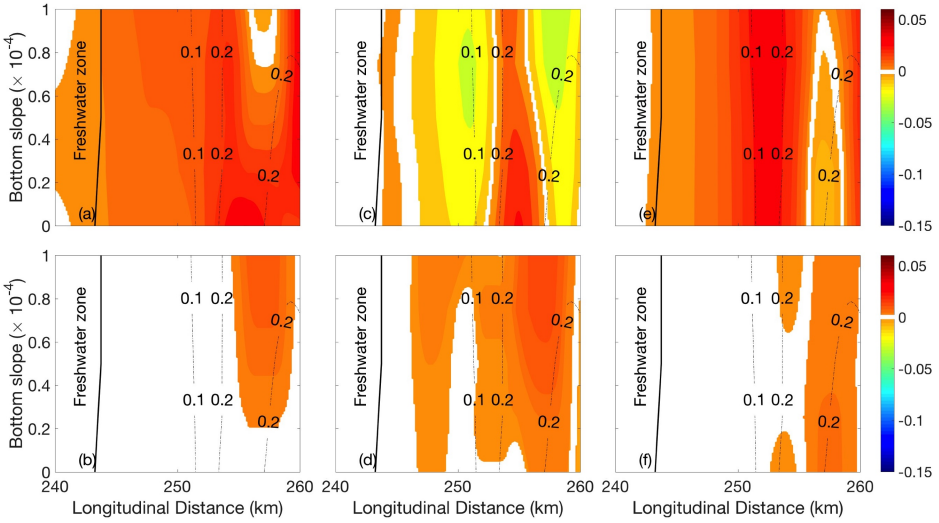

Figure S2-3: As Figure S2-1, but for series 3 (see Table 3-3 of chapter 3). In this series, depth at the mouth $x = L_c$ is 10 m and it linearly decreases towards $x = L_e$. The depth landward of $x = L_e$ is constant and equals the depth at $x = L_e$.

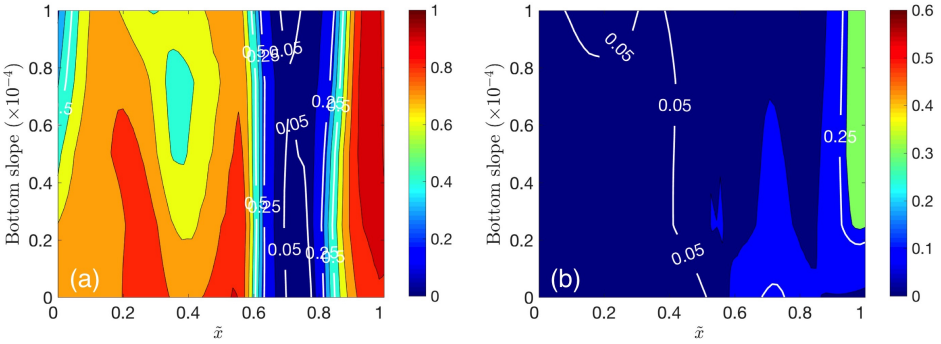

Figure S2-4: As Figure S2-2, but for series 3 (see Table 3-3 of chapter 3).

σ_2) is around 4 m on the seaside of the salt intrusion limit for all bottom slopes investigated. The thickness of the lower vorticity layer thickness of $u_{\tau,M_2'}$, as shown in panel (d), reaches its largest value for a moderate bottom slope (0.5×10^{-4}) and it is small for both flat bottom and strong sloping cases ($> 0.8 \times 10^{-4}$). Panels (e) and (f) show thicknesses related to $u_{\tau,M_4'}$ in the upper and lower vorticity layer. The thickness of the upper vorticity layer increases from 4 m to 8 m with increasing bottom slope. However, the thickness of the lower vorticity layer in general is less than 4 m. Note that by definition (Eq. 3-11 of chapter 3), adding up the thickness of the upper and lower vorticity layers yields a value smaller than the water depth (also see in Figure 3-2 of chapter 3).

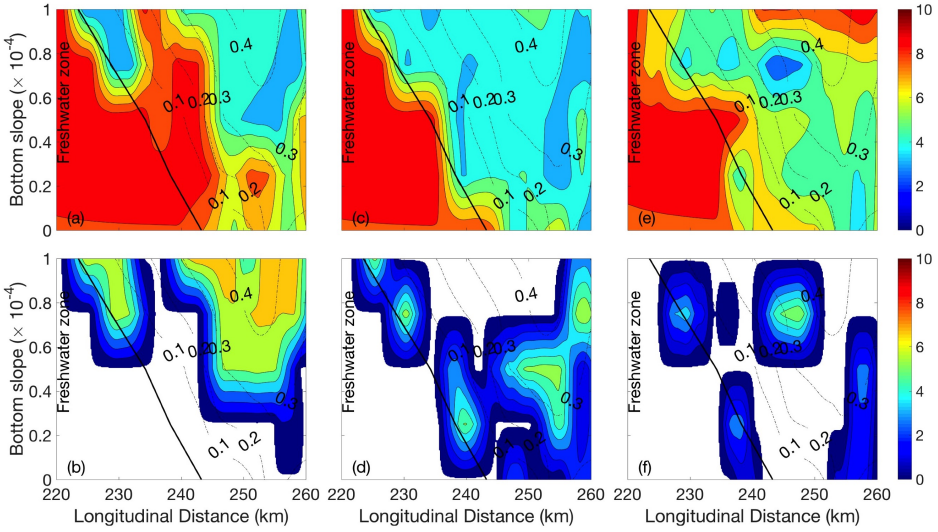

Figure S2-5: Color-contour plots of thickness of vorticity layers as functions of longitudinal distance and bottom slope (Experiment series 1). The panels in the first row are the thickness of the upper vorticity layer $H(\sigma_1 - \sigma_2)$ and the panels in the second row are the thickness of the lower vorticity layer $H(\sigma_2 - \sigma_3)$. The left, middle and right columns are results related to the total ESCO current u_τ, the ESCO current $u_{\tau,M_2'}$ and $u_{\tau,M_4'}$, respectively. Black solid lines denote the location where depth and time mean salinity is 1 psu. The thickness that $H(\sigma_i - \sigma_{i+1}) < 0.1$ m are blanked. Dashed lines denote contours of $\Delta S/S$. Values of the thickness are in m.

Figure S2-6 and Figure S2-7 are similar to Figure S2-5, and show the thickness of vorticity layers as functions of longitudinal distance and bottom slope for series 2 and 3, respectively. Like in experiments of series 1, with increasing bottom slope, thicknesses of the upper vorticity layers become smaller, but to a lesser extent than in series 1. Moreover, thicknesses of the lower vorticity layers for the same bottom slope are larger in series 2 and 3 than in series 1. For a

bottom slope of 1×10^{-4} as an example, in series 1 the thickness of the lower layer of vorticity that is related to total ESCO current u_τ is 7 m near the mouth (257 km), which accounts for 50% of the total water column (see Figure S2-5b), whereas it is 5 m (40% of the water column) in series 2 (Figure S2-6b) and 1 m (10% of the water column) in series 3 (Figure S2-7b), respectively.

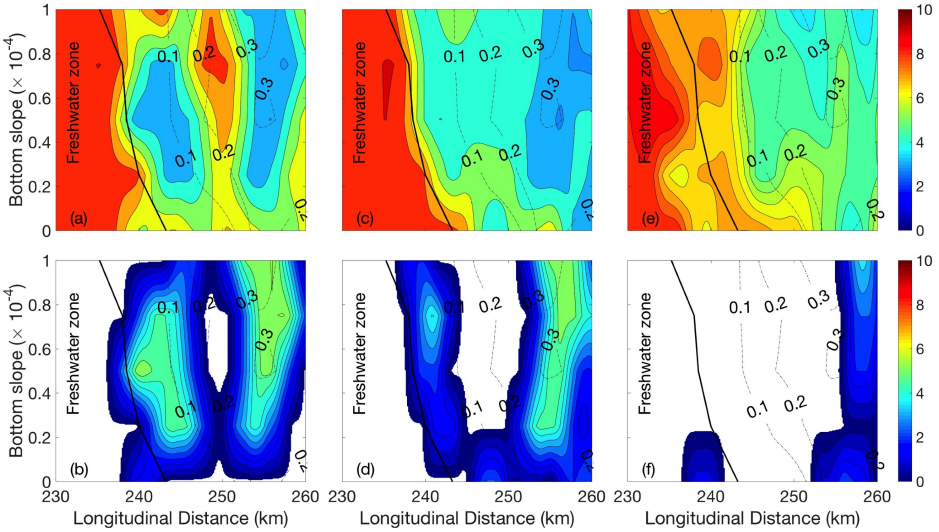

Figure S2-6: As Figure S2-5, but for series 2.

Figure S2-8 is as Figure S2-5, but shows the thickness of vorticity layers of series 4 (see Table 3-3 of chapter 3) as functions of the longitudinal distance and the parameter M, where the latter is defined in Eq. 3-3 of chapter 3 and it is a measure for the intensity of external tidal forcing. It appears that the thickness of the upper vorticity layer $H(\sigma_1 - \sigma_2)$ related to total ESCO current u_τ is 3 to 4 m when M is small (see Figure S2-8a), and it increases to about 7 m with M reaches 1.4. As is shown in Figure S2-8b, the lower vorticity layer related to u_τ exists between $0.8 < M < 1.1$ and the thickness $H(\sigma_2 - \sigma_3)$ is 2 to 4 m. Panel (c) show the thickness of the upper layer with vorticity that is related to $u_{\tau,M_2'}$. For $M < 0.8$, the thickness $H(\sigma_1 - \sigma_2)$ is about 2 to 4 m in the estuary. When $M > 1.4$, the value of $H(\sigma_1 - \sigma_2)$ is about 7 m. In panel (d), the value of $H(\sigma_2 - \sigma_3)$ is about 4 m, which is only observed near the mouth (252 to 260 km) and in the upper reach (240 to 247 km). The upper layer of vorticity related to $u_{\tau,M_4'}$, as shown in panel (e), is around 3 m for $M < 1.1$ and near the mouth for $M > 1.1$. Note that the thickness of the lower layer of vorticity related to $u_{\tau,M_4'}$ is in general less than 3 m and is observed near the mouth for $M > 1.1$ (Figure S2-8f).

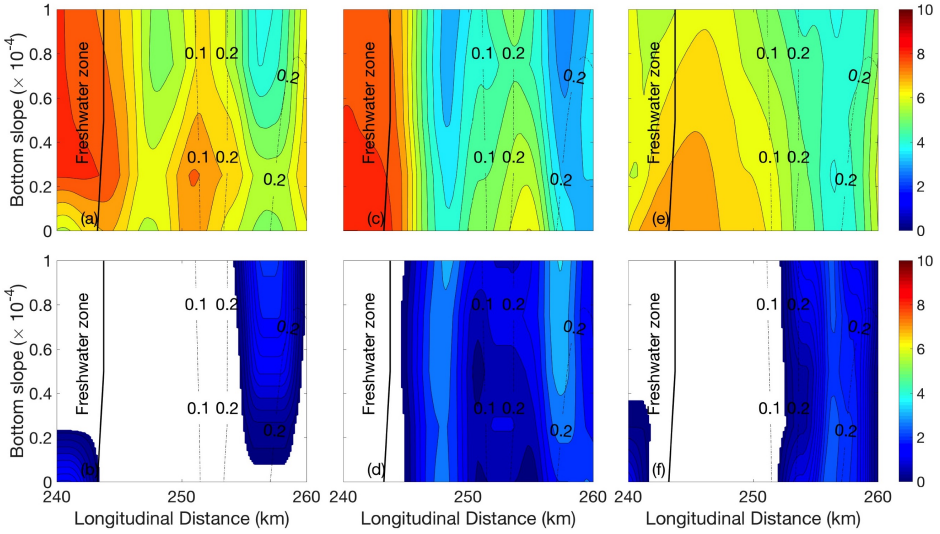

Figure S2-7: As Figure S2-5, but for series 3.

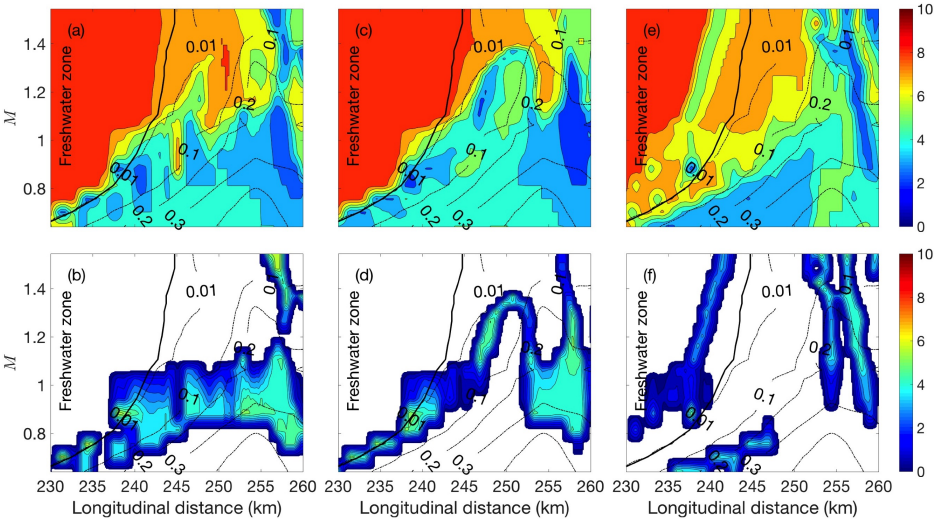

Figure S2-8: As Figure S2-5, but for series 4: thickness $H(\sigma_1 - \sigma_2)$ (first row) and $H(\sigma_2 - \sigma_3)$ (second row) of vorticity layers are plotted as functions of the longitudinal distance and the parameter M for total ESCO current (left column), the ESCO current due to M_2' tide (middle column) and due to M_4' tide (right column). Parameter M is defined in Eq. 3-3 of chapter 3 and it is a measure for the intensity of external tidal forcing.

Figure S2-9 is as Figure S2-8 and shows thickness $H(\sigma_1 - \sigma_2)$ of the upper vorticity layer, and thickness $H(\sigma_2 - \sigma_3)$ of the lower vorticity layer that are related to u_τ, the ESCO current due to diurnal tides, and that due to semi-diurnal tides. Note that stratification conditions at the mouth are the same in these cases. As is shown in panel (a), for $F' < 0.2$ (tidal forcing is primarily semi-diurnal), the thickness of the upper vorticity layer $H(\sigma_1 - \sigma_2)$ is about 4 m, and for $F' > 0.2$, $H(\sigma_1 - \sigma_2)$ is about 6 m. The lower vorticity layer, which exists only for $F' < 0.2$, $H(\sigma_1 - \sigma_2)$ decreases from 5 m to zero (Figure S2-9b). Regarding vorticities related to the ESCO current induced by diurnal tides, the thickness of the upper vorticity layer is 4 to 7 m (Figure S2-9c), whereas $H(\sigma_2 - \sigma_3)$ of the lower vorticity layer (Figure S2-9d) has value of less than 2 m. For the ESCO current due to semi-diurnal tides (Figure S2-9e and f), a thin vorticity layer is mainly observed for $F' < 0.2$. The value of $H(\sigma_1 - \sigma_2)$ is less than 5 m and the value of $H(\sigma_2 - \sigma_3)$, which exists mainly between 250 and 260 km, is about 4 m. With increasing F', the thickness of the upper layer increases until it becomes 4 to 6 m for $F' = 0.95$, while the lower vorticity layer disappears.

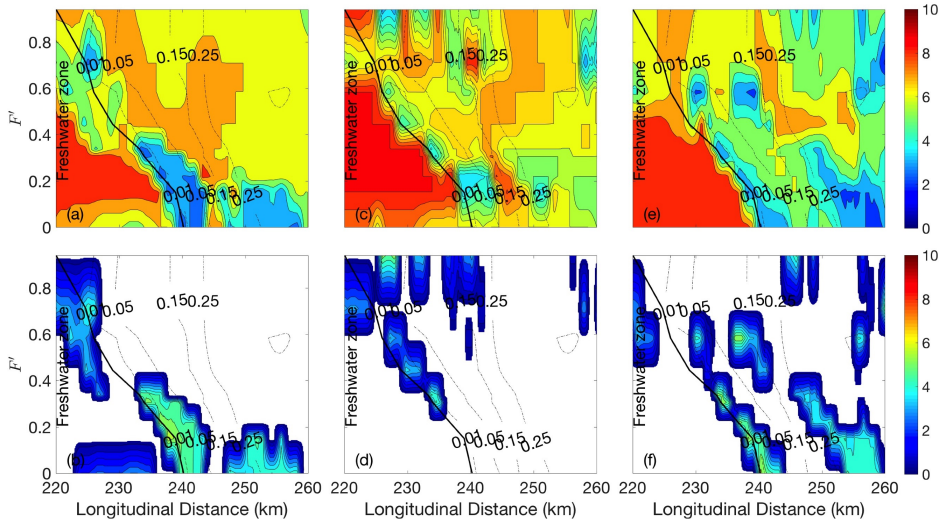

Figure S2-9: As Figure S2-5, but for series 5: thickness $H(\sigma_1 - \sigma_2)$ (first row) and $H(\sigma_2 - \sigma_3)$ (second row) of vorticity layers are plotted as functions of the longitudinal distance and the parameter F' for total ESCO current (left column), the ESCO current due to diurnal tides (middle column) and due to semi-diurnal tides (right column). The parameter F' is defined in Eq. 3-4 of chapter 3 and it is a measure for the intensity of external tidal forcing.

The thicknesses of vorticity layers that are related to ESCO current due to ter-diurnal tides, the quarter-diurnal tide and the long-periodic tide (Mf′) are presented in Figure S2-10. For the upper vorticity layers, the value of $H(\sigma_1 - \sigma_2)$ ranges from 3 to 6 m (Figure S2-9a, c and e). For the lower vorticity layers, $H(\sigma_2 - \sigma_3)$ is smaller than 3 m (Figure S2-9b, d and f).

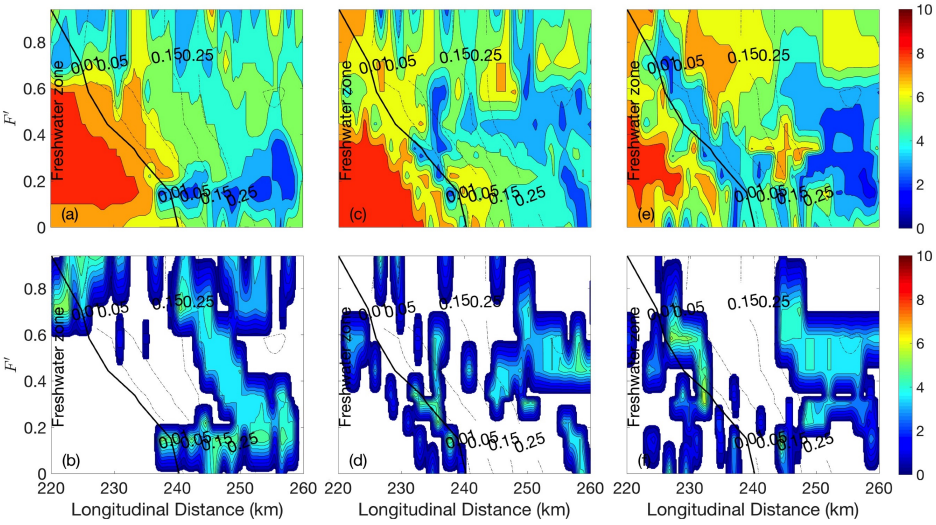

Figure S2-10: As Figure S2-9, but for the ESCO current due to ter-diurnal tides (left column), due to quarter-diurnal tides (middle column) and due to the long-periodic tide Mf′ (right column).

S.2.3 *Sensitivity of results to model inputs*

Figure S2-11a shows the vertical distribution of the tidally mean salinity in the longitudinal direction for different values of horizontal eddy viscosity A_h and horizontal diffusivity K_h. Solid lines denote results that are computed by the model using default A_h and K_h (Table 3-2 of chapter 3) and dotted lines are for $A_h = K_h = 5\ m^2\ s^{-1}$. Tide is forced by M_2' with an amplitude of 0.8 m. Compared to the default case, the model with smaller A_h and K_h produces a similar salinity profile. The tidal mean top-to-bottom salinity difference increases about $1 - 2$ psu.

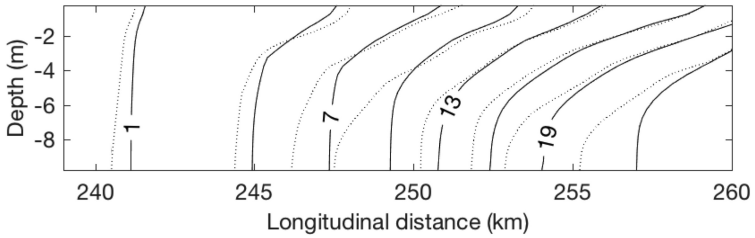

Figure S2-11: Contours of tidal mean salinity as a function of longitudinal distance and depth computed with the model using default values of A_h and K_h (Table 3-2 of chapter 3) (solid lines) and using $A_h = K_h = 5\ m^2\ s^{-1}$ (dotted lines). Unit of contour values is psu.

S.3 SUPPLEMENTARY MATERIAL FOR CHAPTER 4

S.3.1 *Derivation of the model equations*

In this supplement, some more background and details of the model equations and solutions are given. Section S.3.1.1 contains the derivation of the equations for the residual current in the longitudinal and lateral direction, followed by the derivation of the residual suspended sediment concentration in S.3.1.2. The derivation of an expression for the friction velocity that appears in the expressions for vertical eddy viscosity and diffusivity is presented in S.3.1.3.

S.3.1.1 *Hydrodynamics*

The hydrodynamic equations considered in this study are derived from the 3D shallow water equations in σ−coordinates, which read

$$\frac{\partial u}{\partial t} + F_x - fv = -g\frac{\partial \eta}{\partial x} - \frac{g}{\rho_r} D \int_\sigma^0 \left(\frac{\partial \rho}{\partial x}\right)^* d\tilde{\sigma} - \frac{uv}{R+y} + \frac{1}{D}\frac{\partial}{\partial \sigma}\left(\frac{A_v}{D}\frac{\partial u}{\partial \sigma}\right), \tag{S3-1a}$$

$$\frac{\partial v}{\partial t} + F_y + fu = -g\frac{\partial \eta}{\partial y} - \frac{g}{\rho_r} D \int_\sigma^0 \left(\frac{\partial \rho}{\partial y}\right)^* d\tilde{\sigma} + \frac{u^2}{R+y} + \frac{1}{D}\frac{\partial}{\partial \sigma}\left(\frac{A_v}{D}\frac{\partial v}{\partial \sigma}\right), \tag{S3-1b}$$

$$\frac{\partial \eta}{\partial t} + \frac{\partial (uD)}{\partial x} + \frac{\partial (vD)}{\partial y} + \frac{\partial w}{\partial \sigma} = 0. \tag{S3-1c}$$

Here, u, v are the the longitudinal and lateral velocity components in $\sigma-$coordinates, respectively, t is time and $\tilde{\sigma}$ is a dummy variable. The relative depth $\sigma = (z-\eta)/D$, in which $D = h+\eta$ is the distance from bottom (located at $z=-h$) to the free surface (η). The superscript $*$ denotes that the horizontal density gradients in both the longitudinal and lateral direction are taken at a fixed $z^{\dagger}$ level. Note that in these equations w is defined as $w = D\,d\sigma/dt$ and has the unit m s^{-1}.

The second term on the left hand sides of Eq. S3-1a and S3-1b are nonlinear advection of momentum in the longitudinal and lateral directions with the expression $F_x = u\frac{\partial u}{\partial x} + v\frac{\partial u}{\partial y} + \frac{w}{D}\frac{\partial u}{\partial \sigma}$ and $F_y = u\frac{\partial v}{\partial x} + v\frac{\partial v}{\partial y} + \frac{w}{D}\frac{\partial v}{\partial \sigma}$, respectively. Furthermore, f is the Coriolis parameter, g is gravitational acceleration, R is the radius of the channel curvature and ρ_r is a constant reference density, and A_v is the vertical eddy viscosity coefficient.

Taking the time average of momentum and continuity over a tidal cycle yields

$$\begin{aligned} < F_x > - f < v > = & -g\frac{\partial < \eta >}{\partial x} - \frac{g}{\rho_r} < D\int_\sigma^0 \left(\frac{\partial \rho}{\partial x}\right)^* d\tilde{\sigma} > \\ & - < \frac{uv}{R+y} > + < \frac{1}{D}\frac{\partial}{\partial \sigma}\left(\frac{A_v}{D}\frac{\partial u}{\partial \sigma}\right) > \end{aligned} \tag{S3-2a}$$

$$\begin{aligned} < F_y > + f < u > = & -g\frac{\partial < \eta >}{\partial y} - \frac{g}{\rho_r} < D\int_\sigma^0 \left(\frac{\partial \rho}{\partial y}\right)^* d\tilde{\sigma} > \\ & + < \frac{u^2}{R+y} > + < \frac{1}{D}\frac{\partial}{\partial \sigma}\left(\frac{A_v}{D}\frac{\partial v}{\partial \sigma}\right) > \end{aligned} \tag{S3-2b}$$

$$\frac{\partial < uD >}{\partial x} + \frac{\partial < vD >}{\partial y} + \frac{\partial < w >}{\partial \sigma} = 0. \tag{S3-2c}$$

Here, $< \cdot >$ denotes an average over the tidal period. Integrating Eq. S3-1c over the vertical and using boundary condition no-slip at the bottom and no stress and the surface yields

$$\frac{\partial}{\partial x}\int_{-1}^{0} < uD > d\sigma + \frac{\partial}{\partial y}\int_{-1}^{0} < vD > d\sigma = 0. \tag{S3-3}$$

Based on observed typical magnitudes of the different variables, several assumptions are made. First, tide dominated estuaries are considered, in which the longitudinal tidal motion is much stronger than the lateral tidal motion. Second, the local sea-surface elevation is negligible compared to mean water

depth ($\eta \ll h$), which yields $D \simeq h$. The radius of estuarine channel curvature is large with respect to the channel width, so that $R + y \simeq R$. Nonlinear advection of momentum, i.e., F_x and F_y in Eq. S3-1a and S3-1b are neglected. Moreover, it is also assumed that the residual current caused by suppression of turbulence due to density stratification is not considered. Many studies have pointed out that current due to nonlinear advection (Lerczak and Geyer, 2004; Scully and Friedrichs, 2007; Huijts et al., 2009) and variation of A_v during the tidal cycle (Burchard and Hetland, 2010; Cheng et al., 2011, 2013) contribute to the residual estuarine circulation. Interestingly, these two contributions are often found to partially cancel (Scully et al., 2009; Cheng, 2014). Lastly, the contribution due to curvature is neglected. Taking these statements into account and dropping the brackets $< \cdot >$ yields the equations that presented in Eq. 4-2 of chapter 4.

S.3.1.2 *Sediment dynamics*

The three-dimensional mass balance of suspended sediment in a σ-coordinate system reads

$$\frac{\partial c}{\partial t} + \frac{\partial}{\partial x}\left(uc - K_{hx}\frac{\partial c}{\partial x}\right) + \frac{\partial}{\partial y}\left(vc - K_{hy}\frac{\partial c}{\partial y}\right) + \frac{1}{D}\frac{\partial}{\partial \sigma}\left((w - w_s)c - \frac{K_v}{D}\frac{\partial c}{\partial \sigma}\right) = 0. \tag{S3-4}$$

Here, c is the suspended sediment concentration, w_s is the settling velocity and K_{hx} and K_{hy} are horizontal diffusion coefficient in the longitudinal and lateral direction, respectively. The vertical eddy diffusivity is represented by K_v. The boundary conditions are given in chapter 4.

By performing the time average of S3-4 over the tidal cycle, it follows

$$\begin{aligned} &\frac{\partial}{\partial x}\left(< u >< c > + < u'c' > - K_{hx}\frac{\partial < c >}{\partial x}\right) \\ &+ \frac{\partial}{\partial y}\left(< v >< c > + < v'c' > - K_{hy}\frac{\partial < c >}{\partial y}\right) \\ &+ \frac{1}{h}\frac{\partial}{\partial \sigma}\left(< w >< c > + < w'c' > - w_s < c > - \frac{K_v}{h}\frac{\partial < c >}{\partial \sigma}\right) = 0. \end{aligned} \tag{S3-5}$$

Here ($'$) denotes tidal components of a variable, $< u'c' >$, $< v'c' >$ and $< w'c' >$ are sediment fluxes that are called tidal pumping terms. Tidal pumping is found to be of minor importance in the lateral direction (Huijts et al., 2006). However, in the longitudinal direction, tidal pumping can be significant (Dyer, 1988; Becherer et al., 2016, and references herein). Following e.g. Festa and Hansen, 1978 and Geyer (1993), tidal pumping terms will be ignored.

Further analysis of Eq. S3-5 reveals that its last two terms are much larger than all previous terms. This results in Eq. 4-8 of chapter 4. If Eq. S3-5 is integrated over the vertical and boundary conditions at bottom and surface are used, it follows Eq. 4-12 of chapter 4.

S.3.1.3 *Expression for the friction velocity*

To determine the value of the representative, constant friction velocity $\check{u}_*$ in expression Eq. 4-19 of chapter 4, the kinematic bottom stress is considered, which by definition reads

$$\frac{\tau_b}{\rho_r} = |u_*|u_*, \tag{S3-6}$$

with u_* the friction velocity. Here, τ_b is the bottom shear stress of the total current (including tides). Following Dronkers (1964) and Godin (1999), the right hand side of this expression can be approximated as

$$|u_*|u_* = \mathcal{T}_1 u_* + \mathcal{T}_2 u_*^3, \tag{S3-7}$$

where $\mathcal{T}_1 = u_{*,max}16/15\pi$, $\mathcal{T}_2 = 2\mathcal{T}_1/u_{*,max}^2$ and $u_{*,max}$ is the maximum value of the friction velocity during a tidal cycle. Furthermore, a harmonic truncation is applied to u_*, i.e.,

$$u_* = \overline{u}_* + u'_{t*}, \tag{S3-8}$$

where $\overline{u}_*$ is a constant and u'_{t*} oscillates with the frequency ω of the the principal tide and has an amplitude $\hat{u}_*$. Hence, $u_{*,max} = |\overline{u}_*| + \hat{u}_*$. Substitution of Eq. S3-8 into Eq. S3-7 yields

$$|u_*|u_* = \underbrace{\check{u}_*\overline{u}_*}_{\overline{\tau}} + \underbrace{u_*^\dagger u'_{t*}}_{\tau'}, \tag{S3-9}$$

in which the first and the second term are mean and time varying component of the kinematic bottom stress. In chapter 4, to focus on tidally averaged motion, only the mean stress component $\overline{\tau} = \check{u}_*\overline{u}_*$ is considered, where

$$\check{u}_* = \frac{16}{15\pi}u_{*,max}\left[1 + 2\left(\left(\frac{|\overline{u}_*|}{u_{*,max}}\right)^2 + \frac{3}{2}\left(\frac{\hat{u}_*}{u_{*,max}}\right)^2\right)\right]. \tag{S3-10}$$

It is further assumed that

$$\overline{u}_*^2 = C_d U_{res}^2, \qquad \hat{u}_*^2 = C_d U_t^2, \qquad u_{*,max}^2 = C_d U_T^2. \tag{S3-11}$$

Here, $C_d \sim 1 \cdot 10^{-3}$ is a drag coefficient, U_{res}, U_t and $U_T = U_{res} + U_t$ are scales of the residual current, tidal current and total current. Substitution of Eq. S3-11 into Eq. S3-10 yields the representative friction velocity for the tidally mean stress, which is Eq. 4-20 of chapter 4.

S.3.2 *Model solutions*

Since the residual current system is linear, it can be decomposed into subsystems that describe current components due to different drivers. In the longitudinal direction the residual current is split into components due to the density gradient and due to longitudinal net water discharge, with the equations and solutions presented in section S.3.2.1. Likewise, lateral current is decomposed into components that result from Coriolis deflection of the longitudinal current, the lateral density gradient and from leakage. The details are presented in S.3.2.2, while S.3.2.3 contains the expression for the vertical distribution of SSC, $\phi(\sigma, h(y))$.

S.3.2.1 *Solutions for longitudinal residual current components*

The balance for net water transport in the longitudinal direction reads

$$0 = -g\frac{\partial \eta_Q}{\partial x} + \frac{1}{h}\frac{\partial}{\partial \sigma}\left(\frac{A_v}{h}\frac{\partial u_Q}{\partial \sigma}\right). \tag{S3-12}$$

Integration of the continuity equation (Eq. 4-2c) over the width and using boundary conditions Eq. 4-4a and b yields

$$\frac{\partial}{\partial x}\int_{-B}^{B}\int_{-1}^{0} h u_Q \, d\sigma dy + q_0 f(x) = 0. \tag{S3-13}$$

To obtain the solution for u_Q, Eq. S3-12 is first integrated from the bottom up and then from the surface down with applying conditions no-slip at the bottom and no stress at the surface. The water slope due to net water transport is found by integrating S3-13 from $x = 0$ to x and using boundary condition Eq. 4-7 of chapter 4.

The equations for density driven current in the longitudinal direction are

$$\frac{g}{\rho_r} h \int_{\sigma}^{0} \frac{\partial \rho}{\partial x} d\tilde{\sigma} = -g \frac{\partial \eta_d}{\partial x} + \frac{1}{h^2} \frac{\partial}{\partial \sigma} \left(A_v \frac{\partial u_d}{\partial \sigma} \right), \tag{S3-14a}$$

$$\int_{-B}^{B} \int_{-1}^{0} h u_d \, d\sigma dy = 0. \tag{S3-14b}$$

Similarly, integrating Eq. S3-14a in the vertical direction twice and using the boundaries yields the expression for u_d, in which the water slope is obtained by using Eq. S3-14b.

The expressions for each residual current component and its corresponding water slope in the longitudinal direction read

$$u_Q = \frac{\partial \eta_Q}{\partial x} p_1, \qquad \frac{\partial \eta_Q}{\partial x} = Q/P_1, \tag{S3-15a}$$

$$u_d = \frac{\partial \eta_d}{\partial x} p_1 - \frac{1}{\rho_r} \frac{\partial \rho}{\partial x} p_2, \qquad \frac{\partial \eta_d}{\partial x} = \frac{1}{\rho_r} \frac{\partial \rho}{\partial x} P_2/P_1. \tag{S3-15b}$$

The polynomials used in Eq. S3-15a and S3-15b are

$$p_1 = \begin{cases} \frac{-gh}{\kappa \check{u}_* (1+\sigma_p)} \left(\ln \sigma' + \sigma_p \ln \sigma'' \right) & \text{for } \sigma \leqslant \sigma_h, \\ p_1|_{\sigma=\sigma_h} + \frac{gh\sigma_h{}^2}{2\kappa \check{u}_* (A_I - A_s)} \ln \left(\frac{A_\sigma}{A_I} \right) & \text{for } \sigma > \sigma_h, \end{cases}$$

$$p_2 = \begin{cases} \frac{-gh^2}{2\kappa \check{u}_* (1+\sigma_p)} \left(\sigma''' - \ln \sigma' + \sigma_p{}^2 \ln \sigma'' \right) & \text{for } \sigma \leqslant \sigma_h, \\ p_2|_{\sigma=\sigma_h} + \frac{gh^2\sigma_h{}^2}{2\kappa \check{u}_* (A_I - A_s)} \left[(\sigma - \sigma_h) - \frac{\chi_\sigma}{A_i} \right] & \text{for } \sigma > \sigma_h, \end{cases}$$

where

$$p_1|_{\sigma=\sigma_h} = \frac{-gh}{\kappa \check{u}_* (1+\sigma_p)} \left(\ln \sigma_h' + \sigma_p \ln \sigma_h'' \right),$$

$$p_2|_{\sigma=\sigma_h} = \frac{-gh^2}{2\kappa \check{u}_* (1+\sigma_p)} \left(\sigma_h''' - \ln \sigma_h' + \sigma_p{}^2 \ln \sigma_h'' \right),$$

$$\sigma' = \frac{\sigma+1}{\sigma_0}, \quad \sigma'' = \frac{\sigma_p - \sigma}{1+\sigma_p-\sigma_0}, \quad \sigma''' = (\sigma+1-\sigma_0)(1+\sigma_p),$$

$$\sigma_h' = \frac{\sigma_h+1}{\sigma_0}, \quad \sigma_h'' = \frac{\sigma_p - \sigma_h}{1+\sigma_p-\sigma_0}, \quad \sigma_h''' = (\sigma_h+1-\sigma_0)(1+\sigma_p),$$

$$\chi_\sigma = \sigma_h \left[\arctan \left(\sqrt{\frac{(A_I - A_s)}{A_s}} \frac{\sigma}{\sigma_h} \right) - \arctan \left(\sqrt{\frac{(A_I - A_s)}{A_s}} \right) \right],$$

$$Q = \int_0^x q_0 f(x)dx + Q_r.$$

Note that the capital "P" represents the cross-sectional integration of polynomial p, i.e., $\int_{-B}^{B} h \int_{-1}^{0} p \, d\sigma dy$.

s.3.2.2 *Solutions for lateral residual current components*

The equations for the lateral current due to Coriolis deflection of the longitudinal residual current are

$$fu = -g\frac{\partial \eta_f}{\partial y} + \frac{1}{h^2}\frac{\partial}{\partial \sigma}\left(A_v \frac{\partial v_f}{\partial \sigma}\right), \tag{S3-16a}$$

$$\frac{\partial}{\partial y}\int_{-1}^{0} h v_f d\sigma = 0. \tag{S3-16b}$$

Those for the residual current due to the lateral density gradient read

$$\frac{g}{\rho_r} h \int_{\sigma}^{0} \frac{\partial \rho}{\partial y} d\tilde{\sigma} = -g\frac{\partial \eta_d}{\partial y} + \frac{1}{h^2}\frac{\partial}{\partial \sigma}\left(A_v \frac{\partial v_d}{\partial \sigma}\right), \tag{S3-17a}$$

$$\int_{-B}^{B}\int_{-1}^{0} h u_d d\sigma dy = 0. \tag{S3-17b}$$

Finally, the equations

$$0 = -g\frac{\partial \eta_R}{\partial y} + \frac{1}{h}\frac{\partial}{\partial \sigma}\left(\frac{A_v}{h}\frac{\partial v_R}{\partial \sigma}\right), \tag{S3-18a}$$

$$\frac{\partial}{\partial x}\int_{-1}^{0} h u_Q d\sigma + \frac{\partial}{\partial y}\int_{-1}^{0} h v_R d\sigma = 0 \tag{S3-18b}$$

describe the residual current due to leakage. The corresponding solutions are

$$v_j = \frac{\partial \eta_j}{\partial y} p_1 - p_j, \qquad \frac{\partial \eta_j}{\partial y} = \int_{-1}^{0} h p_j d\sigma \Big/ \int_{-1}^{0} h p_1 d\sigma, \tag{S3-19}$$

with "j" denoting the lateral residual component due to Coriolis ("f"), lateral density gradient ("d") and leakage ("R"), with

$$p_f = \frac{h}{\kappa \check{u}_*}\int_{-1}^{\sigma} \frac{\int_{\tilde{\sigma}}^{0} f\overline{u} d\tilde{\sigma}_1}{A_\sigma} d\tilde{\sigma}, \quad p_d = \frac{h}{\kappa \check{u}_*}\int_{-1}^{\sigma} \frac{\int_{\tilde{\sigma}_1}^{0} \frac{g}{\rho_r} h \int_{\tilde{\sigma}_1}^{0} \left(\frac{\partial \overline{\rho}}{\partial y}\right)_{z^\dagger} d\tilde{\sigma}_1}{A_\sigma} d\tilde{\sigma},$$

$$p_R = -\frac{\partial}{\partial x}\int_{-B}^{y} u_Q d\sigma d\tilde{y} \Big/ \int_{-1}^{0} h p_1 d\sigma.$$

S.3.2.3 *Solution for the vertical distribution of SSC*

The dimensionless function $\phi(\sigma, h(y))$ in Eq. 4-11 of chapter 4 describes the vertical distribution of SSC. Its solution reads

$$\phi(\sigma, h(y)) = \begin{cases} P^0_{c1} \exp\left[\delta_K \frac{\ln(\sigma_p - \sigma) - \ln(1+\sigma)}{1+\sigma_p}\right], & \sigma \leqslant \sigma_h, \\ P^0_{c2} \exp\left[\delta_K \frac{\sigma_h \arctan\left(\sqrt{\frac{(A_I - A_s)}{A_s}} \frac{\sigma}{\sigma_h}\right)}{\sqrt{(A_I - A_s)A_s}}\right], & \sigma > \sigma_h. \end{cases} \tag{S3-20}$$

Here,

$$\delta_K = \frac{w_s}{S_c \kappa \breve{u}_*}, \quad P^0_{c1} = \exp\left[\delta_K \frac{\ln(\sigma_p + 1 - \sigma_0) - \ln(\sigma_0)}{1+\sigma_p}\right],$$

$$P^0_{c2} = P^0_{c1} \exp\left[\delta_K \frac{\ln(\sigma_p - \sigma_h) - \ln(1+\sigma_h)}{1+\sigma_p}\right] \exp\left[\delta_K \frac{\sigma_h \arctan\left(\sqrt{\frac{(A_I - A_s)}{A_s}}\right)}{\sqrt{(A_I - A_s)A_s}}\right].$$

S.3.3 *The sediment transport caused by curvature induced lateral current*

The equation that governs the residual current due to curvature (v_c) reads

$$-\frac{< u'u' >}{R} = -g\frac{\partial \eta_c}{\partial y} + \frac{1}{h^2}\frac{\partial}{\partial \sigma}\left(A_v \frac{\partial v_c}{\partial \sigma}\right), \tag{S3-21}$$

$$\frac{\partial}{\partial y}\int_{-1}^{0} h v_c \, d\sigma = 0. \tag{S3-22}$$

The boundary conditions for Eq. S3-21 are no-slip at the top of roughness height and free stress at the water surface.

Now the forcing $< u'u' >/R$ of v_c is compared with the forcing $f < u >$ of lateral current due to Coriolis deflection of the longitudinal residual current. The ratio of these two forcings is of order $(U_t^2/R_{min})/fU_R$. Here U_t, U_R are velocity scales of tidal current and residual current in the longitudinal direction. Note that this can be further written as $(U_t/U_R)/R_o$, in which $R_o = U_t/(fR_{min})$ is the Rossby number. In the North Passage of the Yangtze Estuary, $R_{min} =$ 50 km (Table 4-1 of chapter 4) and field data are used to estimate the scales of U_t and U_R during spring tide and neap tide, respectively. It is found that

$(U_t/U_R)/R_o$ is of order 1 during spring tide and $(U_t/U_R)/R_o \ll 1$ during neap tide.

It implies that the magnitude of the residual current v_c induced by curvature is comparable to residual current v_f induced by Coriolis deflection of longitudinal residual current during spring tide, but it is much weaker than the latter during neap tide. Note that v_c only acts in the curved part of the channel, where the current driven by lateral density gradient and leakage are much larger than v_f (Figure 4-12 of chapter 4). Thus, for this setting curvature induced lateral current can be neglected. In contrast, the residual current due to Coriolis deflection of longitudinal current is active in the entire channel and is of similar order as the lateral density driven current.

s.3.4 *Evidence of water leakage at the sampled transects*

Figure S3-1 shows the net water transport rate $\int_{-1}^{0} \vec{u} h d\sigma$, where $\vec{u}$ is the horizontal velocity vector, at cross-section A (black arrows) and B (red arrows) during spring tide (a) and during neap tide (b). At both two cross-sections, a northward directed water transport component is observed. During spring tide, at the cross-section A (which is closer to the curve), the northward directed component is stronger than that at the cross-section B. During neap tide, the northward directed component is weak both at two cross-sections.

s.3.5 *Sensitivity of results to model inputs*

In case the water leakage at the noruth side of the curved segment is compensated by inflow at the south bank, Eq. 4-6 of chapter 4 becomes

$$\int_{-1}^{0} h v d\sigma = f_c \qquad \text{at} \quad y = -B, \tag{S3-23a}$$

$$\int_{-1}^{0} h v d\sigma = q_0 f(x) \quad \text{at} \quad y = B. \tag{S3-23b}$$

Here, $f_c = L^{-1} \int_{x_1}^{x_2} \check{R}^{-1} dx$ is given in chapter 4. Correspondingly, Eq. 4-7 of chapter 4 becomes

$$f(x) = \begin{cases} 1/\check{R}, & x_1 \leqslant x \leqslant x_2, \\ 0, & 0 \leqslant x \leqslant x_1 \ \text{ and } \ x_2 \leqslant x \leqslant L. \end{cases} \tag{S3-24}$$

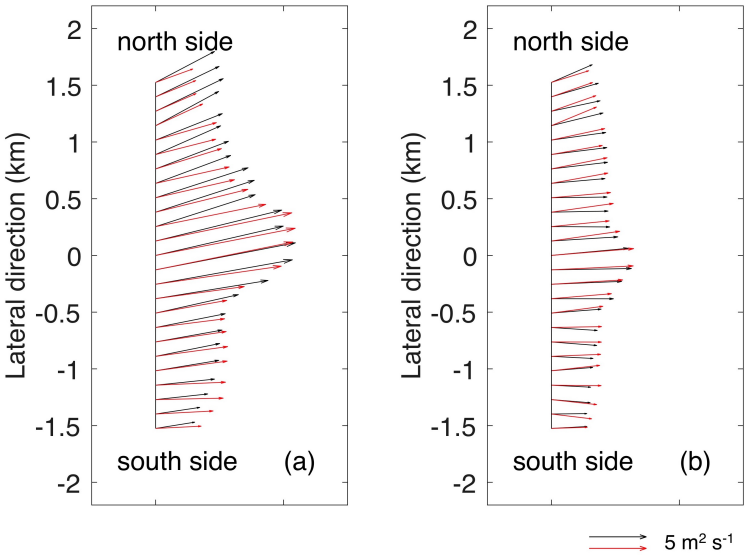

Figure S3-1: Net water transport rate at two sampled transects in the North Passage of the Yangtze Estuary during (a) spring tide and during (b) neap tide. Black and red arrows denote results for transects A and B, respectively.

Moreover, Eq. S3-16a and S3-16b read

$$T_y = q_{sed} f_c \quad \text{at} \quad y = -B, \tag{S3-25a}$$

$$T_y = q_{sed} f(x) \quad \text{at} \quad y = B. \tag{S3-25b}$$

The modelled near bed SSC distributions for model runs RS and RN, but with the compensation of leakage occuring at the southern regulation line is shown in Figure S3-2. It turns out that the SSC structures are similar to that of the of default runs (see Figure 4-13a and b of chapter 4). Figure S3-2c and d show model results for different values of n in Eq. 4-25 of chapter 4. Comparing with results of default run (see Figure 4-13a), the overall near bed SSC distributions are hardly changed.

Figure S3-3a shows the transverse distribution of residual current in cross-section T1 during spring tide. The overall structure is similar to that of the default runs as in chapter 4. The main difference is when a constant A_s is used in the model, the maximum seaward current is found at the surface above the two shoals. Larger SSC values are attained in the lower reach of the estuary. Moreover, two high SSC values occur near both the south and north sides of the middle section of the estuary (Figure S3-3b). During neap tide, a clear two

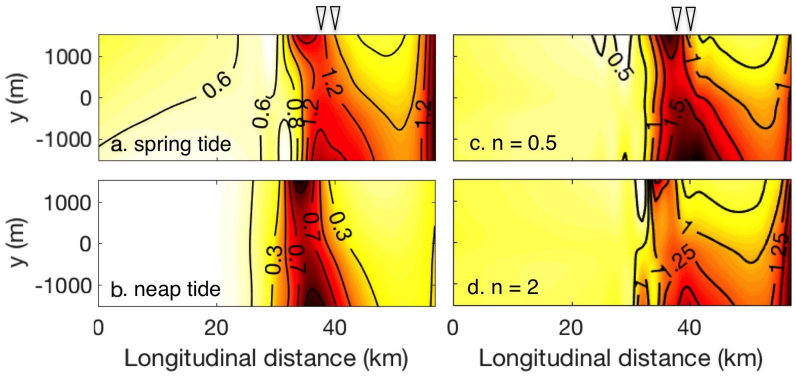

Figure S3-2: Near bed ($\sigma = -0.95$) distribution of SSC (in kg m^{-3}) in the estuary (a) during spring and (b) during neap tide in the case that the compensation of water leakage occurs at the south regulation line. (c) and (d) are as (a) and (b) but for the model run RS with $n = 0.5$ and $n = 2$ in Eq. 4-25 of chapter 4, respectively. Triangles at 37 km and 39 km denote the location of transects T1 and T2 in the longitudinal direction, respectively.

layer structure with landward current is observed in the lower part of the deep channel and near the north side. Near the water surface, the maximum seaward current is also found at the two shoals (Figure S3-3c). The maximum values of SSC are obtained at both the south and north sides inside the estuary (Figure S3-3d). The pattern in this figure is similar to that is shown in Figure 4-13a of chapter 4.

Figure S3-4 displays the near bed SSC distribution of model runs that using different values of q_{sed}, Q_{sed}. Results show that the choice of these parameters will locally change the value of SSC, however does not significantly affect the overall structure of SSC in the model domain.

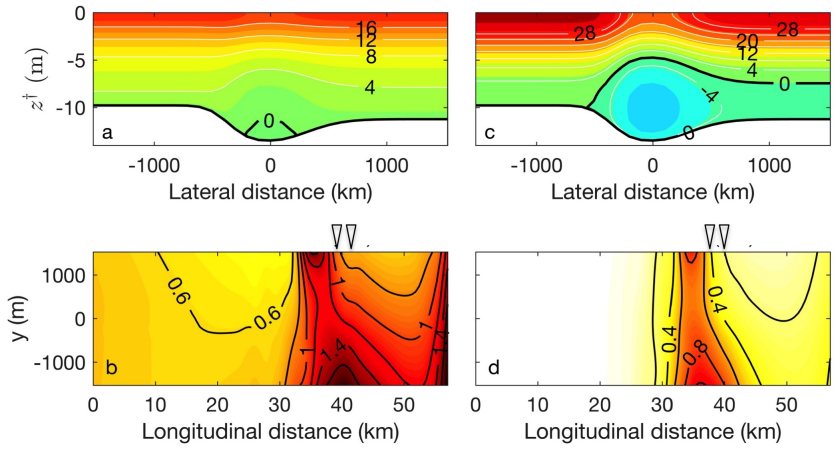

Figure S3-3: a. Transverse distribution of longitudinal residual current (in cm s^{-1}) in T1 and b. near-bed distribution of the SSC (in kg m^{-3}) result from the model run that $A_s = 0.005$ during spring tide. Plots (c) and (d) are the same as (a) and (b), respectively, but during neap tide. Orientation in (a) and (c) is into the estuary. In (b) and (d), triangles at 37 km and 39 km denote the location of transects T1 and T2 in the longitudinal direction, respectively.

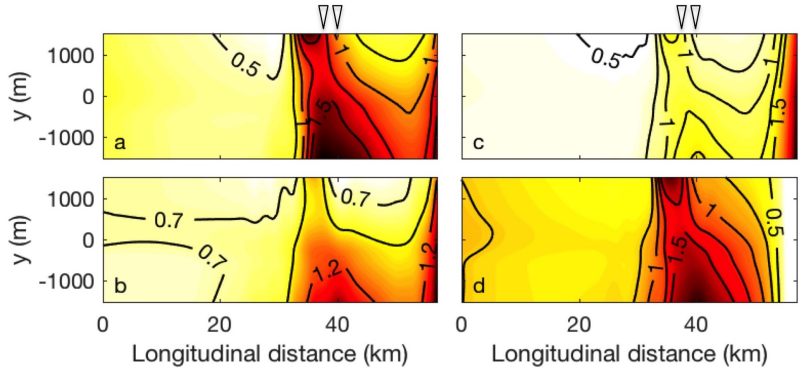

Figure S3-4: Near bed ($\sigma = -0.95$) distribution of the SSC (in kg m^{-3}) for the model run RS but with (a) $q_{sed} = 0.05$ kg s^{-1} m^{-1}, (b) $q_{sed} = 0.2$ kg s^{-1} m^{-1}, (c) $Q_{sed} = 700$kg s^{-1}, (d) $Q_{sed} = 900$kg s^{-1}.

BIBLIOGRAPHY

Anwar, H. O. (1983). "Turbulence measurements in stratified and well-mixed estuarine flows." In: *Estuar. Coast. Shelf Sci.* 17, pp. 243–260. DOI: 10.1016/0272-7714(83)90021-5 (cit. on p. 24).

Basdurak, N B, A Valle-Levinson, and P Cheng (2013). "Lateral structure of tidal asymmetry in vertical mixing and its impact on exchange flow in a coastal plain estuary." In: *Cont. Shelf Res.* 64, pp. 20–32. DOI: 10.1016/j.csr.2013.05.005 (cit. on pp. 22, 29, 33, 35, 39, 64).

Becherer, Johannes, Götz Flöser, Lars Umlauf, and Hans Burchard (2016). "Estuarine circulation versus tidal pumping: Sediment transport in a well-mixed tidal inlet." In: *J. Geophys. Res.* 121, pp. 6251–6270. DOI: 10.1002/2016JC011640 (cit. on p. 128).

Bowden, K. F. and S. H. Sharaf El Din (1966). "Circulation, salinity and river discharge in the Mersey estuary." In: *Geophys. J. Roy. Astron. Soc.* 10, pp. 383–399. DOI: 10.1111/j.1365-246X.1966.tb03066.x (cit. on pp. 13, 20, 22, 29, 33, 35).

Bowden, K. F., L. A. Fairbairn, and P. Hughes (1959). "The distribution of shearing stresses in a tidal current." In: *Geophys. J. Roy. Astron. Soc.* 2, pp. 288–305. DOI: 10.1111/j.1365-246X.1959.tb05801.x (cit. on p. 27).

Burchard, H. and H. Baumert (1998). "The formation of estuarine turbidity maxima due to density effects in the salt wedge." In: *J. Phys. Oceanogr.* 28, pp. 309–321. DOI: 10.1175/1520-0485(1998)028$<$0309:TFOETM$>$2.0.CO;2 (cit. on p. 37).

Burchard, H. and R. D. Hetland (2010). "Quantifying the contributions of tidal straining and gravitational circulation to residual circulation in periodically stratified tidal estuaries." In: *J. Phys. Oceanogr.* 40, pp. 1243–1262. DOI: 10.1175/2010JPO4270.1 (cit. on pp. 6, 11, 15, 24, 37, 43, 128).

Burchard, H. and H. M. Schuttelaars (2012). "Analysis of Tidal Straining as Driver for Estuarine Circulation in Well-Mixed Estuaries." In: *J. Phys. Oceanogr.* 42, pp. 261–271. DOI: 10.1175/JPO-D-11-0110.1 (cit. on pp. 37, 39).

Burchard, H., K. Bolding, and M. R. Villarreal (2004). "Three-dimensional modelling of estuarine turbidity maxima in a tidal estuary." In: *Ocean. Dyn.* 54, pp. 250–265. DOI: 10.1007/s10236-003-0073-4 (cit. on p. 68).

Burchard, H., R. D. Hetland, E. Schulz, and H. M. Schuttelaars (2011). "Drivers of Residual Estuarine Circulation in Tidally Energetic Estuaries: Straight and Irrotational Channels with Parabolic Cross Section." In: *J. Phys. Oceanogr.* 41.3, pp. 548–570. DOI: 10.1175/2010JPO4453.1 (cit. on p. 108).

Burchard, H., H M Schuttelaars, and W R Geyer (2013). "Residual Sediment Fluxes in Weakly-to-Periodically Stratified Estuaries and Tidal Inlets." In: *J. Phys. Oceanogr.* 43, pp. 1843–1860. DOI: 10.1175/JPO-D-12-0231.1 (cit. on p. 93).

Burchard, H., E. Schulz, and H. M. Schuttelaars (2014). "Impact of estuarine convergence on residual circulation in tidally energetic estuaries and inlets." In: *Geophys. Res. Lett.* 41, pp. 913–919. DOI: 10.1002/2013GL058494 (cit. on p. 64).

Chant, R. J. (2002). "Secondary circulation in a region of flow curvature: Relationship with tidal forcing and river discharge." In: *J. Geophys. Res.* 107.C9, p. 3131. DOI: 10.1029/2001JC001082 (cit. on pp. 2, 64).

Chen, S.-N. and L. P. Sanford (2009). "Lateral circulation driven by boundary mixing and the associated transport of sediments in idealised partially mixed estuaries." In: *Cont. Shelf Res.* 29, pp. 101–118. DOI: 10.1016/j.csr.2008.01.001 (cit. on pp. 8, 68).

Chen, W. and H. E. de Swart (2016). " Dynamic links between shape of the eddy viscosity profile and the vertical structure of tidal current amplitude in bays and estuaries." In: *Ocean Dyn.* 66, pp. 299–312. DOI: 10.1007/s10236-015-0919-6 (cit. on pp. 38, 60, 80, 81).

Chen, Z. and J. Le (2005). "Regulation principle of the Yangtze River Estuary deep channel." In: *Hydro-science and Engineering* 1, 1–7, (in Chinese with English abstract) (cit. on p. 84).

Cheng, P (2014). "Decomposition of Residual Circulation in Estuaries." In: *J. Atmos. Oceanic Technol.* 31.3, pp. 698–713. DOI: 10.1175/JTECH-D-13-00099.1 (cit. on pp. 64, 81, 107, 128).

Cheng, P, R E Wilson, R J Chant, D C Fugate, and R D Flood (2009). "Modeling influence of stratification on lateral circulation in a stratified estuary." In: *J. Phys. Oceanogr.* 39.9, pp. 2324–2337. DOI: 10.1175/2009JPO4157.1 (cit. on p. 64).

Cheng, P., A. Valle-Levinson, and H. E. de Swart (2010). "Residual currents induced by asymmetric tidal mixing in weakly stratified narrow estuaries." In: *J. Phys. Oceanogr.* 40, pp. 2135–2147. DOI: 10.1175/2010JPO4314.1 (cit. on pp. 37, 38).

Cheng, P., A. Valle-Levinson, and H. E. de Swart (2011). "A numerical study of residual circulation induced by asymmetric tidal mixing in tidally dominated estuaries." In: *J. Geophys. Res.* 116, p. C01017. DOI: 10.1029/2010JC006137 (cit. on pp. 7, 38, 65, 128).

Cheng, P., H. E. de Swart, and A. Valle-Levinson (2013). "Role of asymmetric tidal mixing in the subtidal dynamics of narrow estuaries." In: *J. Geophys. Res.* 118. DOI: 10.1002/jgrc.20189 (cit. on pp. 7, 12, 15, 21, 38, 43, 60, 65, 128).

Chernetsky, A. S., H. M. Schuttelaars, and S. A. Talke (2010). " The effect of tidal asymmetry and temporal settling lag on sediment trapping in tidal estuaries." In: *Ocean Dyn.* 60, pp. 1219–1241. DOI: 10.1007/s10236-010-0329-8 (cit. on pp. 8, 67, 83, 108).

Cloern, J. E., S. Q. Foster, and A. E. Kleckner (2013). "Review: phytoplankton primary production in the world's estuarine-coastal ecosystems." In: *Biogeosci. Discuss* 10, pp. 17725–17783. DOI: {10.5194/bgd-10-17725-2013} (cit. on pp. 5, 67).

Conomos, T. J., R. E. Smith, and J. W. Gartner (1985). "Environmental setting of San Francisco Bay." In: *Hydrobiologia* 129, pp. 1–12 (cit. on p. 30).

Cox, B A (2003). "A review of dissolved oxygen modelling techniques for lowland rivers." In: *Science of the Total Environment* 314, pp. 303–334. DOI: 10.1016/S0048-9697(03)00062-7 (cit. on p. 5).

Defant, Albert (1958). *Ebb and flow: The tides of earth, air, and water*. 1st. Ann Arbor: University of Michigan Press, 121 pp (cit. on p. 45).

Delft Hydraulics (2006). *Delft3D-FLOW user manual*. Delft, the Netherlands (cit. on pp. 39, 65).

Dijkstra, Y. M., H. M. Schuttelaars, and H. Burchard (2017). "Generation of exchange flows in estuaries by tidal and gravitational eddy viscosity-shear covariance (ESCO)." In: *J. Geophys. Res., Oceans* 122, pp. 4217–4237. DOI: 10.1002/2016JC012379 (cit. on pp. 7, 37).

Donker, J J A and H E de Swart (2013). "Effects of bottom slope, flocculation and hindered settling on the coupled dynamics of currents and suspended sediment in highly turbid estuaries, a simple model." In: *Ocean Dyn.* 63.4, pp. 311–327. DOI: 10.1007/s10236-013-0593-5 (cit. on pp. 8, 67).

Dronkers, J. J. (1964). *Tidal computations in rivers and coastal waters*. New York, 518 pp: Inter-science (Wiley) (cit. on p. 129).

Dyer, K R (1988). "Fine sediment particle transport in estuaries." In: *Physical processes in estuaries*, pp. 295–310 (cit. on pp. 8, 128).

Dyer, K. R. (1997). *Estuaries: a physical introduction*. 2nd. Chichester, England, 195 pp: John Wiley and sons (cit. on pp. 22, 24, 71).

Fan, Q. (2010). "Causes of back-siltation in the North Passage of Yangtze Estuary and evaluation of the engineering measures." In: *Proc. 32nd Conference on Coastal Engineering (ICCE 2010)*. Vol. 32 (cit. on p. 5).

Festa, J. F. and D. V. Hansen (1978). "Turbidity maxima in partially mixed estuaries: a two-dimensional numerical model." In: *Estuar. Coast. Mar. Sci.* 7, pp. 347–359. DOI: {10.1016/0302-3524(78)90087-7} (cit. on pp. 8, 67, 68, 128).

Fischer, H. (1972). "Mass transport mechanisms in partially stratified estuaries." In: *J. Fluid Mech.* 53.04, pp. 671–687. DOI: 10.1017/S0022112072000412 (cit. on p. 2).

Friedrichs, C. T. and J. M. Hamrick (1996). "Effects of channel geometry on cross sectional variations in along-channel velocity in partially stratified estuaries." In: *Buoyancy Effects on Coastal and Estuarine Dynamics*. Ed. by D. G. Aubrey and C. T. Friedrichs. Vol. 53. Washington, D. C.: Amer. Geophys. Union, pp. 283–300 (cit. on pp. 11, 13, 112).

Ge, J., C. Chen, J. Qi, P. Ding, and R. C. Beardsley (2012). "A dike–groyne algorithm in a terrain-following coordinate ocean model (FVCOM): Development, validation and application." In: *Ocean Model.* 47, pp. 26–40. DOI: 10.1016/j.ocemod.2012.01.006 (cit. on p. 94).

Geyer, W. R. (1993). "The importance of suppression of turbulence by stratification on the estuarine turbidity maximum." In: *Estuaries* 16, pp. 113–125. DOI: {10.2307/1352769} (cit. on pp. 8, 67, 128).

Geyer, W. R., J. H. Trowbridge, and M. Bowen (2000). "The Dynamics of a Partially Mixed Estuary." In: *J. Phys. Oceanogr.* 30, pp. 2035–2048. DOI: 10.1175/1520-0485(2000)030$<$2035:TDOAPM$>$2.0.CO;2 (cit. on pp. 6, 12, 13, 21, 22, 29, 33, 35, 37, 80).

Geyer, W. R., J. D. Woodruff, and P. Traykovski (2001). "Sediment transport and trapping in the Hudson River estuary." In: *Estuar. Coast.* 24, pp. 670–679. DOI: 10.2307/1352875 (cit. on pp. 8, 68, 94).

Geyer, W Rockwell and Parker MacCready (2014). "The estuarine circulation." In: *Annu. Rev. Fluid Mech.* 46, pp. 175–197. DOI: 10.1146/annurev-fluid-010313-141302 (cit. on pp. 2–4, 37, 39, 43–45, 48, 51, 53).

Giddings, S. N., S. G. Monismith, D. A. Fong, and M. T. Stacey (2014). "Using depth-normalized coordinates to examine mass transport residual circulation in estuaries with large tidal amplitude relative to the mean depth." In: *J. Phys. Oceanogr.* 44.1, pp. 128–148. DOI: 10.1175/JPO-D-12-0201.1 (cit. on p. 65).

Godin, G. (1999). "The propagation of tides up rivers with special considerations on the Upper Saint Lawrence River." In: *Est. Coast. Shelf Sci.* 48, pp. 307–324. DOI: 10.1006/ecss.1998.0422 (cit. on pp. 2, 129).

Green, M. O. (2011). "Very small waves and associated sediment resuspension on an estuarine intertidal flat." In: *Est. Coast. Shelf Sci.* 93, pp. 449–459. DOI: 10.1016/j.ecss.2011.05.021 (cit. on p. 93).

Hansen, D. V. and M. Jr. Rattray (1965). "Gravitational circulation in straits and estuaries." In: *J. Mar. Res.* 23, pp. 104–122 (cit. on pp. 2, 75).

Heaps, N. S. and J. E. Jones (1981). "Three-dimensional model for tides and surges with vertical eddy viscosity prescribed in two layers-II. Irish Sea with bed friction layer." In: *Geophys. J. Roy. Astron. Soc.* 64, pp. 303–320. DOI: 10.1111/j.1365-246X.1981.tb02670.x (cit. on pp. 6, 7, 11, 26–28).

Hoitink, A J F and D A Jay (2016). "Tidal river dynamics: Implications for deltas." In: *Rev. Geophys.* 54.1, pp. 240–272. DOI: 10.1002/2015RG000507 (cit. on p. 2).

Huijts, K. M. H., H. M. Schuttelaars, H. E. de Swart, and A. Valle-Levinson (2006). "Lateral entrapment of sediment in tidal estuaries: An idealized model study." In: *J. Geophys. Res.* 111, p. C12016. DOI: 10.1029/2006JC003615 (cit. on pp. 8, 11, 68, 83, 93, 128).

Huijts, K. M. H., H. M. Schuttelaars, H. E. de Swart, and C. T. Friedrichs (2009). "Analytical study of the transverse distribution of along-channel and transverse residual flows in tidal estuaries." In: *Cont. Shelf Res.* 29, pp. 89–100. DOI: 10.1016/j.csr.2007.09.007 (cit. on pp. 2, 13, 64, 112, 128).

Huijts, K M H, H E de Swart, G P Schramkowski, and H M Schuttelaars (2011). "Transverse structure of tidal and residual flow and sediment concentration in estuaries." In: *Ocean Dyn.* 61.8, pp. 1067–1091. DOI: 10.1007/s10236-011-0414-7 (cit. on p. 64).

Ianniello, J. P. (1977). "Tidally induced residual currents in estuaries of constant breadth and depth." In: *J. Mar. Res.* 35, pp. 755–786 (cit. on pp. 2, 6, 11, 13–15, 38, 93).

Jay, D. A. and J. D. Musiak (1994). "Particle trapping in estuarine tidal flows." In: *J. Geophys. Res.* 99, pp. 20,445–20,461. DOI: 10.1029/94JC00971 (cit. on pp. 6–8, 12, 29, 30, 37, 67).

Jay, D. A. and J. D. Musiak (1996). "Internal tidal asymmetry in channel flows: origins and consequences." In: *Mixing in Estuaries and Coastal Seas*. Ed. by C. Pattiaratchi. American Geophysical Union, pp. 211–249 (cit. on pp. 6, 11, 13, 21, 22, 33, 35).

Jiang, C., H. E. de Swart, J. Li, and G. Liu (2013). "Mechanisms of along-channel sediment transport in the North Passage of the Yangtze Estuary and their response to large-scale interventions." In: *Ocean Dyn.* 63, pp. 283–305. DOI: 10.1007/s10236-011-0414-7 (cit. on pp. 6, 7, 12, 13, 26, 27, 73, 93).

Jiang, Z., J. Chen, F. Zhou, L. Shou, Q. Chen, B. Tao, X. Yan, and K. Wang (2015). "Controlling factors of summer phytoplankton community in the Changjiang (Yangtze River) Estuary and adjacent East China Sea shelf." In: *Cont. Shelf Res.* 101, pp. 71–84. DOI: 10.1016/j.csr.2015.04.009 (cit. on p. 67).

Johns, B. (1966). "On the representation of the Reynolds stress in a tidal estuary." In: *Geophys. J. Roy. Astron. Soc.* 12, pp. 103–110 (cit. on pp. 6, 11).

Jonge, V N de, H M Schuttelaars, J E E van Beusekom, S A Talke, and H E de Swart (2014). "The influence of channel deepening on estuarine turbidity levels and dynamics, as exemplified by the Ems estuary." In: *Estuar. Coast. Shelf Sci.* 139, pp. 46–59. DOI: 10.1016/j.ecss.2013.12.030 (cit. on p. 5).

Kajiura, K. (1964). "On the bottom friction in an oscillatory current." In: *Bull. Earthquake Res. Inst.* 42, pp. 147–174 (cit. on p. 17).

Kim, Y. H. and G. Voulgaris (2008). "Lateral circulation and suspended sediment transport in a curved estuarine channel: Winyah Bay, SC, USA." In: *J. Geoph. Res.* 113, p. C09006. DOI: 10.1029/2007JC004509 (cit. on pp. 8, 68, 76).

Kumar, M, H M Schuttelaars, and P C Roos (2017). "Three-dimensional semi-idealized model for estuarine turbidity maxima in tidally dominated estuaries." In: *Ocean Model.* 113, pp. 1–21. DOI: 10.1016/j.ocemod.2017.03.005 (cit. on pp. 8, 108).

Lacy, J R and S G Monismith (2001). "Secondary currents in a curved, stratified, estuarine channel." In: *J. Geophys. Res.: Oceans* 106.C12, pp. 31283–31302. DOI: 10.1029/2000JC000606 (cit. on p. 2).

Lacy, J R, M T Stacey, J R Burau, and S G Monismith (2003). "Interaction of lateral baroclinic forcing and turbulence in an estuary." In: *J. Geophys. Res.: Oceans* 108.C3. DOI: 10.1029/2002JC001392 (cit. on pp. 12, 29, 31, 39).

Lamb, H. (1932). *Hydrodynamics*. 6th. Cambridge, England: Cambridge University Press (cit. on pp. 12, 25).

Lane, A., D. Prandle, A. J. Harrison, P. D. Jones, and C. J. Jarvis (1997). "Measuring fluxes in tidal estuaries: Sensitivity to instrumentation and associated data analyses." In: *Estuar. Coast. Shelf Sci.* 45, pp. 433–451. DOI: 10.1006/ecss.1996.0220 (cit. on p. 13).

Lerczak, J. A. and W. R. Geyer (2004). "Modeling the lateral circulation in straight, stratified estuaries." In: *J. Phys. Oceanogr.* 34, pp. 1410–1428. DOI: 10.1175/1520-0485(2004) (cit. on pp. 2, 31, 64, 128).

Lesser, G. R., J. A. Roelvink, J. A. T. M. Van Kester, and G. S. Stelling (2004). "Development and validation of a three-dimensional morphological model." In: *Coast. Eng.* 51.8, pp. 883–915. DOI: 10.1016/j.coastaleng.2004.07.014 (cit. on pp. 9, 39).

Li, J and C Zhang (1998). "Sediment resuspension and implications for turbidity maximum in the Changjiang Estuary." In: *Mar. Geol.* 148, pp. 117–124. DOI: 10.1016/S0025-3227(98)00003-6 (cit. on p. 93).

Li, M. and L. Zhong (2009). "Flood-ebb and spring-neap variations of mixing, stratification and circulation in Chesapeake Bay." In: *Cont. Shelf Res.* 29, pp. 4–14. DOI: 10.1016/j.csr.2007.06.012 (cit. on pp. 22, 33, 35).

Liu, G., J. Zhu, Y. Wang, H. Wu, and J Wu (2011). "Tripod measured residual currents and sediment flux: impacts on the silting of the deepwater navigation channel in the Changjiang estuary." In: *Est. Coast. Shelf Sci.* 93, pp. 192–201. DOI: 10.1016/j.ecss.2010.08.008 (cit. on p. 67).

Lorentz, H. A. (1922). "Het in rekening brengen van den weerstand bij schommelende vloeistofbewegingen." In: *De Ingenieur* 37, pp. 695–696 (cit. on pp. 17, 107).

May, C. L., J. R. Koseff, L. V. Lucas, J. E. Cloern, and D. H. Schoellhamer (2003). "Effects of spatial and temporal variability of turbidity on phytoplankton blooms." In: *Mar. Ecol. Prog. Ser.* 254, pp. 111–128. DOI: 10.3354/meps254111 (cit. on p. 67).

Mellor, G. L. and T. Yamada (1974). "A hierarchy of turbulence closure models for planetary boundary layers." In: *J. Atmos. Sci.* 31, pp. 1791–1806. DOI: 10.1175/1520-0469(1974)031$<$1791:AHOTCM$>$2.0.CO;2 (cit. on p. 24).

Monismith, S. G., W. Kimmerer, J. R. Burau, and M. T. Stacey (2002). "Structure and flow-induced variability of the subtidal salinity field in northern San Francisco Bay." In: *J. Phys. Oceanogr.* 32, pp. 3003–3019. DOI: 10.1175/1520-0485(2002)032$<$3003:SAFIVO$>$2.0.CO;2 (cit. on p. 94).

Munk, W. H. and E. R. Anderson (1948). "Note on the theory of the thermocline." In: *J. Mar. Res.* 7, pp. 276–295 (cit. on p. 82).

North, E. W., S. Y. Chao, L. P. Sanford, and R. R. Hood (2004). "The influence of wind and river pulses on an estuarine turbidity maximum: Numerical studies and field observations in Chesapeake Bay." In: *Estuar. Coast.* 27, pp. 132–146 (cit. on p. 93).

Nunes, R A and J H Simpson (1985). "Axial convergence in a well-mixed estuary." In: *Estuar. Coast. Shelf Sci.* 20.5, pp. 637–649. DOI: 10.1016/0272-7714(85)90112-X (cit. on p. 64).

Ozmidov, R V (1965). "On the turbulent exchange in a stably stratified ocean." In: *Izv. Atmos. Oceanic Phys.* 1.8, pp. 853–860 (cit. on p. 3).

Postma, H. (1961). "Transport and accumulation of suspended matter in the Dutch Wadden Sea." In: *Neth. J. Sea Res.* 1, pp. 148–190 (cit. on p. 8).

Postma, H. (1967). "Sediment transport and sedimentation in the estuarine environment." In: *American Association of Advanced Sciences* 83, pp. 158–179 (cit. on p. 67).

Prandle, D. (1982). "The vertical structure of tidal currents and other oscillatory flows." In: *Cont. Shelf Res.* 1, pp. 191–207. DOI: 10.1016/0278-4343(82)90004-8 (cit. on pp. 12, 13, 25, 27).

Pritchard, D W (1956). "The dynamic structure of a coastal plain estuary." In: *J. Mar. Res.* 15.1, pp. 33–42 (cit. on p. 2).

Pritchard, D. W. (1967). "What is an estuary: physical viewpoint." In: vol. 83. American Association for the Advancement of Science, pp. 3–5 (cit. on p. 1).

Ralston, D. K., W. R. Geyer, and J. A. Lerczak (2008). "Subtidal salinity and velocity in the Hudson River Estuary: Observations and modeling." In: *J. Phys. Oceanogr.* 38, pp. 753–770. DOI: 10.1175/2007JPO3808.1 (cit. on pp. 14, 81).

Ross, D. A. (1995). *Introduction to Oceanography*. New York, USA: Harper Collins (cit. on p. 5).

Ruijter, W. P. M. de (1983). "Effects of velocity shear in advective mixed-layer models." In: *J. Phys. Oceanogr.* 13.9, pp. 1589–1599. DOI: 10.1175/1520-0485(1983)013$<$1589:EOVSIA$>$2.0.CO;2 (cit. on pp. 6, 37).

Sanford, L. P., S. E. Suttles, and J. P. Halka (2001). "Reconsidering the physics of the Chesapeake Bay estuarine turbidity maximum." In: *Estuaries* 24, pp. 655–669. DOI: 10.2307/1352874 (cit. on p. 67).

Schubel, J. R. and H. H. Carter (1984). "The estuary as a filter for fine-grained suspended sediment." In: *The estuary as a filter*. Elsevier, pp. 81–105 (cit. on p. 67).

Schulz, E., H. M. Schuttelaars, U. Grwe, and H. Burchard (2015). "Impact of the Depth-to-Width Ratio of Periodically Stratified Tidal Channels on the Estuarine Circulation." In: *J. Phys. Oceanogr.* 45, pp. 2048–2069. DOI: 10.1175/JPO-D-14-0084.1 (cit. on p. 108).

Schuttelaars, H. M., V. N. de Jonge, and A. Chernetsky (2013). "Improving the predictive power when modelling physical effects of human interventions in estuarine systems." In: *Ocean Coast. Manage.* 79, pp. 70–82. DOI: 10.1016/j.ocecoaman.2012.05.009 (cit. on p. 68).

Scully, M. E. and C. T. Friedrichs (2007). "The importance of tidal and lateral asymmetries in stratification to residual circulation in partially mixed estuaries." In: *J. Phys. Oceanogr.* 37, pp. 1496–1511. DOI: 10.1175/JPO3071.1 (cit. on pp. 64, 128).

Scully, M. E., W. R. Geyer, and J. A. Lerczak (2009). "The influence of lateral advection on the residual estuarine circulation: A numerical modeling study of the Hudson River Estuary." In: *J. Phys. Oceanogr.* 39, pp. 107–124. DOI: 10.1175/2008JPO3952.1 (cit. on pp. 2, 93, 128).

Seim, H. E. and M. C. Gregg (1997). "The importance of aspiration and channel curvature in producing strong vertical mixing over a sill." In: *J. Geophys. Res., Oceans* 102, pp. 3451–3472. DOI: 10.1029/96JC03415 (cit. on p. 64).

Shi, J Z (2004). "Behaviour of fine suspended sediment at the North passage of the Changjiang Estuary, China." In: *J. Hydrol.* 293, pp. 180–190. DOI: 10.1016/j.jhydrol.2004.01.014 (cit. on p. 69).

Shi, Z., H. J. Zhou, S. L. Eittreim, and J. C. Winterwerp (2003). "Settling velocities of fine suspended particles in the Changjiang Estuary, China." In: *J. Asian Earth Sci.* 22, pp. 245–251. DOI: 10.1016/S1367-9120(03)00067-1 (cit. on p. 84).

Simpson, J. H., J. Brown, J. Matthew, and G. Allen (1990). "Tidal straining, density currents, and stirring in the control of estuarine stratification." In: *Estuaries* 13, pp. 125–132. DOI: 110.2307/1351581 (cit. on pp. 6, 31, 37).

Simpson, J. H., H. Burchard, N. R. Fisher, and T. P. Rippeth (2002). "The semidiurnal cycle of dissipation in a ROFI: model-measurement comparisons." In: *Cont. Shelf Res.* 22, pp. 1615–1628. DOI: 10.1016/S0278-4343(02)00025-0 (cit. on pp. 26, 37).

Simpson, J. H., E. Williams, L. H. Brasseur, and J. M. Brubaker (2005). "The impact of tidal straining on the cycle of turbulence in a partially stratified estuary." In: *Coast. Shelf Res.* 25, pp. 51–64. DOI: 10.1016/j.csr.2004.08.003 (cit. on pp. 37, 38).

Song, D. and X. H. Wang (2013). "Suspended sediment transport in the Deep-water Navigation Channel, Yangtze River Estuary, China, in the dry season

2009: 2. Numerical simulations." In: *J. Geophys. Res.* 118, pp. 5568–5590. DOI: 10.1002/jgrc.20411 (cit. on pp. 27, 68, 73, 93, 108).

Soulsby, R. L. (1983). "The bottom boundary layer of shelf seas." In: *Physical oceanography of coastal and shelf seas*. Ed. by B. Johns. Vol. 35. Amsterdam, the Netherlands: Elsevier Science Publishers B. V., pp. 189–266 (cit. on pp. 13, 27, 28).

Souza, A. J. (2013). "On the use of the Stokes number to explain frictional tidal dynamics and water column structure in shelf seas." In: *Ocean Sci.* 9, pp. 391–398. DOI: 10.5194/os-9-391-2013 (cit. on pp. 13, 28).

Stacey, M. T. and D. K. Ralston (2005). "The Scaling and Structure of the Estuarine Bottom Boundary Layer." In: *J. Phys. Oceanogr.* 35, pp. 55–71. DOI: 10.1175/JPO-2672.1 (cit. on p. 14).

Stacey, M. T., S. G. Monismith, and J. R. Burau (1999). "Measurements of Reynolds stress profiles in unstratified tidal flow." In: *J. Geophys. Res.* 104, pp. 10933–10949 (cit. on p. 24).

Stacey, M. T., J. R. Burau, and S. G. Monismith (2001). "Creation of residual flows in a partially stratified estuary." In: *J. Geophys. Res.* 106, pp. 17,013–17,037. DOI: 10.1029/2000JC000576 (cit. on pp. 6, 37).

Stacey, M. T., J. P. Fram, and F. K. Chow (2008). "Role of tidally periodic density stratification in the creation of estuarine subtidal circulation." In: *J. Geophys. Res.* 113, p. C08016. DOI: 10.1029/2007JC004581 (cit. on pp. 21, 37).

Stacey, M. T., M. L. Brennan, J. R. Burau, and S. G. Monismith (2010). "The tidally averaged momentum balance in a partially and periodically stratified estuary." In: *J. Phys. Oceanogr.* 40.11, pp. 2418–2434. DOI: 10.1175/2010JPO4389.1 (cit. on p. 37).

Talke, S. A., H. E. de Swart, and V. N. de Jonge (2009a). "An idealized model and systematic process study of oxygen depletion in highly turbid estuaries." In: *Estuar. Coast.* 32, pp. 602–620. DOI: 10.1007/s12237-009-9171-y (cit. on pp. 3, 67).

Talke, S. A., H. E. de Swart, and H. M. Schuttelaars (2009b). "Feedback between residual circulation and sediment distribution in highly turbid estuaries: an analytical model." In: *Cont. Shelf Res.* 29, pp. 119–135. DOI: 10.1016/j.csr.2007.09.002 (cit. on pp. 67, 68, 93).

Thill, Antoine, Stéphane Moustier, Jean-Marie Garnier, Claude Estournel, Jean-Jacques Naudin, and Jean-Yves Bottero (2001). "Evolution of particle size and concentration in the Rhône river mixing zone:: influence of salt flocculation." In: *Continental Shelf Research* 21.18, pp. 2127–2140. DOI: 10.1016/S0278-4343(01)00047-4 (cit. on p. 3).

Valle-Levinson, A. (2010). *Contemporary issues in estuarine physics*. Cambridge, UK: Cambridge University Press (cit. on p. 2).

Valle-Levinson, Arnoldo, Cristobal Reyes, and Rosario Sanay (2003). "Effects of bathymetry, friction, and rotation on estuary–ocean exchange." In: *J. Phys.*

Oceanogr. 33, pp. 2375–2393. DOI: 1520-0485(2003)033$<$2375:EOBFAR$>$2.0.CO;2 (cit. on p. 94).

Verspecht, F. I., T. P. Rippeth, A. J. Souza, H. Burchard, and M. J. Howarth (2009). "Residual circulation and stratification in the LiverpoolBay region of freshwater influence." In: *Ocean Dyn.* 59, pp. 765–779. DOI: 10.1007/s10236-009-0233-2 (cit. on p. 38).

Wan, Y and D Zhao (2017). "Observation of saltwater intrusion and ETM dynamics in a stably stratified estuary: the Yangtze Estuary, China." In: *Environ. Monit. Assess.* 189, p. 89. DOI: 10.1007/s10661-017-5797-6 (cit. on p. 73).

Wang, X. H. (2002). "Tide-induced sediment resuspension and the bottom boundary layer in an idealised estuary with a muddy bed." In: *J. Phys. Oceanogr.* 32, pp. 3113–3131. DOI: 10.1175/1520-0485(2002) (cit. on pp. 23, 24).

Wang, Y., J. Gao, and S. Pan (2006). "Measurement of bottom boundary layer parameters of the Yangtze River Estuary." In: *Marine Geology Letters* 22, 16–20, (in Chinese with English abstract) (cit. on p. 84).

Warner, J. C., W. R. Geyer, and J. A. Lerczak (2005). "Numerical modeling of an estuary: A comprehensive skill assessment." In: *J. Geophys. Res.* 110, p. C05001. DOI: 10.1029/2004JC002691 (cit. on pp. 6, 11, 76).

Winant, C. D. (2007). "Three-dimensional tidal flow in an elongated, rotating basin." In: *J. Phys. Oceanogr.* 37, pp. 2345–2362. DOI: 10.1175/JPO3122.1 (cit. on pp. 6, 11).

Winant, C D (2008). "Three-dimensional residual tidal circulation in an elongated, rotating basin." In: *J. Phys. Oceanogr.* 38.6, pp. 1278–1295. DOI: 10.1175/2007JPO3819.1 (cit. on p. 2).

Winterwerp, J. C., Z. Wang, A. van Braeckel, G. van Holland, and F. Kösters (2013). "Man-induced regime shifts in small estuaries - II: a comparison of rivers." In: *Ocean Dyn.* 63.11-12, pp. 1293–1306. DOI: 10.1007/s10236-013-0663-8 (cit. on pp. 5, 67, 93).

Winterwerp, J.C. (2002). "On the flocculation and settling velocity of estuarine mud." In: *Cont. Shelf Res.* 22, pp. 1339–1360. DOI: 10.1016/S0278-4343(02) (cit. on p. 8).

Wolf, J. (1980). "Estimation of shearing stresses in a tidal current with application to the Irish sea." In: *Marine Turbulence, Proceedings of the 11th Liège International Colloquium on Ocean Hydrodynamics*. Ed. by J. C. J. Nihoul. Amsterdam: Elsevier Oceanography Series, 28, pp. 319–344 (cit. on p. 26).

Wu, H, J Zhu, and B H Choi (2010). "Links between saltwater intrusion and subtidal circulation in the Changjiang Estuary: A model-guided study." In: *Cont. Shelf Res.* 30.17, pp. 1891–1905. DOI: 10.1016/j.csr.2010.09.001 (cit. on p. 5).

Wu, J., Y. Wang, and H. Cheng (2009). "Bedforms and bed material transport pathways in the Changjiang (Yangtze) Estuary." In: *Geomorphology* 104, pp. 175–184. DOI: 10.1016/j.geomorph.2008.08.011 (cit. on p. 84).

Wu, J, J T Liu, and X Wang (2012). "Sediment trapping of turbidity maxima in the Changjiang Estuary." In: *Mar. Geol.* 303, pp. 14–25. DOI: 10.1016/j.margeo.2012.02.011 (cit. on p. 73).

Yang, Z., H. E. de Swart, H. Cheng, C. Jiang, and A. Valle-Levinson (2014). "Modelling lateral entrapment of suspended sediment in estuaries - The role of spatial lags in settling and M_4 tidal flow." In: *Cont. Shelf Res.* 85, pp. 126–142. DOI: 10.1016/j.csr.2014.06.005 (cit. on pp. 8, 68).

Zhu, Z., J. Zhang, Y. Wu, Y. Zhang, J. Lin, and S. Liu (2011). "Hypoxia off the Changjiang (Yangtze River) Estuary: Oxygen depletion and organic matter decomposition." In: *Mar. Chem.* 125.1, pp. 108–116. DOI: 10.1016/j.marchem.2011.03.005 (cit. on p. 67).

Zimmerman, J. T. F. (1982). "On the Lorentz linearization of a quadratically damped forced oscillator." In: *Phys. Lett.* 89, pp. 123–124. DOI: 10.1016/0375-9601(82)90871-4 (cit. on p. 17).

Zimmerman, J. T. F. (1986). "The tidal whirlpool: A review of horizontal dispersion by tidal and residual currents." In: *Neth. J. Sea Res.* 20, pp. 133–154. DOI: 10.1016/0077-7579(86)90037-2 (cit. on p. 82).

Zitman, T. J. and H. M. Schuttelaars (2012). "Importance of cross-channel bathymetry and eddy viscosity parameterization in modelling estuarine flow." In: *Ocean Dyn.* 62, pp. 755–786. DOI: 10.1007/s10236-011-0513-5 (cit. on pp. 11, 15, 24).

van Aken, H. M. (1986). "The onset of seasonal stratification in shelf seas due to differential advection in the presence of a salinity gradient." In: *Cont. Shelf Res.* 5, pp. 475–485. DOI: 10.1016/0278-4343(86)90071-3 (cit. on pp. 6, 37).

van Maren, D. S., A. P. Oost, Z. B. Wang, and P. C. Vos (2016). "The effect of land reclamations and sediment extraction on the suspended sediment concentration in the Ems Estuary." In: *Mar. Geol.* 376, pp. 147–157. DOI: 10.1016/j.margeo.2016.03.007 (cit. on p. 68).

ACKNOWLEDGMENTS

One afternoon in September 2012, I showed the dissertation of Karin Huijts to my parents and I said: "By the day that I stand in the Academiegebouw Utrecht University, I will also have a book of my own!" They looked at me, eyes were full of doubts, worries and encouragement. Completing a PhD was one of the most intensive, challenging and interesting experience that I have ever had so far. Today, I made it, with the great help and support of many people around me.

Thank you Huib, for giving me the opportunity to specialize my research in physical processes of estuaries! In 2011, when I visited Utrecht University as an exchange student, I was completely fascinated by your passion for teaching and research topics. It is my great honour and pleasure working with you. Your endless support, careful supervision and encouragement gave me power and confidence to complete such a "mission impossible". Every time when I was struggling in "swamps", you were there helping me out with inspirations, patience and comprehensive answerings. Sometimes you apologized for being too strict with me. However, I greatly appreciate your strict. There is an old Chinese saying said a strict teacher produces outstanding students. I can feel my improvement in my scientific life.

A big "Thank you" to my coastal group! Niels, you are the first Dutch I met. You helped me with solving a lot of problems in research. You are also a great friend in my life. We played Mahjong over a whole night, sang karaoke in Shanghai. You invited me to your family dinner. You are the photographer of my love shoot as well! Wim, you are very easygoing! We had a lot of happy trips together! We went to Zurich for running event, to Denmark for summer school. You also supported me in numerical simulation with Delft3D. Abdel, do you know what I miss a lot after I left IMAU? Your well prepared Morocco Tea (I still have some with me), Tricolore cappuccino with interesting stories, and of course, your Morocco cooking! Erik, you helped me a lot with my research. We had similar research methods. Your work allowed me to quickly get in the right direction! Captain Tjebbe, thank you for inviting me to your boat 'Gudsekop' and to experience a traditional Dutch sailing life! Carles, Miguel, Stavros and Konstantinos, it was great to have you guys in our group and to play basketball together! Those games released me from the heave work.

I would like to thank my officemates, Michael and Paul. Thank you for all jokes you made in these years, they made our office a happy room. I hope the competition of body mass index (BMI) and body fat percentage (BFP) between us will continue. Will Michael still have the highest BFP? Thank you IMAUers

for making these years fun: Alexis, Davide, Claudia, Andr, Getachew and Sudhanshu, you made the sixth floor of Buys Ballotgebouw a great place. I would also like to thank Sandra, Yvonne and Floor, who helped me a lot in dealing with formalities, and Marcel for all technical support!

My Chinese friends supported and enriched my daily life in Utrecht. Gu Xin, Guanning, Yuan Bin, Liu Bo, Yin Zun, Qingyi, Kangming, Xiaoli, Donglong and many others shared with me a lot of wonderful memories during the years I stayed in Utrecht! I also give my thankfulness to my master supervisor Jiufa Li for his support in my research. I especially thank Qinhua Ye from Deltares for his assistance in my Delft3D hydrodynamic modelling. Besides, I owe a big debt of gratitude to Hualin Wu and Yuanye Wang from Shanghai Estuarine and Coastal Science Research Center, who provided first-hand data that has been used in this dissertation.

Finally, a big thankfulness goes to my family from the bottom of my heart. Thank you, mum and dad, for your respect for my decision, the unconditional and consistent support from far away. Thank you for your understanding of my absence in the family reunion of last four years. Thank you, my wife, Li Qian. Your companionship carried me through the hardest moment of my PhD. Your endless love offered me the greatest motivation overcoming difficulties. Your meticulous care allowed me delivering all-out performance on this challenging dissertation.

CURRICULUM VITAE

Wei Chen was born on February 24, 1986, in Songzi, China. He grew up by the river Yangtze (Changjiang), which runs a thousand kilometres eastward to the Pacific Ocean. He had read in books, watched on TV, and dreamed in mind all beauties about seas from a young age. At the age of 23, after four years studying in Applied Physics at Zhengzhou University in an inland city, he decided to work on something that allows him to be beside the seaside. He went to Shanghai, started his master programme in State Key Laboratory of Estuarine and Coastal research at East China Normal University (ECNU). His work focuses on recent current and sediment transport in bifurcation area of the North and South Passage of the Yangtze Estuary and their response to human interventions. After the master study, he shortly worked in Shanghai Estuarine and Coastal Science Research Center for an internship. In October 2012, Wei obtained a funding from Chinese Scholarship Council (CSC) and move to the Institute for Marine and Atmospheric research Utrecht (IMAU) to pursue a PhD degree under the direction of Huib de Swart. His PhD project aims to improve understanding of hydrodynamics and sediment dynamics in estuaries with different density stratification conditions, of which this dissertation is the result.

This document was typeset using `classicthesis` developed by André Miede.